



The University of
Nottingham

**Detailed Structure of the Venous
Drainage of the Brain: Relevance to
Accidental and Non-Accidental
Traumatic Head Injuries**

Seneka Nakagawa, BMedSci

**Thesis submitted to the University of Nottingham
for the degree of Doctor of Philosophy**

March 2014

Contents

Contents.....	i
Abstract	viii
Conferences and Peer-reviewed Publications	ix
Acknowledgements	x
List of Definitions and Abbreviations.....	xi
List of Figures	xiv
List of Tables.....	xxiv
Chapter 1. Introduction and Literature Review	1
1.1. Background.....	1
1.2. Summary of Anatomy of the Meninges and Venous System.....	2
1.3. Introduction to NAHI and SBS.....	9
1.4. Introduction to Hypotheses and Theories regarding SDH in NAHI ..	10
1.4.1. Rotational Acceleration of the Head causing Bridging Vein Rupture.....	11
1.4.2. Multiple Acceleration/Deceleration and Whiplash Injuries causing Bridging Vein Damage.....	12
1.4.3. Impact-Deceleration Injury and Short Distance Falls	14
1.4.4. Neck and Cervical-Spinal Cord Injury.....	17
1.4.5. Hypoxic-Ischaemic Injury	19
1.4.6. Unified Hypothesis	21
1.4.7. Further Mechanisms.....	22
1.4.8. Evidence against Bridging Vein Rupture	22
1.4.9. Intradural Vascular Plexus	24
1.4.10. Chronic Subdural Haemorrhage (CSDH).....	25
1.4.11. Birth-Related SDH.....	27
1.4.12. Neomembrane Formation.....	28
1.4.13. Movement of CSF.....	29

1.4.14. Involvement of the Arachnoid Membrane.....	29
1.4.15. Involvement of CSF and the Intravascular Plexus	30
1.5. Brief Introduction into Tissue Fixation.....	30
1.5.1. Perfusion Fixation	31
1.5.1.1. Formaldehyde Fixative	31
1.5.2.1. Glutaraldehyde Fixative.....	31
1.6. Brief History of Resins and Vascular Corrosion Casting (VCC)	32
1.6.1. Delivery of Fluids into the Circulatory System.....	33
1.6.2. Vascular Casting	33
1.7. Introduction to Imaging	34
1.7.1. Imaging of the Intracranial Venous System	35
1.7.2. Qualitative Analysis	35
1.7.2.1. MRI and CT.....	35
1.7.2.2. SEM and TEM	36
1.7.2.3. Combining MRI and EM in a Clinical Setting.....	37
1.7.3. Quantitative Analysis	37
1.7.3.1. Confocal Microscopy.....	37
1.7.3.2. MicroCT and 3D X-Ray Microscopy (XRM)	38
1.7.4. Combining Qualitative and Quantitative Analysis Techniques ...	40
1.7.5. Imaging of Intracranial Vessels and Investigating Head Trauma Cases.....	40
1.7.5.1. General Overview	40
1.7.5.2. Investigating Retinal Haemorrhage	41
1.7.5.3. Skeletal Surveys.....	42
1.7.5.4. MRI and CT Scanning	42
1.7.5.5. Discrepancies and Distinguishing Between Accidental and NAHIs	43
1.7.6. Summary, Aims and Objectives	44
Chapter 2. Cerebral Microvasculature of the Rat: Resin Casting and SEM.....	46
2.1. Introduction	46

2.2. Materials and Methods	47
2.2.1. Methodology for Cardiac Perfusion Fixation and PU4ii Resin Perfusion.....	52
2.2.1.1. Calculation of the Total Blood Volume of a Rat	52
2.2.1.2. Vascular Resin Casting	55
2.2.2. Tissue Processing.....	55
2.2.2.1. Dissection and Decalcification.....	55
2.2.2.2. Maceration and Osmocation	55
2.2.2.3. Lyophilisation (Freeze-drying)	56
2.2.3. Tissue Analysis	56
2.2.3.1. Macroscopy.....	56
2.2.3.2. Scanning Electron Microscopy (SEM)	56
2.2.3.3. Environmental Scanning Electron Microscopy (ESEM)	57
2.2.3.4. Histology and FM Imaging	58
2.2.3.5. Preparation of Histological Specimens	59
2.2.3.6. Acquiring Bright Field (BF) and Fluorescence Microscopy (FM) Images.....	61
2.2.3.7. Acquiring Confocal Microscopy (CM) Images	62
2.2.3.8. MicroCT Imaging of Vascular Casts	63
2.2.3.9. Volume Rendering and Approximating Vessel Size from MicroCT Imaging Datasets	64
2.3. Results.....	65
2.3.1. Vascular Resin Casting and SEM Imaging.....	65
2.3.2. Vascular Resin Casting and ESEM Imaging.....	67
2.3.2.1. ESEM Imaging of VCCs	67
2.3.2.2. ESEM Imaging of 1mm Coronal Sections of Resin Perfused Brain and Skull	86
2.3.3. Histology and Fluorescence Microscopy (FM) Imaging	89
2.3.4. Confocal Microscopy of Resin Perfused Tissue	91
2.3.5. MicroCT Imaging.....	91

2.3.6. Volume Rendering and Approximating Vessel Size from microCT Imaging Datasets.....	93
2.4. Discussion.....	94
2.4.1. Intradural and Subdural Vessels	95
2.4.2. ESEM Imaging of VCCs	95
Chapter 3. Investigating Venous Anatomy in the Human (<i>Homo sapiens</i>)	98
3.1. Introduction.....	98
3.2. Materials and Methods	98
3.2.1. Perfusion Fixation and PU4ii Resin Perfusion of Fresh Cadaveric Material.....	98
3.2.1.1. Calculation of the Cerebral Blood Volume (CBV) of an Adult Human	98
3.2.1.2. Perfusion Fixation and PU4ii Resin Perfusion of Fresh Cadaveric Material.....	99
.....	100
3.2.2. Gross Dissection of Cadaveric Material.....	100
3.2.3. Histological Evaluation of Prefixed and Resin Perfused Cadaveric Material.....	100
3.2.4. MRI Imaging of Pre-fixed Cadaveric Material.....	101
3.2.5. MRI Imaging of the Human Head <i>in Vivo</i>	102
3.2.6. Small Vein Segmentation using MRI Data	103
3.3. Results.....	105
3.3.1. Gross Dissection of Pre-fixed Cadaveric Material.....	105
3.3.2. Resin Casting and Gross Dissection of Resin Perfused Cadaveric Material.....	107
3.3.3. Histology - Prefixed and Resin Perfused Cadaveric Material....	108
3.3.4. MRI Imaging of the Human Head <i>in Vivo</i>	111
3.3.5. Small Vein Segmentation using MRI Data	116
3.4. Discussion.....	118

Chapter 4. Investigating Venous Anatomy in the Primate (<i>Callithrix jacchus</i> and <i>Macaca mulatta</i>).....	121
4.1. Introduction.....	121
4.2. Materials and Methods	123
4.2.1. Marmoset (<i>Callithrix jacchus</i>)	123
4.2.1.1. PU4ii Resin Perfusion.....	123
4.2.1.2. Gross Dissection and Decalcification.....	124
4.2.1.3. Dissection.....	125
4.2.1.4. Maceration.....	125
4.2.1.5. Osmocation and Lyophilisation (Freeze-drying)	125
4.2.1.6. Macroscopy.....	126
4.2.1.7. Environmental Scanning Electron Microscopy (ESEM)	126
4.2.1.8. Histology: LM and TEM Imaging	126
4.2.1.9. Magnetic Resonance Imaging (MRI)	127
4.2.1.10. MicroCT Imaging of Vascular Casts.....	127
4.2.1.11. Computer-Aided Analysis of MicroCT Imaging Datasets.....	127
4.2.2. Rhesus Macaque (<i>Macaca Mulatta</i>)	129
4.2.2.1. Cardiac Perfusion Fixation and PU4ii Resin Vascular Casting.....	129
4.2.2.2. Gross Dissection and Decalcification.....	139
4.2.2.3. Dissection.....	139
4.2.2.4. Maceration.....	139
4.2.2.5. Osmocation and Lyophilisation (Freeze-drying)	139
4.2.2.6. Macroscopy.....	140
4.2.2.7. Environmental Scanning Electron Microscopy (ESEM)	140
4.2.2.8. 3D XRM of VCCs	140
4.2.2.9. Computer-Aided Analysis of 3D XRM Imaging Datasets	141
4.2.2.10. Histology and FM Imaging.....	141
4.3. Results.....	144
4.3.1. Marmoset (<i>Callithrix jacchus</i>)	145
4.3.1.1. Gross Dissection of Prefixed Marmoset Material	145

4.3.1.2. Vascular Resin Casting and ESEM Imaging of VCCs	147
4.3.1.3. Histology: LM and TEM Imaging of Pre-fixed Marmoset Material	153
4.3.1.4. Magnetic Resonance Imaging (MRI)	158
4.3.1.5. MicroCT Imaging	158
4.3.1.6. Computer-Aided Analysis of MicroCT Imaging Datasets	159
4.3.2. Macaque (<i>Macaca mulatta</i>)	160
4.3.2.1. Gross Dissection of Macaque Material	160
4.3.2.2. Vascular Resin Casting and ESEM Imaging	163
4.3.2.3. 3D XRM and Computer-Aided Analysis of Imaging Datasets	166
4.3.2.4. Gold Nanoparticles and 3D XRM Imaging	168
4.3.2.5. Histology and FM Imaging	169
4.4. Discussion	173
4.4.1. Gross Dissection	173
4.4.2. Histological Analysis	174
4.4.3. LM and TEM of Marmoset Specimens	174
4.4.4. LM and FM of Macaque Specimens	175
4.4.5. Further Work	175
4.4.5.1. Resin Casting and Histological Processing of Tissue	175
4.4.5.2. MicroCT, 3D XRM and Further Analysis	176
4.4.5.3. MRI Scanning	177
Chapter 5. Concluding Discussion	178
5.1. Main Findings of the Thesis	178
5.1.1. Conclusions	178
5.1.2. Discussion	178
5.1.2.1. Summary of Project Findings	178
5.1.2.2. Anatomy of the PS and SS	179
5.1.2.3. Bridging Veins, Venous Tributaries and Subdural Vessels	182
5.2. Future Directions	184
5.2.1. Vascular Perfusion	184

5.2.2. Vessel Morphology	185
5.2.3. Correlating morphological findings with Clinical MR Imaging ..	186
5.2.4. Volume Rendering of Imaging Datasets	187
5.2.5. Macaque Work	187
5.2.6. Cadaveric Work	188
5.2.7. Biomechanical Modelling	189
References.....	190
Appendices	214
Appendix 1: Brief History of Resins and VCC.....	214
Appendix 2: Protocol for Optical Clearing of Tissue using Scaleview-A2	215
Appendix 3: Solutions required for transcadiac perfusion.....	216
Appendix 4: Procedure for Volume Rendering and Approximating Vessel Size from microCT and 3D XRM Imaging Datasets	218
Appendix 5: Procedure for Processing Tissue and Embedding in Araldite Resin for Transmission Electron Microscopy.....	219
Appendix 6: Protocol for Resin Embedding Samples for TEM: using Durcupan (a water soluble embedding medium)	220
Appendix 7: Procedure for Staining Semi-thin Sections with Toluidine Blue O.....	222
Appendix 8: Procedure for Staining Ultra-Thin Sections for TEM.....	223
Appendix 9: Protocol for Anaesthesia of the Rhesus macaque (<i>Macaca mulatta</i>).....	225
Appendix 10: Protocol for tissue processing and wax embedding of pre- fixed brain tissue for histology	226
Appendix 11: Protocol for Microtome Sectioning of Wax-embedded Tissue	226
Appendix 12: Procedure for Staining tissue with Haematoxylin and Eosin (H&E) and Cover-slipping Prepared Histology Slides.....	227

Abstract

This project aimed to prove the existence of fine subdural veins hypothesised to be the source of intracranial bleeding seen in cases of accidental and non-accidental traumatic head injuries, and consequently illustrate their anatomical structure. This was important in contributing towards establishing the causal mechanism for traumatic intracranial bleeding, and was particularly applicable in unexplained traumatic head injuries in cases of possible child abuse. These issues are on-going, worldwide concerns that have been of public as well as scientific concern for many years.

To illustrate the fine cerebral vessels, a unique modelling technique was recently developed involving polyurethane resin casting of the brain vasculature. Rat, marmoset (*Callithrix jacchus*), rhesus macaque (*Macaca mulatta*) and human (*Homo sapiens*) brain tissue were all used. Tissue surrounding the resin perfused vessels were then either macerated to reveal the whole cast, or dissected to illustrate the resin cast as it would appear in situ. To allow analysis of these fine subdural vessels, various imaging techniques including fluorescence microscopy (FM), light microscopy (LM), confocal microscopy (CM), scanning electron microscopy (SEM), transmission electron microscopy (TEM), magnetic resonance imaging (MRI), micro-computed tomography (microCT) and 3D X-ray microscopy (3D XRM) were used.

The existence of subdural vessels was clearly illustrated via gross dissection of both primate and cadaveric material. Fluorescence imaging of resin-filled rat brain histological sections also showed orientation of fine vessels to be within the subdural space. MRI images (7.0 Tesla scanner) of the human head *in vivo*, as well as cadaveric material have both shown signs of small calibre vessels that have never been previously documented, that are too fine to be bridging veins, yet seem to drain into the superior sagittal sinus (SSS).

These results prove the existence of subdural vessels, present in a range of different species. Future work will further illustrate the exact morphological structure of these vessels, and biomechanical modelling will be applied to determine the exact forces required to cause them to rupture.

Conferences and Peer-reviewed Publications

Conferences

Nakagawa, SC., and Parker, T., 2011, Investigating the Cerebrovascular Anatomy in a Rat Model using Polyurethane Elastomer (PU4ii) Resin Casts, presented at the *National Academic Medicine Student Conference*, Newcastle, UK.

Nakagawa, SC., and Parker, T., 2011, Detailed Examination of the Cerebrovascular Anatomy in a Rat Model using Polyurethane Elastomer Resin Casts, presented at the *UKMSA International Conference*, Bournemouth, UK.

Published Abstracts

Nakagawa, SC., Gowland, P., Jaspan, T., and Parker, T., 2013, Investigating the Detailed Structure of the Venous Drainage of the Wistar Rat (*Rattus norvegicus*), Marmoset (*Callithrix jacchus*) and Human Brains: A MicroCT, MRI and ESEM Study using Resin Casting Techniques, presented at *The Anatomical Society Summer Meeting*, Royal College of Surgeons, Dublin, Ireland (Royal College of Surgeons in Ireland, 2014).

Acknowledgements

I would like to thank my supervisor Dr Tim Jaspan in assisting throughout the many aspects of this investigation, as it would not have been possible without his expertise, guidance and support throughout the project. I would especially like to give thanks to Dr Terry Parker, who sadly passed away before I was able to fully complete this project. As well as being invaluable as a supervisor, he was also a friend and a great support for me throughout the project, and I was very fortunate to have been able to work with him.

Thanks also go to Professor Penny Gowland for her invaluable help with the MRI imaging carried in this project, which otherwise would not have been possible. I am grateful to Sue Willington who was always there to assist with different parts of the project wherever possible, especially when having to obtain unusual laboratory items which was very common for this project.

Thanks also go to Dr Long-Bao Lv, from the Kunming Institute of Zoology in China, for his valued help throughout this collaboration with the institution in providing the required specimens essential for this project. I would also like to thank Dr Weina Meng, as well as Drs Wang, Jihong and Simon from the Kunming Institute of Zoology for assisting in various different aspects as well as translating information required for the collaboration with the Kunming Institute of Zoology to be successful. Additionally, I would also like to thank Dr Eric Meyer (VasQtec) for his help and advice regarding application of the PU4ii resin for the vascular resin casting technique used throughout this project.

I would also like to thank Denise Christie, Ian Ward and Dr Emma King from the AMU, who were able to teach and advise me regarding carrying out numerous different techniques required for this project. Thank you to Natasha Russell whose help was invaluable in providing essential material required for this project, as well as preparing tissues required for the MRIs carried out in this investigation. I would also like to thank Dr Kostas Tsintzas for the generous lending of laboratory equipment, as well as the BMSU staff for their assistance in this project. Thanks also go to Dr Lisa White whose help was essential in acquiring all relevant microCT images of the vascular casts. I would also like to thank Nicola Weston for her invaluable help in acquiring ESEM images of the vascular casts of various different specimens, as well as Dr Pearl Agyakwa for assisting in carrying out the 3D XRM imaging of the resin casts. I would like to thank Dr Malcolm Prior for helping to acquire MR images of some of the animal specimens, as well as Dr Bai Li, Dr Lee Buttery and Ding Yuchun for assistance in volume rendering of imaging data, as well as with whom a collaborative project has been set up. Thanks also go to Dr Alain Pitiot for assistance in segmentation of some of the MRI datasets.

I would like to acknowledge the School of Biomedical Sciences, and the Faculty of Medicine and Health Sciences for my PhD studentship at the University of Nottingham.

I would also like to thank all members of my lab, and especially my family and friends who have all given me advice, encouragement, and supported me throughout my PhD.

List of Definitions and Abbreviations

Definitions

Infant: 'n. a child incapable of any form of independence from its mother: the term is usually used to refer to a child under one year of age, especially a premature or new-born child. In legal use the term denotes a child up to the age of seven years' (Martin, 2007).

Adult: 'noun, a grown-up person or animal; esp a human being of or past an age specified by law (in Britain, '18') (Allen, 2004)

Gravitational (G) Force: the acceleration of an object during free-fall against negligible air resistance

Abbreviations

Anatomy

BBB: Blood Brain Barrier

CNS: Central Nervous System

CSF: Cerebrospinal Fluid

IJV: Internal Jugular Vein

ISS: Inferior Sagittal Sinus

IVC: Inferior Vena Cava

LA: Left Atrium

LV: Left Ventricle

PS: Petrosquamous Sinus

RA: Right Atrium

RV: Right Ventricle

SAS: Subarachnoid Space

SDS: Subdural Space

SNS: Sympathetic Nervous System

SS: Sigmoid Sinus

SSS: Superior Sagittal Sinus

SVC: Superior Vena Cava

TS: Transverse Sinus

Imaging

2D: Two-Dimensional

3D: Three-Dimensional

3D FSE MRI: 3D Fast Spin Echo Magnetic Resonance Imaging

BF Microscopy: Bright Field Microscopy

CM: Confocal Microscopy

CR: Conventional Radiology

CT: Computed Tomography

CTV: Computed Tomography Venography

DIC: Differential Interference Contrast

DSA: Digital Subtraction Angiography

ESEM: Environmental Scanning Electron Microscopy

FLASH MRI: Fast Low Angle Shot Magnetic Resonance Imaging

FM: Fluorescent Microscopy

MicroCT: Micro-Computed Tomography

MRI: Magnetic Resonance Imaging

MRV: Magnetic Resonance Venography

OCT: Optical Coherence Tomography

SEM: Scanning Electron Microscope

TEM: Transmission Electron Microscopy

VCC: Vascular Corrosion Casting

XRM: X-Ray Microscopy

Solutions

APES: 3-aminopropyltriethoxy-silane

DPX: Distrene, Plasticiser and Xylene

Gd: Gadolinium

H&E: Haematoxylin and Eosin

KOH: Potassium Hydroxide

OsO₄: Osmium Tetroxide

PBS: Phosphate Buffered Saline

PFA: Paraformaldehyde

Terminology and Miscellaneous

ASDH: Acute Subdural Haematoma

CBV: Cerebral Blood Volume
CPR: Cardiopulmonary Resuscitation
CSDH: Chronic Subdural Haematoma
HI: Hypoxia-Ischaemia
ICP: Intracranial Pressure
NAHI: Non-Accidental Head Injury
NHTSA: National Highway Traffic Safety Administration
RH: Retinal Haemorrhage
ROI: Region of Interest
SAH: Sub-Arachnoid Haemorrhage
SBS: Shaken-Baby Syndrome
SDH: Subdural Haematoma

List of Figures

Figure 1: Cross-section illustrating the Anatomical Structures of the Head and Brain (Wedro, 2012)	2
Figure 2: Superior coronal view of the meninges (Drake et al., 2005)	3
Figure 3: Veins and Dural Venous Sinuses – Sagittal section (Drake et al., 2005)	4
Figure 4: Dural Venous Sinuses – Transverse section (Hoa and Micheau, 2010) .	4
Figure 5: The Cerebral Venous System: Principal internal and external veins of the brain and their relationship to the dural venous sinuses (Gray, 2008).....	6
Figure 6: Illustration of the flow of venous blood that drains into the great cerebral vein of Galen and straight sinus (Kilic and Akakin, 2008).....	7
Figure 7: Meninges – Coronal Section (Netter, 2006)	8
Figure 8: Comparison between a normal uninjured baby and the injured brain of a shaken baby (Kfolio, 2012b)	9
Figure 9: MRI images illustrating typical cases of SDH seen in both adult and infant cases. From left to right, MRI images illustrating a normal healthy adult (axial FLAIR), an adult with a SDH (axial T1), and a 5 month old infant with a SDH (axial FLAIR). The skull bone (asterisks), brain tissue (BT) and SDH (arrows) are illustrated. <i>MRI images courtesy of Dr T Jaspan.</i>	10
Figure 10: The Mechanism of Subdural Haemorrhage: The bridging veins travel from the cortical surface of the brain, and through both the arachnoid and potential subdural spaces (the potential subdural space however is illustrated here as an actual space) (left). When head injury causes shearing of the bridging veins (right), the subdural space rapidly fills with blood (Nakagawa and Conway, 2004).	11
Figure 11: Illustration of the acceleration/deceleration forces subjected to the infant head during a shaking motion (Cwavusa, 2012)	12
Figure 12: The Magnifying Force of an Impact Injury: The impact of an infant's head against a solid surface can magnify the force applied to the brain by up to 50 times, compared to that of shaking alone (Nakagawa and Conway, 2004).	14
Figure 13: Neck and Cervical-Spinal Cord Injury: Violent shaking can cause trauma directly to the spinal cord (Nakagawa and Conway, 2004).	18
Figure 14: Superficially located Cerebral Blood Vessels (Netter, 2006)	23
Figure 15: Coronal section through the brain and dura, illustrating the intradural vascular plexus (Squier, 2009)	24
Figure 16: The Meningeal Layers (Patel and Kirmi, 2009)	25
Figure 17: Neomembrane Formation (Kfolio, 2012a)	28
Figure 18: Method for Cardiac Perfusion Fixation and PU4ii Resin (containing coloured fluorescent dye) Perfusion of a 250g Wistar Rat.....	53
Figure 19: Apparatus used for fixation and resin perfusion (not to scale). System is pressurised using a nitrogen tank attached to an air pressure perfusion control unit. Specimen is cannulated before opening Stop-Cock 1 to allow perfusion of prewash. Stop-Cock 1 is then closed before Stop-Cock 2 is opened to allow perfusion of fixative. Stop-Cock 2 is then closed before activation of the mechanical syringe pump for perfusion of final resin mixture.	54
Figure 20: A: Macrograph of brain tissue of a Wistar rat perfused with fluorescent resin. The left cerebral hemisphere (1a) and right cerebral hemisphere (1b) can be seen. B: Grossly dissected resin perfused rat brain, illustrating the presence of possible intradural vessels (arrow) as well as subdural vessels (arrowhead). C: Macrograph of a freeze-dried rat cerebral resin cast with the surrounding brain tissue macerated away, allowing preservation of the normal vessel structure without surrounding tissue support. The SSS (asterisk) and transverse sinuses (arrows) can be seen, as well as the fine vessels surrounding these sinuses. D: SEM image (x75) of a rat cerebral specimen. The SSS (asterisk) as well as a capillary plexus (arrowhead) consisting of 5-10µm diameter vessels can be seen.	

A 120 μ m diameter vessel (possibly a bridging vein), can be seen branching into a smaller vessel (arrow) approximately 35 μ m in diameter.66

Figure 21: Frequency histogram of the diameters of the bridging veins and their tributaries, draining into the SSS, TS, SS and PS.69

Figure 22: Probability histogram of the diameters of the venular tributaries draining the highest vascular density 1500 μ m sections of the SS and PS.70

Figure 23 A: Photomontage of ESEM images of a cerebral VCC, illustrating both the arteries (asterisks) and veins (arrows) forming a complex vascular network in resin perfused rat specimen D2. The location of these same vessels are shown in macrographs of the VCC illustrated in Figure 24. **B:** A small vessel (arrow) draining into a bridging vein (arrowhead) situated on the right hand side of the brain can be seen, which then further drains into the SSS on the far left of the image (cannot see the SSS in this image). Characteristic imprint features of the venous endothelial cell nuclei can be seen on the surface of the bridging vein cast. **C:** Characteristic imprint features of the endothelial cell nuclei of various arterial vessels (arrows) can be seen.71

Figure 24: Macrographs of an OsO₄ stained VCC of RAT D2 showing both arterial and venous vessels, forming a complex vascular network. ESEM images of these vessels are shown in Figure 23. **A:** Here, the cerebellum (1a); left cerebral hemisphere (1b); right cerebral hemisphere (1c); SSS (1d); and transverse sinuses (1e) are illustrated. **B:** A higher magnification image of the area enclosed in the white box shown in A. The black outline indicates the area illustrated in Figure 23A.72

Figure 25: Photomontages of ESEM images of a cerebral VCC of rat specimen E, mounted on a 45° stub. **A:** The photomontage illustrates bridging veins (arrows) and their tributaries draining into the SSS (asterisk). **B:** ESEM image of a section of the whole width of the SSS (asterisk), illustrating the lack of draining vessels seen along the length of the venous sinus, as compared to the sigmoid and petrosquamous sinuses. **C:** Photomontage of bridging veins (arrows) and their tributaries draining into the SSS (asterisk) on either side of the venous sinus. ...73

Figure 26: Images of a cerebral VCC of a Wistar rat specimen. Images A and B are ESEM images, and C and D are macrographs of a cerebral VCC of Rat E. **A:** ESEM image of a VCC seen from above (sample was mounted on a flat stub). A bridging vein (arrow) can be seen draining into the SSS (asterisk) on the right. The diameter of the bridging vein at the point of entry into the SSS is 497 μ m. **B:** ESEM image of a VCC mounted on a 45° stub. A bridging vein (arrow) can be seen draining into the SSS (asterisk) on the left hand side of the image. The diameter of the bridging vein at the point of entry into the SSS is 362 μ m. **C:** The same bridging vein draining into the SSS, as seen in A can be seen in this image (white box). Here, the cerebellum (1a); left cerebral hemisphere (1b); right cerebral hemisphere (1c); SSS (1d); and transverse sinuses (1e) are illustrated. **D:** The same bridging vein draining into the SSS, as seen in B can be seen in this image (white box).74

Figure 27: ESEM images of cerebral VCCs of Wistar rat specimens. Images A and E (Rat E) are taken from a different VCC to images B, C and D (Rat D2). The same VCCs are also shown in Figure 28. **A:** Sample mounted on a 45° stub. A branching network of bridging veins (arrows) can be seen draining into the right TS (arrowhead). The diameters of the bridging veins at the point of entry into the sinus are 130-190 μ m. **B:** Sample mounted on a 45° stub. A bridging vein (arrow) can be seen draining into the left TS (asterisk). The diameter of the bridging vein at the point of entry into the sinus is 340 μ m. **C:** A smaller calibre bridging vein (arrow) draining into left TS (asterisk). The diameter of the bridging vein at the point of entry into the sinus is 165 μ m. **D:** A bridging vein (arrow) draining into left TS (asterisk). The diameter of the bridging vein at the point of entry into the sinus is 60 μ m. **E:** A large bridging vein (arrow) is shown draining into the left TS, illustrating the distinct narrowing seen at the junction point as the bridging vein drains into the sinus. This is a structure that is consistently seen throughout other

resin cast samples. The image also shows a large section of the whole width of the transverse sinus, illustrating the lack of draining vessels seen along the length of the venous sinus, as compared to the SS and PS.75

Figure 28: Macrographs of cerebral VCCs of Rats E and D2, illustrating bridging veins that drain directly into the transverse sinuses. These vessels are also shown in Figure 27. **A:** Macrograph of a VCC of Rat E, illustrating the location of a branching network of bridging veins (black box) draining into the right transverse sinus (asterisk), as seen in Figure 27A as well another larger bridging vein (white box) draining into the left transverse sinus (arrowhead) as seen in Figure 27E. Here, the cerebellum (1a); left cerebral hemisphere (1b); right cerebral hemisphere (1c); and SSS (1d) are illustrated. **B:** Macrograph of a VCC (stained with OSO_4) of RAT D2, illustrating the location of bridging veins draining into the left transverse sinus (arrowhead), as seen in Figure 27B (asterisk), Figure 27C (white box), and Figure 27D (black box).....76

Figure 29: ESEM images of a cerebral VCC of rat specimen E, mounted on a 45° stub. **A:** The photomontage illustrates a network of venous vessels which drain into a network of bridging veins (arrows), which then further drain into the right sigmoid sinus (asterisks), to form a complex vascular system. The same vessels are also shown in Figure 32B (white box). **B:** A photomontage of ESEM images, illustrating the approximate diameters of a few of the bridging veins (arrows) which are seen to drain directly into the right sigmoid sinus (asterisk) of a VCC of rat E. This can also be seen in the white box illustrated in image A.77

Figure 30: ESEM images of a cerebral VCC of rat specimen E, mounted on a 45° stub. These vessels are the same as those illustrated in Figure 31 which were mounted on a flat stub. **A:** Photomontage illustrating a network of venous vessels, draining into a network of bridging veins (arrows) which are seen to then further drain into the right sigmoid sinus (asterisks), to form a complex vascular network. Macrographs of the same vessels are also illustrated in Figure 32B (black box). **B, C:** Magnified ESEM images of sections of image A, illustrating the complex structure of some of the venous vessels seen to drain into bridging veins (arrows), which are then seen to further drain into the right sigmoid sinus (asterisks) of a VCC of rat E.....78

Figure 31: ESEM images of a cerebral VCC of rat specimen E, mounted on a flat stub. **A:** Photomontage illustrating a network of venous vessels, draining into a network of bridging veins (arrows), which are then seen to further drain into the right sigmoid sinus (asterisk), to form a complex vascular network. These vessels are the exact same vessels illustrated in the ESEM photomontage in Figure 30A, imaged from a different angle. Macrographs of the same vessels are also illustrated in Figure 32B (black box). **B:** A magnified ESEM image of a section of image A (white box), illustrating the complex network of vessels seen to drain into a bridging vein, which then further drains into the right sigmoid sinus (cannot be seen in this image) of a VCC of rat E.79

Figure 32: **A:** Macrograph of a cerebral VCC of RAT E. Here, the cerebellum (1a); left cerebral hemisphere (1b); right cerebral hemisphere (1c); SSS (1d); and transverse sinuses (1e) are illustrated. **B:** Magnified image of macrograph A, illustrating the same complex vascular network of venous vessels draining into a network of bridging veins, which are seen to then further drain into the right sigmoid sinus (asterisk) as in Figure 29A (white box) as well as Figure 30A and Figure 31A (black box).79

Figure 33: A Photomontage of ESEM images of a cerebral VCC of rat specimen E, mounted on a flat stub. The photomontage illustrates a network of bridging veins (arrows) and their tributaries which drain into the right petrosquamous sinus (asterisk). Distinct flattening of the bridging veins can often be seen at the junction between the vessel and the sinus, as the vessels enter and drain into the venous sinuses (A, B and C). Macrographs of the same vessels are also illustrated in Figure 36.80

Figure 34: ESEM images of a cerebral VCC of rat specimen E, mounted on a flat stub. These are magnified images of sections of the photomontage seen in Figure 33, illustrating a network of bridging veins and vessels which drain into the right petrosquamous sinus. Macrographs of the same vessels are also illustrated in Figure 36. **A:** Magnified image of Figure 33A, illustrating the size of the junction ($36.1\mu\text{m} \times 100\mu\text{m}$) as the bridging vein (arrow) enters the petrosquamous sinus (asterisk). **B:** Magnified image of Figure 33B, illustrating flattening of a bridging vein at the junction between the vessel and the sinus (arrow) as it enters and drains into the petrosquamous sinus (asterisk). **C:** The same vessel as seen in Figure 34B, however imaged after the specimen was tilted slightly to allow visualisation of the vessel junction from above. **D:** Magnified image of Figure 33C, illustrating flattening of a bridging vein (arrow) at the junction between the vessel and the petrosquamous sinus (asterisk). **E, F:** Magnified images of Figure 33D illustrating flattening of a bridging vein (arrow) at the junction between the vessel and the petrosquamous sinus (asterisk), as well as showing finer tributaries also draining into this bridging vein (arrowheads).81

Figure 35: A: Photomontage of ESEM images of a cerebral VCC of rat specimen D2 mounted on a flat stub. The photomontage illustrates a network of venous vessels which drain into bridging veins (arrows) which further drain into the right transverse sinus (arrowhead), to form a complex vascular network. Further bridging veins and their tributaries can also be seen draining into the intracranial section of the right petrosquamous sinus (asterisk) as well as the right sigmoid sinus (SS). Macrographs of the same vessels are also illustrated in Figure 37. **B:** ESEM image of a cerebral VCC of rat specimen D2. Bridging veins (arrows) and their tributaries can be seen draining into the junction between the right transverse sinus (arrowhead) and the right petrosquamous sinus (asterisk). Macrographs of the same vessels are also illustrated in Figure 37.82

Figure 36: A, B: Macrographs of a cerebral VCC of rat specimen E, mounted on a flat stub. These images illustrate a network of bridging veins (arrows) and their tributaries, which drain into the right petrosquamous sinus (asterisk). Here, the cerebellum (1a); left cerebral hemisphere (1b); right cerebral hemisphere (1c); SSS (1d); and transverse sinuses (1e) are illustrated. These vessels are also illustrated in Figure 34 and Figure 33.83

Figure 37: Macrographs of a cerebral VCC of rat specimen D2 (stained with OSO_4) mounted on a flat stub. **A:** Here, the cerebellum (1a); left cerebral hemisphere (1b); right cerebral hemisphere (1c); SSS (1d); and transverse sinuses (1e) are illustrated. **B:** A magnified image of a section of image A, illustrating a network of bridging veins and their tributaries, draining into the right transverse sinus (1e), the right petrosquamous sinus (asterisk), as well as the right sigmoid sinus (SS), to form a complex vascular network. ESEM images of these vessels are also illustrated in Figure 35.83

Figure 38: Photomontage of ESEM images of a cerebral VCC of rat specimen D2 mounted on a flat stub. The photomontage illustrates a network of bridging veins and their tributaries (arrows) which drain into the left petrosquamous sinus (asterisks). Macrographs of the same vessels are also illustrated in Figure 39. The location and structure of these vessels are similar to those found on the right hand side of the same VCC, near to the junction between the left petrosquamous and sigmoid sinus (Figure 35), as well as vessels seen in other rat VCCs (Figure 33, Figure 31, Figure 30 and Figure 29).84

Figure 39: A, B: Macrographs of a cerebral VCC of rat specimen D2 mounted on a flat stub. These images illustrate a network of bridging veins and their tributaries, which drain into the left petrosquamous sinus (asterisk). Here, the cerebellum (1a); left cerebral hemisphere (1b); right cerebral hemisphere (1c); SSS (1d); and transverse sinuses (1e) are illustrated. ESEM images of these vessels are also illustrated in Figure 38.84

Figure 40: Photomontage of ESEM images of a cerebral VCC of rat specimen D2, mounted on a 45° stub. This illustrates the junction point between the left

transverse sinus (arrowhead), left sigmoid sinus (SS) and left petrosquamous sinus (asterisk).85

Figure 41: Images of resin perfused 1mm thick sections of Wistar rat specimen D3 brain and skull specimens. These images illustrate the structure of the different meningeal layers which lie in between the skull and surface of the brain. **A:** Photomontage of ESEM images illustrating the skull bone (SB) on the left hand side of the image. Both the endosteal dura mater layer (asterisk) and the meningeal layer (arrowhead) of the dura mater can be seen, situated adjacent to a thin arachnoid membrane (arrow), which can be seen folded around vessels situated within the subarachnoid space (SAS). The brainstem (BS) can also be seen on the right hand side of the image. **B:** Macrograph illustrating the skull bone which lies on the left hand side of the image, the dural membrane cannot be differentiated in this image, however the subdural space (SDS) can be seen, adjacent to the arachnoid membrane (arrow) which is covering the occipital sinus (OS) and other surrounding vessels. The brainstem can be seen on the right hand side of the image. **C:** Macrograph of resin perfused rat specimen D3 coronal section. Here, the brainstem; cerebellum (C); and skull bone are illustrated. **D:** ESEM image illustrating the skull bone which can be seen on the left hand side of an epidural vessel (ED) which is enclosed by the endosteal dural membrane. On the right hand side of this, an intradural vessel (ID) can also be seen enclosed in between the endostal and meningeal layers of the dura mater. Adjacent to this, the subdural space can be seen, which is situated to the left of a subarachnoid vessel (SA), enclosed by the arachnoid membrane. The cerebellum can also be seen on the right hand side of the image.87

Figure 42: ESEM images of a 1mm thick coronal slice of resin perfused rat specimen C3 section. **A:** A photomontage illustrating the brainstem (BS) seen on the left hand side of the image, as well as the SAS containing vessels of different sizes, covered by the arachnoid membrane (arrowhead). A subdural vessel (asterisk) can also be seen traversing across the SDS to the dural membrane (arrow) and the skull bone (SB). **B, C:** Magnified ESEM images of areas of image A, illustrating the diameter of some of the vessels within the SAS. **D:** Macrograph of rat C3 section. The white box indicates the location in which the structures shown in image A lie in relation to the surrounding anatomy. Here, the brainstem (BS); cerebellum (C); and skull bone (SB) are illustrated.88

Figure 43: Fluorescent microscopy (FM) images of fluorescent powder-containing resin perfused vessels, overlaid onto histological images of H&E stained, DPX mounted histological sections (10µm thick) of resin perfused Wistar *Rat Specimen Y* skull and brain tissue. **A:** Whole map (coronal section) of the brain tissue (BT) and skull bone (SB) of a PU4ii resin perfused Wistar rat. FM image (red channel) is overlaid onto a BF microscopy (grey scale) histological image (Leica DM IRB Fluorescence Microscope). **B:** Magnified image of the area indicated in image A, illustrating general histology of the dura mater (asterisk) and layers of the skull (arrows). **C:** (x10) FM image (red channel) overlaid onto a BF microscopy (green channel) histological image (Leica DMRB Fluorescence Microscope) of the same area as seen in image B. The resin perfused vessel (red) is located within the dura mater layer, as the meningeal layer lies medial to the compact (arrows) and spongy (asterisk) layers of the skull bone. **D:** Higher (x20) magnification of structures seen in image C. **E:** Higher (x40) magnification of structures seen in image D.90

Figure 44: **A, B:** (x20) Fluorescence microscopy (red channel) image overlaid onto BF microscopy (grey scale) histological image using DIC (Leica DM IRB Fluorescence Microscope) of Wistar *rat specimen Y*. Here the brain tissue (BT) and dural membrane (arrow) are illustrated.91

Figure 45: MicroCT images of rat specimens. The anterior (ANT), posterior (POST), superior (SUP) and inferior (INF) orientations of each image are indicated, as well as the skull bone (SB), midbrain (MB), cerebellum (1a), left hemisphere (1b) and right hemispheres (1c). **A:** Cerebral VCC of rat specimen L2. **B:** Resin

perfused whole brain of rat specimen Z2, still covered in the dural membrane. **C:** 1mm thick section of resin perfused brain and skull of rat specimen C3, section 12.92

Figure 46: Images of a small section of the VCC of Rat Specimen J2. **A:** MicroCT projection image of a rat VCC. **B:** 3D reconstructed image produced from the microCT imaging dataset of the same rat VCC shown in image A, alongside a calibration bar (whereby 27 on the scale represents a vessel diameter of approximately 2mm, and 0 represents 0mm) indicating the approximate sizes of all the cerebral vessels.93

Figure 47: Method for PU4ii Resin Perfusion (containing coloured fluorescent dye) of a Cadaveric Specimen.100

Figure 48: Human cadaveric material (*Homo sapiens*). Images A and B are taken from dissections of cadaveric specimen A, and images C and D are acquired from dissections of cadaveric specimen C. Bridging veins (asterisks) and subdural vessels (arrows) traversing the subdural space (SDS) are indicated in each image. **A:** Bridging veins and subdural vessels located in between the right occipital lobe (ROL) and the superior surface of the tentorium cerebelli (TC). **B:** Macrograph of the same subdural vessels as seen in image A. **C:** Bridging and subdural veins located in between the inferior part of the tentorium cerebelli (TC) and the superior part of the cerebellum (C). **D:** Macrograph of the same subdural vessels as seen in image C.106

Figure 49: Macrograph of dissected cadaveric specimen C. **A:** A network of bridging veins and subdural vessels can be seen traversing across the subdural space (SDS), draining from the superior surface of the cerebellum (C) still covered by the arachnoid membrane (AM) indicated in image B, to the tentorium cerebelli superiorly (TC). **B:** A magnified image of the same vessels illustrated in image A (white box).108

Figure 50: Histological images of cadaveric specimen C (illustrated in the white box in Figure 49) where network of bridging veins and subdural vessels can be seen, traversing across the subdural space from the superior surface of the cerebellum to the tentorium cerebelli superiorly. **A:** Macrograph of the dura and surrounding vessels, Slide 111. **B, C:** LM image of the dura and vessels, Slide 111: x2.5 (area indicated by the black box in image A) and x10 (area indicated by the black box in image B) respectively. **D:** Macrograph of the bridging veins and subdural vessels without surrounding brain tissue or dura, Slide 101. **E, F:** LM image of the bridging veins and subdural vessels, Slide 101: x2.5 (area indicated by the black box in image D) and x20 (area indicated by the black box in image E) respectively. F1-F4 indicate 4 different vessel lumina. **G:** Macrograph of the cerebellum and surrounding vessels, Slide 11. **H, I:** LM image of the cerebellum and surrounding vessels, Slide 11: x2.5 (indicated by black box in image G) and x20 (indicated by black box in image H) respectively.110

Figure 51: MRI images acquired at the anatomical point just above both the left and right lateral ventricles, to allow a comparison to be made between the brain sizes of a younger (22 years) and an older (78 years) volunteer. The scalp (arrowhead), skull (arrow) and brain tissue (BT) are indicated in each image. **A:** MRI image illustrating the anatomical point (blue line) at which the coronal sections shown in images B and C are acquired. **B:** 3D Fast Spin Echo (FSE) MRI image of a transverse section of the brain of a 22 year old female. **C:** 3D FSE MRI image of a transverse section of the brain of a 78 year old female.112

Figure 52: MRI Scan of human (*Homo sapiens*) head *in vivo* (7.0 Tesla Scanner) of a 22 year old individual. **A:** 3D Fast Spin Echo (FSE) Magnetic resonance imaging (MRI) sequence image of a transverse section of the head illustrating a small calibre vein (arrow) draining into the SSS (asterisk). **B:** Fast Low Angle Shot (FLASH) MRI sequence image of a transverse section of the head illustrating the same small calibre vein (arrow) as seen in image A. **C:** FLASH MRI sequence image of a transverse section of the head illustrating a very small vein (arrow) draining into the SSS (asterisk). **D:** FLASH MRI sequence image of a coronal

section of the head illustrating a small calibre vein (arrow) draining into the SSS (asterisk)..... 113

Figure 53: Transverse MRI Scan sections of a human (*Homo sapiens*) head in vivo (7.0 Tesla Scanner) of a 22 year old individual. A: 3D FSE MRI sequence image illustrating a fine calibre vessel (white box) seen to traverse across from the cerebral surface through the subarachnoid space to enter the dura. B: The same fine vessel (arrow) as illustrated in A. C: 3D FSE MRI sequence image illustrating fine calibre vessels (white box) seen to also traverse the subarachnoid space to enter the dura. D: The same fine vessels (arrows) as illustrated in C..114

Figure 54: 3D FSE MRI sequence scans of human (*Homo sapiens*) heads in vivo (7.0 Tesla Scanner), of an 87 (images A and B) and 78 (image C) year old individual. **A:** Coronal section illustrating a small calibre vein (arrow) entering the tentorium cerebelli (a dural fold). The cerebral falx (CF) and tentorium (TC) are illustrated. **B:** Coronal section illustrating a venous plexus (VP) and bridging vein (BV) surrounded by a dural layer, a small calibre vein (arrowhead) draining into the plexus inferiorly, and another small vein (arrow) crossing an arachnoid granulation (AG) before entering the venous plexus. **C:** Transverse section illustrating a small calibre vessel (arrow) entering directly into the SSS (asterisk) through the dura mater (DM).115

Figure 55: T2 weighted MR images (acquired in the axial plane and reformatted in the sagittal and coronal planes from bottom to top) of the same unaltered MRI head scan dataset (left hand column), compared to the results of small vein segmentation (right hand column) and non-local means filtering that was applied to the same MRI data as shown in the left hand column.117

Figure 56: The Primate Family Tree: shows the points at which different evolutionary lineages split off from a common ancestor. Images are not to scale (MRC and The Wellcome Trust, 2006).122

Figure 57: Method for PU4ii Resin Perfusion (containing coloured fluorescent dye) of a prefixed marmoset specimen.124

Figure 58: Method for Cardiac Perfusion Fixation (1% Glutaraldehyde and 4% PFA) of a 745g rhesus macaque, in preparation for EM analysis.....134

Figure 59: Method for Cardiac Perfusion Fixation (4% PFA) and PU4ii Resin Perfusion (containing coloured fluorescent dye) of a 745g rhesus macaque.....135

Figure 60: Method for Cardiac Perfusion Fixation (4% PFA) and PU4ii Resin Perfusion (containing coloured fluorescent dye and 40mg/kg of amphiphilic gold nanoparticles) of a 745g rhesus macaque.137

Figure 61: Method for Cardiac Perfusion Fixation (4% PFA) and PU4ii Resin Perfusion (containing coloured fluorescent dye and 160mg/kg of amphiphilic gold nanoparticles) of a 745g rhesus macaque.138

Figure 62: Macrographs of adult (A, B) and infant (C, D) common marmoset (*Callithrix jacchus*) specimens taken in the sagittal plane, which were dissected to illustrate bridging veins draining directly into the superior sagittal sinus (SSS). **A:** Macrograph of bridging veins (arrows) draining into the SSS (asterisk). **B:** Higher magnification image of the same bridging veins (arrows) as illustrated in image A. **C:** Macrograph of a bridging vein (black box) draining into the SSS (asterisk). **D:** Higher magnification image of the same bridging vein as illustrated in image C.145

Figure 63: Macrographs of adult (A, B) and infant (C, D) common marmoset (*Callithrix jacchus*) specimens, dissected to illustrate subdurally located veins. **A:** Subdural vessels (black box) draining from the surface of the right cerebral hemisphere (1c), to the tentorium cerebelli (TC) below. **B:** Higher magnification image of the same subdural veins as seen in image A. **C:** Subdural vessels (black box) draining from the left cerebral hemisphere (1b) of the brain, to the tentorium (TC) cerebelli covering the cerebellum below. **D:** Higher magnification image of the same vessels as seen in image C.146

Figure 64: Marmoset E mounted on a flat stub, at a 30° tilt for A and C, 45° for B and at 85° for D. **A:** SSS (asterisk) with a diameter of approximately 608µm, with

a surrounding network and overlying of vessels. **B:** Bridging vein (arrow) with a diameter of approximately 48 μ m draining directly into the SSS (asterisk). **C:** Bridging vein (arrow) with a diameter of approximately 110 μ m, draining into the SSS (asterisk). **D:** Higher magnification image of the same bridging vein (arrow) as shown in image C (white box) as it drains into the SSS (asterisk).....148

Figure 65: Marmoset E mounted on a flat stub, at a 85° tilt for A, B and D, and a 30° tilt for C. **A:** Left TS (asterisk) with a diameter of 973 μ m. **B:** Bridging veins (arrows) draining to the right TS (asterisk), with the vein on the left being 301 μ m, and the vein on the right being 288 μ m in diameter. **C:** A bridging vein (arrow) with a diameter of 194 μ m, draining into the left TS (asterisk) with a diameter of 761 μ m. A network of tributaries (arrowheads) can also be seen draining into this bridging vein. **D:** Higher magnification image of the same bridging vein (arrow) as shown in image C, draining into the left TS (asterisk).....149

Figure 66: Marmoset E mounted on a flat stub and tilted at 45°. **A:** Bridging veins (arrows) and their tributaries (arrowheads) draining into the right (RTS) and left (LTS) transverse sinuses. **B:** Higher magnification image of the bridging vein (arrow) as seen in the white box in image A, draining into the left TS (LTS).....149

Figure 67: Marmoset E mounted on a flat stub and tilted at 85° for A and B, and at 45° for C. **A:** Right sigmoid sinus (asterisk) with a diameter of 1.08mm. **B:** Left SS (asterisk) with a diameter of 439 μ m. **C:** Bridging veins (arrows) and their tributaries (arrowheads) shown draining into the left sigmoid sinus (asterisk). .150

Figure 68: Marmoset E mounted on a flat stub and tilted at 85° for A and B, and at 45° for C. **A:** Left PS (asterisk) with a diameter of approximately 550 μ m. **B:** Right PS (asterisk) with a diameter of approximately 644 μ m. A number of bridging veins (arrows) and their tributaries (arrowheads) can also be seen draining into the PS. **C:** Bridging veins (arrows) draining into the left PS (asterisk) with a diameter of 586 μ m.150

Figure 69: Marmoset E mounted on a flat stub, and tilted at 45°. **A:** Bridging veins (arrows) and their tributaries (arrowheads) draining into the right PS (asterisk) with a diameter of 472 μ m. **B:** Vascular network of bridging veins (arrows) and their tributaries (arrowheads) draining into the right PS (asterisk) with a diameter of 373 μ m. **C:** Higher magnification image of the bridging vein (arrow) as it drains into the PS (asterisk), as illustrated by the white box in image B.151

Figure 70: Marmoset E mounted on a flat stub and tilted at 30° for A and at 45° for B. **A:** Junction between the left transverse sinus (TS), left sigmoid sinus (SS) and left petrosquamous sinus (PS) can be seen, the diameters of which are μ m, μ m and μ m respectively. The superior petrosal sinus (SPS) can also be seen in this image. Bridging veins (arrows) and their tributaries (arrowheads) can also be seen draining into both the left SS and the left TS. **B:** Bridging vein (arrow) and its tributaries (arrowheads) draining into the left petrosquamous sinus (PS). This ESEM image is acquired from a different angle to the image taken of the same bridging vein as seen in image A.152

Figure 71: LM and TEM images of a cross section of the SSS of an infant *Marmoset B*. **A, B:** LM images of a semi-thin section (1 μ m) of a marmoset SSS, at magnifications of x2.5 and x20 respectively. The venous sinus lumen (asterisks), falx cerebri (arrows), and intradural vessels (ID) are indicated. **C, D, E:** TEM images at magnifications of x610, x8200 and x8200 respectively. Transverse (CT1) and longitudinal (CT2) sections of collagen fibrils, as well as endothelial cells (EC), endothelial cell nuclei (EN) and pericytes (PC) are indicated.155

Figure 72: Images of a cross section of a bridging vein and the dural membrane of an adult *marmoset A*. **A:** Macrograph of a bridging vein (black box) traversing across the subdural space (SDS) from the surface of the right hemisphere of the brain (BT), through the dura mater layer (DM), and into the SSS above. **B:** LM image (x2.5) of a semi-thin (1 μ m thick) section of the bridging vein (arrow) as seen in image A, and the dural membrane (arrowhead) into which the vessel ultimately drains. **C:** Higher (x10) magnification image of the dural membrane

shown in image B. Here, many intradural vessels can be seen (asterisks). **D:** Higher (x10) magnification image of the bridging vein shown in image B. 156

Figure 73: TEM images of an ultra-thin 70nm thick section of an adult *marmoset* A specimen (also illustrated in Figure 72). **A:** TEM image (x790) photomontage of the same bridging vein as illustrated in Figure 72D. **B:** Higher magnification image (x2550) of the bridging vein illustrated in image A (black box). **C:** Higher magnification image (x8200) of the bridging vein illustrated in image B (black box). Transverse (CT1) and longitudinal (CT2) sections of collagen fibrils, as well as endothelial cells (EC), endothelial cell nuclei (EN) and pericytes (PC) are indicated. The vessel lumen (L) is also indicated in each case..... 157

Figure 74: Projection image from the microCT scan data of the VCC of *Macaque E* specimen..... 159

Figure 75: Grossly dissected resin perfused cerebral vessels of *Macaque D*. **A:** Resin perfused macaque sample illustrating the right transverse sinus (TS), into which a number of converging bridging veins (asterisks) can be seen to drain. There are further networks of smaller subdural veins (arrows), situated within the subdural space (SDS), which can be seen then draining into the bridging veins of the transverse sinus. **B:** Bridging and subdural veins (they cannot be differentiated with certainty from this image alone) (arrowheads) traversing across from the cerebellar brain surface (BT) to the tentorium cerebelli (TC) above. **C, D:** Subdural vessels (arrows) traversing across the subdural space (SDS) from the arachnoid membrane covering the brain tissue (BT) below, to the dural membrane (DM) above..... 161

Figure 76: Grossly dissected *Macaque A* sample, illustrating the cerebral vessels of the brain. **A:** Bridging veins (asterisks) draining from the arachnoid membrane covering the brain tissue (BT), across the subdural space (SDS), and into the superior sagittal sinus (SSS) above which is situated within the 2 layers of the dural membrane. **B:** Bridging and subdural veins (they cannot be differentiated with certainty from this image alone) (arrowheads) traversing across from the cerebellar surface (C) to the tentorium cerebelli (TC) above. **C:** A bridging vein (asterisk) and subdural vessels (arrows) traversing across the subdural space (SDS) from the left cerebral hemisphere (1b), down to the tentorium cerebelli (TC) inferiorly. **D:** Subdural vessels (arrows) traversing across the subdural space (SDS) from the left cerebral hemisphere (1b) to the dural membrane (DM) above. 162

Figure 77: Macrographs of the VCC of *Macaque* specimen C, illustrating the posterior, lateral and superior views of the cast (from left to right). The superior (SUP), inferior (INF), anterior (ANT) and posterior (POST) orientations of each image are indicated, as well as the cerebellum (1a), left hemisphere (1b) and right hemisphere (1c). 163

Figure 78: ESEM images of *Macaque C* mounted on a flat stub, however tilted at 15° for samples A-C, and at -15° for samples D and E. **A:** ESEM image illustrating the 1.58mm diameter of the Inferior Sagittal Sinus (ISS) (asterisk), which narrows as it traverses anteriorly. **B, C, D:** Bridging veins (arrows) draining into the ISS (asterisks). **E:** Incompletely filled bridging vein (arrow) draining into the right petrosquamous sinus (arrowhead). 164

Figure 79: ESEM images of *macaque C* VCC. **A, B, C:** Incompletely filled bridging veins (arrows), draining into the ISS (asterisks). This specimen was mounted on a flat stub and tilted at -15° in image A, and at +15° in images B and C. **D:** ESEM image illustrating complete filling of resin into other much finer cerebral vessels, in contrast to images A, B and C acquired from the same VCC. 165

Figure 80: Imaging of *Macaque C* VCC. The ISS (asterisk) and some of bridging veins (arrows) draining into the venous sinus can be seen in each image. Here, the cerebellum (1a); left cerebral hemisphere (1b) and part of the right cerebral hemisphere (1c) are illustrated. **A:** Macrograph of the *Macaque C* VCC after dissecting away part of the right cerebral hemisphere to reveal the underlying ISS and surrounding vessels. **B:** A serial section of the 3D XRM projection of the whole

macaque brain VCC (25µm resolution). **C:** Serial section of a higher magnification projection (12.5µm resolution) of the anatomical area indicated by the white box shown in image B.166

Figure 81: **A:** A coronal section from the 3D XRM scanned dataset of Macaque C VCC. **B:** 3D reconstruction of the 3D XRM scanning dataset of macaque C cerebral VCC. The superior (SUP) and inferior (INF) parts of the resin cast, as well as the ISS (arrow) are indicated in both images **A** and **B**.167

Figure 82: Images of the VCC of *Macaque C* with the ISS (asterisk), cerebellum (1a); left cerebral hemisphere (1b) and right cerebral hemisphere (1c) being illustrated. **A:** Macrograph of the *Macaque C* VCC after dissecting away part of the right cerebral hemisphere to reveal the underlying ISS and surrounding vessels. **B:** 3D reconstructed image from the 3D XRM dataset of the same macaque VCC shown in image A, alongside a calibration bar (whereby 27 on the scale represents a vessel diameter of approximately 2mm, and 0 represents 0mm) indicating the approximate sizes of all the cerebral vessels.168

Figure 83: Histological sections of *macaque D* specimen. **A:** FM image (x2.5) of slide 55 from the serial sections that were cut from macaque D specimen. Artificial colour (red) was added to the already acquired FM image due to lack of fluorescence emitted from the tissue sample. The image illustrates the presence of resin located within the lumen of a bridging vein (asterisk) seen at the bottom of the image, as well as resin located within the lumina of subarachnoid vessels (arrows) which are located within the subarachnoid space (arrowheads). These structures are situated just superior to the subdural space (SDS), in which the bridging vein lies. **B:** An overlay of BF and FM images of the same H&E stained and DPX mounted histological specimen (slide 61). A bridging vein (asterisk) draining into the dural membrane (DM) can be seen, as well as subarachnoid vessels located within the SAS (arrowheads). This bridging vein and subarachnoid vessels are the same as those vessels illustrated in image A, however without the perfused luminal resin. **C:** Slide 96 (x2.5). Similar structures as described in image B. The bridging vein (asterisk) can be seen draining from the surface of the brain (BT), traversing across the subarachnoid and subdural spaces (SDS) before draining into the dural membrane (DM). Additionally, a smaller vein (white box) can be seen draining directly into the bridging vein, showing again that branches of the bridging veins do exist.172

Figure 84: Illustration comparing the anatomical differences in the venous anatomy between an infant (left) and an adult (right) (Padget, 1957).180

List of Tables

Table 1: Experimental rat specimens used during the study. The main purpose of these experiments was to refine the protocol for cardiac perfusion fixation and PU4ii resin perfusion. The table also details how the tissues were processed and analysed following perfusion. Specimens with incomplete resin casts, or those with excess damage caused during processing of the tissue were discarded (asterisk).	51
Table 2: Experimental cadaveric specimens used during the study. The main use of these specimens was to dissect out and therefore illustrate the anatomical structure of the cerebral anatomy, while demonstrating the similarities in anatomical structure with that of rat and primate material. The table also details how the tissues were further processed and analysed.	104
Table 3: In vivo human (<i>homo sapiens</i>) volunteers used during the study. These volunteers were used for MRI imaging of the head and brain.....	104
Table 4: Experimental primate specimens (Common Marmosets: <i>Callithrix jacchus</i>) used during the study. The main use of these specimens was to dissect out and therefore illustrate the anatomical structure of the cerebral anatomy, while demonstrating the similarities in anatomical structure with that of rat and cadaveric material. The table also details how the tissues were further processed and analysed.....	128
Table 5: Experimental primate specimens (Rhesus monkeys: <i>Macaca mulatta</i>) used during the study. The main use of these specimens was to illustrate the anatomical structure of the cerebral anatomy using as many different tissue processing, imaging and analysis techniques as possible, while demonstrating the similarities in the cerebral anatomical structure of the primate, with that of the rat and human.	130

Chapter 1. Introduction and Literature Review

1.1. Background

This project aims to investigate in detail the anatomical structure of the fine vessels of the brain, and their relevance to accidental and non-accidental traumatic head injuries. Expert opinions are often required in Court to establish whether injuries are of an accidental or non-accidental nature, as well as to determine their most probable cause. However it is extremely difficult to determine exactly how injuries such as subdural haemorrhage (SDH) may have occurred (Brown and Minns, 2008). This is because there are currently many controversies regarding the underlying mechanisms involved in non-accidental head injuries (NAHI) as countless hypotheses have been proposed, however discrepancies in the validity of each are difficult to resolve. This is because although there is a lot of research involving many different fields, the experimental models in many cases are not sufficient with regards to accuracy and applicability of results, mainly due to ethical reasons. This leaves a lot of current research open to much criticism (Tuerkheimer, 2009).

The hypothesis of this investigation is that traumatic disruption and rupturing of fine subdural venules causes the subdural haemorrhaging (SDH) often found in NAHIs. These vessels are thought to either first traverse in between the dural layers, or drain directly into cerebral vessels called bridging veins, before then draining into the venous sinuses. This project aims to first illustrate the existence of these fine venules, which in turn will allow the origin of haemorrhaging caused by NAHI to be more accurately located as we hypothesise that these vessels are in fact the source of this bleeding. This may allow further elucidation as to the cause of intracranial bleeding, particularly applicable in the field of unexplained traumatic head injuries in cases of possible child abuse. These issues are on-going worldwide concerns whereby elucidation of the cause of intracranial bleeding seen in accidental and NAHI is essential due to the universal occurrence of subdural haematomas. Further advancements in this field are vital, as findings which have been derived from studies carried out over 50 years ago are still being referred to and applied in legal proceedings, and on which current law is still based.

To illustrate the fine cerebral vessels, a unique modelling technique called vascular corrosion casting (VCC) was recently developed, involving polyurethane (PU4ii) resin (VasQtec, Switzerland) casting of the brain vasculature (VasQtec,

2004). Tissue surrounding the resin-perfused vessels was either macerated to reveal the whole cast of the cerebral vessels, or dissected to illustrate the resin cast as it would appear in situ. To allow further morphological analysis of the anatomical structure of these fine subdural vessels, histological sections were also produced from the resin perfused specimens, and various imaging techniques including fluorescent microscopy, confocal microscopy (CM), conventional scanning electron microscopy (SEM), environmental scanning electron microscopy (ESEM), magnetic resonance imaging (MRI, 7.0 Tesla scanner) and micro-computed tomography (microCT) were used. Rat (*Rattus norvegicus*), marmoset (*Callithrix jacchus*), rhesus macaque (*Macaca mulatta*) and human (*Homo sapiens*) brain tissue were all used for various purposes throughout the course of this project.

1.2. Summary of Anatomy of the Meninges and Venous System

There are 3 layers of membranes called the meninges which line the brain and spinal cord. They consist of an outer layer which is called the dura mater, a middle layer called the arachnoid mater and an inner layer which is attached to the surface of the brain, called the pia mater (Figure 1).

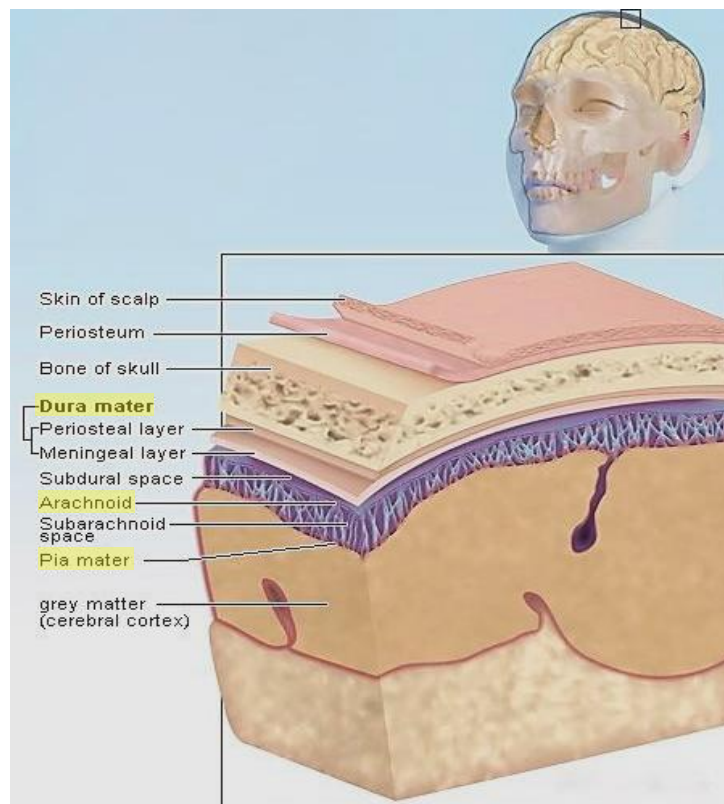


Figure 1: Cross-section illustrating the Anatomical Structures of the Head and Brain (Wedro, 2012, with permission requested)

Membranes which are continuous with the spinal meninges of the spinal cord, through the foramen magnum, are called the cranial meninges. These are similar in structure to the spinal meninges except that the cranial dura mater consists of an outer periosteal layer, which is attached to the skull, and an inner meningeal layer which comes in close contact with the arachnoid mater. The two layers of the cranial dura mater separate at certain points to form either dural partitions that partially subdivide the cranial cavity by projecting inwards or intracranial venous structures such as dural venous sinuses (Figure 2). The location of these dural venous sinuses in between the two rigid layers of dura mater means that they are relatively well protected from compression forces during sudden rises of intracranial pressure (Uddin et al., 2006).

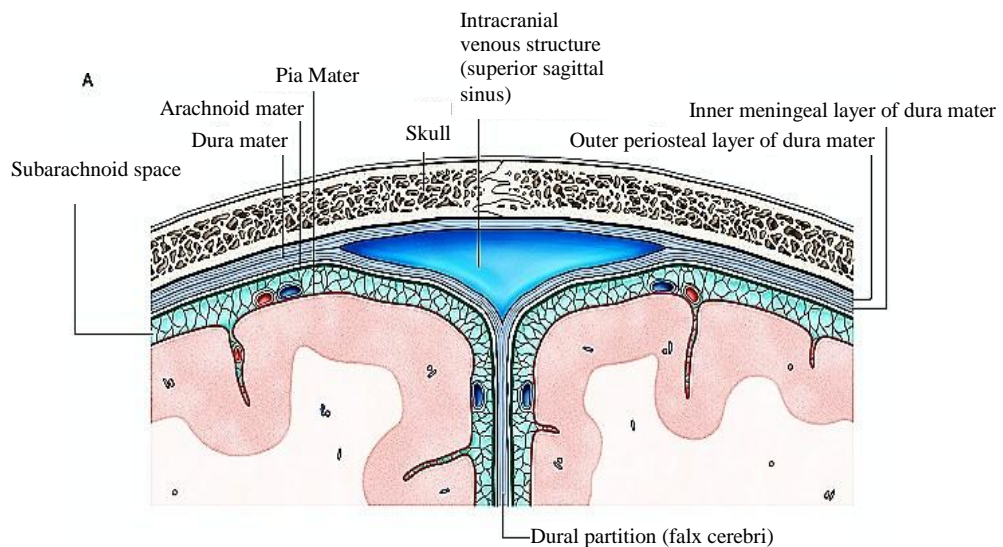


Figure 2: Superior coronal view of the meninges (Drake et al., 2005, with permission requested)

The dural venous sinuses include the superior and inferior sagittal sinuses, the superior and inferior petrosal sinuses, the straight (tentorial), transverse (lateral), sigmoid and occipital sinuses, the basilar, cavernous, and sphenoparietal sinuses, and the confluence of sinuses (Figure 3 and Figure 4). The superior sagittal sinus (SSS) is particularly important in the context of this investigation.

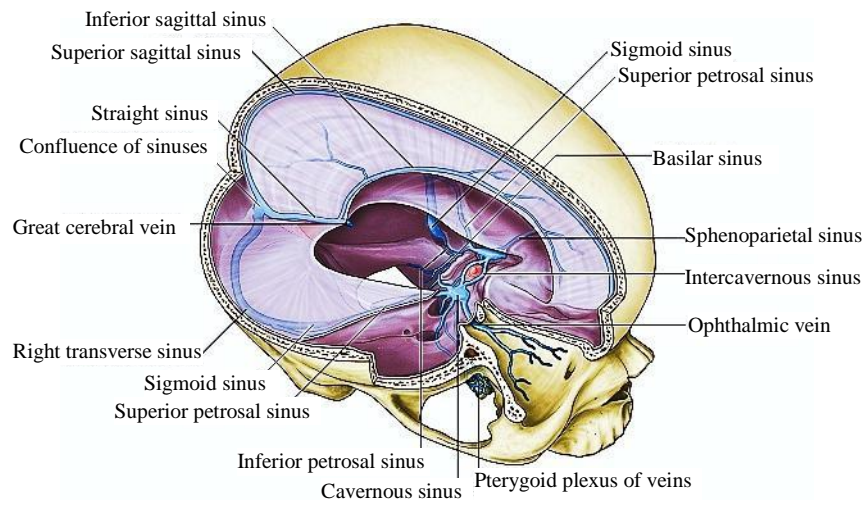


Figure 3: Veins and Dural Venous Sinuses – Sagittal section (Drake et al., 2005, with permission requested)

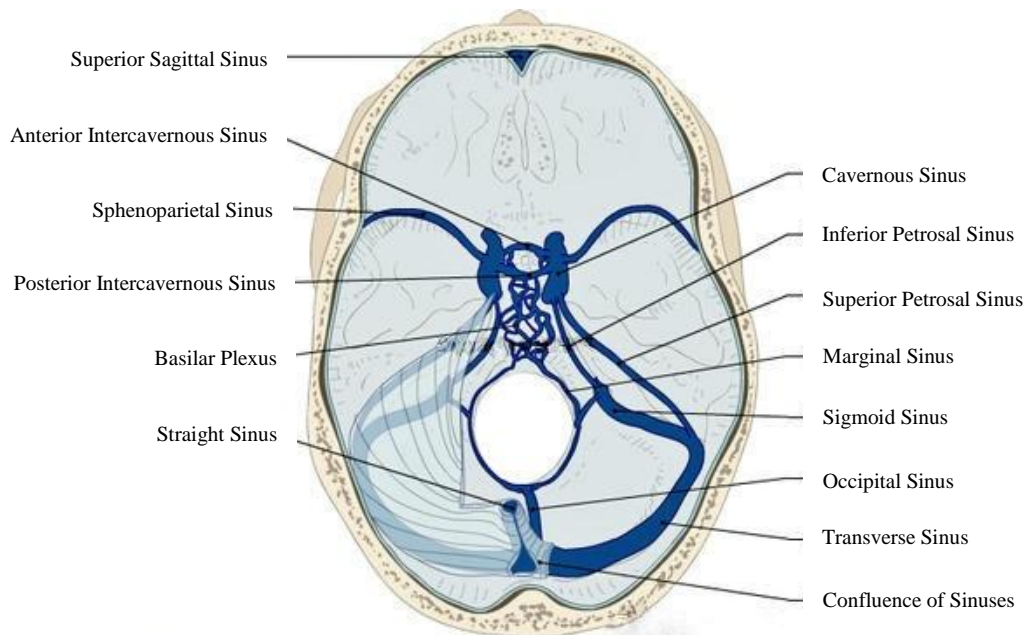


Figure 4: Dural Venous Sinuses – Transverse section (Hoa and Micheau, 2010, with permission)

Small venous networks drain specific parts of the brain, which then merge together to form larger cerebral veins. The cerebral venous system can be divided into 5 parts. These include the internal and external cerebral veins, the dural sinuses, the meningeal veins, and the posterior fossa veins (Gray, 2003; Kilic and Akakin, 2008).

The cerebral veins are often divided into either the internal or external cerebral veins as this correlates to the areas of the brain that they drain. The external venous system consists of the cortical veins and the sagittal sinuses which drain the superficial surfaces of the cerebral hemispheres while the internal venous system consists of the straight sinus, transverse sinus (TS) and sigmoid sinus (SS) as well as draining the deeper cortical veins.

The external cerebral veins consist mainly of the superior, inferior and middle cerebral veins, which drain mainly into the basal vein (of Rosenthal). These veins are extremely variable as they drain into the nearest dural venous sinus, however can still be categorised into 4 groups of bridging veins or major veins (Kilic and Akakin, 2008). The first system is the superior sagittal group which drains into the SSS, the second system is the sphenoidal group which drains into the sphenoparietal and cavernous sinuses, the third system is the falcine group with drains into the inferior sagittal sinus and great cerebral vein (of Galen), and the fourth system is the tentorial group which drains into the tributaries of the sinuses associated with the tentorium cerebelli (Kilic and Akakin, 2008). These veins are further interlinked by the superior anastomotic veins (of Trolard) and inferior anastomotic veins (of Labbé) (Figure 5). The SSS runs back from the foramen caecum towards the internal occipital protuberance, where it joins the straight sinus and occipital sinus at a point called the confluence of sinuses (torcular herophili), before draining into the transverse sinuses.

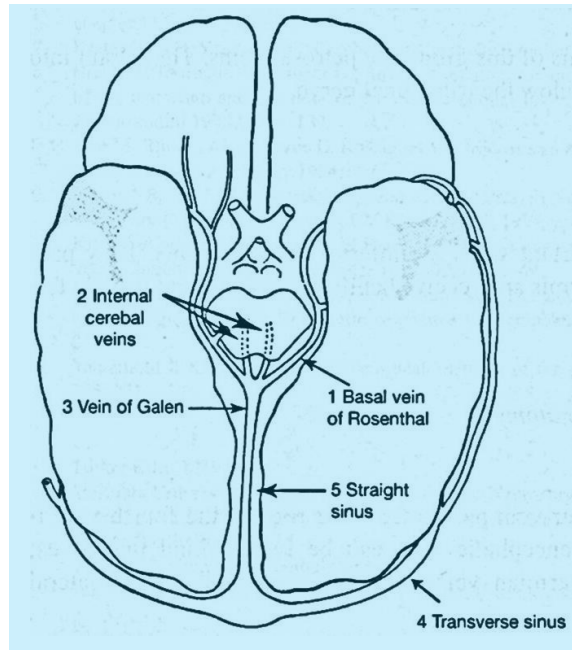


Figure 6: Illustration of the flow of venous blood that drains into the great cerebral vein of Galen and straight sinus (Kilic and Akakin, 2008, with permission)

In contrast to the anatomy of most of the human body, venous drainage pathways do not follow the same course as that of the arterial supply to the brain. Compared to that of the external cerebral veins, the structure of the internal cerebral venous system is relatively constant between individuals, with the exception of the basal vein of Rosenthal. Venous blood also often drains into the nearest venous sinus, with the exception of the deeper structures of the brain which first drain into the internal veins before draining into the venous sinuses. As well as this, the venous vessels draining the brain are valve-less; they form an intricate network through anastomotic connections, and have also been found to have no tunica muscularis. These properties are different to that of most of the rest of the human body. The absence of a tunica muscularis layer means that the veins remain dilated, allowing compensation during brain volume shifts caused by changes in intracranial pressure (ICP) (McKinnon, 1998; Uddin et al., 2006). The effect of changes in ICP on cerebral venous pressure and therefore venous blood flow is important. This is because changes in ICP can often be caused by oedema or generalised swelling of the brain as a result of traumatic injury to the brain, or an adverse event causing hypoxia for example. Approximately 70-80% of intracranial blood volume is located within the venous vessels, which means that the large volume capacity of the venous vessels is an important property for compensation during brain volume shifts (Stolz, 2006). In addition to this, the

lack of valves within the cerebral venous system means that blood flow is possible in different directions, as well as the fact that the direction of venous blood flow in cerebral veins and dural sinuses is controlled by pressure gradients (Epstein et al., 1970). This is the reason why centrifugal drainage causes blood to flow towards the dural sinuses, while centripetal drainage results in blood flow towards the Galenic drainage system. This all occurs within the deep white matter of the brain (Stolz, 2006).

In addition to this, there are small venous networks, which drain into cerebellar veins, as well as veins that drain the brainstem. These veins, along with the external and internal cerebral veins, then empty into the dural venous sinuses. These sinuses are flattened endothelial-lined spaces which lie between the inner meningeal layer and outer periosteal layer of the dura mater. They are of significant importance as the internal and external cerebral veins drain into them; they receive cerebrospinal fluid (CSF) from the subarachnoid space (SAS) via the arachnoid villi and granulations; and they also drain into the internal jugular veins. Other important veins which empty into the dural venous sinuses, in addition to those listed above, include the meningeal veins which drain the dura mater, the diploic veins which run between the internal and external layers of compact bone of the skull, and the emissary veins which originate outside of the cranial cavity (Figure 7).

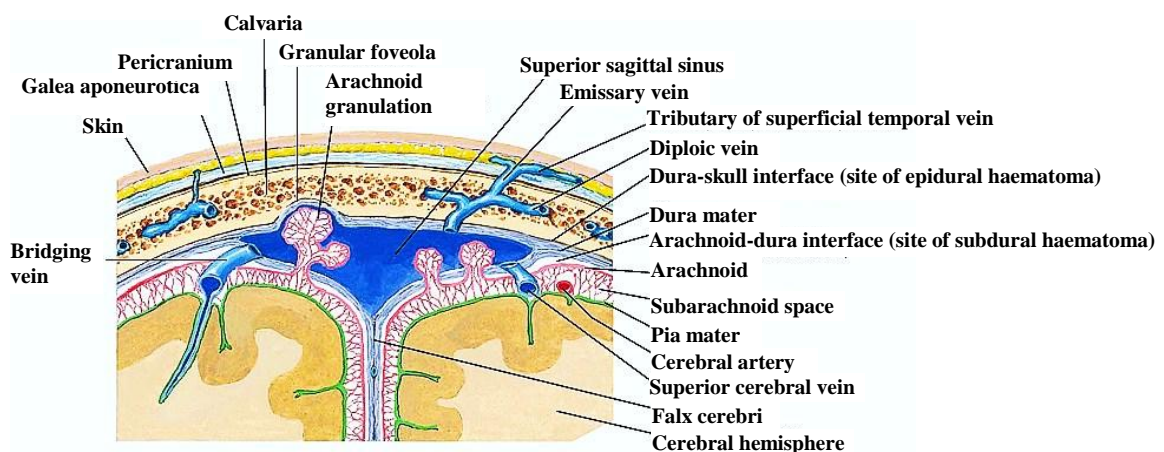


Figure 7: Meninges – Coronal Section (Netter, 2006, with permission requested)

1.3. Introduction to NAHI and SBS

There is a large spectrum of clinical features linked to inflicted brain injury in infants, depending on the intensity and type of injury that is caused. This can range from trivial bruising to severe trauma and fatality. There are also a large number of ways in which an infant or child can be injured; however in most cases no clear description of the circumstances is forthcoming. NAHI is therefore a generic term used for this type of injury. In contrast to this, shaken baby syndrome (SBS) has a more specific mechanism of injury (Minns and Busuttill, 2004). SBS is typically characterised by the triad of SDH, encephalopathy and retinal haemorrhage (RH) with little or no evidence of extra-cranial trauma, and in the absence of an adequate explanation for these injuries. RH and SDH are considered as hallmarks for SBS as they occur very rarely in young children under the age of 2 (Daly and Connor, 2001). Encephalopathy and more specifically hypoxic ischaemic brain injury is the most significant component with regards to long term damage, with subsequent neurodevelopmental impairment. However, out of all the presentations of SBS, SDH is possibly the most characteristic manifestation of the triad. It is demonstrated by a collection of blood in the subdural compartment (Figure 8 and Figure 9) as this pathway between the dural and arachnoid membranes presents the least resistance (Schachenmayr and Friede, 1978) when blood volume reaches a certain level.

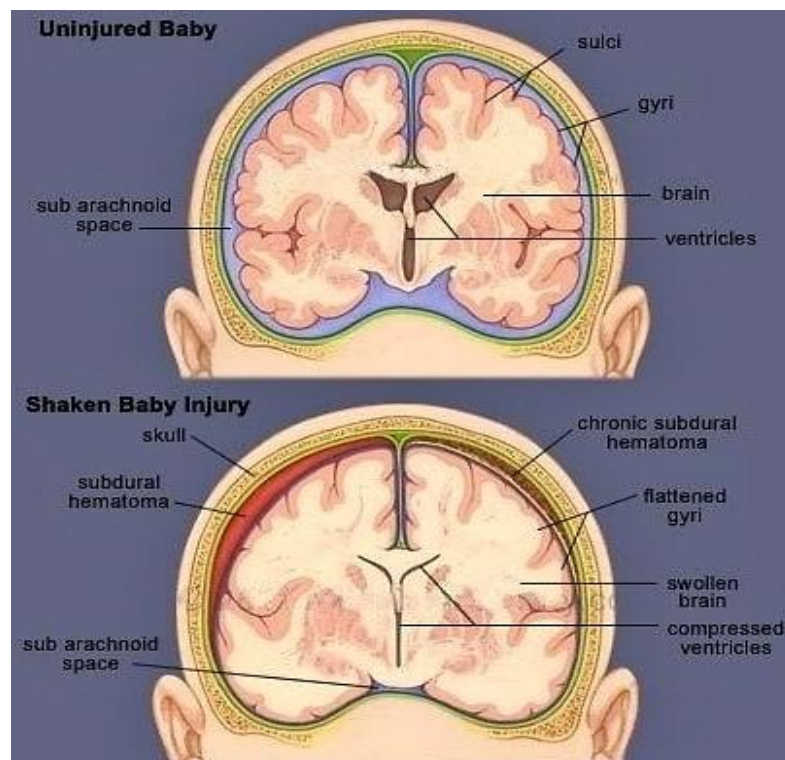


Figure 8: Comparison between a normal uninjured baby and the injured brain of a shaken baby (Kfolio, 2012b, with permission)

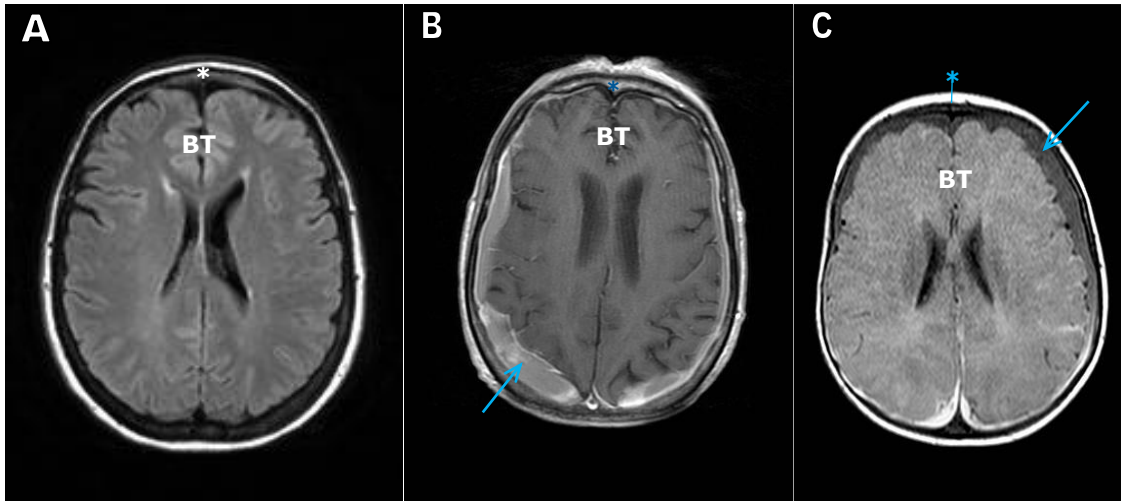


Figure 9: MRI images illustrating typical cases of SDH seen in both adult and infant cases. From left to right, MRI images illustrating a normal healthy adult (axial FLAIR), an adult with a SDH (axial T1), and a 5 month old infant with a SDH (axial FLAIR). The skull bone (asterisks), brain tissue (BT) and SDH (arrows) are illustrated. *MRI images courtesy of Dr T Jaspán.*

Common patterns in the way that SBS presents, including the child's social background and history, are frequently seen. SBS has been found to be most prevalent in children under 1 year of age. This is important as it has been calculated that up to 80% of fatalities due to head injuries in children under the age of 1 are as a result of abuse (Daly and Connor, 2001) as abused children at this age have the highest risk of death (Kasim et al., 1995). Cases of SBS have been found to be more common during autumn and winter months, as well as being more concentrated in urban areas (Barlow and Minns, 2000). It has also been found that the majority of perpetrators are men, and often the child's father, step-father, or the mother's boyfriend (Kasim et al., 1995; Starling et al., 1995). As well as these findings, it has been shown that mortality can be up to 30% and up to 70% of survivors suffer long-term impairment after NAHI (Matschke et al., 2009a). Due to the high mortality and morbidity rates, failure to identify abuse may lead to serious consequences (Dashti et al., 1999). The converse of this is that an incorrect diagnosis of child abuse can have profound consequences on the accused and the integrity of the family unit.

1.4. Introduction to Hypotheses and Theories regarding SDH in NAHI

There have been many hypotheses and theories put forward regarding the mechanisms causing SDH and other intracranial injuries in NAHI. Although none of

these theories have enough evidence required for complete validation, the key theories proposed regarding this topic will now be further discussed.

1.4.1. Rotational Acceleration of the Head causing Bridging Vein Rupture

Some of the first studies into the biomechanics of central nervous system (CNS) trauma were carried out by subjecting rhesus monkeys to whiplash forces without direct head impact. Whiplash is a rotational force whereby the head rotates in an arc around a point in the lower cervical spine (Gabaeff, 2011; Ommaya et al., 1968). In these studies it was demonstrated that rotational acceleration levels of the head of a monkey exceeding 40,000 radians/ second could produce cerebral concussion if the duration of acceleration was greater than 5 milliseconds. The majority of concussed animals showed evidence of visible brain injury such as SDH, illustrating the importance of head rotation as a mechanism of injury (Yarnell and Ommaya, 1969). In a more recent study, the rotational component of this shaking motion was shown to be the cause of the majority (93%) of strain placed on bridging veins. Bridging veins can be defined as veins which drain the superficial cerebral vessels, traverse across the pia, arachnoid and dura mater layers, before then draining either directly or indirectly into the cerebral dural venous sinuses. This motion of rotational acceleration was thought to cause bridging veins to rupture and result in SDH (Figure 10), and thus thought to be very dangerous, especially in infants (Morison and Minns, 2005).

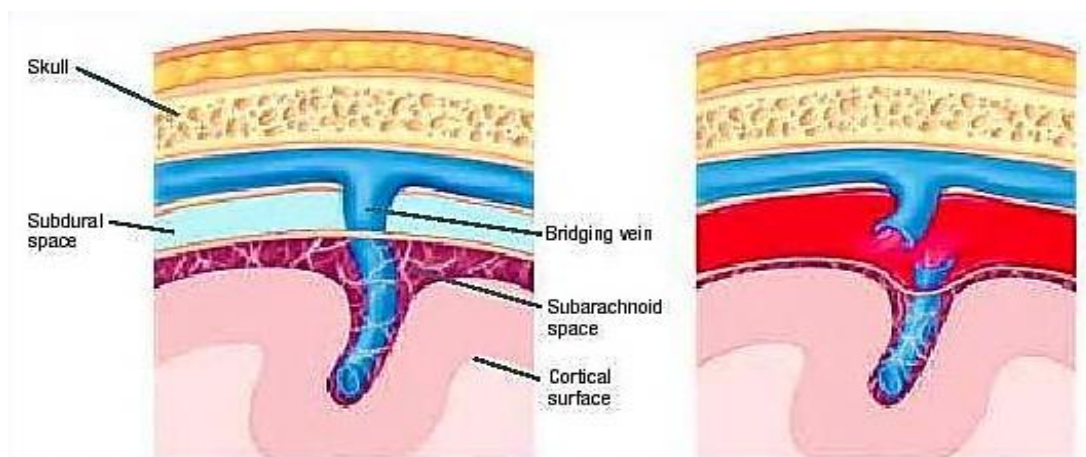


Figure 10: The Mechanism of Subdural Haemorrhage: The bridging veins travel from the cortical surface of the brain, and through both the arachnoid and potential subdural spaces (the potential subdural space however is illustrated here as an actual space) (left). When head injury causes shearing of the bridging veins (right), the subdural space rapidly fills with blood (Nakagawa and Conway, 2004, with permission requested).

1.4.2. Multiple Acceleration/Deceleration and Whiplash Injuries causing Bridging Vein Damage

Further studies were carried out, extrapolating from the study carried out by Yarnell and Ommaya (1969). A hypothesis was formed suggesting that multiple indirect applications of force such as repeated acceleration and deceleration (Figure 11), when for example an infant is shaken, would increase total strain on bridging veins compared to application of a single direct force such as striking an infant on the head. Guthkelch (1971) hypothesised that this would increase the incidence of rupture of these veins, thereby resulting in SDH. It was thought that the rotation-acceleration forces would cause damage to the anterior and posterior regions of the brain, and therefore would explain why SDH is often bilateral. This would also explain why SDH in 'shaken children' is more frequent compared to its incidence in head injuries from other causes. It was also hypothesised that as infants have a relatively large head and weak neck muscles in comparison to more developed older children and adults, this makes infants particularly vulnerable to whiplash injury (Guthkelch, 1971).

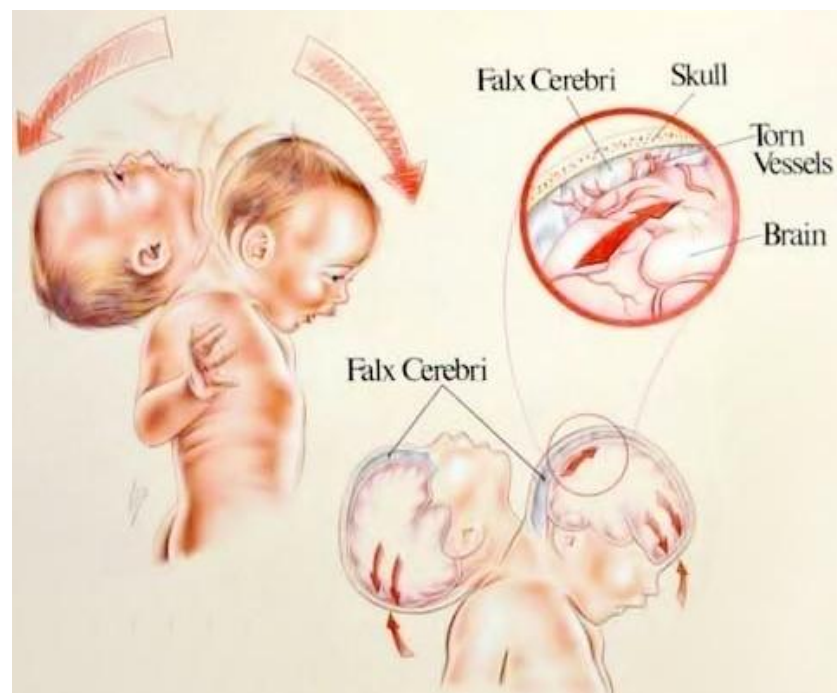


Figure 11: Illustration of the acceleration/deceleration forces subjected to the infant head during a shaking motion (Cwavirusa, 2012, with permission requested)

Caffey (1972), first defined the term 'whiplash shaken baby syndrome' or SBS. He used SBS to explain SDH, subarachnoid haemorrhage (SAH) and RH (usually bilateral and thought to be caused by retinal capillary damage) with minimal or absent signs of external trauma (Caffey, 1972; Caffey, 1974). This was based upon earlier studies linking rotational acceleration of the head to SDH and cerebral concussion (as discussed in section 1.4.1.).

However, it is particularly significant that the main justification for both Guthkelch (1971) and Caffey's (1972) claims that shaking is the cause of intracranial haemorrhage in infants, is derived from one single paper (Ommaya et al., 1968). This study aimed to quantify the rotational acceleration required to generate whiplash movements that would cause intracranial injuries in vehicular collisions. However, it was never investigated as to whether it was physically possible for a human adult to shake an infant with enough force to simulate the acceleration forces generated and applied to the Rhesus monkeys in these studies. The Rhesus monkeys in this study were subjected to forces of approximately 600Gs (one G being the acceleration of an object during free-fall against negligible air resistance), however data from the National Highway Traffic Safety Administration (NHTSA) states that injury thresholds to the brain occur from 80-100Gs (Klinich et al., 2002; Prange et al., 2003). Therefore forces subjected upon the test subjects were over 6 times that which have been found to cause intracranial injuries; and 60 times the amount of force that can be generated by humans with the most forceful shaking (Gabaeff, 2011). Hence the investigation carried out by Yarnell and Ommaya (1969) is possibly not the most appropriate study from which to extrapolate data, for application in determining possible SBS.

The difference in anatomy of the head and neck muscles of the Rhesus monkey compared to that of the human infant was also not established or taken into account. It has been found that the lower the mass of the brain, the more rotational acceleration is required to cause intracranial damage (Holbourn, 1943; Ommaya et al., 1968). This would therefore imply that a much smaller magnitude of force would be required in order to cause intracranial injuries in infants than has been calculated in previous studies. However these parameters have not been further investigated. Therefore, these factors bring into question the scientific validity of the use of the Ommaya *et al.* (1968) study as evidence to prove that manual shaking is the cause of unexplained intracranial injury in infants (Uscinski, 2006).

1.4.3. Impact-Deceleration Injury and Short Distance Falls

Recent findings from biomechanical studies suggest that the force required to produce the triad of SDH, RH and encephalopathy is not enough by shaking or whiplash-shaking alone, but also requires an impact force (Figure 12). This is because it has been found that it would be very difficult for a human adult to replicate the forces required to produce an acute subdural haematoma (ASDH) by manually shaking alone. In one study, models of 1 month old infants were instrumented with accelerometers before being shaken or impacted against various different surfaces. On average, impact accelerations exceeded shake accelerations by a factor of nearly 50 times. The mean tangential acceleration for shaking episodes was 9.29G, however 428.18G for impacts. All shakes did not reach the injury thresholds which had been calculated from previous work with subhuman primates. It was also found that the only stresses that exceeded the injury thresholds associated with concussion, SDH, and diffuse axonal injury (DAI) were the forces caused by impact. However this would mean that severe head injuries, commonly diagnosed as shaking injuries, require an impact to occur and therefore shaking alone is unlikely to cause SBS (Duhaime et al., 1987; Geddes and Plunkett, 2004; Prange et al., 2003). Parallel to these findings, a study investigating the relationship between RH and acceleration forces without impact suggests that RHs cannot be caused by high accelerations, even at rates above which can be physically generated by humans via shaking (Gabaeff, 2011).



Figure 12: The Magnifying Force of an Impact Injury: The impact of an infant's head against a solid surface can magnify the force applied to the brain by up to 50 times, compared to that of shaking alone (Nakagawa and Conway, 2004, with permission requested)

However in spite of this data, one flaw in these conclusions is that the force thought to be required to cause intracranial bleeding is calculated from the assumption that it is rupturing of bridging veins that are the cause of subdural bleeding. However, as is later discussed, there are currently many different theories which attempt to explain the causation of SDH in NAHI. In particular, the possibility whereby there are much smaller calibre vessels that are the cause of intracranial bleeding, which traverse between the dural layers before draining into the bridging veins, or alternatively drain into the bridging veins directly. If this is in fact the case, it would be reasonable to suggest that the magnitude of force thought to be required to cause SDH would be much lower than is currently proposed, as these values depend directly upon the assumed causational theory and the current data available.

The current problem is that it would be extremely difficult to construct a biomechanical model to replicate the shaking motion and the effects that this would have on an infant as seen in SBS, while taking into account all possible extraneous variables. A lot of studies that have been conducted over the years, present conflicting findings by claiming that shaking alone can in fact cause SDHs (Bell et al., 2011; Biron and Shelton, 2005; Roth et al., 2007). For example, in one study which looked at cases of infantile inflicted brain injuries whereby abuse was admitted by the said perpetrator, it was concluded that shaking alone could in fact cause the symptoms seen in inflicted traumatic brain injuries (Starling et al., 2004).

Alternative to these theories, it has been suggested that in cases involving impact forces whereby intracranial bleeding is present however external signs of injury are absent, the absence of external signs could potentially be explained by dissipation of these forces against a padded surface (Duhaime et al., 1987). Another theory that has been put forward suggests that alternatively, this could be due to the deformable characteristics of the infant skull, as well as the fact that the infant scalp and skull are specifically designed to protect the brain from traumatic injuries by absorbing much of the impact force (Uscinski and McBride, 2008). This could then explain the absence of external signs of traumatic injury in cases of intracranial bleeding caused by impact forces. In one particular study which investigated 167 cases (subjects had a mean age of 5.2 months) of infants sustaining vertical falls of <4 feet (1.22 metres), it was found that none of the studied infants sustained any significant intracranial injuries from the short distance falls (Tarantino et al., 1999). Similar findings have also been mirrored in

many other studies, showing that accidental trauma such as short falls very rarely cause SDH (Laurent-Vannier et al., 2011), or any other significant intracranial injuries (Helfer et al., 1977; Hobbs, 1984; Nimityongskul and Anderson, 1987). In addition to this, there have been no reports of children under the age of 1 who have fallen from a low height and developed both SDH and RH; whereas both SDH and RH are commonly found in NAHI (Laurent-Vannier et al., 2011).

However it should also be noted that the energy absorbed by the skull upon impact is significantly less in an infant compared to that of an older child or adult (Margulies and Thibault, 2000). Therefore it has also been found in a few studies that although short distance falls do not always result in intracranial injuries, the risk of asymptomatic brain injury is the highest in <6 month old infants (Glaser, 2004; Rubin et al., 2003). So much so that this age bracket has even been categorised into the 'high risk' criteria for occult head injuries in neurologically asymptomatic children, with other evidence of abuse (Rubin et al., 2003).

Conversely however, there are also a few studies whereby findings are in direct opposition to the theory that suggests that the deformable characteristics of the infant skull allows absorption of the majority of the impact force. Although these cases are extremely rare, it has been found that although head impacts caused by short distance falls are often harmless events, they can also cause serious injuries (Gabaeff, 2011; Reiber, 1993) and even lead to fatalities (Hall et al., 1989; Plunkett, 2001). This is illustrated in one study where it was found that 18% of 101 infants with radiographically proven skull fractures, had sustained these injuries from falling less than 3 feet (0.91 metres) (Greenes and Schutzman, 1997). However a possible flaw in these results is that the free fall velocity measured from the height of 3 foot is approximately the same as the head velocity generated from manual shaking of an infant carried out by a human adult (Bandak, 2005). Therefore in conjunction with the fact that the head often impacts against the torso and back of the neck during a shaking motion, this should mean that in theory the shaking and impact forces acting together would cause serious injuries such as skull fractures, or even lead to fatalities. However many cases of NAHI show no external signs of trauma.

It can be concluded that as a result of the deformable characteristics of the infant skull, impact to the head due to for example falling from a small height, would be unlikely to cause SDH without any other underlying pathology such as damage to the scalp or skull (Margulies and Thibault, 2000). In addition, despite the results

of a few studies which report infantile fatalities, it has been found that overall the rate of mortality after a short distance fall is in reality very low. This is emphasised by the fact that falls from a height of up to 10 feet (3.05 metres) are unlikely to produce serious injury (Williams, 1991), and falls from greater heights still result in a low mortality rate (Laurent-Vannier et al., 2011). Therefore it has even been stated that when children incur fatal injuries which are reported to be due to falling from a height of <4 feet, the information obtained regarding the case must be incorrect (Chadwick et al., 1991).

In an attempt to investigate the validity of the studies carried out by Duhaime *et al.* (1987), a replica of the model originally used was constructed and tested. It was found that differences in certain parameters could increase angular head accelerations, and the results obtained were closer to the internal head injury and SDH injury thresholds (Cory and Jones, 2003). This is important as most cases of impact to the head occur in conjunction with a rotational motion as the head is hinged onto the neck, and rotation is thought to be one of the most important factors in the causation of intracranial injury. As well as this, in the same study impact against the torso was found to occur at the end of the shake cycle, which highlighted the potential for shaking and impact forces to act together to produce forces exceeding head injury thresholds. Since this study was carried out, further investigations have shown that shaking in the absence of impact is in fact able to cause SDH and RH (Laurent-Vannier et al., 2011). However from a biomechanical perspective, it has also been shown that shaking alone cannot cause fatal head injuries in an infant (Cory and Jones, 2003; Jaspan, 2008).

1.4.4. Neck and Cervical-Spinal Cord Injury

While these previously discussed studies aimed to show how manual shaking could not cause intracranial injury in infants, they did not take into account the potential mechanisms and consequences of neck injury in infants. This is despite the fact that the neck is the important link between the head where injuries often occur, and the torso where the shaking is usually initiated (Uscinski, 2006). Quantitative studies analysing injury biomechanics were therefore carried out which focussed on the shaking forces reported to be required to cause SDH and their resultant effect on the infant head and neck. It was found that if an infant is subjected to the acceleration/deceleration forces reported in the literature to be required to cause SDH, potentially severe injuries in the neck, and therefore often structural failure in the cervical spinal cord and brainstem (Figure 13) should be

seen before injuries are seen in the head (Bandak, 2005). This is thought to be because the anatomical structures and biomechanical features of an infant means that they have a higher centre of gravity than adults; thereby making them more susceptible to injury, particularly in the cervical spinal region (Fuchs et al., 1989). Factors increasing susceptibility to damage are thought to be due to the infant's disproportionately large head and weak muscles of the neck. This is thought to increase the likelihood of flexion-extension injuries as the shaking forces produced via shaking of the torso are transmitted through the weak and undeveloped infant neck (Fuchs et al., 1989; Watson and Monteiro, 2009). Laxity and therefore excess mobility of the ligaments as well as increased elasticity of the infant spine could also increase susceptibility of the spinal cord to injury, even though the vertebral column may be better protected (Pang and Pollack, 1989). Immature development of the joints between the spinal vertebrae may also mean that damage could occur with relatively little force as the ability to withstand flexion-rotation forces would be diminished compared to that of an adult (Fuchs et al., 1989). Therefore many studies even argue that neck injuries should occur, even if infants are subjected to significantly lower shaking forces than has previously been reported to cause SDH in NAHI (Bandak, 2005).



Figure 13: Neck and Cervical-Spinal Cord Injury: Violent shaking can cause trauma directly to the spinal cord (Nakagawa and Conway, 2004, with permission requested).

However, if it were the case that cervical spinal cord and brainstem injuries are always seen before intracranial injuries, it would logically follow that any type of intracranial injury would also present with the accompanying clinical signs of neck injury (Uscinski, 2006). These findings would also then suggest that injuries caused by shaking of an infant should result in completely different injuries,

biomechanically, clinically and physiologically (Uscinski, 2006), in contrast to that of current literature on which current diagnostic criteria for SBS is based. In addition to this, from the routine MRIs that are now carried out in suspected cases of SBS, it has been found that neck injuries in the form of soft tissue swelling due to haematoma or oedema are not present in almost all cases (Gabaeff, 2011). Therefore a re-evaluation of the application of the criteria regarding SBS may be required, given the important social and medico-legal significance of the given findings (Bandak, 2005).

In this way, as evidence suggests, there are many controversies concerning biomechanical studies regarding the validity of the proposed hypotheses and their relevance to pathological or clinical observations. This is because there are currently no diagnostic tests for inflicted head injuries (Hobbs et al., 2005). The problem lies with the fact that the hypotheses cannot be confirmed using living humans as research can only be directed towards using cadavers, animal specimens or computer-based models (Jaspan, 2008). This therefore means that even the most carefully constructed experiments cannot be designed to account for all possible confounding effects of extraneous variables that should be considered when designing a biomechanical model to simulate the effects of shaking motions applied to a human infant (Ommaya et al., 2002). However the aim is to minimise these confounding factors in order to obtain results that are as accurate as possible.

1.4.5. Hypoxic-Ischaemic Injury

More recently, the role of hypoxic-ischaemic (HI) injury in the pathogenesis of severe brain damage in NAHI has been closely examined. It has been suggested that hypoxia could be caused by potential non-specific physiological responses to head injuries such as vomiting and aspiration as well as seizures (Uscinski, 2006). It was also suggested that damage to the cranio-cervical junction caused during a stretch injury from cervical hyperextension or hyperflexion of the infant neck (particularly vulnerable to injury in young children) may cause respiratory abnormalities. In one particular study involving a group of infants and children with fatal NAHI, neuropathological research involving use of immunocytochemistry to look for microscopic damage was carried out (Geddes et al., 2001a). In these cases, tissue damage was thought to be caused by HI-mediated axonal injury as apnoea was found at presentation in 75% of the 37 cases of infantile head injury examined (Geddes et al., 2001b). Additionally, it has also been suggested that the

degree of haemorrhaging is correlated to the degree of hypoxia found (Cohen and Scheimberg, 2009).

However it still has not been proven whether HI leads to intracranial injury as has been previously suggested, or vice versa (Hymel et al., 2007). For example it can be seen in the aforementioned studies regarding hypoxic-ischaemia, that the cohort sizes of the cases that were examined were very small, therefore the validity of the conclusions that were made are questionable. Furthermore, other research studies suggest that there is very little evidence to support the link between SDH and HIE with cerebral swelling, in cases where evidence of external signs of trauma are absent. In one retrospective study which looked at 82 cases of HIE, no macroscopic evidence of SDH was found in any of the studied cases (Byard et al., 2007), which therefore contradicts the hypothesis that infantile HIE in the absence of trauma can cause SDH. A further paper addressed the imaging and post mortem findings of a cohort of 50 infants suffering documented non-trauma related cardiorespiratory arrests admitted to a tertiary paediatric centre (Hurley et al., 2010). In one 18 day-old infant a small clot was found adherent to the dura, which was felt to be birth related, and microscopic intradural blood was found in a further 2 children. No subdural haematomas were identified in the remaining 49 children. As well as this, it was found that SDH is not part of the common pathophysiology of HIE as a result of hypoxic episodes such as drowning and asphyxia (Byard et al., 2007), even though cerebral oedema is commonly found after significant HI insults caused by drowning (Orlowski and Szpilman, 2001).

The largest study to date, which includes data of CT findings in 156 cases of paediatric drowning, clearly shows that neither intra- nor extra-axial bleeding are found following submersion injuries (Rafaat et al., 2008) although significant anoxic-ischaemic insult occurs secondary to drowning (Orlowski and Szpilman, 2001; Romano et al., 1993; Taylor et al., 1985). It has been shown in numerous studies that CT findings in patients following accidental injuries are often normal, and so differ significantly to those taken in patients following NAHI (Hymel et al., 1997), which often show some form of haemorrhaging or oedema (Merten et al., 1984; Rafaat et al., 2008). From these various studies, it can be deduced that current evidence suggests that the HI hypothesis is an unlikely cause of SDH found in cases of infantile NAHI (Pollanen, 2011).

1.4.6. Unified Hypothesis

A 'unified hypothesis' was proposed in 2003 as an alternative mechanism for the clinical neuropathological findings in cases of infant head injury without impact (Geddes et al., 2003). It was suggested that in infants, severe hypoxia would cause damage to the endothelial cells of the intradural blood vessels, as well as leading to brain swelling, which in turn would cause raised ICP. This combination of events was thought to cause blood to leak into the subdural space, causing SDH as well as resulting in RH (due to anatomical communication between the intracranial SDS, and the SDS surrounding the optic nerves) (Levin, 2010), suggesting that the formation of bilateral thin-film SDH often observed in NAHI is not due to traumatic disruption of bridging veins as previously thought, but due to hypoxic injury to intracranial vessels in some cases of infant head injury. As hypoxia with brain swelling would also account for retinal haemorrhages, this would therefore be consistent with the unified hypothesis (Geddes and Plunkett, 2004). However countering this, a joint Royal College of Paediatrics and Child Health and the Royal College of Ophthalmologists consensus document on abusive head trauma and the eye in infancy, which involved a meta-analysis of the data, concluded that acute hypoxia does not result in or cause retinal haemorrhages, although it may cause potentially fatal brain swelling (RCPCH and RCOphth, 2013).

This 'unified hypothesis' met a large amount of criticism as it challenged the supposed infallibility of the triad of injuries used to help diagnose NAHI, while lacking in sufficient evidence to support this new theory. The majority of existing evidence in fact supports the idea that disruption of intracranial vessels causes hypoxia, not that hypoxia causes intracranial bleeding. In a test case in the UK, the Court therefore ruled that it could not be regarded as an alternative cause of the triad of injuries and therefore, the hypothesis had to be retracted (R v Harris and Other Appeals 2005).

However the UK Royal College of Pathologists later stated that although the triad of injuries was a strong indicator of NAHI, it should also not be used as absolute proof of NAHI in the absence of further evidence (RCPPath, 2009). This is because the cause of the pathophysiological effects, often seen as a consequence of NAHI, is multifactorial in nature (Adamsbaum et al., 2010; Barnes and Krasnokutsky, 2007; De Leeuw and Jacobs, 2007).

1.4.7. Further Mechanisms

The two main theories to date that have already been discussed are mechanisms involving either the rupture of bridging veins or hypoxic-ischaemic injury leading to intracranial haemorrhaging. Since the establishment of these hypotheses, alternative theories regarding the cause of SDH in NAHI involving infants have been suggested. These include vitamin deficiencies (Alan and Clemetson, 2004), reactions to vaccines and infections (Buttram and Yazbak, 2004; Innis, 2006) including inflammation and excitotoxicity (Ichord et al., 2007), formation and bleeding of intracranial dural arterio-venous fistulae (DAVF) (Wilson et al., 2008), as well as the occurrence of spontaneous SDH in infants (Vinchon et al., 2010a). These factors are rare and are also difficult to prove to be the cause of intracranial bleeding, however they should always be considered in a differential diagnosis (Forbes et al., 2004) as they could lead to exacerbation of concurrent bleeding (Uscinski and McBride, 2008). There is now increasing evidence for the involvement of the intradural vascular plexus in SDH found in cases of NAHI. This plexus is also thought to be involved with CSF movement, and therefore may be a contributing factor to SDH in NAHI. This is therefore a particularly important theory to explore. As well as this, subdural bleeding can also be caused via various other mechanisms. These include mechanical deformation of the dura during delivery of a child (Whitby et al., 2004) as well as impact trauma which includes accidental and NAHI. These more recent theories attempting to explain mechanisms behind SDH in NAHI will now be explored in further detail.

1.4.8. Evidence against Bridging Vein Rupture

During venous cleavage and separation of the dural venous drainage from the venous drainage of the brain, there is resorption of the majority of primary venous anastomoses that lie between the dura and pia mater. The bridging veins are formed as a result of enlargement of the remaining anastomoses, which penetrate the dural border cell layer which is situated between the arachnoid and dural meningeal membranes (Miller and Nader, 2013; Nabeshima et al., 1975), and travel through the dura before entering the SSS (Figure 14). These bridging veins which conduct blood between the systemic circulation and the brain have been found to be fairly robust, considerable force being needed to cause them to rupture (Lee and Haut, 1989). This challenges the hypothesis that bridging vein rupture is a primary cause of SDH in many cases of NAHI and is emphasised by the fact that infantile SDH can be found in different cases and conditions in which

there is no evidence of mechanical trauma (Buttram and Yazbak, 2004; Innis, 2006).

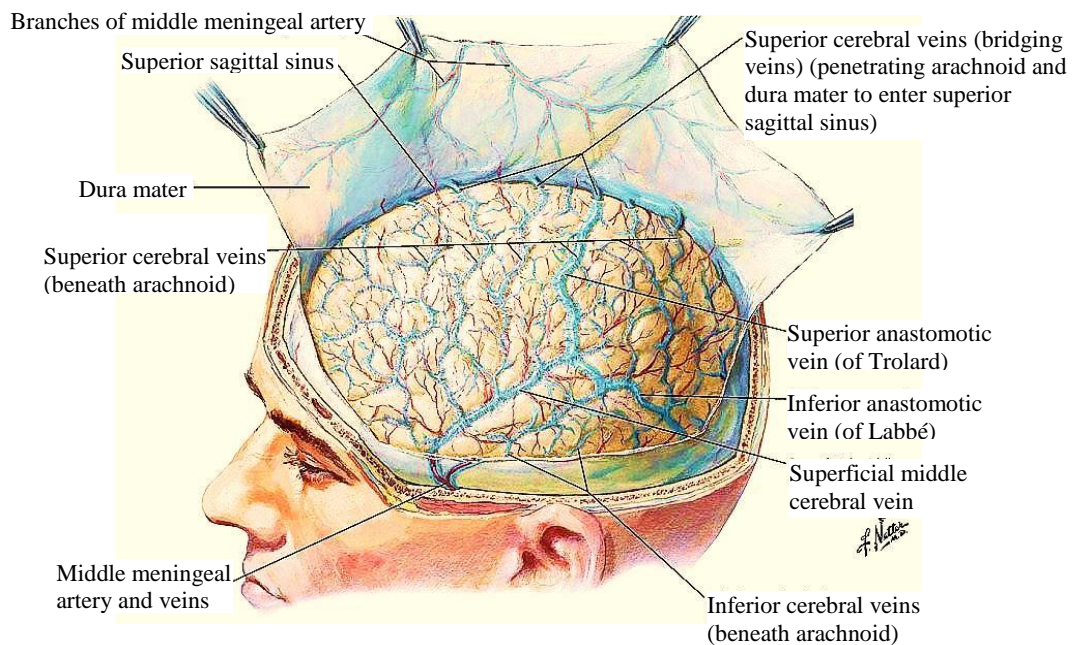


Figure 14: Superficially located Cerebral Blood Vessels (Netter, 2006, with permission requested)

Although most cases of SDH in infants are thought to be caused by trauma, there are also numerous non-traumatic causes. It has long been considered that the rupture of bridging veins is the cause of SDH in NAHI. However very few biomechanical studies show this to be the case (Lee and Haut, 1989). The bridging veins are large in calibre and the vessel walls contain a muscular component which helps to maintain intravenous pressure. However due to their considerable size and strength, vessel rupture would be unlikely to cause thin film SDH, typically found in infants. A study investigating 126 cases of intracranial haemorrhage in new-borns found that bridging vein rupture was uncommon; 62 of the neonatal autopsies revealed SDH, whereas only 3 of the 126 cases showed torn bridging veins (Craig, 1938). This illustrates the now increasing body of evidence against the traditional theory of rupturing of bridging veins as the biomechanical basis of this concept is more carefully scrutinised and as more theories are presented.

1.4.9. Intradural Vascular Plexus

The dura mater is commonly thought of as being a fibrous membrane, generally lacking in a specific function or having a purely protective function as a physical barrier to external injury. However, through the study of its embryology and anatomy, it can be seen that the dura is a complex structure. In a fetus, the dural venous connections are constantly being modified as they have to supply the cerebral hemispheres which are growing at a rapid rate (Streeter, 1915). This means that the dural venous sinuses into which the bridging veins flow are constantly changing during gestation and are not fully formed until a few months after birth. In order for these modifications to occur, a plexus (Figure 15) of venous vessels located in between the outer periosteal and inner meningeal layer of the dura mater (intradural vascular plexus), which is also situated adjacent to the dural venous sinuses and continuous with the venous lacunae (out-pouchings within the dural folds) is required to allow continuing development of the cerebral venous anatomy. This intradural vascular plexus has been found to be more vascularised in an infant compared to that of an adult due to these continuing changes that occur even after birth (Browder et al., 1975).

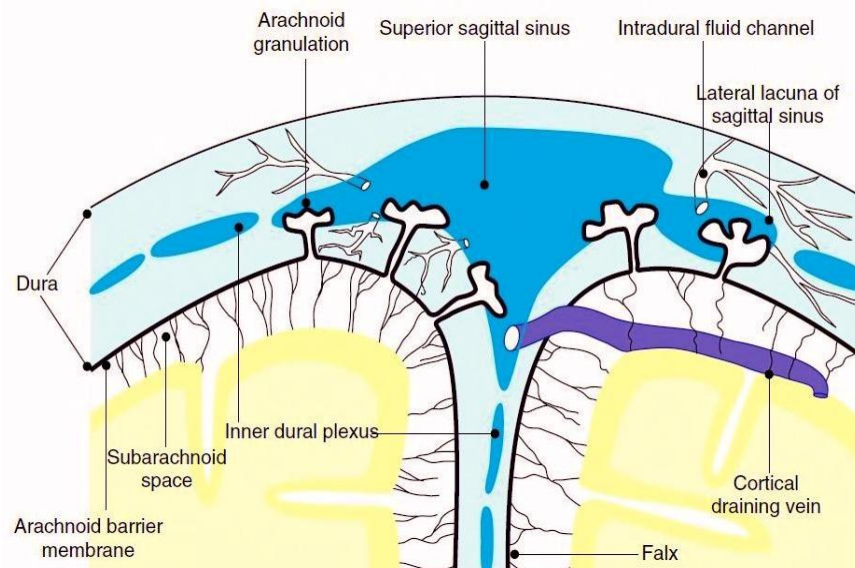


Figure 15: Coronal section through the brain and dura, illustrating the intradural vascular plexus (Squier, 2009, with permission)

One hypothesis suggests the possibility of rupture of this intradural venous plexus as the cause of bleeding seen in both accidental and non-accidental traumatic head conditions. The reasoning for this is that, relatively, much smaller forces are required to rupture these thinner-walled vessels compared to that of more robust

bridging veins. In addition, this venous plexus borders the subdural compartment (Figure 16) which consists of 10-15 layers of loosely adhering (due to lack of tight junctions) flake-like cells (Nabeshima et al., 1975), which are easily disrupted when blood collects in this region. This has therefore been suggested to be the cause of the wide-spread distribution of blood seen in infantile SDH (Hannah, 1936; Mack et al., 2009). It has also been shown that early venous cleavage causes a decrease in the number of connections between the pia and dura mater, which reduces communication between the venous drainage of the brain and the systemic circulation (Mack et al., 2009). This allows the blood brain barrier (BBB) to form correctly. However, unlike the vessels of the brain where substances must pass through the BBB, it has been found that dural venules are permeable. They have been found to allow plasma protein extravasation following immunological, chemical or electrical stimulation due to extensive vascular innervation. This further supports the hypothesis that these leaky intradural venous plexus vessels may be the source of SDH in NAHI (Bolay et al., 2002; Markowitz et al., 1987).

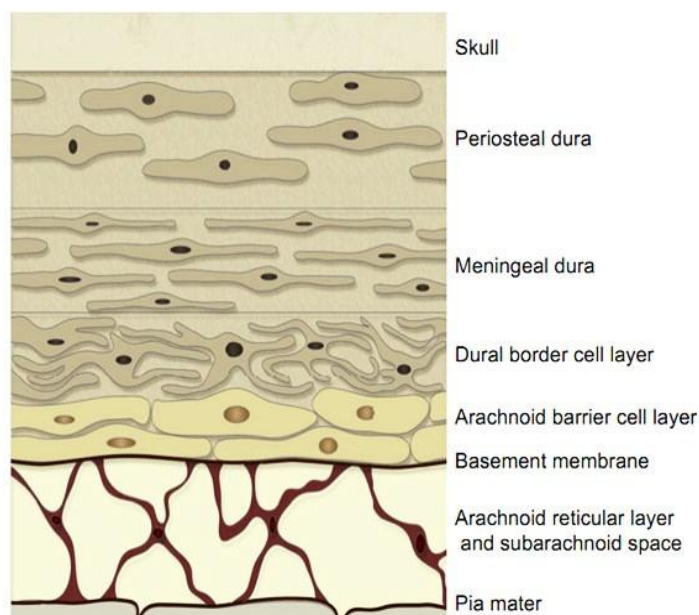


Figure 16: The Meningeal Layers (Mack et al., 2009, with permission)

1.4.10. Chronic Subdural Haemorrhage (CSDH)

CSDH may present either as a thin resolving membrane; a wide-spread, bilateral, thin-film haemorrhage usually found in infants; or a unilateral, thick, space-occupying haemorrhage often found in adults. Characteristics of SDHs in infants

are therefore considerably different to those found in adults (Geddes et al., 2001a; Squier and Mack, 2009), and particularly in the elderly.

CSDH is a disease commonly presenting in the elderly following minor trauma. Generalised cerebral atrophy that occurs with normal aging leads to enlargement of the space in between the brain and skull. This causes stretching of the bridging veins (along with the surrounding vessels and tributaries) and allows greater movement of the brain within the cranium, which ultimately renders these vessels more vulnerable to trauma (Adhiyaman et al., 2002; Ellis, 1990). The thickness of the haematomas found in cases of CSDH is typically greater with increasing age (Fogelholm et al., 1975), likely due to re-bleeding following initial ASDH, and therefore usually presents as a thick, space occupying haemorrhage.

However as well as developing following minor trauma to the head, CSDHs have also been known to expand due to re-bleeding in the absence of additional trauma (Ito et al., 1975, 1978) in both adults and infants. It has been shown that excessive activation of the coagulation and fibrinolysis systems may occur in CSDH following the clot formation consequent upon an initial SDH (Kawakami et al., 1989). In addition, the degradation products of fibrin caused by the increase in fibrinolysis are associated with tissue inflammation and therefore have some vascular permeability inducing effects, which leads to leakage from the micro-capillary endothelial gap junctions (Harada et al., 1989; Yamashima et al., 1983). Therefore it has been suggested that fresh blood due to re-bleeding may sometimes present in addition to an already existing CSDH and may therefore be mistaken for evidence of a new injury (Ito et al., 1976). It is essential to be able to differentiate CSDH from ASDH as although CSDH begins as an acute event which has failed to be recognised at the time of injury, this does not necessarily indicate an intentional cause.

The possibility of multiple episodes of re-bleeding as opposed to an ASDH is therefore one of the reasons why MRI scans are routinely carried out in cases of suspected NAHI. This is because an MRI scanner is able to detect a difference in the appearances of residual blood products of different ages according to their respective signal intensities after intracranial bleeding, and depending upon the number of episodes of bleeding that have occurred (Adamsbaum et al., 2010) over an indefinite amount of time. It should therefore be possible to detect presence of a single intracranial bleed as a result of a singular recent event, or due to multiple haematomas that have occurred over time (Renton, 2004).

1.4.11. Birth-Related SDH

A combination of encephalisation (development of a larger brain with evolutionary time which requires a broader pelvic opening) and bipedalism (movement of an organism via two legs which requires a narrower pelvic opening) in the human has ultimately lead to vulnerability of the neonate during childbirth (Rosenberg and Trevathan; Schultz, 1949). This is because in order to accommodate the relatively large infant brain, the skull develops to its maximal possible volume during the gestational period; therefore in order for the infant head to pass through the narrow pelvis, head moulding must occur. In addition to this, the fetus is usually forced head first through the pelvic opening via a total of 80-160 uterine contractions, each exerting 60-70mmHg of force (Buhimschi et al., 2003) during parturition. It would therefore logically follow that this may cause some form of intracranial damage (Uscinski and McBride, 2008). This is the reason why SDH has long been recognised as a possible complication of the birthing process (Craig, 1938; Cushing, 1905; Holland, 1922), albeit, until recently, an uncommon consequence in term infants. This may be because examinations are only mainly carried out in symptomatic neonates in order to verify their symptoms (Whitby et al., 2004).

More recent studies now show that small amounts of subdural bleeding are in fact relatively common occurrences as a consequence of birth trauma resulting from various different modes of delivery (Holland, 1922; Towner et al., 1999), including apparently uneventful vaginal birth. This is because although it is thought that lack of rigidity in an unfused infant skull is able to protect against raised intracranial pressure during birth, as a result of this, the vessel walls are poorly supported and consequently vulnerable to rupture.

A series of recent investigations found that the prevalence of SDH in asymptomatic term neonates was up to 45.5% (Looney et al.; Rooks et al., 2008). The theory is further exemplified as it has been found that there is a significantly higher incidence of birth-trauma related SDH in neonate males than in females. The cause of this is believed to be due to the larger head size and extra-cerebral fluid spaces found in males compared to females, a larger head circumference being thought to increase the likelihood of SDH caused by minor trauma during birth (Miller and Miller, 2010).

In addition to this, CSDH has been found in infants as young as 2 weeks old. This could be explained by the fact that as CSDHs often expand very slowly and therefore only present clinically weeks to months after the initial bleed (Uscinski and McBride, 2008), in these particular cases it would be reasonable to assume that the haematomas developed earlier than at 2 weeks of age. This could mean that they could be the result of parturition as birth-related intracranial haematoma generation is a lot more common than was previously thought (Uscinski and McBride, 2008).

1.4.12. Neomembrane Formation

Healing has been found to occur following SDH (Rooks et al., 2008), and involves formation of a membrane (neomembrane) (Figure 17) that contains numerous thin-walled capillaries. It has also been found that this process may be more common than has previously been recognised. In one particular study subdural neomembranes were found in 25% of infants that were examined (Rogers et al., 1998) although these membranes can be easily missed without microscopic examination.

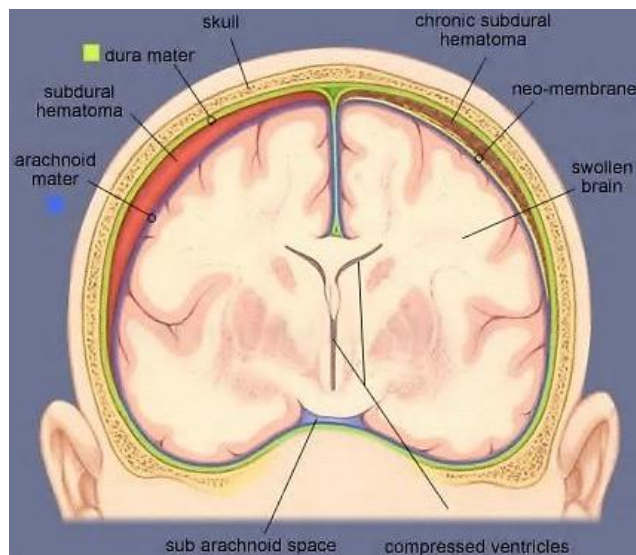


Figure 17: Neomembrane Formation (Kfolio, 2012a, with permission)

Neomembranes are thought to confer vulnerability to re-bleeding in infants. It has been proposed that bleeding may be exacerbated by upper airway obstruction from choking on food or vomitus, as well as paroxysmal coughing or following

cardiopulmonary resuscitation (CPR). It has been suggested that these could cause hypoxia in addition to an increase in intracranial and intravascular pressure; factors which have been suggested to be sufficient to cause the thin-walled intracranial veins to rupture and therefore resulting in intracranial bleeding (Geddes and Talbert, 2006). However, there has essentially been no direct observational evidence to support this proposed hypothesis (Pollanen, 2011), as well as the fact that, as has been previously discussed, it has been shown that SDH is not seen in cases involving hypoxia and asphyxia alone (Byard et al., 2007; Hurley et al., 2010). Additionally it has been found that regardless of its duration, CPR is not associated with the presence of haemorrhaging; although it is often found in cases of NAHI (Rafaat et al., 2008).

Therefore although this theory of intracranial bleeding caused by birth trauma followed by re-bleeding of the neomembranes seems plausible, current literature shows the suggested mechanism by which the re-bleeding is thought to occur via choking on food or vomitus, paroxysmal coughing or CPR is very unlikely. It therefore logically follows that an alternative mechanism would be responsible for the re-bleeding of these neomembranes; an issue of evidential mismatch which this project aims to resolve.

1.4.13. Movement of CSF

It has been suggested that impaired CSF drainage plays a major part in the pathogenesis of SDH in infants. Different pathways for CSF absorption in an infant compared to that of an adult may explain the difference in presentation of SDH in both groups (Geddes et al., 2001a). Therefore further investigation into the mechanisms involving CSF movement is important, as the presence of a CSF transport pathway could help to explain many of the common clinical findings in SDH (Fox et al., 1996).

1.4.14. Involvement of the Arachnoid Membrane

A hypothesis was put forward claiming that tearing of the arachnoid membrane may be the cause of accumulation of CSF in subdural collections in cases of NAHI (Kristof et al., 2008).

However if a primary event such as haemorrhaging was to produce a subdural collection, and then following this if a secondary tear was to occur within the

arachnoid membrane, this would disrupt the Blood-CSF barrier. This would then cause the plasma and blood to flow out of the subdural compartment into the SAS, but not into the subdural compartment as proposed. In addition to this, it is unlikely that a non-traumatic event would cause the arachnoid membrane to rupture, leading to the formation of subdural collections (Mack et al., 2009).

1.4.15. Involvement of CSF and the Intravascular Plexus

It has since been suggested that the intradural vascular plexus has an important role in the movement of CSF into the lymphatic and venous systems (Stroobandt et al., 1978). It is believed that CSF moves from the SAS into the dural interstitium, which then enters the dural sinuses via the dural venous plexus. In one study, dye injected into the subarachnoid compartment appeared in the dural venous system before then being found later in the SSS (Fox et al., 1996). An extensive network of intradural channels have been found, which communicate with the SSS via separate entry routes to the bridging veins and indicate a possible pathway for CSF absorption (Papaiconomou et al., 2004).

There have been numerous literature reviews over the years that have analysed scientific data regarding SDH in NAHI, most of which have concluded that there is inadequate definitive evidence to confirm the validity of any causation regarding intracranial injuries in NAHI (Donohoe, 2003). It was also found to be difficult to determine what role shaking has in causing intracranial injuries as well as being able to pinpoint a particular form of intracranial pathology caused as a result of shaking (Leestma, 2005). The above observations therefore illustrate the importance of careful evaluation of each individual case rather than the use of generalised rules to determine whether or not an injury is intentional, as there are numerous different mechanisms that appear to be credible causes of intracranial bleeding (Uscinski, 2006).

1.5. Brief Introduction into Tissue Fixation

Fixation causes denaturation and unmasking of certain groups within tissue proteins (Hopwood, 1967). Good quality fixation is essential for quantitative analysis of tissue structures to allow preservation and therefore visualisation of tissues on structural and ultrastructural scales. The composition of fixative required depends on how the resultant tissue will be further analysed (Trachsel et al., 2011).

1.5.1. Perfusion Fixation

Perfusion of fixative through the vasculature is able to rapidly and thoroughly fix tissues while fixation of tissue by immersion into fixative is extremely slow, and therefore is often only used when perfusion fixation cannot be used (Muhlfeld et al., 2007).

The most commonly used fixatives contain paraformaldehyde (PFA) and glutaraldehyde (GA), which are often combined with a post-fixative. The choice of fixative used depends on the purpose for which the tissue is fixed. This is because chemical fixation always requires a compromise between preservation of tissue cellular ultrastructure with a higher GA concentration, and maintaining antigenicity with a lower GA concentration (Muhlfeld et al., 2007).

1.5.1.1. Formaldehyde Fixative

The reaction of formaldehyde with tissue proteins is mostly complete within 24 hours due to rapid penetration of the small molecules into the surrounding tissue. However, tighter cross-linking via formation of methylene bridges takes 48 hours or more. Tissues that are fixed with formalin for a shorter amount of time than this are therefore less well fixed and are more likely to be damaged by reagents added to the tissues post-fixation. This includes the dehydrating agent ethanol which may fix and cause coagulation of protein tissue that formalin has failed to protect completely (Kiernan, 2000).

Fixation using formaldehyde for even a short period of time can reduce autolysis and allow tissue resistance to non-isosmotic substances. This in turn improves the structural integrity of frozen sections, especially if a cryoprotectant such as sucrose is later added (Kiernan, 2000). Formaldehyde does not completely destroy immunogenicity of tissue protein and therefore is a good fixative to be used in light microscopy (LM). However as tissue is not stabilised on an ultra-structural scale, it is not adequate for use in electron microscopy (EM) (Connie et al., 2010).

1.5.2.1. Glutaraldehyde Fixative

Glutaraldehyde has larger molecules than formaldehyde; therefore it penetrates the tissues more slowly. However its reaction with protein is rapid, and its

superior cross-linking abilities that are most effective at pH 6.5 (Cater, 1963; Oshita et al., 2002) are able to stabilize cell structure, meaning that glutaraldehyde is the best fixative to be used for EM (Connie et al., 2010).

Enzyme activity in tissues is reduced by the inhibitory effects of fixatives. Therefore enzyme activity post-fixation is dependent upon time and temperature of fixation, the buffer that is used, the length of post-fixative wash and the duration and temperature of homogenisation (Christie and Stoward, 1974). Glutaraldehyde is able to inhibit enzyme action considerably more than that of formaldehyde, with enhanced effectiveness in correlation to increasing time left within the fixative (Hopwood, 1967).

The combination of formaldehyde and glutaraldehyde for fixation of tissue used in EM means that tissues will first be rapidly penetrated (at five times the rate of glutaraldehyde alone) by the smaller formaldehyde molecules allowing initial tissue stabilization, while glutaraldehyde will allow more slowly penetrating, however more effective, cross-linking of tissue (Karnovsky, 1965).

Tissue which has been treated with formaldehyde or glutaraldehyde can be externally post-fixed (Trachsel et al., 2011) in 1% osmium tetroxide (OsO_4) mixed with an isosmotic buffer for EM analysis. Post-fixation decreases tissue membrane permeability by stabilizing the cell membranes, which in turn reduces susceptibility to osmotic effects. Uranyl acetate is also used as a second post-fixative agent and reduces the amount of axial lipid diffusion. Only small blocks of tissue can be fixed adequately for EM as the depth of tissue penetration is limited and whole organs require at least 24 hours to allow for tissue fixation. In addition to this, the dehydrating agent ethanol causes denaturation of proteins and helps to stabilize elastic fibres. Tissue samples are usually dehydrated in graded concentrations of ethanol which are then embedded into a medium such as epoxy resin, which can be used for high resolution LM as well as EM (Connie et al., 2010). Once fixation is complete, tissue samples can be stored at 4°C to preserve the tissue.

1.6. Brief History of Resins and Vascular Corrosion Casting (VCC)

VCC is a technique which has been used to obtain and examine high resolution three-dimensional (3D) imaging of vascular architecture in various different tissues (Murakami, 1971; Murakami et al., 1997; Reina-De La Torre et al., 1998).

Capabilities of this technique are ideally suited for investigating the vasculature and venous drainage of the brain. VCC can be done by capturing a positive impression of vessel lumina using low-viscosity resin, before maceration of tissue surrounding the cured resin (Auer et al., 1987).

Properties of resin mixtures used for vascular casting have been continually improved for over 500 years (Haviland and Parish, 1970). A low viscosity semi-polymerised methyl methacrylate medium was first introduced in 1971 (Murakami et al., 1997), combining characteristics such as resistance to further processing, electron conductivity and rapid but even polymerisation of capillaries. It has therefore been the most widely used resin for producing vascular casts.

However, a new polyurethane based resin, PU4ii has recently been developed which has proven to have superior characteristics compared to other resins. It is highly elastic, low in viscosity, resistant to corrosion and causes little shrinkage (Heinzer et al., 2006; Meyer et al., 2007). In addition to these characteristics, the PU4ii resin has an inherent fluorescence sufficient to allow fluorescent microscopy (FM) and confocal microscopy (CM) imaging of the resin casts. This will allow determination of the anatomical position of the resin perfused into the cerebral vessels within histological sections (Krucker et al., 2006). Due to these many advantages, this new PU4ii resin was therefore used for production of VCCs of the vessels under investigation in this study to allow their structural architecture to be closely analysed.

Further supplementary information regarding the history of resins and VCC is detailed in Appendix 1.

1.6.1. Delivery of Fluids into the Circulatory System

Routine techniques for fluid delivery into the rat circulatory system include injection into the femoral artery, tail vein and the heart (Lipton, 1972). There are also many ways to access the vascular system for perfusion of resin into the arterial and/or venous vessels during vascular casting.

1.6.2. Vascular Casting

A cannula needle is first inserted and fixed in the region of the vasculature that is being studied (Verli et al., 2007). For example a resin cast of a specimen's head

and neck can be produced by cannulating the jugular vein (Kogushi et al., 1988). Flow of resin can then be restricted to certain areas of the body by ligating appropriate vessels that perfuse specific parts of the body. This helps to regulate the casting procedure (Verli et al., 2007).

Methods for vascular casting include resin perfusion via the splenic artery (Murakami et al., 1997), abdominal aorta (Sangiorgi et al., 2006), common carotid arteries (Funk and Rohen, 1987), vena cava (Majno et al., 2005) and the left ventricle (Ulmann-Schuler et al., 2007). These different routes of resin delivery and perfusion techniques will be further explored during the course of this study.

1.7. Introduction to Imaging

There are many different methods of visualising the micro-architecture of vessels, however each method differs in various ways including its feasibility and reliability. MRI can be used to image the architecture of micro-vessels, and is often used in order to determine the presence of a haematoma. It is therefore especially valuable for use as evidence for NAHI (Datta et al., 2005). However, its relatively low resolution means that MRI cannot be used for accurate detection and ultra-structural localisation of SDH, thought to originate from the small calibre venules which this investigation aims to identify.

Alternatively, using scanning electron microscopy (SEM) and transmission electron microscopy (TEM) to analyse VCCs, will allow visualisation of the vascular architecture and provide detail on an ultra-structural scale. EM can be used for production of detailed images of microvasculature, such as information regarding orientation and identification of the location of the vessels in question. However, although SEM is able to produce high-resolution 3D impressions, in reality this only reproduces casts in a two-dimensional (2D) form. Similarly, although TEM is able to produce a 'tilt series' consisting of multiple views of the same specimen produced by rotating the angle of the sample, TEM samples can still not be viewed from 360°. Therefore images produced during 3D reconstruction of these TEM images contain missing data; which means that this technique is unable to produce complete high-resolution representations of the morphology of tissue specimens.

However there are currently many different imaging techniques that are being developed which allow 3D reproduction of vascular structures. These newer imaging techniques, as well as some of the most common imaging techniques currently used in both clinical and non-clinical settings, will now be discussed in further detail.

1.7.1. Imaging of the Intracranial Venous System

Investigation into the intracranial venous system in a clinical setting has traditionally been carried out using conventional catheter angiography or digital subtraction angiography (DSA). This is because it is the most definitive diagnostic reference standard for investigation into venous diseases (Agid et al., 2008). However as it is an invasive procedure with numerous associated risks and limitations, there is now increasing use of non-invasive imaging techniques for the assessment of the intracranial venous system. These techniques include various types of cerebral computed tomography venography (CTV) (Casey et al., 1996; Matsumoto et al., 2005) as well as magnetic resonance venography (MRV) (Chakeres et al., 1991; Liauw et al., 2000), which is currently the method of choice for intracranial venous system imaging (Agid et al., 2008). However even with these advancements in technology, the resolution at which current *in vivo* imaging techniques can analyse the cerebral vessel anatomy is much too low for the purposes required in this investigation.

1.7.2. Qualitative Analysis

1.7.2.1. MRI and CT

MRI and computed tomography (CT) are both useful tools for visualisation of vascular architecture and are often used for detection of haematomas. Both MRI and CT are equally as useful for diagnosing surgically correctable intracranial lesions in an acute setting. However, MRI has been shown to be more sensitive than CT in detecting intracranial lesions (Lee et al., 2008) such as subtle neuronal damage, axonal injury and small areas of contusion in cases of suspected abuse (Glauser, 2004; Masters et al., 1987). As well as this, certain types of MRI sequences are particularly sensitive in detecting specific types of intracranial injuries (Provenzale, 2010) as well as being able to detect SDH along the falx cerebri and tentorium cerebelli of the brain which is not visible using CT (Case, 2007). This imaging technique has therefore been found to provide superior

visualisation of SDH (Glauser, 2004; Masters et al., 1987). This is important in cases where there are minimal external signs of injury and therefore SDH may be the only form of evidence of NAHI (Sane et al., 2000). This is one of the reasons why MRI is often used to provide evidence in cases of suspected NAHI, and has even proven to be valuable at post-mortem in directing the autopsy to the main areas of injury (Barlow et al., 1999). MRI can detect the presence of residual blood after cerebral haemorrhaging has occurred for an indefinite amount of time, whereas evidence of the same haemorrhage can no longer be detected after 1-2 weeks using CT. CT should therefore not be used to determine the chronicity of abuse as it would not be able to detect a difference in SDH density dependent upon the number of episodes of abuse (Adamsbaum et al., 2010). However, development and evolution of an intracranial haematoma can be tracked using MRI as it is more sensitive in detecting the sequelae of abusive intracranial injuries (Alexander et al., 1986; Levin et al., 1989). It can therefore be used to determine whether multiple haematomas are a result of a single event or due to multiple injuries over time (Renton, 2004).

One disadvantage of MRI is that it may not be as readily available as CT (Rubin et al., 2003). However the use of MRI avoids the use of ionizing radiation emitted by CT scanning and is therefore considered to be a lot safer, especially for young children. MRI is also very useful in the assessment of children suspected of intracranial injury due to abuse (Sato et al., 1989). It should therefore be part of the routine investigations performed in children who may not have overt neurological signs or symptoms, but where NAHI is suspected (ACR, 2009; Barlow et al., 1999). However, as a person's intent cannot be fully determined via the use of imaging techniques alone, these should be used in conjunction with appropriate investigations which should comprise of taking a thorough medical history including laboratory and biomechanical investigations, as well as taking into account pathological factors (Barnes and Krasnokutsky, 2007; Vezina, 2009).

1.7.2.2. SEM and TEM

Although MRI is the best imaging technique for assessment of intracranial injuries in a clinical setting (Sane et al., 2000) due to its relatively low resolution compared to that of SEM and TEM, MRI images alone would be unable to provide the detail required to detect microvascular lesions of the fine vessels that are of particular interest in this investigation. However, both SEM and TEM are able to produce images of a significantly higher resolution and with a 3D appearance, so

that spatial relationships between the vessels can be studied in detail (Giuvarasteanu, 2007).

1.7.2.3. Combining MRI and EM in a Clinical Setting

As has been discussed, there are many benefits to SEM and TEM imaging, however these are invasive techniques which cannot be used on live patients. Nevertheless, if images detailing the exact orientation and structure of the vessels under investigation could be produced using VCC, SEM and TEM, this topographic information could then be correlated to MRI images (this is important as this is a non-invasive technique) of the brain revealing SDH, which may allow the source of this bleeding to be pin-pointed. Anatomical knowledge gained from this could hopefully then be applied to a clinical setting, when presented with patients with signs of possible NAHI. This combination of imaging techniques could therefore have the potential to allow the origin of intracranial haemorrhages to be traced.

1.7.3. Quantitative Analysis

While VCCs represent the 3D architecture of the cerebral vasculature, and imaging using SEM and TEM analysis can provide high resolution 3D impressions (pseudo-three-dimensional images), in reality this only reproduces casts in 2D (Krucker et al., 2006; Schneider et al., 2009). SEM limits the assessment of the vascular casts to the visible vessels at the surface of the tissue specimen being examined (Minnich et al., 1999). Although techniques have since been developed whereby SEM images of the vascular surfaces can be reconstructed to produce a height map (Manelli et al., 2007); and numerical techniques now exist which can improve the collected data for TEM 3D reconstruction, the resultant product is still only pseudo-3D (Malkusch et al., 1995). In order to produce a true 3D vascular model, techniques such as CM, microCT and 3D X-Ray Microscopy (XRM) are required to allow digital reconstructions of VCCs (Meyer and Krucker, 2007). In combination with the PU4ii resin vascular casts, these techniques will allow imaging and sufficient quantification of the structural properties of the cerebral vascular networks for the purposes of this investigation (Heinzer et al., 2006; Heinzer et al., 2008).

1.7.3.1. Confocal Microscopy

CM offers many advantages over the use of more conventional wide-field optical microscopes such as standard light microscopy or fluorescence microscopy. In standard wide-field microscopy, the whole specimen is illuminated by a light source and therefore includes any unfocused background noise. CM in contrast uses point illumination and a pinhole that is able to eliminate any unfocused signals and therefore produces a much higher optical resolution than that of wide-field microscopes. Although this results in decreased signal intensity, which therefore requires longer exposure times, CM also has the capability to image and assemble serial optical sections from relatively thick tissue samples of up to 100-150µm in thickness (Takaku et al., 2010), allowing 3D reconstruction of the tissue being analysed. Therefore CM used in combination with the PU4ii resin vascular casts with their inherent fluorescent characteristics would allow the production of sufficient information to allow complete morphometrical analysis of the cerebral vascular architecture (Krucker et al., 2006), which is vital for purposes of this investigation.

1.7.3.2. MicroCT and 3D X-Ray Microscopy (XRM)

X-Ray Contrast Agents

It is essential for radiopacity to be introduced into a specimen to allow it to be scanned using microCT or 3D XRM. In order to produce high quality images using microCT or 3D XRM imaging, high quality X-ray contrast agents are also required. Currently, the most commonly used contrast agents contain iodine or barium compounds, and few significant improvements have been made to the available X-ray contrast agents over the last 25 years (Hainfeld et al., 2006).

Until very recently, no radiopaque material could be mixed with resin without causing it to become too viscous, and the only known solution to this was to immerse the resin casts into osmium solution (Heinzer et al., 2008; Riew and Smith, 1971; Schneider et al., 2009)

A radiopaque polymer, Microfil (Flow Tech Inc., Massachusetts) was first developed to allow optimisation of microCT images, as well as allowing quantitation of blood vessel diameters (Vasquez et al., 2011). This was designed for use in corrosion-cast techniques similar to that of the PU4ii resin used in this project. However although the Microfil is able to perfuse the capillary vessels,

unlike the PU4ii resin, the resultant casts were seen to fragment post-maceration of the surrounding supportive tissue (Flow Tech Inc., 1999).

However, gold nanoparticles, a new X-ray contrast agent, were developed, which allow high resolution imaging and reconstruction of the fine architecture of the vascular systems (Nanoprobes Inc., 1992). This is possible partially due to the extremely small size (3-5nm) of these gold nanoparticles, which even at a high concentration are able to produce solutions similar to water in viscosity. These gold nanoparticles also produce less tissue interference, thereby providing 2.7X greater contrast per unit of weight than that of iodine-based contrast agents (Hainfeld et al., 2005; Hainfeld et al., 2006). Additionally, these amphiphilic gold nanoparticles are also miscible in both aqueous and organic solvents (Powell, 2012). Therefore, it would be possible to perfuse this X-ray contrast agent along with the PU4ii resin mixture into the cerebral vasculature to produce resin casts that can be analysed in detail using microCT imaging or 3D XRM.

MicroCT and 3D XRM Scanning

Both MicroCT and 3D XRM imaging fundamentally work in the same way, as both reconstruct 3D images from a series of 2D x-ray projection images. The sample that is being scanned is placed onto a stage and a series of contiguous 2D images are collected by the machine detector as the sample slowly rotates 360°. Projection images are then produced by combining serial slice images of the sample, which are then used to reconstruct a 3D image. These 3D images are then able to undergo further analysis.

MicroCT imaging combined with 3D XRM could be used effectively in this project to produce high-resolution images of the VCCs, which would allow the production of non-destructive in situ images of the cerebral vascular structures. MicroCT imaging (up to 5µm in resolution) allows rapid scanning of small samples, while allowing specific regions of interest (ROI) of tissue to be selected for further investigation.

3D XRM works in a similar way to that of the microCT scanner; however, it allows further magnification of the specimen at a larger working distance than is possible with the conventional microCT scanner. This allows for large sample imaging, while also allowing 3D imaging with a true submicron spatial resolution down to <0.7µm. This imaging technique should therefore allow visualisation of structures

smaller than the size of capillary networks within the brain, and the resultant 3D volumetric data could then be used for analysis, quantification and visualisation of these vessels (Zagorchev et al., 2010).

1.7.4. Combining Qualitative and Quantitative Analysis Techniques

Standard parameters revealed from the use of 2D histological techniques are insufficient to gain enough detailed information about the architecture of the venous drainage of the brain in its full complexity. Knowledge to this extent demands high resolution 3D visualisation of the vessels by applying stereological methods (Kiessling et al., 2010). Analysis of VCCs (produced from PU4ii resin with its improved casting and imaging properties) with the appropriate imaging technologies has the capacity to provide significantly more information regarding the vascular architecture than has presently been revealed through the use of other trialled techniques (Krucker et al., 2006). Therefore a combination of different imaging techniques will be employed in this investigation to allow, through morphological analysis of the cerebral vascular casts from as many perspectives as possible, an overall view of the anatomy of the vascular structures present.

1.7.5. Imaging of Intracranial Vessels and Investigating Head Trauma Cases

1.7.5.1. General Overview

Head trauma is the most common cause of child abuse fatalities (Duhaime et al., 1998; Kellogg, 2007) particularly in children <24 months old (Lloyd et al., 1997; Rubin et al., 2003). This is why high quality imaging is essential for the detection of intracranial injuries as it directly affects the ability to correctly determine the likelihood of child abuse, which therefore influences the safety recommendations of a child before medical discharge (Rubin et al., 2003).

The specific type and amount of imaging carried out in an infant of suspected child abuse depends on many factors. These include the child's age and social factors as well as any detectable signs and symptoms of injury (ACR, 2009; Kellogg, 2007). There are numerous opinions regarding imaging of neurologically asymptomatic infants suspected of being abused (ACR, 2009; Jaspan et al., 2003; Rubin et al., 2003; Stoodley, 2005). It has been found that children, particularly

<12 months of age, could be neurologically asymptomatic upon initial examination (Glauser, 2004), however still have extensive intracranial injuries such as intracranial haematomas (Greenes and Schutzman, 1999; Laskey et al., 2004; Rubin et al., 2003). In one particular study, 19% of infants who were admitted to hospital with no signs or symptoms of brain injury were later found to have intracranial injuries (Schutzman and Greenes, 2001). Accompanying symptoms such as seizures and vomiting have also been shown to be poorly specific (Glauser, 2004).

1.7.5.2. Investigating Retinal Haemorrhage

Fundoscopy should be considered for detection of RH when screening for occult head injury in children suspected of being abused (Kellogg, 2007; Rubin et al., 2003). RH is still thought to be a cardinal feature of SBS (Wyganski-Jaffe et al., 2009), even though RH has also been found to be present in cases unrelated to abusive head injuries (Lopez et al., 2010). This is because the number, extent and type of RH present has been found to correlate with cranial trauma (Forbes et al., 2004; Greenwald et al., 1986; Morad et al., 2002). This could therefore be used to help to differentiate between abusive and non-abusive causes of head injuries (Kellogg, 2007). RHs have been found to be present in 50-100% of shaken infants (Altman et al., 1998; Forbes et al., 2004; Greenwald et al., 1986; Morad et al., 2002). Therefore when accompanied by other signs of NAHI, presence of RH is determined by many to be diagnostic of child abuse (Eisenbrey, 1979; Emerson et al., 2001; Trenchs et al., 2005).

However it is also known that RHs are common in the immediate postnatal period and have been found to be present in up to 75% of new-borns (Emerson et al., 2001). It is known that gradual resolution of these RHs is seen in 2-6 weeks (Forbes et al., 2004) following birth, however clinicians should bear this in mind when carrying out physical examinations. However RH found in infants >6 weeks should heighten suspicion of causes other than birth trauma (Emerson et al., 2001). It should also be noted that the results of physical examinations by clinicians, particularly the absence of RH, should also not be used as the sole determinant for establishing the requirement and type of imaging that needs to be carried out. This is because intracranial damage can occur in the absence of RH (Laskey et al., 2004; Rubin et al., 2003). In addition one study found that in the majority of cases of suspected abuse, non-ophthalmologists were not successful in visualising and therefore examining the retina adequately (Morad et al., 2003).

1.7.5.3. Skeletal Surveys

In general, radiographic skeletal surveying is the method of choice for global skeletal imaging, in cases of suspected child abuse (Di Pietro et al., 2009). However carrying out a skeletal survey alone is not an adequate screening measure for detection of intracranial injuries and therefore the likelihood of abuse. In one study it was found that nearly 10% of individuals found to have intracranial damage would have been overlooked with skeletal survey alone (Rubin et al., 2003). In addition to this, although skull radiography is a useful diagnostic tool (Saulsbury and Alford, 1982), it does not provide adequate screening (Quayle et al., 1997). This is because intracranial injury often occurs in the absence of skull fractures (Laskey et al., 2004; Lloyd et al., 1997).

1.7.5.4. MRI and CT Scanning

In cases of suspected child abuse, although no particular clinical criteria have been established determining which patients should undergo imaging studies (Glauser, 2004), clinicians should have a relatively low threshold for carrying out imaging such as MRI or CT scans (ACR, 2009; Hymel, 2004), even in the absence of neurological symptoms and in spite of their associated risks (Kellogg, 2007; Kraus et al., 1986). Careful imaging has been found to be particularly vital when investigating cases where children have been categorised into higher-risk groups such as age <6 months, having multiple fractures or having facial injuries (Rubin et al., 2003). In one particular study which looked at children with symptomatic head injuries, it was found that abusive head trauma was more likely to go unrecognised in younger children (Jenny et al., 1999). This is particularly disconcerting, as in a study whereby all cases of children <1 year of age who were admitted to a hospital over a 2 year period were reviewed, it was found that 64% of all head injuries and 95% of serious intracranial injuries were due to child abuse (Billmire and Myers, 1985).

Furthermore, in another study it was found that clinical signs of brain injury are insensitive markers of infantile intracranial trauma (Greenes and Schutzman, 1999). It is not surprising that it has also been found that neurological examinations carried out by physicians, predominantly on younger children, can be particularly difficult and therefore can lead to misdiagnosis (Durham et al., 2000; Forbes et al., 2004). This may be a contributing factor to the poor utility of the application of clinical indicators in screening for occult head injuries (Rubin et

al., 2003). To further illustrate this, in one study it was found that 74% of children with occult head injuries who had normal physical examinations were then subsequently found to have scalp injuries using CT or MRI (Rubin et al., 2003). Results of another investigation found that among a group of children with fatal abusive head injuries, evidence of blunt head trauma was only found after autopsy had been performed in 54% of individuals (Duhaime et al., 1987).

1.7.5.5. Discrepancies and Distinguishing Between Accidental and NAHIs

As has been illustrated, there is a lot of discrepancy regarding imaging of neurologically asymptomatic infants suspected of being victims of child abuse. There have been countless studies which have tried to establish specific clinical criteria for application in clinical situations (Maguire et al., 2009), which would allow a relatively accurate evaluation of the presence of intracranial lesions in children. Many different studies have been carried out in order to determine this; however it is very difficult to find studies that have used cohorts truly representative of the data set in question due to the many restrictions regarding the sensitive and ethical issues involving child abuse. Due to the same issue, the number of subjects analysed in each of these studies is also relatively small and therefore often do not yield statistically significant results that could be transferred to most clinical situations.

Another important point is that first of all, it is often very difficult to accurately identify the abuser (Kasim et al., 1995), as well as to then ascertain whether a case is accidental or non-accidental (Cradock, 2011). This is because even when a full confession has been made by the alleged perpetrator (Leestma, 2005) admissions do not provide any scientific evidence (Adamsbaum et al., 2010). Cases often involve either the child's parent or carer, and therefore there are issues of veracity with any confession. This is because important details may be purposefully omitted, or certain facts may be fabricated in order to give a better impression of the supposed event during an interrogation (Caffey, 1957; Leestma, 2006). Conversely however, in some cases accused individuals may confess to crimes which they in fact did not commit due to issues of duress or employment of various methods of subterfuge by interrogators who believe the alleged perpetrator to be guilty (Caffey, 1957; Kempe et al., 1962; Leestma, 2006). One study found there to be a steady increase in the number of admissions for child abuse over the years (Lauer et al., 1974). Despite this, as there are still so few confessions in cases where children are suspected to have been shaken, the small

number of cases whereby shaking has been admitted does not provide valid statistical support for validation of any supposed findings (Leestma, 2005). However, even when taking these factors into account, confessions made by the perpetrator is still the best form of support that is possible (excluding for example, video footage of an event) in distinguishing between cases of accidental and NAHI, in conjunction with any clinical findings (Bell et al., 2011; Leestma, 2006; Starling et al., 2004; Vinchon et al., 2010b).

Regardless of these many complications, it is essential for further research to be continued in this area in order to be able to accurately differentiate between abusive and non-abusive injuries. This is particularly vital as when physicians misdiagnose abuse as unintentional trauma or a medical disorder, approximately 1 out of 4 infants will sustain further injuries before the correct diagnosis is made (Forbes et al., 2004). Another study found that in cases where abusive head trauma was missed, 9.3% of children died as a result of their head injuries (Jenny et al., 1999). This therefore illustrates the dangerous consequences of the misdiagnosis of abuse, and the importance and requirement for further research.

1.7.6. Summary, Aims and Objectives

As has been discussed, there are many conflicting hypotheses and theories regarding the causation of subdural haemorrhaging found in cases of NAHI. It is important that we are able to recognise and accurately differentiate between accidental and NAHI so that appropriate action can be taken against abusers, as well as preventing false convictions. This requires a multidisciplinary approach including laboratory, radiological, ophthalmological and forensic investigations as well as understanding of the underlying pathophysiology (Matschke et al., 2009b).

The hypothesis of this investigation is that intracranial bleeding often found in cases of accidental and NAHI is due to rupturing of fine subdural venules. These vessels are thought to either first traverse in between the dural layers, or drain directly into cerebral vessels called bridging veins, before then draining into the venous sinuses. At the moment, no research has yet been conducted which investigates the ultrastructure of the cerebral microvasculature, with particular reference to the possible existence of fine subdural venules as the source of subdural haematomas often found in cases of accidental and NAHIs. This project therefore aims to illustrate the existence of these fine subdural venules so that the origin of SDH in NAHIs can be isolated to a specific location; as well as then proceeding to determine the morphological parameters that correlate with the risk

of rupturing of these vessels on application of certain forces. In doing so, this project will hopefully contribute towards establishing the mechanism of intracranial haemorrhaging often seen in cases of accidental and NAHIs. It may also provide insight into the causation of the birth related subdural haematomas that are now recognised to be a common occurrence following normal births.

Chapter 2. Cerebral Microvasculature of the Rat: Resin Casting and SEM

2.1. Introduction

This project encompasses three main parts that will allow thorough analysis of the subdural vessels, thought to be the cause of subdural haemorrhaging (SDH) found in cases of accidental and non-accidental head injuries (NAHI). These include gross tissue dissection, vascular corrosion (resin) casting of the vessels, and histological evaluation of the vessels [involving light microscopy (LM), fluorescence microscopy (FM), confocal microscopy (CM) and transmission electron microscopy (TEM) imaging]. Additionally conventional scanning electron microscopy (SEM), environmental scanning electron microscopy (ESEM), micro-computed tomography (microCT), 3D X-Ray Microscopy (XRM) and finally magnetic resonance imaging (MRI) will be used which will allow findings to be put into a clinical context.

Rat material was initially used in this project in order to develop the vascular corrosion casting (VCC) protocol, which is described in detail later on in this chapter. VCC involves perfusion of resin via the heart into the cerebral vessels, followed by maceration of the surrounding brain tissue, which leaves behind vascular resin casts. The VCC protocol was used to demonstrate the gross morphological structure of the cerebral vessels, before then using various different forms of imaging to further analyse the more detailed cerebral vessel morphology.

2.2. Materials and Methods

Rat Specimen	Species/Gender (M/F)	Age (Weeks)	Weight (g)	Procedure	Method of Perfusion	Needle Size (G)	Pressure (mmHg) a) Prewash; b) Fixative Perfusion	Resin Perfusion Rate (ml/min)	Decalcification (Days); Temperature (°C)	Tissue Processing and Analysis
A	Albino Wistar/M	8	250	Fixation, Resin perfusion (blue fluorescent dye)	Left Ventricle	19 Needle	a) 50 (1 min) b) 50 (2-3 mins) and 20 (10 mins)	1.5	13 ; 21	Wax embedded , sectioned and H&E stained cross-sectional samples of the brain and skull
B	Albino Wistar/M	8	250	Fixation, Resin perfusion (blue fluorescent dye)	Left Ventricle	19 Needle	a) 50 (1 min) b) 50 (2-3 mins) and 20 (10 mins)	1.5	N/A	No further processing*
C	Albino Wistar/F	8	125	Fixation, Resin perfusion (blue fluorescent dye)	Entrance to the Ascending Aorta	15 Needle	a) 50 (1 min) b) 50 (2-3 mins) and 20 (10 mins)	1.5	8 ; 21	Tissue maceration and freeze-drying *
D	Albino Wistar/F	8	150	Fixation, Resin perfusion (blue fluorescent dye)	Entrance to the Ascending Aorta	15 Needle	a) 50 (1 min) b) 50 (2-3 mins) and 20 (10 mins)	1.5	13 ; 21	Wax embedded , sectioned and H&E stained cross-sectional samples of the brain and skull
E	Albino Wistar/F	8	125	Fixation, Resin perfusion (blue fluorescent dye)	Entrance to the Ascending Aorta	15 Needle	a) 50 (1 min) b) 50 (2-3 mins) and 20 (10 mins)	1.5	8 ; 21	Tissue maceration, freeze-drying and ESEM imaging: both before and after osmocation of the VCC (imaged at 0° and 45°).
F	Albino Wistar/F	2	50	Fixation, Resin perfusion (blue fluorescent dye)	Entrance to the Ascending Aorta	15 Needle	a) 50 (1 min) b) 50 (2-3 mins) and 20 (10 mins)	1.5	9 ; 21	Tissue maceration, freeze-drying .
G	Albino Wistar/F	2	50	Fixation, Resin perfusion (blue fluorescent dye)	Entrance to the Ascending Aorta	15 Needle	a) 50 (1 min) b) 50 (2-3 mins) and 20 (10 mins)	1.5	9 ; 21	Tissue maceration and freeze-drying *
H	Albino Wistar/M	8	250	Fixation, Resin perfusion (blue fluorescent dye)	Entrance to the Ascending Aorta	15 Needle	a) 50 (1 min) b) 50 (2-3 mins) and 20 (10 mins)	1.5	6 ; 21	No further processing*
I	Albino Wistar/M	8	250	Fixation, Resin perfusion (blue fluorescent dye)	Entrance to the Ascending Aorta	15 Needle	a) 50 (1 min) b) 50 (2-3 mins) and 20 (10 mins)	1.5	6 ; 21	Tissue maceration and freeze-drying *
J	Albino Wistar/M	8	250	Fixation, Resin perfusion (blue fluorescent dye)	Entrance to the Ascending Aorta	16 Cannula	a) 50 (1 min) b) 50 (2-3 mins) and 20 (10 mins)	1.5	6 ; 21	Tissue maceration, freeze-drying .
K	Albino Wistar/M	8	250	Fixation, Resin perfusion (blue fluorescent dye)	Entrance to the Ascending Aorta	16 Cannula	a) 50 (1 min) b) 50 (2-3 mins) and 20 (10 mins)	1.5	6 ; 21	No further processing*
L	Albino Wistar/M	7/8	200	Fixation	Entrance to the Ascending Aorta	16 Cannula	a) 50 (1 min) b) 50 (2-3 mins) and 20 (10 mins)	N/A	66 ; 21 + 6 ; 37	Gross dissection *
M	Albino	8	250	Fixation, Resin	Entrance to	16	a) 140 (400ml)	1.5	6 ; 21	Tissue maceration and

	Wistar/M			perfusion (blue fluorescent dye)	the Ascending Aorta	Cannula	b) 160 (500ml)			freeze-drying*
N	Albino Wistar/M	8	250	Fixation, Resin perfusion (blue fluorescent dye)	Entrance to the Ascending Aorta	16 Cannula	a) 140 (400ml) b) 140 (500ml)	1.5	6; 21	No further processing*
O	Albino Wistar/M	8	250	Fixation, Resin perfusion (blue fluorescent dye)	Entrance to the Ascending Aorta	16 Cannula	a) 140 (500ml) b) 140 (500ml)	1.5	6; 21	Tissue maceration, freeze-drying.
P	Albino Wistar/M	8	250	Fixation, Resin perfusion (blue fluorescent dye)	Entrance to the Ascending Aorta	16 Cannula	a) 140 (500ml) b) 140 (500ml)	1.5	6; 21	No further processing*
Q	Albino Wistar/M	8	250	Fixation, Resin perfusion (blue fluorescent dye)	Entrance to the Ascending Aorta	16 Cannula	a) 180 (100ml) b) 180-200 (150ml)	6.0	4; 37	No further processing*
R	Albino Wistar/M	8	250	Fixation, Resin perfusion (blue fluorescent dye)	Entrance to the Ascending Aorta	16 Cannula	a) 180 (300ml) b) 180 (350ml)	6.0	4; 37	The VCC was insufficiently complete following maceration therefore it was not used for further imaging. The VCC however was used as a model to test whether Scaleview-A2 solution (Appendix 2) damages the resin casts.
S	Albino Wistar/M	8	250	Fixation, Resin perfusion (blue fluorescent dye)	Entrance to the Ascending Aorta	16 Cannula	a) 160-200 (300ml) b) 160 (500ml)	6.0	4; 37	No further processing*
T	Albino Wistar/M	8	250	Fixation, Resin perfusion (blue fluorescent dye)	Entrance to the Ascending Aorta	15 Needle	a) 100 (400ml) b) 100 (500ml)	6.0	20; 37	Tissue maceration and OsO₄ staining*
U	Albino Wistar/M	8	250	Fixation, Resin perfusion (blue fluorescent dye)	Entrance to the Ascending Aorta	16 Cannula	a) 100/110 (250ml) b) 100/110 (500ml)	6.0	4; 37	Tissue maceration, LM imaging.
V	Albino Wistar/M	8	250	Fixation, Resin perfusion (blue fluorescent dye)	Entrance to the Ascending Aorta	15 Needle	a) 120 (500ml) b) 160 (500ml)	6.0	4; 37	Tissue maceration, freeze-drying*
W	Albino Wistar/M	8	250	Fixation, Resin perfusion (blue fluorescent dye)	Entrance to the Ascending Aorta	15 Needle	a) 100 (500ml) b) 100 (500ml)	6.0	4; 37	Tissue maceration, freeze-drying.
X	Albino Wistar/M	8	250	Fixation, Resin perfusion (blue fluorescent dye)	Entrance to the Ascending Aorta	16 Cannula	a) 100 (500ml) b) 100 (500ml)	6.0	4; 37	Tissue maceration, freeze-drying.
Y	Albino Wistar/M	8	250	Fixation, Resin perfusion (blue fluorescent dye)	Entrance to the Ascending Aorta	15 Needle	a) 160 (500ml) b) 200 (500ml)	6.0	6; 37	Produced histological sections (H&E stained) using a microtome which underwent LM and CM .
Z	Albino Wistar/M	8	250	Fixation, Resin perfusion (blue fluorescent dye)	Entrance to the Ascending Aorta	16 Cannula	a) 160 (500ml) b) 180 (500ml)	6.0	3; 37	Tissue maceration, OsO₄ staining*

A2	Albino Wistar/M	8	250	Fixation, Resin perfusion (blue fluorescent dye)	Entrance to the Ascending Aorta	15 Needle	a) 120 (500ml) b) 120 (500ml)	6.0	3; 37	Tissue maceration, Freeze-drying.
B2	Albino Wistar/M	8	250	Fixation, Resin perfusion (blue fluorescent dye)	Entrance to the Ascending Aorta	16 Cannula	a) 120 (500ml) b) 120 (500ml)	6.0	3; 37	Tissue maceration, Freeze-drying and SEM imaging.
C2	Albino Wistar/M	8	250	Fixation, Resin perfusion (red fluorescent dye)	Entrance to the Ascending Aorta	16 Cannula	a) 160 (500ml) b) 160 (500ml)	6.0	2; 37	Tissue maceration, OsO₄ staining, Freeze-drying, microCT.
D2	Albino Wistar/M	8	250	Fixation, Resin perfusion (red fluorescent dye)	Entrance to the Ascending Aorta	15 Needle	a) 160 (500ml) b) 160 (500ml)	6.0	2; 37	Tissue maceration, OsO₄ staining and freeze-drying , followed by microCT and ESEM scanning (45°).
E2	Albino Wistar/M	8	250	Fixation, Resin perfusion (yellow fluorescent dye)	Entrance to the Ascending Aorta	15 Needle	a) 120 (500ml) b) 120 (500ml)	6.0	3; 37	No further processing*
F2	Albino Wistar/M	8	250	Fixation, Resin perfusion (yellow fluorescent dye)	Entrance to the Ascending Aorta	16 Cannula	a) 120 (500ml) b) 120 (300ml)	6.0	3; 37	Tissue maceration, OsO₄ staining, Freeze-drying, microCT.
G2	Albino Wistar/M	8	250	Fixation, Resin perfusion (blue fluorescent dye)	Entrance to the Ascending Aorta	16 Cannula	a) 140 (500ml) b) 140 (500ml)	6.0	3; 37	Tissue maceration *
H2	Albino Wistar/M	8	250	Fixation, Resin perfusion (blue fluorescent dye)	Entrance to the Ascending Aorta	15 Needle	a) 140 (500ml) b) 140 (300ml)	6.0	3; 37	Gross dissection and optical clearing using Scaleview-A2 . Analysis using multi-photon FM was unsuccessful however due to the solution causing the resin to break down. Produced histological sections (H&E stained) of the skull tissue using a microtome
I2	Albino Wistar/M	10	280	Fixation, Resin perfusion (red fluorescent dye)	Entrance to the Ascending Aorta	15 Needle	a) 100 (250ml) b) 100 (100ml)	6.0	3; 37	No further processing*
J2	Albino Wistar/M	10	280	Fixation, Resin perfusion (red fluorescent dye)	Entrance to the Ascending Aorta	16 Cannula	a) 80 (450ml) b) 80 (100ml)	6.0	3; 37	Tissue maceration, OsO₄ staining, microCT (scanned before and after Freeze-drying), producing a 360° view video of the VCC.
K2	Albino Wistar/M	8	250	Fixation, Resin perfusion (yellow fluorescent dye)	Entrance to the Ascending Aorta	15 Needle	a) 160 (500ml) b) 160 (500ml)	12.0	4 ; 37	Tissue maceration, freeze-drying.

L2	Albino Wistar/M	8	250	Fixation, Resin perfusion (yellow fluorescent dye)	Entrance to the Ascending Aorta	16 Cannula	a) 200 (500ml) b) 200 (500ml)	12.0	4 ; 37	Tissue maceration , OsO₄ staining, Freeze-drying , microCT .
M2	Albino Wistar/M	9	270	Fixation, Resin perfusion (blue fluorescent dye)	Entrance to the Ascending Aorta	15 Needle	a) 190 (500ml) b) 190 (500ml)	12.0	3 ; 37	Tissue maceration *
N2	Albino Wistar/M	9	270	Fixation, Resin perfusion (blue fluorescent dye)	Entrance to the Ascending Aorta	16 Cannula	a) 200 (500ml) b) 200 (500ml)	12.0	3 ; 37	Tissue maceration, freeze-drying , SEM and microCT .
O2	Albino Wistar/M	9	270	Fixation, Resin perfusion (red fluorescent dye)	Entrance to the Ascending Aorta	15 Needle	a) 200 (500ml) b) 200 (500ml)	12.0	4 ; 37	Gross dissection , photographed (macrographs) and freeze-dried before microCT .
P2	Albino Wistar/M	9	270	Fixation, Resin perfusion (red fluorescent dye)	Entrance to the Ascending Aorta	16 Cannula	a) 200 (500ml) b) 200 (500ml)	800	4 ; 37	Gross dissection , wax embedding and thick sectioning (120µm) of the sample with a sledge microtome for CM . Trialled processing method for sample preparation and mounting.
Q2	Albino Wistar/M	8	250	Fixation, Resin perfusion (blue fluorescent dye)	Entrance to the Ascending Aorta	16 Cannula	a) 200 (500ml) b) 200 (500ml)	12.0	3 ; 37	Gross dissection , photographed (macrographs). Optical clearing in Scaleview-A2 *
R2	Albino Wistar/M	8	250	Fixation, Resin perfusion (blue fluorescent dye)	Entrance to the Ascending Aorta	15 Needle	a) 200 (500ml) b) 200-300 (500ml)	12.0	3 ; 37	MicroCT before and after gross dissection followed by freeze-drying and SEM .
S2	Albino Wistar/M	8	250	N/A	Entrance to the Ascending Aorta	15 Needle	a) 200 (500ml) b) 200 (500ml)	N/A	; 37	Animal MRI.
T2	Albino Wistar/M	8	250	Fixation, Resin perfusion (blue fluorescent dye)	Entrance to the Ascending Aorta	15 Needle	a) 200 (500ml) b) 200 (500ml)	15.0	; 37	Animal MRI.
U2	Albino Wistar/M	8	250	Fixation, OsO₄ perfusion, Resin perfusion (blue fluorescent dye)	Entrance to the Ascending Aorta	16 Cannula	a) 200 (500ml) b) 200 (500ml)	15.0	3 ; 37	MicroCT before gross dissection, followed by freeze-drying and microCT again.
V2	Albino Wistar/M	8	250	Fixation, OsO₄ perfusion, Gold nanoparticle and Resin perfusion (blue fluorescent dye)	Entrance to the Ascending Aorta	16 Cannula	a) 200 (500ml) b) 200 (500ml)	15.0	3 ; 37	MicroCT before gross dissection, followed by freeze-drying and microCT again. Then macerated the freeze-dried tissue, before re- freeze-drying for ESEM .
W2	Albino Wistar/M	8	250	Fixation only (4% PFA)	Entrance to the Ascending Aorta	16 Needle	a) 200 (500ml) b) 200 (500ml)	N/A	4; 37	Gross dissection , OsO₄ , embedded in agarose and sectioned into 1mm slices *
X2	Albino Wistar/M	8	250	Fixation only (4% PFA)	Entrance to the Ascending Aorta	16 Needle	a) 200 (500ml) b) 200 (500ml)	N/A	4; 37	Gross dissection , embedded in agarose and

					Aorta					sectioned into 2mm and 3mm slices. Osmocated and analysed samples using interference colours, followed by freeze-drying.
Y2	Albino Wistar/M	8	250	Fixation, Resin perfusion (blue fluorescent dye)	Entrance to the Ascending Aorta	16 Needle	a) 200 (500ml) b) 200 (500ml)	50.0	N/A	Tissue maceration .
Z2	Albino Wistar/M	8	250	Fixation, Resin perfusion (blue fluorescent dye)	Entrance to the Ascending Aorta	16 Needle	a) 200 (500ml) b) 200 (500ml)	50.0	4 ; 37	Gross dissection , freeze-drying, microCT .
A3	Albino Wistar/M	8	250	Fixation only (4% PFA)	Entrance to the Ascending Aorta	16 Needle	a) 200 (500ml) b) 200 (500ml)	N/A		Gross dissection .
B3	Albino Wistar/M	8	250	Fixation only (4% PFA)	Entrance to the Ascending Aorta	16 Needle	a) 200 (500ml) b) 200 (500ml)	N/A		Gross dissection , embedded in agarose and sectioned into 2 and 3mm slices. Osmocated and analysed samples using interference colours, followed by freeze-drying.
C3	Albino Wistar/M	8	250	Fixation (1% Glutaraldehyde, 4% PFA), Resin perfusion (blue fluorescent dye)	Entrance to the Ascending Aorta	16 Needle	a) 80 (1 minute) b) 80 (5 minutes); 20 (15 minutes)	50.0	7 ; 37	Embedded in agarose and sectioned into 1mm slices. Osmocated tissues for ESEM imaging. Freeze-dried further slices for microCT and ESEM .
D3	Albino Wistar/M	8	250	Fixation (1% Glutaraldehyde, 4% PFA), Resin perfusion (blue fluorescent dye)	Entrance to the Ascending Aorta	16 Needle	a) 200 (500ml) b) 200 (500ml)	50.0	11 ; 37	Embedded in agarose , and sectioned into 1mm slices which were photographed (macrographs). Samples were H&E stained and imaged with CM (in DPX or PBS), before acquiring photomicrographs and ESEM images of the same 1mm sections.
E3	Albino Wistar/M	8	250	Fixation (1% Glutaraldehyde, 4% PFA), Resin perfusion (blue fluorescent dye)	Entrance to the Ascending Aorta	16 Needle	a) 80 (1 minute) b) 80 (5 minutes); 20 (15 minutes)	50.0	12 ; 37	Tissue maceration .
F3	Albino Wistar/M	8	250	Fixation (1% Glutaraldehyde, 4% PFA), Resin perfusion (blue fluorescent dye)	Entrance to the Ascending Aorta	16 Needle	a) 200 (500ml) b) 200 (500ml)	50.0	12 ; 37	Tissue maceration .

Table 1: Experimental rat specimens used during the study. The main purpose of these experiments was to refine the protocol for cardiac perfusion fixation and PU4ii resin perfusion. The table also details how the tissues were processed and analysed following perfusion. Specimens with incomplete resin casts, or those with excess damage caused during processing of the tissue were discarded (asterisk).

2.2.1. Methodology for Cardiac Perfusion Fixation and PU4ii Resin Perfusion

Figure 18 is a flow-diagram which details the protocol used for cardiac perfusion fixation and PU4ii resin perfusion of the rat.

All procedures were conducted in accordance with **Schedule I** approved criteria for the humane killing of animals of the Animals Act 1986, and as part of the institutional, UK and international regulations and standards of animal welfare. Ethical approval was granted by the University of Nottingham Animal Welfare and Ethical Review Body (AWERB), under the License Number: **PL 40/1937**.

Arrangement of apparatus used for perfusion is shown in Figure 19 and accompanying information regarding the methodology is also described. Further supplementary information regarding methodology and mixing of solutions is detailed in Appendix 3.

2.2.1.1. Calculation of the Total Blood Volume of a Rat

The total blood volume of a rat can be calculated using the following equation (Lee and Blafox, 1985):

$$\text{Blood volume (ml)} = 0.06 \times \text{body weight (g)} + 0.77$$

The total blood volume of a rat weighing 250g is 15.77ml. Therefore perfusion of a minimum of this volume of resin into a 250g rat specimen should completely fill the rat vasculature. This value is reflected in the volumes used in the following protocol for cardiac perfusion fixation and resin perfusion of the rat.

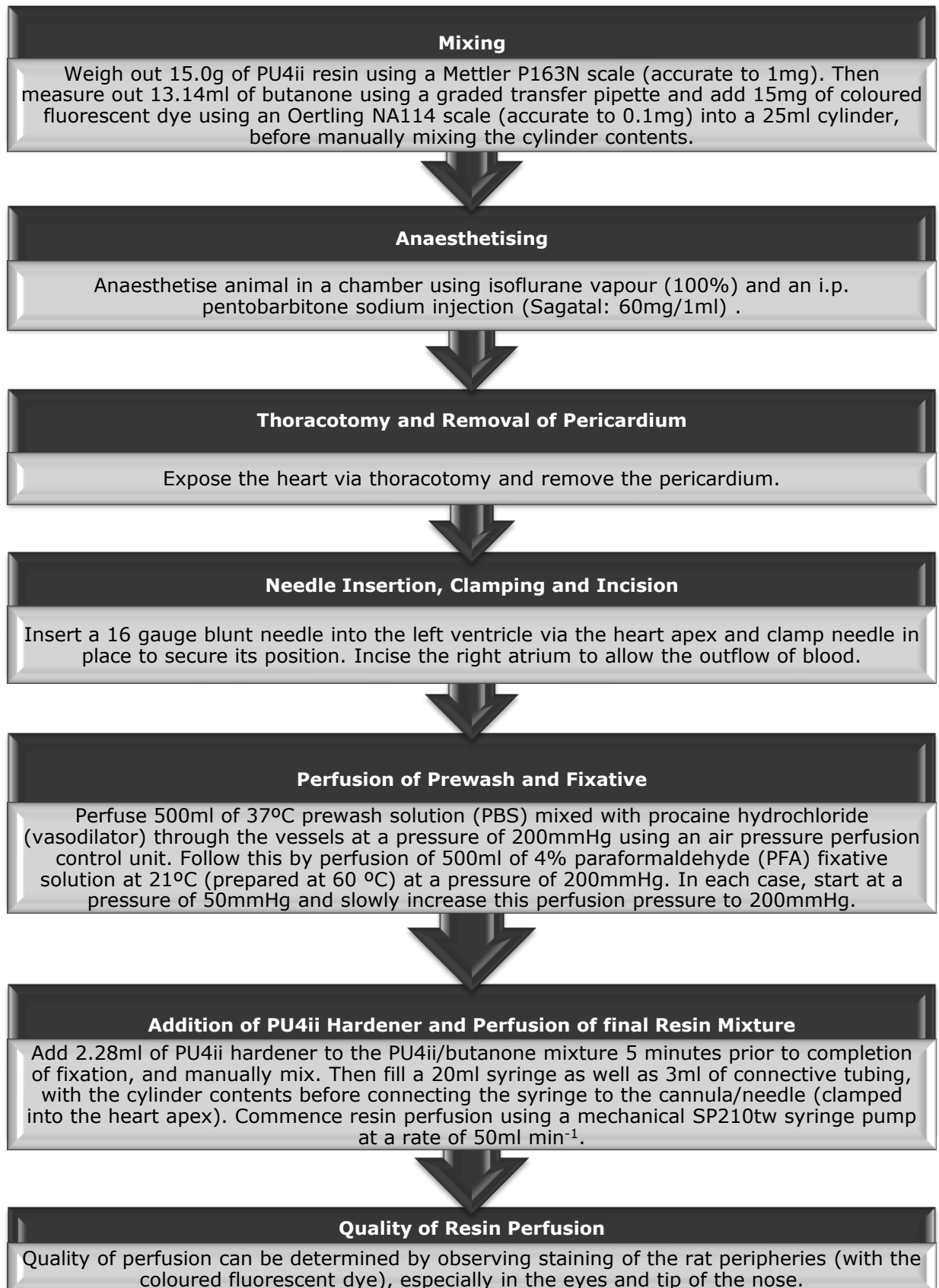


Figure 18: Method for Cardiac Perfusion Fixation and PU4ii Resin (containing coloured fluorescent dye) Perfusion of a 250g Wistar Rat.

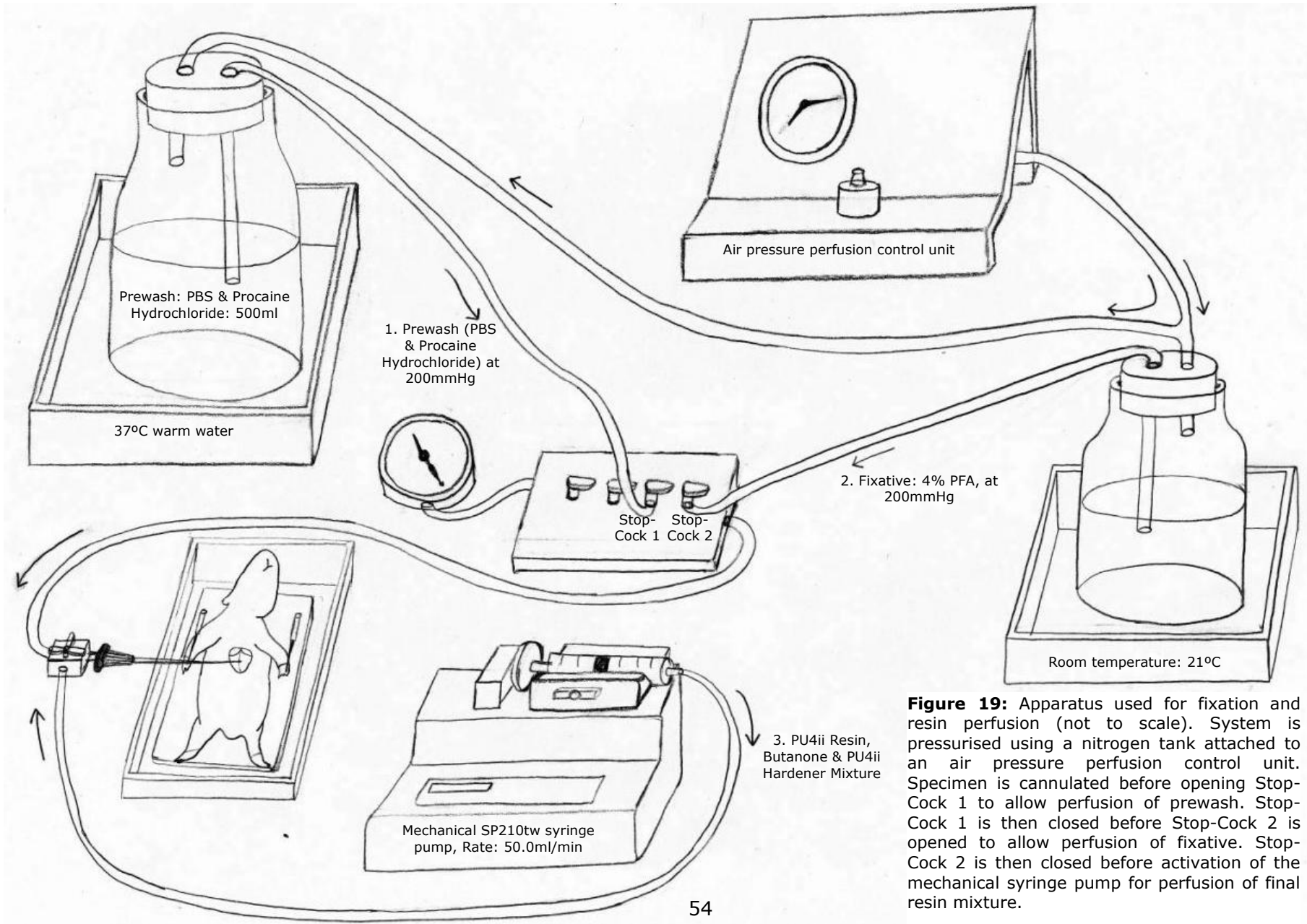


Figure 19: Apparatus used for fixation and resin perfusion (not to scale). System is pressurised using a nitrogen tank attached to an air pressure perfusion control unit. Specimen is cannulated before opening Stop-Cock 1 to allow perfusion of prewash. Stop-Cock 1 is then closed before Stop-Cock 2 is opened to allow perfusion of fixative. Stop-Cock 2 is then closed before activation of the mechanical syringe pump for perfusion of final resin mixture.

2.2.1.2. Vascular Resin Casting

VCC is a unique animal modelling technique that has recently been developed, which allows detailed analysis of the cerebral microvasculature. Anatomical data detailing the exact orientation and structure of the fine vessels thought to be the source of haemorrhaging found in cases of traumatic head injuries is believed to be attainable through use of this casting technique. More specifically, vascular casting was carried out by perfusing the vessels of the brain with a polyurethane (PU4ii) resin shown to have higher quality physically, and better imaging characteristics than has been previously shown using other available resins. This resin was then left to cure over a period of 48 hours at room temperature (Figure 20A).

2.2.2. Tissue Processing

After resin perfusion, various methods of tissue processing were performed. These included dissection and decalcification of the skull before carrying out total tissue maceration as well as embedding some of the resin casts still surrounded by brain tissue in wax before sectioning these slices.

2.2.2.1. Dissection and Decalcification

All surrounding tissue of the rat heads was removed using gross dissection to expose the underlying skulls. These were then submerged in decalcification solution, Biocal C (Biostain Ready Reagents) for at least 3 days at 37°C in an incubator, to allow the bone to soften via decalcification and demineralisation (Lee et al., 2009).

2.2.2.2. Maceration and Osmocation

Soft tissue was fully macerated in 10% potassium hydroxide (KOH) solution at 37°C until all the surrounding tissue had been dissolved away (Figure 20B). The revealed vascular casts were then osmicated in 1% OsO₄ solution for 24 hours, before being thoroughly washed in distilled water. These specimens then underwent lyophilisation and further processing, in preparation for SEM and microCT imaging and analysis. Washing of casts is important for the removal of saponified materials (which would leave unwanted artefacts on the surface of the

VCCs) which are produced as a result of maceration of tissues rich in lipid content (Giuvarasteanu, 2007).

2.2.2.3. Lyophilisation (Freeze-drying)

This is a process by which the water within tissues is frozen before the aqueous phase is removed via sublimation (causes a direct change in state from a solid to gaseous phase).

Following washing, resin casts were submerged into 25ml of distilled deionised water in plastic beakers. These were then covered over with perforated Parafilm 'M' Laboratory film (American National Can) in order to prevent loss of tissue during gentle warming and removal of moisture in a desiccating vacuum. Specimens were freeze-dried in a lyophilisation chamber for 24 hours at -80°C, which allowed for maintenance of normal anatomical shape of the tissue and vascular casts during processing.

2.2.3. Tissue Analysis

Following tissue processing, various different forms of imaging and analysis were then carried out. This was to allow the exact morphological structure of the small venules, thought to be the cause of intracranial bleeding found in cases of traumatic head injuries, to be analysed in as many ways as possible.

2.2.3.1. Macroscopy

Specimens were imaged using professional imaging software, ScopeImage DynamicPro, which involved using a photo-camera connected to a Nikon dissecting microscope and a computer, which was then used to take detailed photographs of the animal tissue at various different stages of processing.

2.2.3.2. Scanning Electron Microscopy (SEM)

A standard SEM machine operates at a high vacuum, and the basic principles of the imaging process are as follows. A primary electron beam is emitted by the machine onto the surface of a specimen, which then emits secondary electrons that are collected by a specialised detector. The information collected by this detector is then processed to produce a SEM image of the original sample.

Preliminary experiments involving the SEM were carried out using vascular corrosion casts which were mounted onto aluminium stubs using double-sided carbon tape and sputter-coated with a thin layer of gold (SCD 030, Balzers Union, FL-9496). In order to prevent build-up of charge during analysis, silver paint was also used to attach the sputter-coated casts to the stubs, as casts had not been fully coated from underneath. Vascular casts were then analysed (Beckmann et al., 2003) using a JEOL JSM-840 scanning electron microscope and electron micrographs were acquired at 23.0 kV (ISS Group, I-Scan image acquisition system).

SEM is able to produce high-resolution images of less than 1nm in size, allowing detailed analysis of the microvasculature of the brain on an ultrastructural scale.

2.2.3.3. Environmental Scanning Electron Microscopy (ESEM)

Following the vast improvements made to the vascular resin casting protocol throughout the course of the project, the complex nature of the fine calibre vessels that could now be resin casted, meant that sputter-coating of these vascular casts with gold would obstruct visualisation of each of these fine vessels. The intricate microarchitecture of the vascular casts meant that all the vessels could not be evenly coated as it would cause clumping of the gold as it was sputter-coated onto the resin casts.

For conventional SEM, the surface of specimens being imaged must be electrically conductive and electrically grounded to prevent the accumulation of electrostatic charge at their surface. This is because charging occurs when the energy from primary electrons being fired at the specimen are retained by the sample, instead of being shed to an electrical ground, which can therefore produce poor quality images.

It was therefore decided that environmental scanning electron microscopy (ESEM) would be used instead of the conventional SEM, as this would allow scanning of uncoated specimens. This is possible as ESEM machines are fitted with a special gaseous secondary electron detector (GSED), which drives water vapour molecules (positive ions) within the gaseous environment of the specimen chamber, towards the sample. These positive ions, which are driven towards the negatively charged sample (due to the primary beam electrons that have been fired at it), then effectively neutralise this negative charge. This enables scanning

of an uncoated specimen within a gaseous environment, while still preventing build-up of charge (thereby still allowing acquisition of high quality images).

Specimens were first mounted onto metal stubs using conductive graphite paint (carbon cement) to completely secure the specimen during imaging. Electron micrographs were acquired using a Philips XL30 FEG ESEM machine (Oxford Instruments INCA Microanalysis System).

2.2.3.4. Histology and FM Imaging

In addition to investigating further the general anatomy of the cerebral vessels through gross dissection of tissues (as described previously), the exact morphological structure of these vessels was investigated using various histological techniques in combination with fluorescence imaging.

Following analysis, this data could then be applied to various modelling techniques which could allow further exploration into the normal blood flow in the cerebral vessels currently under investigation in this project, as well as determining the changes seen in this blood flow as a result of mechanical deformation of the vessels. This will help to determine the physiological properties of the vessels that are being investigated, particularly in terms of the amount and type of forces required to cause vessel rupture.

Wax embedded tissue samples were first sectioned using a SLEE CUT 4060 (Mainz) rotary microtome (Mainz) with a 4689 Accu-Edge Low-Profile Blade, before carrying out further processing.

Further supplementary information regarding the established protocol for tissue processing and wax embedding of pre-fixed tissue for histology; microtome sectioning of wax-embedded tissue; and staining of tissue with haematoxylin and eosin (H&E) and cover-slipping prepared histology slides are detailed in Appendices 10, 11 and 12.

2.2.3.5. Preparation of Histological Specimens

Aim: Determine a protocol for slide preparation which would allow analysis of resin perfused sectioned skull and brain tissue to be clearly illustrated, using a range of analysis techniques including light microscopy, fluorescence microscopy and confocal microscopy.

Methods:

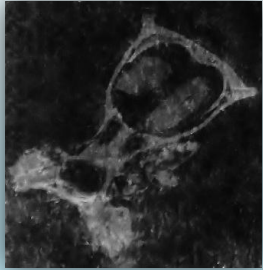
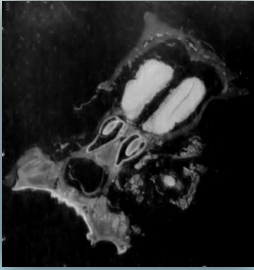
Light Microscopy

A 10µm thick section was stained with H&E, and mounted in DPX (Distrene, Plasticiser and Xylene), allowing tissue analysis using LM.



This method of preparation produced the best results when tissues were subsequently analysed using LM.

Fluorescence Microscopy

<p>A 10µm thick section was left unstained and mounted in DPX.</p> 	<p>A 10µm thick section was left unstained, and mounted in fluorescence mounting medium.</p> 	<p>A 10µm thick section was stained with H&E, and mounted in DPX.</p> 	<p>A 10µm thick section was stained with H&E, and mounted in fluorescence mounting medium.</p> 
--	--	--	--

The best FM images were produced when tissue was H&E stained and mounted in DPX due to the highly fluorescent resin that was perfused into the vessels, surrounded by the histological autofluorescence produced by the H&E stain and DPX of the surrounding tissues.

Confocal Microscopy

A 60µm thick section was left unstained and mounted in DPX.



However as can be seen, the thickness of the section caused air pockets to form around the tissue sample. Therefore gaskets were used during preparation of subsequent sectioned tissue samples.

A 100µm thick section was left unstained, and mounted in DPX using a gasket.



A 100µm thick section was left unstained, and mounted in fluorescence mounting medium using a gasket.



A 100µm thick section was stained with H&E, and mounted in DPX using a gasket.



A 100µm thick section was stained with H&E, and mounted in fluorescence mounting medium using a gasket.



The best confocal microscopy images were produced when tissue was H&E stained and mounted in DPX using a gasket. However during H&E staining, due to the thickness of the section, parts of the tissue became detached from the histology slides. Therefore 1mm tissue sections were cut using hand-made apparatus (Andres and During, 1981) and stained in H&E using histology cassettes. This was so that the tissue slices did not have to be mounted onto histology slides, which allowed the tissues to remain intact.

A 1mm thick section was stained with H&E and mounted in DPX in a glass bottom dish.



A 1mm thick section was stained with H&E and placed directly into a glass bottom dish.



Images produced from the 1mm thick sections (unlike the 100µm thick samples) were best when tissues were stained with H&E, and placed without mounting medium, into a glass bottom dish before scanning.

2.2.3.6. Acquiring Bright Field (BF) and Fluorescence Microscopy (FM) Images

Combining BF and FM Images

Aim: to optimise the quality of the histological and fluorescence images acquired (Leica DMRB fluorescence microscope; monochrome Hamamatsu C4742-95 digital camera) from the same view of one tissue specimen section.

Method:

Acquisition of a bright field (BF) image:

1. Use the 475nm wavelength (blue) excitation filter to allow light at a wavelength of 510nm (green) to be emitted.
2. Invert the acquired image using Openlab (acquisition and analysis software, Perkin Elmer).
3. Contrast enhance the acquired image.
4. Overlay the acquired black and white image with an artificial 'green channel' using the Openlab software.

Acquisition of a fluorescence microscopy (FM) image:

5. The fine focus of the fluorescence microscope may need to be adjusted when switching from the BF to the FM image.
6. Use the 510nm wavelength (green) excitation filter to allow light at a wavelength of 650nm (red) to be emitted.
7. Contrast enhance the acquired image using Openlab software (Perkin Elmer).
8. Overlay the acquired black and white image with an artificial 'red channel' using the Openlab software.
9. Finally, overlay the two BF and FM images to produce the final image.

It was determined that by overlaying a colour (green) onto the histological image of the tissue specimen before then inverting the colours of the image, this would mimic histological staining of the tissue. This is because it would allow the tissue itself to be represented in colour, in contrast to the surrounding space, which would look a lot darker. Additionally, when this histological image was then overlaid with a different coloured (red) fluorescence image of the same tissue

specimen in a combined image, the contrast between the fluorescent resin filled vessels and the surrounding relatively well defined histology was striking.

Imaging of a Whole Rat Brain Section

Aim: to 'stitch' together multiple overlaid histological and FM images (Leica DM IRB Fluorescence Microscope) so as to produce a combined image of a whole section of a rat brain and its surrounding skull, while still retaining microscopic resolution.

Method: set a 65% overlap for the images acquired (Leica DM IRB Fluorescence Microscope) using a Proscan/Orbit XY Stage to automatically stitch together images acquired from a pre-defined region of interest (ROI). The image produced can then be contrast enhanced as required.

Fine-tuning of the method required alteration of a number of parameters. This is because for example, a 40% overlap resulted in irregularities seen in the final image caused by fluctuations in the light as the image frames were stitched together, resulting dark and light streaks to appear across the whole image. In order to ensure the lighting on each image as it is stitched together is even, and to prevent this streaking from occurring, a larger image overlap percentage is required. However for example, a 90% overlap would take an excessive amount of time to generate the final image. A range of image overlap percentages were trialled and the best result was produced with a 65% image overlap, as acquisition of images is completed in 3.5 hours, while additional time is then required for the image to be 'stitched' together and processed.

2.2.3.7. Acquiring Confocal Microscopy (CM) Images

A Leica SP2 confocal laser scanning microscope (CLSM) was used to acquire CM images of thick tissue sections of the rat brain and skull, as this system was particularly useful for 3D reconstruction of the serial optical sections that were produced.

2.2.3.8. MicroCT Imaging of Vascular Casts

Preliminary Experiments

Preliminary experiments were carried out involving perfusion of different combinations of osmium tetroxide (OsO_4), gold nanoparticles (Nanoprobes, Inc., USA) and PU4ii resin mixed with fluorescent powder, into various different rat specimens. MicroCT images of these specimens were then acquired using a SkyScan 1174 machine (Bruker).

It was thought that perfusing a small volume of 1% OsO_4 solution through the vessels, before then perfusing PU4ii resin into the vasculature, would allow the inside of the cerebral vessels to become osmicated, and therefore increase the contrast of these blood vessels when the tissue was imaged using a microCT scanner. However, these preliminary experiments showed that perfusion of OsO_4 solution, prior to resin perfusion into the vasculature (no matter how rapidly the solution was perfused through the vessels) resulted in diffusion of the OsO_4 solution from the cerebral vessels into the surrounding tissue. As osmium is a metal, and therefore an x-ray contrast agent, this caused distortion of the images produced from the microCT scans of the resin casts, as the cerebral vessels could not be adequately distinguished from the surrounding tissues.

Gold nanoparticles (Nanoprobes, Inc., USA) were also trialled in these preliminary experiments as they are x-ray contrast agents, and were therefore expected to produce better defined microCT images of perfused samples. However, in these particular experiments, there were no improvements seen between the microCT images acquired from samples that were perfused with gold nanoparticles and those that were not. This was due to the distortion caused by diffusion of OsO_4 into the vessels and the surrounding tissues beforehand, as discussed previously.

MicroCT Scanning

It was found that the best combination of processing techniques allowing optimal visualisation of the rat cerebral VCCs was achieved by submerging samples into 1% OsO_4 solution for a duration of 24 hours, before then freeze-drying the specimens. These specimens were then placed into 20ml polypropylene universal tubes, which were attached to the stage of the microCT scanner using a carbon adhesive tab in order to minimise drift as much as possible during the scanning

process. MicroCT scanning was then carried out using a SkyScan 1174 machine (Bruker) on a number of specimens, which were processed in different ways. These include the following:

1. Fluorescent resin perfused osmicated and freeze-dried VCCs.
2. Fluorescent resin perfused whole brain tissue covered in dura, which were freeze-dried but not osmicated (as this would block x-rays from reaching the internal vascular structures).
3. Fluorescent resin perfused 1mm thick sections of brain tissue, dura and skull, which were freeze-dried but not osmicated.

2.2.3.9. Volume Rendering and Approximating Vessel Size from MicroCT Imaging Datasets

3D volumetric reconstructions of the microCT datasets (SkyScan 1174, Bruker) that were acquired from the cerebral vascular casts of selected rat specimens were generated using specialised software (SkyScan-1174v2, Bruker). These were then restructured using the same software, to create a video providing a 360° view of the whole specimen.

Although these volumetric reconstructions (using specialised software SkyScan-1174v2, Bruker) were useful in allowing visualisation of the microCT scanned samples from all different angles, the software was unable to determine the size of the individual vessels, as well as to further allow more sophisticated analysis as to their morphology. Therefore the 'Simple Neurite Tracer' plug-in for the computer software Image J (NIH) was used for volume rendering of the microCT scanning datasets of the rat VCCs that were acquired. The same software was then used to approximate the local thicknesses of the cerebral vessels and categorise them by colour. These measurements were illustrated using a calibration bar whereby the larger the vessel diameter, the lighter the colour of the vessel indicated in the image. Further supplementary information regarding the procedure for volume rendering and approximating vessel size from microCT imaging datasets is detailed in Appendix 4.

2.3. Results

2.3.1. Vascular Resin Casting and SEM Imaging

Figure 20A shows the cerebral vessels of a rat specimen, post-perfusion of PU4ii resin mixture containing blue fluorescent powder; while Figure 20B illustrates a grossly dissected resin perfused rat brain, demonstrating the presence of probable intradural vessels (arrow) as well as subdural vessels (arrowhead). Figure 20C illustrates the resin perfused cerebral vessels of a rat specimen post-tissue maceration. Figure 20D is an SEM image of a rat specimen, illustrating the cerebral vessels at x75 magnification. A capillary plexus consisting of 5-10 μ m diameter vessels can be seen on the top left hand corner of the image; as well as much larger calibre vessels, such as the SSS which can be seen arching across from the bottom right hand corner of the SEM image. This illustrates the profound detail that can be demonstrated by employing this casting technique, and its great potential in helping to investigate further the detailed anatomic structure of the brain.

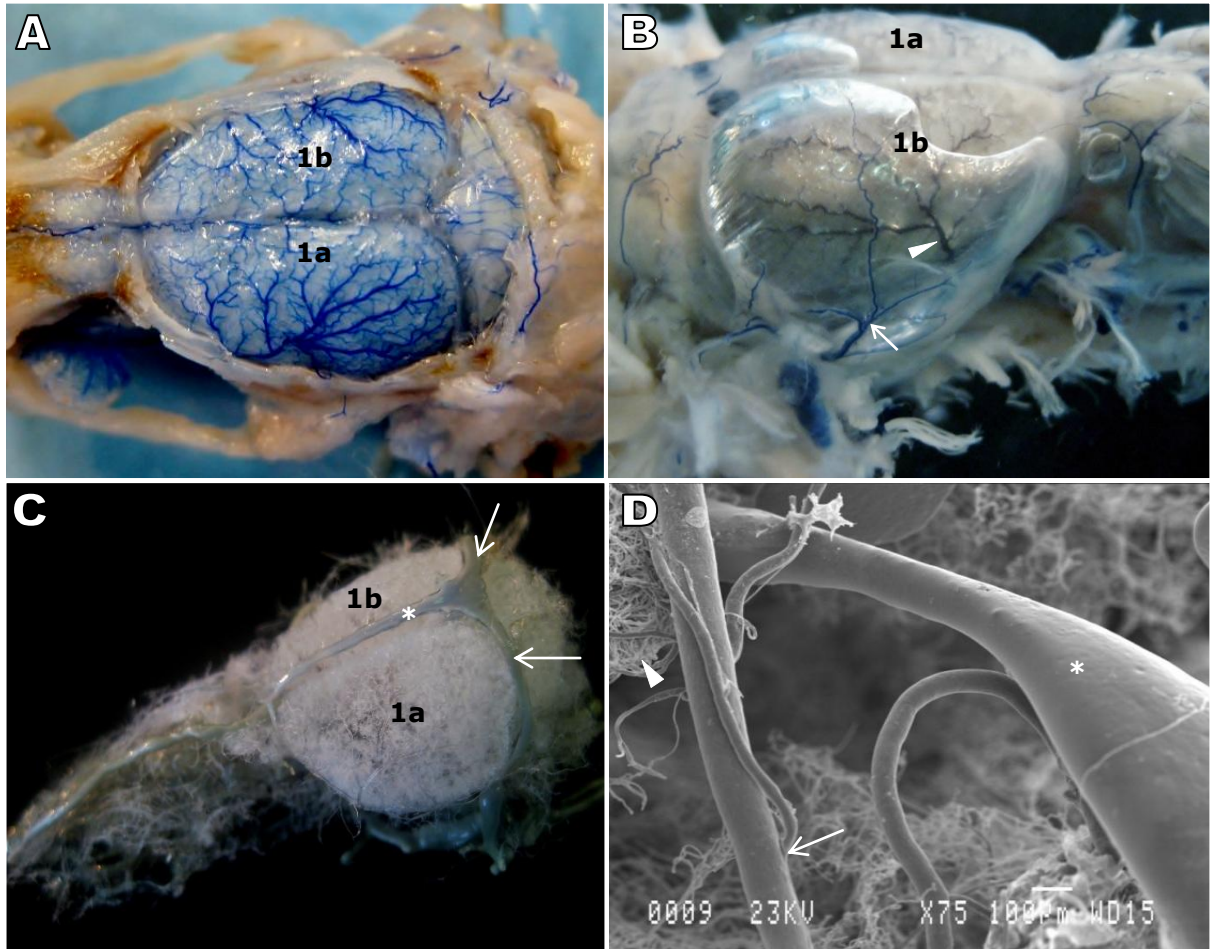


Figure 20: **A:** Macrograph of brain tissue of a Wistar rat perfused with fluorescent resin. The left cerebral hemisphere (1a) and right cerebral hemisphere (1b) can be seen. **B:** Grossly dissected resin perfused rat brain, illustrating the presence of possible intradural vessels (arrow) as well as subdural vessels (arrowhead). **C:** Macrograph of a freeze-dried rat cerebral resin cast with the surrounding brain tissue macerated away, allowing preservation of the normal vessel structure without surrounding tissue support. The SSS (asterisk) and transverse sinuses (arrows) can be seen, as well as the fine vessels surrounding these sinuses. **D:** SEM image (x75) of a rat cerebral specimen. The SSS (asterisk) as well as a capillary plexus (arrowhead) consisting of 5-10 μ m diameter vessels can be seen. A 120 μ m diameter vessel (possibly a bridging vein), can be seen branching into a smaller vessel (arrow) approximately 35 μ m in diameter.

2.3.2. Vascular Resin Casting and ESEM Imaging

2.3.2.1. ESEM Imaging of VCCs

Although bridging veins are often mentioned in the literature as one of the many theories that attempts to explain the origin of subdural haematomas often found in cases of NAHI, there is insufficient literary data that accurately describes the anatomical structure of these vessels. Although bridging veins are often mentioned, specific information regarding a clearly defined size range, number and distribution within specific areas of the brain, and histological factors that allow them to be differentiated from smaller venous tributaries and subdural veins have not yet been defined. This is clearly an important area in which further investigation is required.

Bridging veins can be generally defined as veins which drain the superficial cerebral vessels, traverse across the pia, arachnoid and dura mater layers, before then draining either directly or indirectly into the cerebral venous sinuses. These sinuses are located in between the inner meningeal and outer periosteal layer of the dural membrane.

ESEM images of cerebral VCCs of different resin perfused rat specimens illustrate the distinct differences that can be seen between the characteristic imprint features of arterial and venous endothelial cell nuclei, which can be seen on the surface of vascular casts. Venous endothelial cell nuclei are rounded in shape and less well orientated, compared with the more elongated structure of the endothelial cell nuclei seen on the surface of arterial casts, which run parallel along the axis of the vessels. These structures can clearly be seen in Figure 23.

ESEM images of cerebral VCCs of Wistar rat specimens illustrate the vast differences in size and shape that can be seen between the bridging veins and their tributaries that drain into the SSS (Figure 25), TS (Figure 27, Figure 28, Figure 35, and Figure 37), SS (Figure 29, Figure 30, Figure 31, Figure 32, Figure 35, and Figure 37), petrosquamous sinus (PS) (Figure 33, Figure 34, Figure 35, Figure 36, Figure 37, Figure 38, and Figure 39). As can be seen in these images, the general size and shape of bridging veins and their tributaries, as well as their manner and extent of branching, differs even between the bridging veins which drain into the same venous sinus. For example, it was found that the SSS narrows as it traverses anteriorly, and with this the size of the bridging veins draining into

the SSS also decrease in size. Size and shape of the vessels also seem to vary slightly between different rat resin casts; however anatomical variations seen between individual specimens is normal, even when factors such as age, weight, sex and species of rat are kept constant.

However general anatomical patterns still appear to exist between the bridging veins that drain into different types of venous sinuses. For example distinct narrowing of the bridging vein diameter at the junction point where the vessel enters the venous sinus can be seen in the SSS (Figure 26), TS (Figure 27), SS (Figure 30), as well as the PS (Figure 33, Figure 34, Figure 35 and Figure 38). Furthermore, a similar structural pattern can be seen in the vascular network of tributaries which converge to form the bridging veins, which in turn drain into the venous sinuses (Figure 29, Figure 30, and Figure 31). This narrowing may cause weakening of the vessel walls at the junction between the bridging veins and the venous sinuses, therefore making the vessels more susceptible to rupture on application of a certain type and amount of force. Similar observations regarding this vessel narrowing have also been described in various other studies which suggest a number of possibilities as to their cause (Anderson and Anderson, 1978; Nakai et al., 1981; Nakai et al., 1989; Reina-De La Torre et al., 1998; Vignes et al., 2007). This will be further discussed in section 2.4.

As well as this, individual patterns can be identified between the different types of bridging veins and their tributaries, as well as other smaller draining veins which all drain into the TS, SS, PS and SSS. For example, there is a noticeably smaller number of vessels draining into the larger venous sinuses such as the SSS (Figure 25) and TS (Figure 27E), compared to that of the SS (Figure 29, Figure 35 and Figure 40) and PS (Figure 33, Figure 34, Figure 35, Figure 38 and Figure 40). Figure 40 particularly illustrates a section of the whole width of the SS and PS, illustrating the vast number of bridging veins as well as their tributaries and other smaller draining veins, that are draining into the length of the SS and PS, in contrast to the comparatively much lower number seen to drain into the larger SSS and TS (Figure 25 and Figure 27E).

Furthermore, the size of the bridging veins and their tributaries seems to depend upon the size of the venous sinus into which the vessels are draining. In general, the diameter of the bridging veins and tributaries that drain into the SS and PS seem to be smaller than vessels that drain into larger venous sinuses sizes such as the SSS or TS.

In order to compare the relative sizes of the inner diameters of the SSS, TS, SS and PS, 100 measurements of the inner diameters of each different type of venous sinus was taken at random, and the mean diameter and standard deviation in each case was calculated. The mean diameter of the SSS was $963\mu\text{m}$, with a standard deviation of $264\mu\text{m}$. The mean diameter of the TS was $778\mu\text{m}$, with a standard deviation of $158\mu\text{m}$. The mean diameter of the SS was $401\mu\text{m}$, with a standard deviation of $134\mu\text{m}$, and the mean diameter of the PS was $622\mu\text{m}$, with a standard deviation of $168\mu\text{m}$.

The differences in the diameter of the bridging veins and their tributaries were also analysed and are shown through the use of a frequency histogram as illustrated in Figure 21. This frequency histogram was produced by identifying the location containing the highest density of vessels draining into a $1500\mu\text{m}$ section of a particular venous sinus. The number of vessels present in these $1500\mu\text{m}$ sections was then counted and their diameters measured. This process was carried out for the SSS, TS, SS and PS.

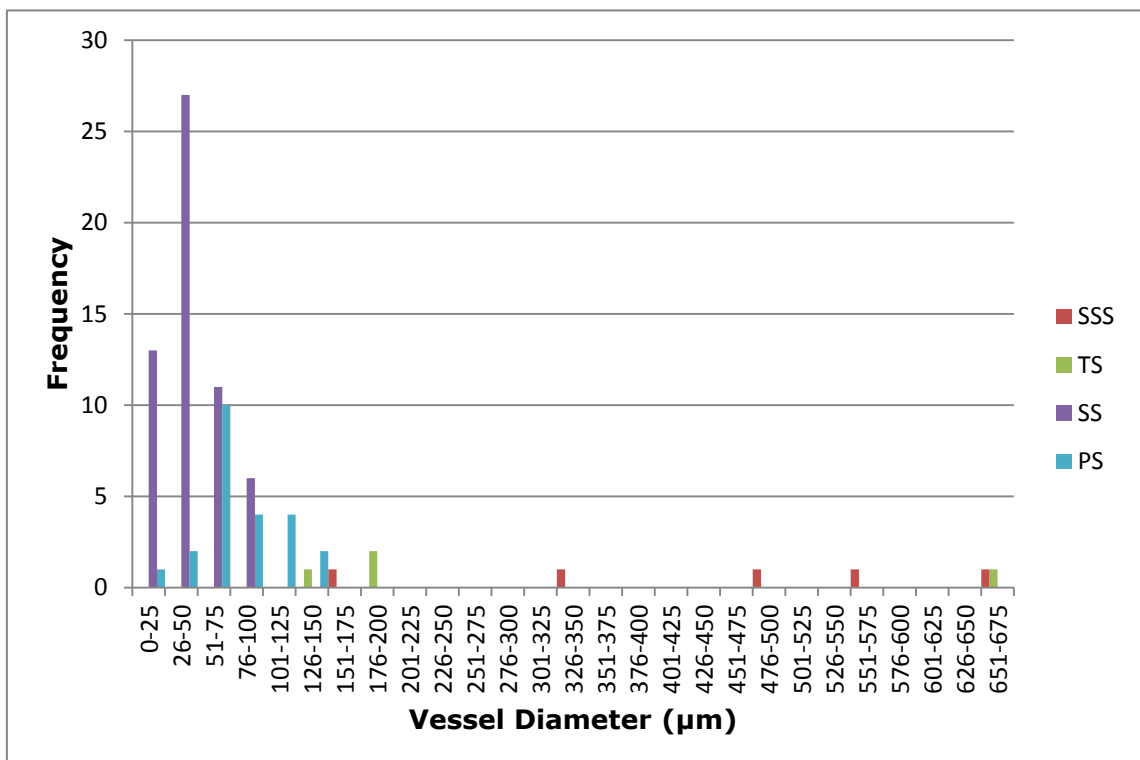


Figure 21: Frequency histogram of the diameters of the bridging veins and their tributaries, draining into the SSS, TS, SS and PS.

From this frequency histogram it can be seen that the range in the diameter of the aforementioned bridging veins and tributaries seems to be wider in the larger SSS and TS, as opposed to the SS and PS, which in comparison have a larger number, however a narrow range of smaller vessels draining into the venous sinuses. This data allows a comparison to be made between the number and range of the different size vessels present in the highest density area that could be found in each of the four venous sinuses mentioned above. It also allows this information to be correlated with the size of the venous sinus into which all of the venous tributaries eventually drain, and therefore allow any generalised patterns to be identified. The finding of the presence of a larger number of smaller diameter vessels draining into the PS and SS in particular, compared to the SSS is important as this may in part explain the more common localisation of subdural haematomas in the peri-tentorial region and posterior fossa in both birth trauma and in NAHI cases.

A probability histogram (Figure 22) constructed using the same data illustrating the diameters of the venular tributaries draining the highest vascular density (1500 μm) sections of the SS and PS, shows a log-normal distribution to be present in both cases. The TS and SSS are not illustrated in this graph due to a significantly smaller number of vascular tributaries present in these areas, meaning that an accurate probability histogram could not be created from the data. Similar findings have also been found in other studies involving both rat and human cerebral microvasculature (Cassot et al., 2006; Hudetz et al., 1993).

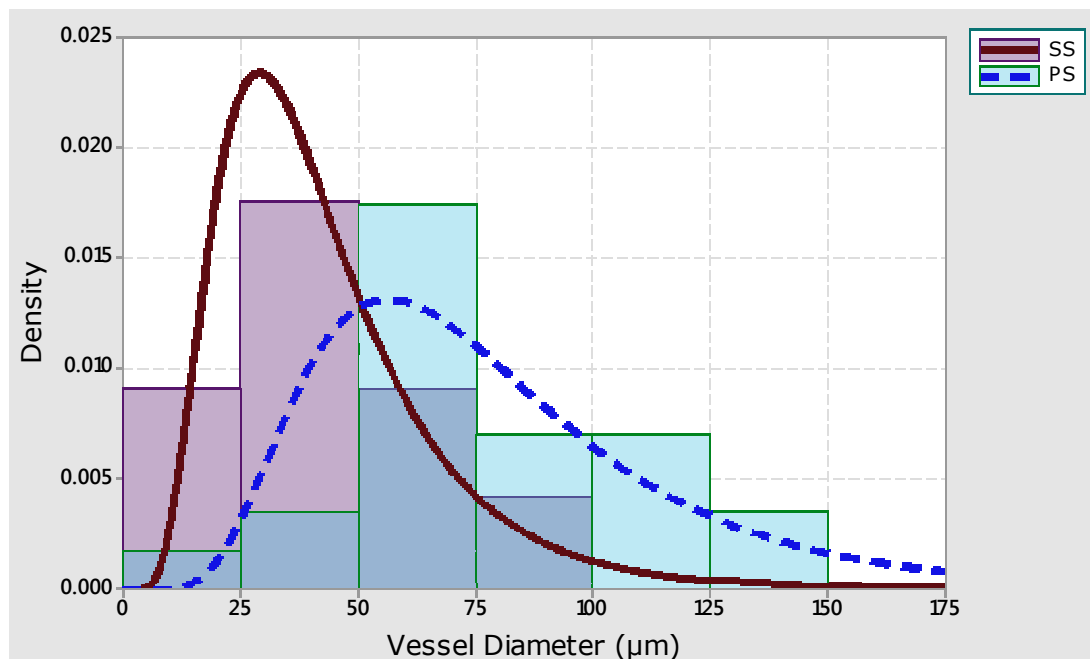


Figure 22: Probability histogram of the diameters of the venular tributaries draining the highest vascular density 1500 μm sections of the SS and PS.

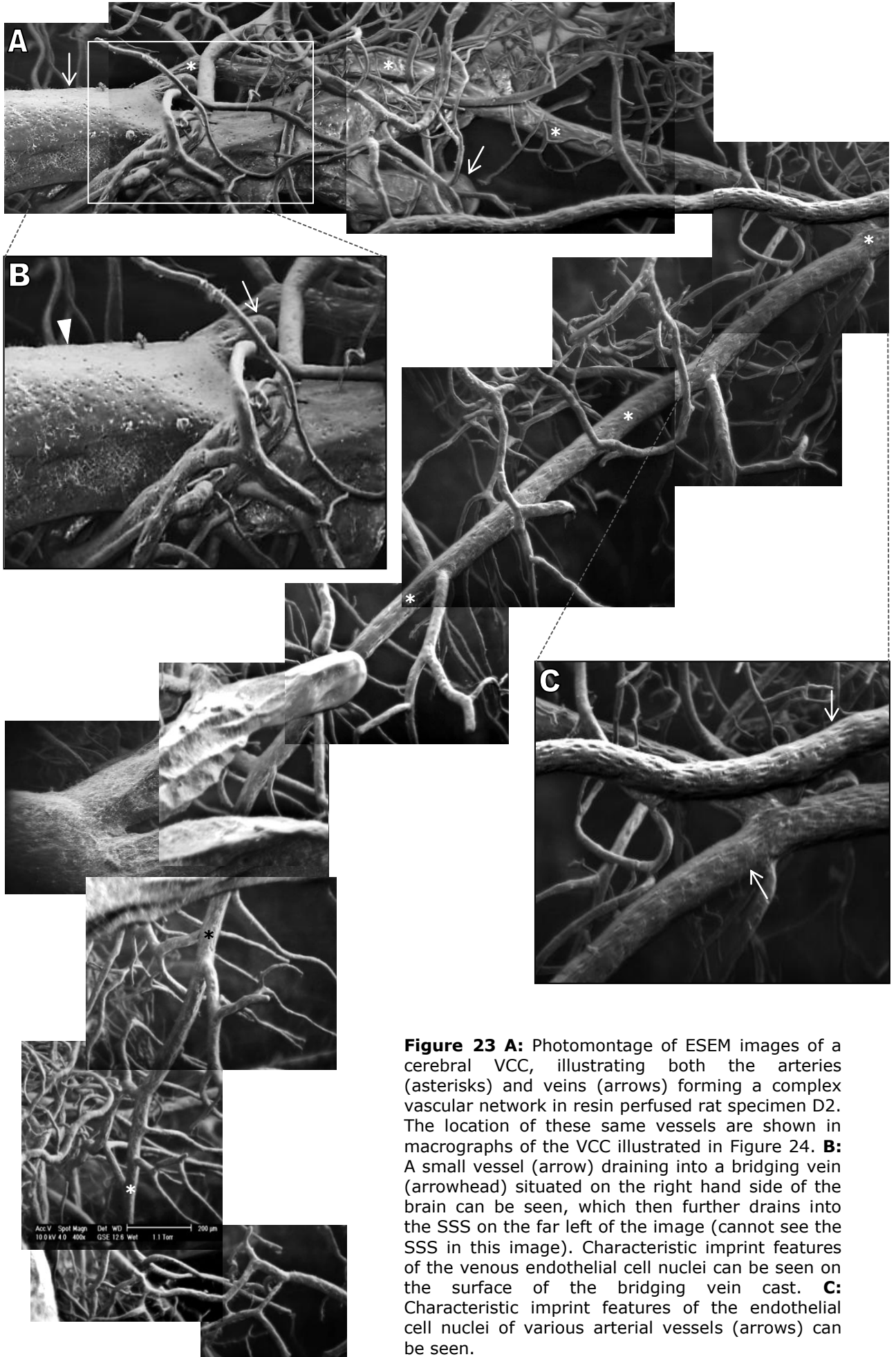


Figure 23 A: Photomontage of ESEM images of a cerebral VCC, illustrating both the arteries (asterisks) and veins (arrows) forming a complex vascular network in resin perfused rat specimen D2. The location of these same vessels are shown in macrographs of the VCC illustrated in Figure 24. **B:** A small vessel (arrow) draining into a bridging vein (arrowhead) situated on the right hand side of the brain can be seen, which then further drains into the SSS on the far left of the image (cannot see the SSS in this image). Characteristic imprint features of the venous endothelial cell nuclei can be seen on the surface of the bridging vein cast. **C:** Characteristic imprint features of the endothelial cell nuclei of various arterial vessels (arrows) can be seen.

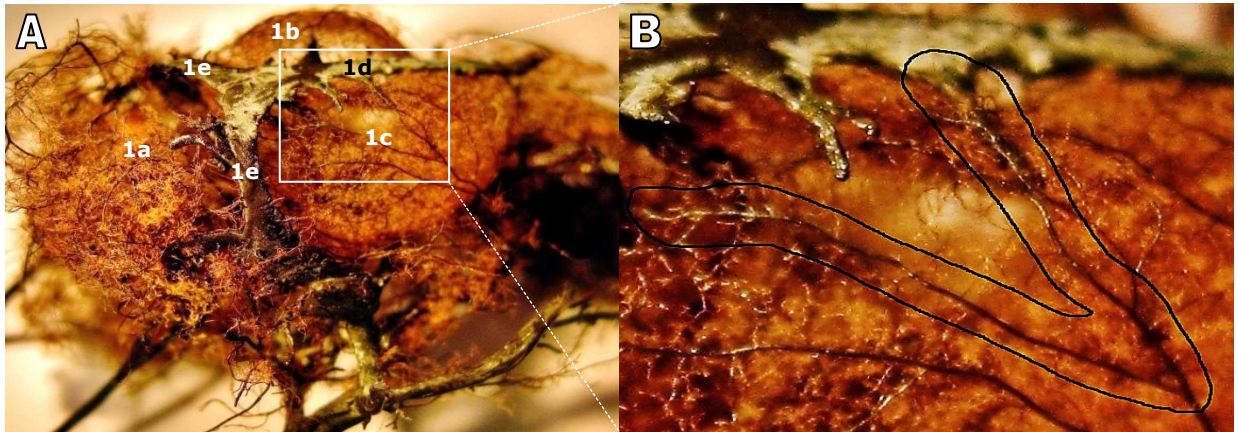


Figure 24: Macrographs of an OsO₄ stained VCC of RAT D2 showing both arterial and venous vessels, forming a complex vascular network. ESEM images of these vessels are shown in Figure 23. **A:** Here, the cerebellum (1a); left cerebral hemisphere (1b); right cerebral hemisphere (1c); SSS (1d); and transverse sinuses (1e) are illustrated. **B:** A higher magnification image of the area enclosed in the white box shown in A. The black outline indicates the area illustrated in Figure 23A.

The Superior Sagittal Sinus (SSS)

Photomontages of ESEM images of rat VCC specimens, illustrating the relatively large size, however small number of bridging veins and tributaries draining into the SSS. Macrographs of these ESEM images are also illustrated in Figure 26C and D.

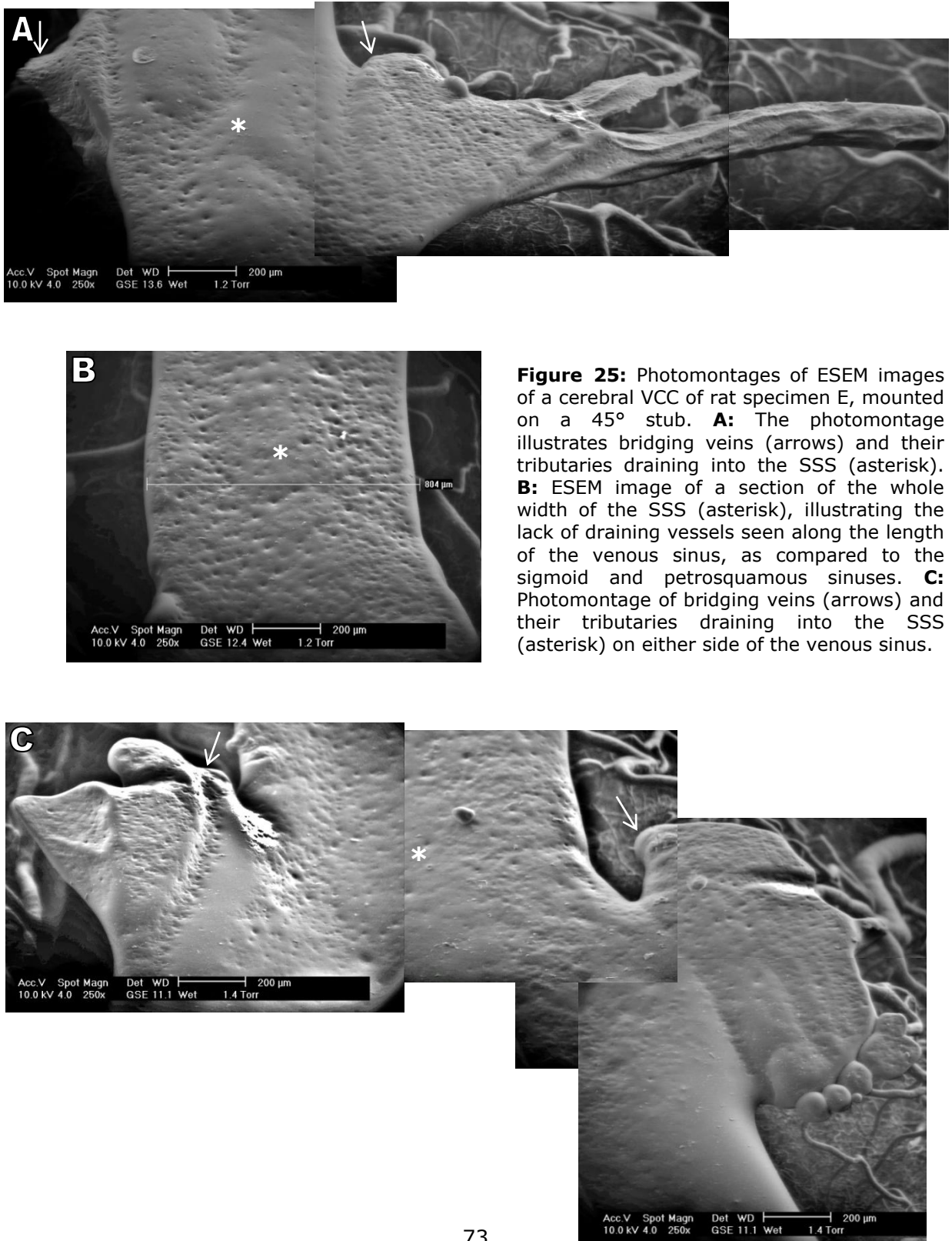


Figure 25: Photomontages of ESEM images of a cerebral VCC of rat specimen E, mounted on a 45° stub. **A:** The photomontage illustrates bridging veins (arrows) and their tributaries draining into the SSS (asterisk). **B:** ESEM image of a section of the whole width of the SSS (asterisk), illustrating the lack of draining vessels seen along the length of the venous sinus, as compared to the sigmoid and petrosquamous sinuses. **C:** Photomontage of bridging veins (arrows) and their tributaries draining into the SSS (asterisk) on either side of the venous sinus.

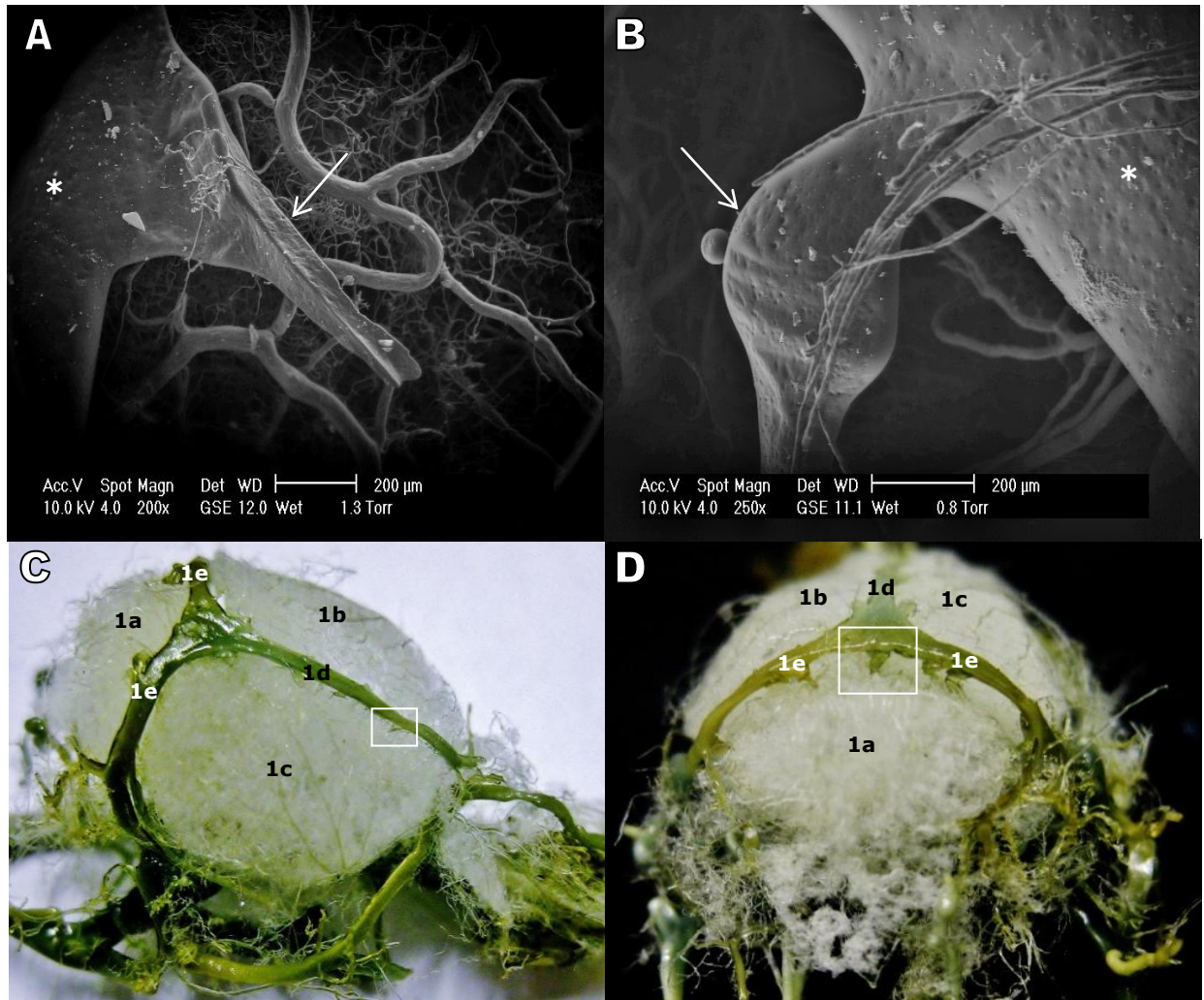


Figure 26: Images of a cerebral VCC of a Wistar rat specimen. Images A and B are ESEM images, and C and D are macrographs of a cerebral VCC of Rat E. **A:** ESEM image of a VCC seen from above (sample was mounted on a flat stub). A bridging vein (arrow) can be seen draining into the SSS (asterisk) on the right. The diameter of the bridging vein at the point of entry into the SSS is $497\mu\text{m}$. **B:** ESEM image of a VCC mounted on a 45° stub. A bridging vein (arrow) can be seen draining into the SSS (asterisk) on the left hand side of the image. The diameter of the bridging vein at the point of entry into the SSS is $362\mu\text{m}$. **C:** The same bridging vein draining into the SSS, as seen in A can be seen in this image (white box). Here, the cerebellum (1a); left cerebral hemisphere (1b); right cerebral hemisphere (1c); SSS (1d); and transverse sinuses (1e) are illustrated. **D:** The same bridging vein draining into the SSS, as seen in B can be seen in this image (white box).

The Transverse Sinus (TS)

ESEM images of rat VCCs illustrating the different structures and calibre of bridging veins and tributaries seen to drain into the TS of different samples. Macrographs of these ESEM images are also illustrated in Figure 28.

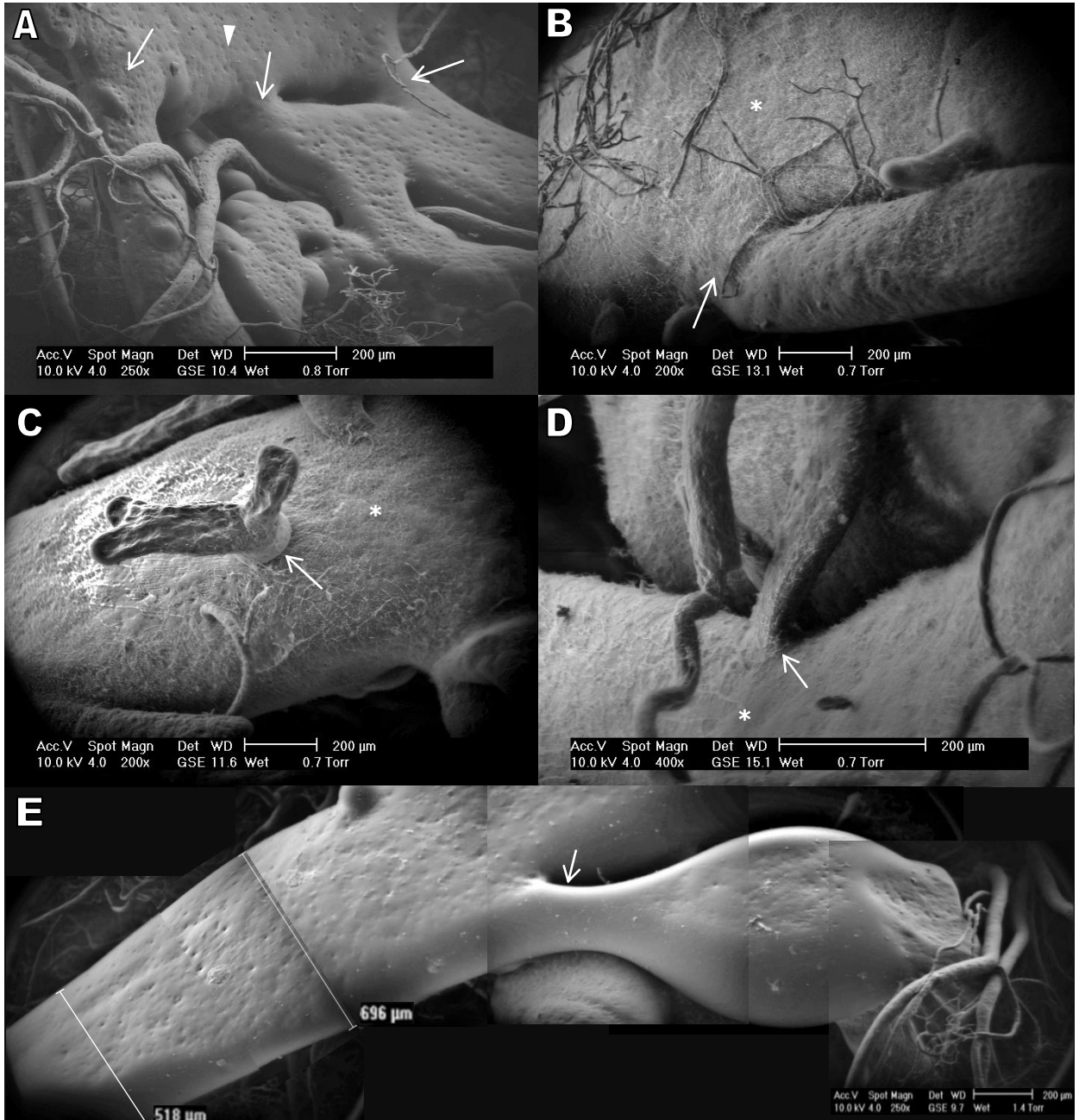


Figure 27: ESEM images of cerebral VCCs of Wistar rat specimens. Images A and E (Rat E) are taken from a different VCC to images B, C and D (Rat D2). The same VCCs are also shown in Figure 28. **A:** Sample mounted on a 45° stub. A branching network of bridging veins (arrows) can be seen draining into the right TS (arrowhead). The diameters of the bridging veins at the point of entry into the sinus are 130-190 μ m. **B:** Sample mounted on a 45° stub. A bridging vein (arrow) can be seen draining into the left TS (asterisk). The diameter of the bridging vein at the point of entry into the sinus is 340 μ m. **C:** A smaller calibre bridging vein (arrow) draining into the left TS (asterisk). The diameter of the bridging vein at the point of entry into the sinus is 165 μ m. **D:** A bridging vein (arrow) draining into left TS (asterisk). The diameter of the bridging vein at the point of entry into the sinus is 60 μ m. **E:** A large bridging vein (arrow) is shown draining into the left TS, illustrating the distinct narrowing seen at the junction point as the bridging vein drains into the sinus. This is a structure that is consistently seen throughout other resin cast samples. The image also shows a large section of the whole width of the transverse sinus, illustrating the lack of draining vessels seen along the length of the venous sinus, as compared to the SS and PS.

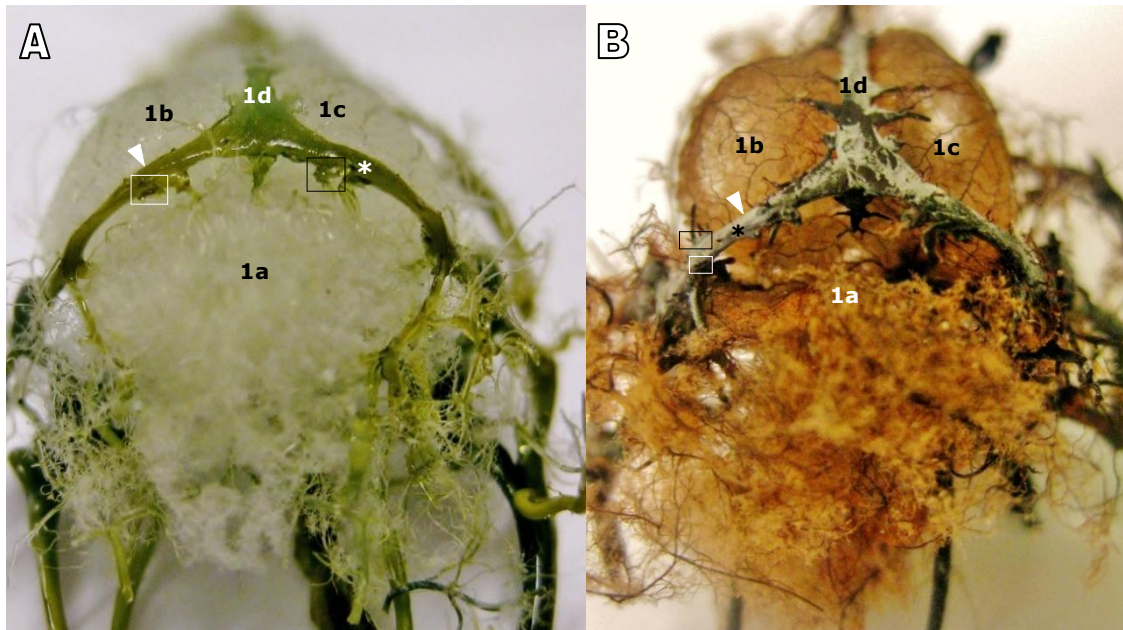


Figure 28: Macrographs of cerebral VCCs of Rats E and D2, illustrating bridging veins that drain directly into the transverse sinuses. These vessels are also shown in Figure 27. **A:** Macrograph of a VCC of Rat E, illustrating the location of a branching network of bridging veins (black box) draining into the right transverse sinus (asterisk), as seen in Figure 27A as well as another larger bridging vein (white box) draining into the left transverse sinus (arrowhead) as seen in Figure 27E. Here, the cerebellum (1a); left cerebral hemisphere (1b); right cerebral hemisphere (1c); and SSS (1d) are illustrated. **B:** Macrograph of a VCC (stained with OsO_4) of Rat D2, illustrating the location of bridging veins draining into the left transverse sinus (arrowhead), as seen in Figure 27B (asterisk), Figure 27C (white box), and Figure 27D (black box).

The ESEM images illustrated, particularly of the SS and PS shown are crucial as they demonstrate numerous vessels entering the venous sinuses, with the majority being very small in diameter as well as a few larger calibre vessels, as shown in the graph in Figure 21.

The terminology used in the past to describe vessels which have traditionally been called 'bridging veins' is imprecise, as it only addresses the presence of large veins that enter the major sinuses. This project demonstrates that there are a wide variety of veins of a range of different sizes draining directly into the venous sinuses, particularly in relation to the SS and PS. This may be especially relevant to birth related SDHs as well as SDHs in NAHI, as these smaller vessels may be the potential source of the SDHs, rather than rupturing of larger bridging veins.

The Sigmoid Sinus (SS)

Photomontages of ESEM images acquired from various rat VCC specimens. These illustrate the detailed vascular network of relatively smaller diameter bridging veins and tributaries, draining into the SS. Macrographs of these ESEM images are also illustrated in Figure 32.

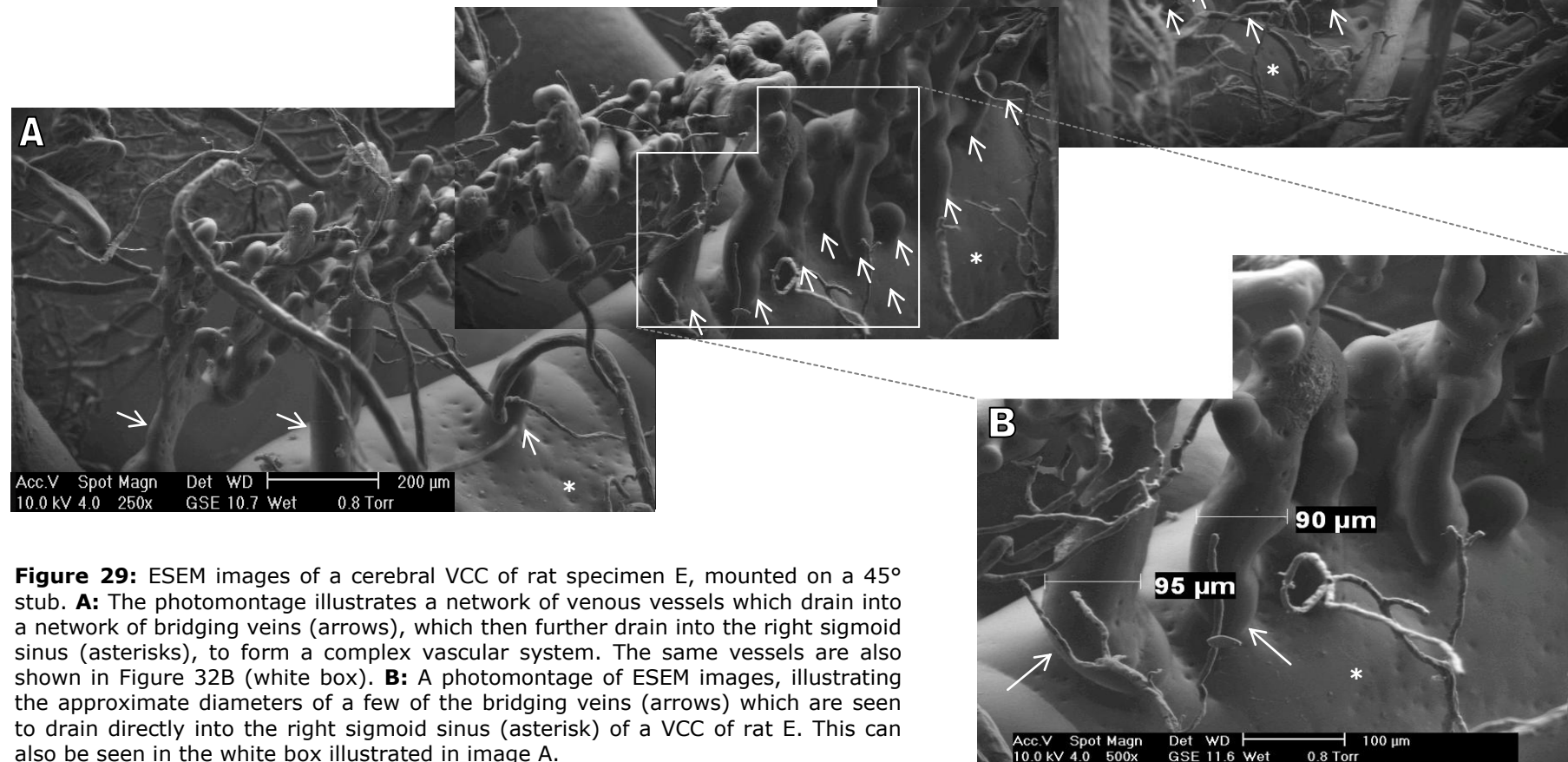


Figure 29: ESEM images of a cerebral VCC of rat specimen E, mounted on a 45° stub. **A:** The photomontage illustrates a network of venous vessels which drain into a network of bridging veins (arrows), which then further drain into the right sigmoid sinus (asterisks), to form a complex vascular system. The same vessels are also shown in Figure 32B (white box). **B:** A photomontage of ESEM images, illustrating the approximate diameters of a few of the bridging veins (arrows) which are seen to drain directly into the right sigmoid sinus (asterisk) of a VCC of rat E. This can also be seen in the white box illustrated in image A.

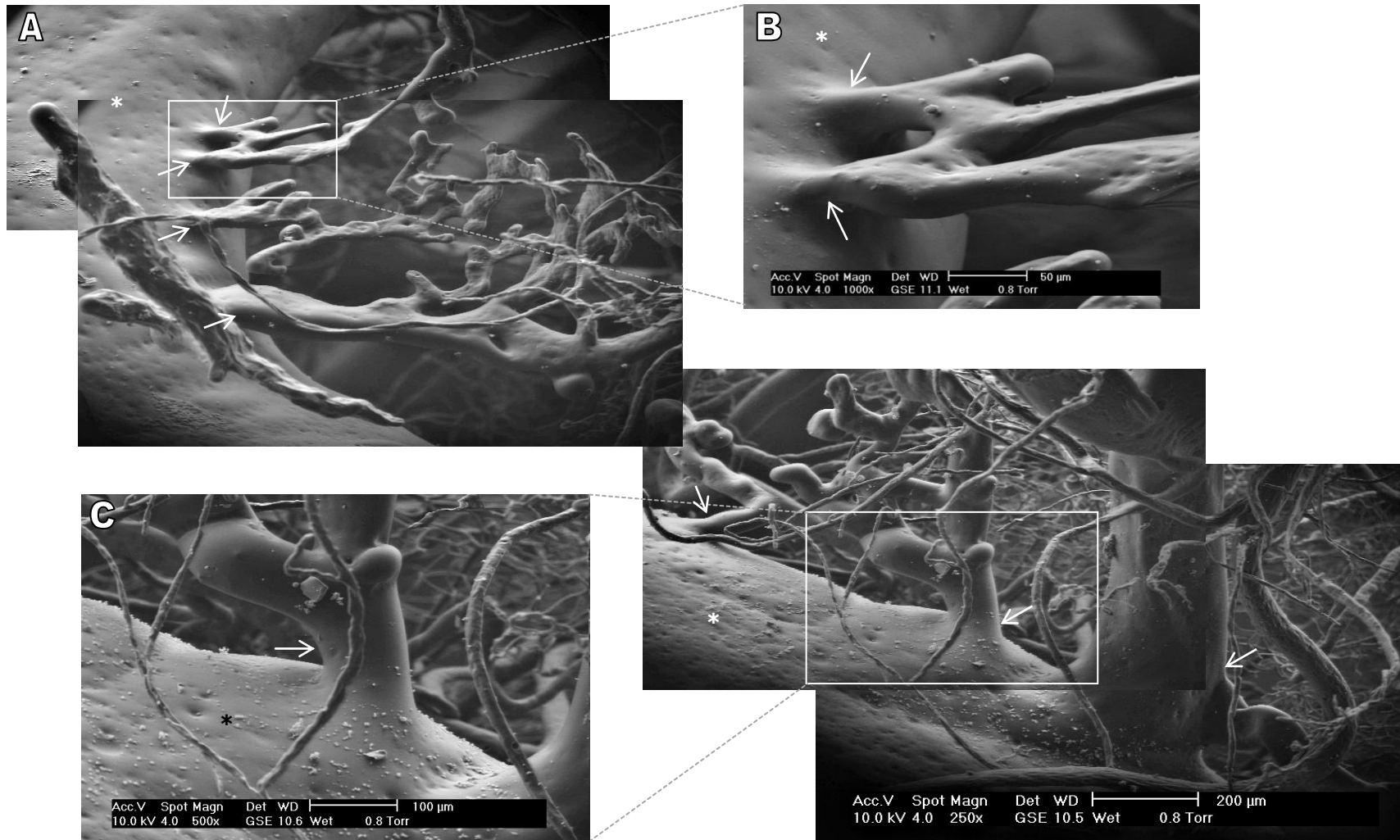
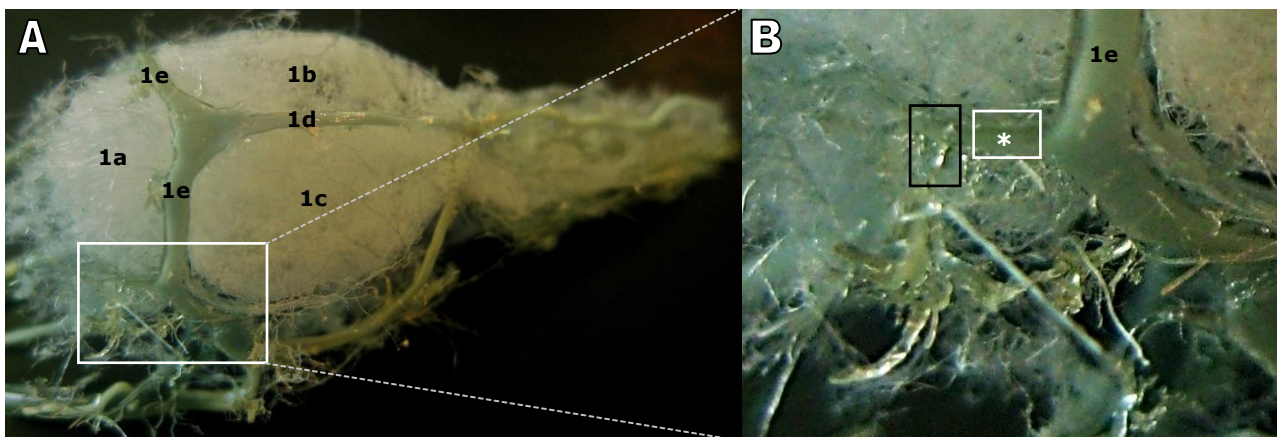
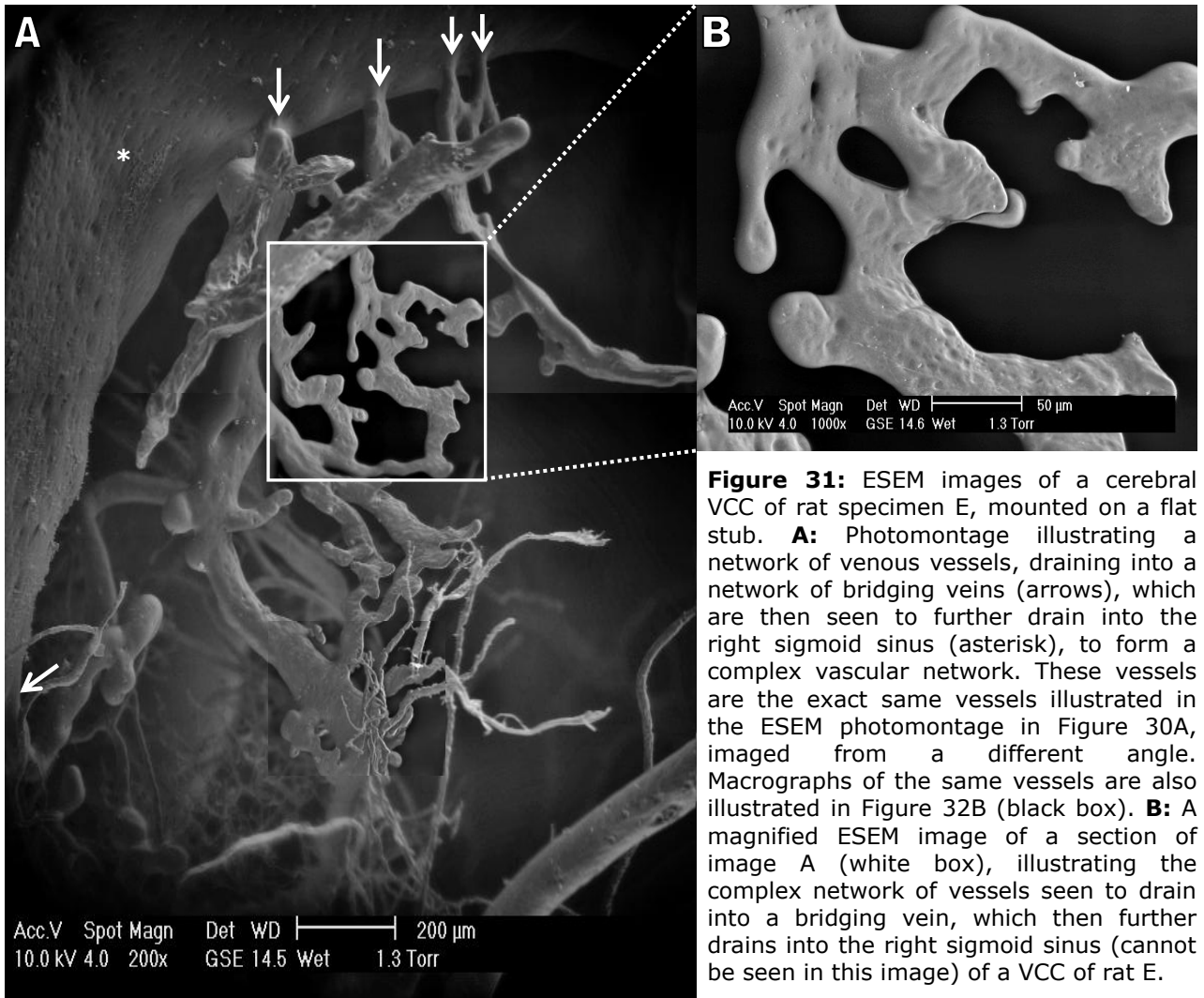


Figure 30: ESEM images of a cerebral VCC of rat specimen E, mounted on a 45° stub. These vessels are the same as those illustrated in Figure 31 which were mounted on a flat stub. **A:** Photomontage illustrating a network of venous vessels, draining into a network of bridging veins (arrows) which are seen to then further drain into the right sigmoid sinus (asterisks), to form a complex vascular network. Macrographs of the same vessels are also illustrated in Figure 32B (black box). **B, C:** Magnified ESEM images of sections of image A, illustrating the complex structure of some of the venous vessels seen to drain into bridging veins (arrows), which are then seen to further drain into the right sigmoid sinus (asterisks) of a VCC of rat E.



The Petrosquamous Sinus (PS)

Photomontages of ESEM images acquired from various rat VCC specimens. These illustrate the detailed vascular network of relatively smaller diameter bridging veins and tributaries, draining into the PS. Macrographs of these ESEM images are also illustrated in Figure 36, Figure 37 and Figure 39.

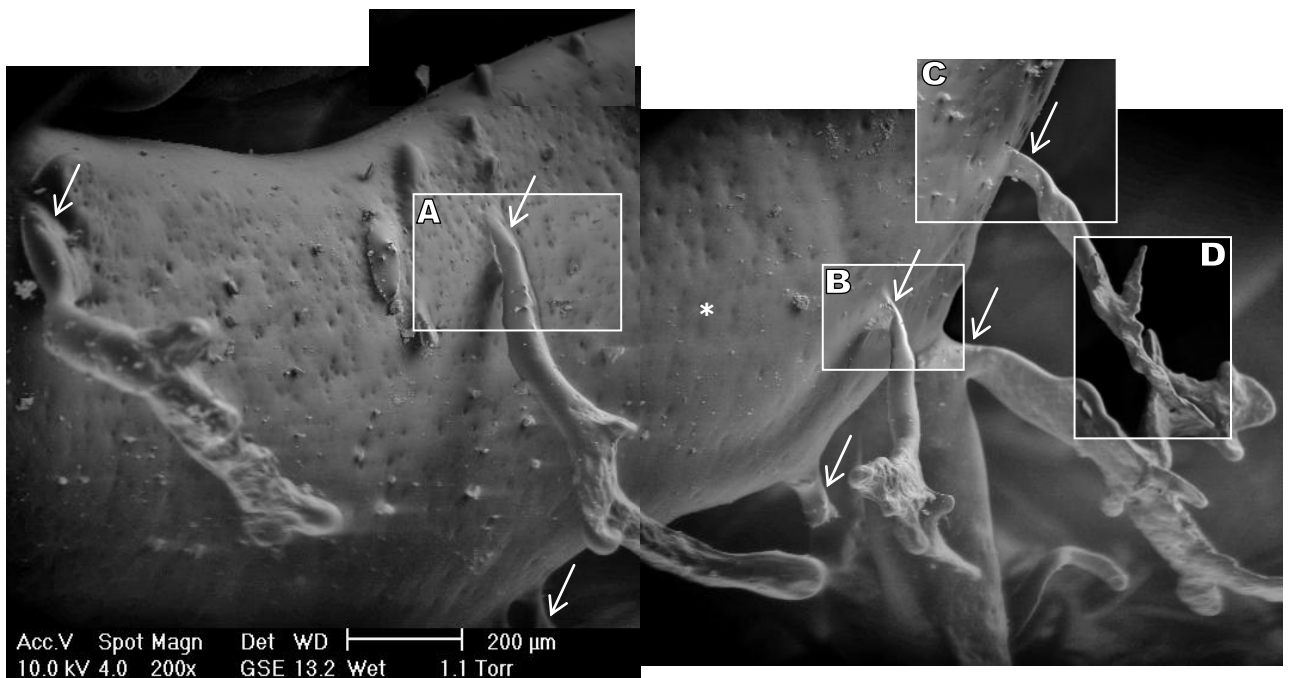


Figure 33: A Photomontage of ESEM images of a cerebral VCC of rat specimen E, mounted on a flat stub. The photomontage illustrates a network of bridging veins (arrows) and their tributaries which drain into the right petrosquamous sinus (asterisk). Distinct flattening of the bridging veins can often be seen at the junction between the vessel and the sinus, as the vessels enter and drain into the venous sinuses (A, B and C). Macrographs of the same vessels are also illustrated in Figure 36.

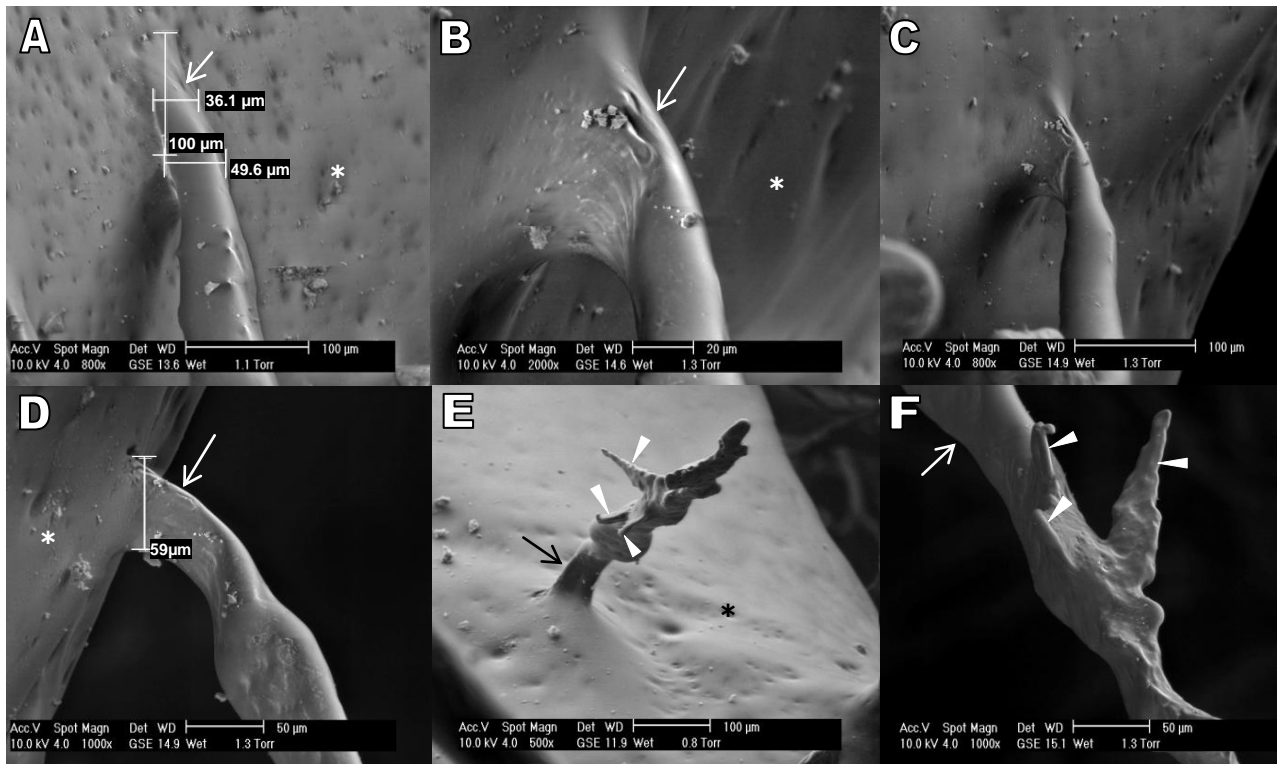


Figure 34: ESEM images of a cerebral VCC of rat specimen E, mounted on a flat stub. These are magnified images of sections of the photomontage seen in Figure 33, illustrating a network of bridging veins and vessels which drain into the right petrosquamous sinus. Macrographs of the same vessels are also illustrated in Figure 36. **A:** Magnified image of Figure 33A, illustrating the size of the junction ($36.1\mu\text{m} \times 100\mu\text{m}$) as the bridging vein (arrow) enters the petrosquamous sinus (asterisk). **B:** Magnified image of Figure 33B, illustrating flattening of a bridging vein at the junction between the vessel and the sinus (arrow) as it enters and drains into the petrosquamous sinus (asterisk). **C:** The same vessel as seen in Figure 34B, however imaged after the specimen was tilted slightly to allow visualisation of the vessel junction from above. **D:** Magnified image of Figure 33C, illustrating flattening of a bridging vein (arrow) at the junction between the vessel and the petrosquamous sinus (asterisk). **E, F:** Magnified images of Figure 33D illustrating flattening of a bridging vein (arrow) at the junction between the vessel and the petrosquamous sinus (asterisk), as well as showing finer tributaries also draining into this bridging vein (arrowheads).

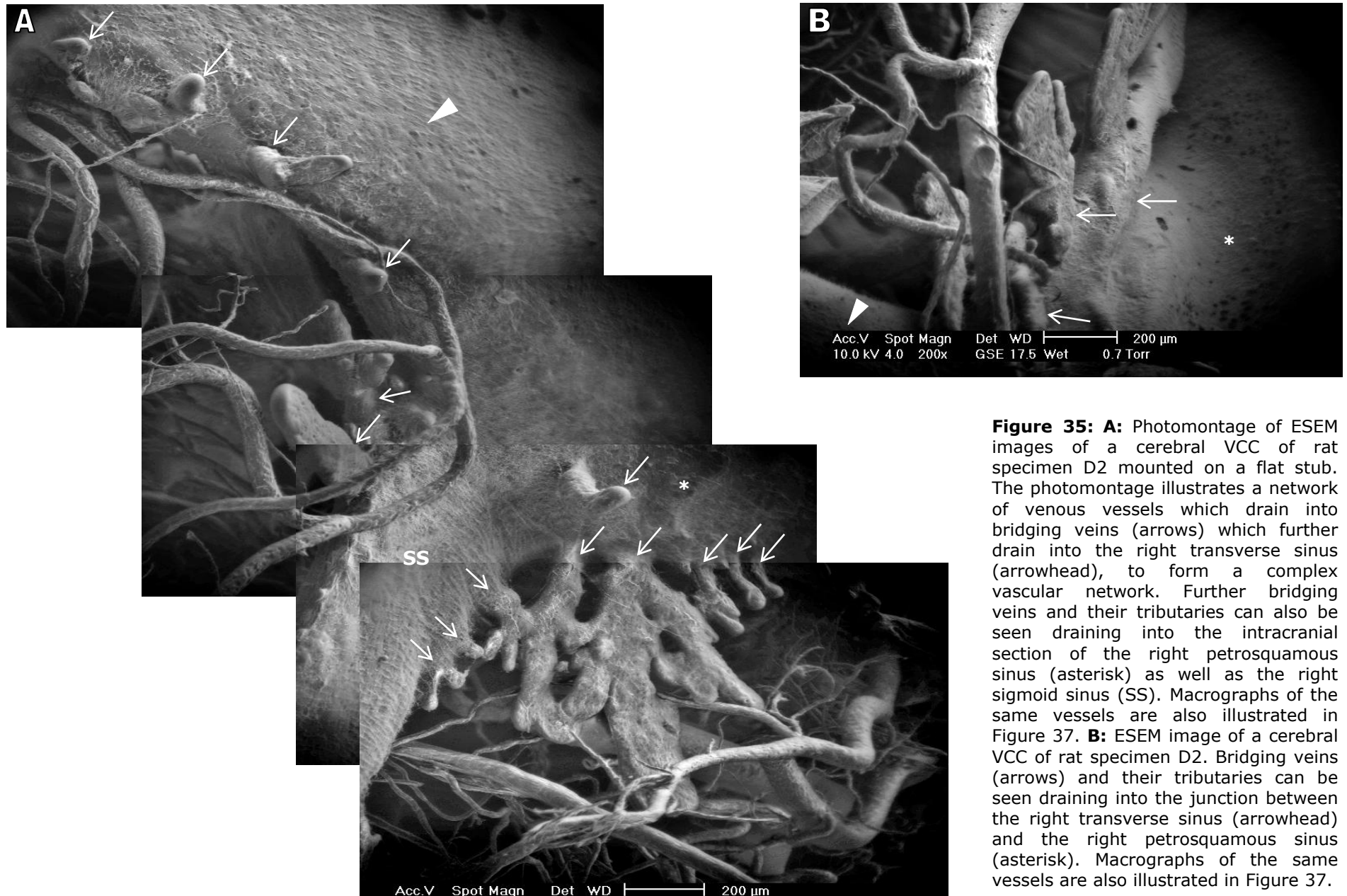


Figure 35: A: Photomontage of ESEM images of a cerebral VCC of rat specimen D2 mounted on a flat stub. The photomontage illustrates a network of venous vessels which drain into bridging veins (arrows) which further drain into the right transverse sinus (arrowhead), to form a complex vascular network. Further bridging veins and their tributaries can also be seen draining into the intracranial section of the right petrosquamous sinus (asterisk) as well as the right sigmoid sinus (SS). Macrographs of the same vessels are also illustrated in Figure 37. **B:** ESEM image of a cerebral VCC of rat specimen D2. Bridging veins (arrows) and their tributaries can be seen draining into the junction between the right transverse sinus (arrowhead) and the right petrosquamous sinus (asterisk). Macrographs of the same vessels are also illustrated in Figure 37.

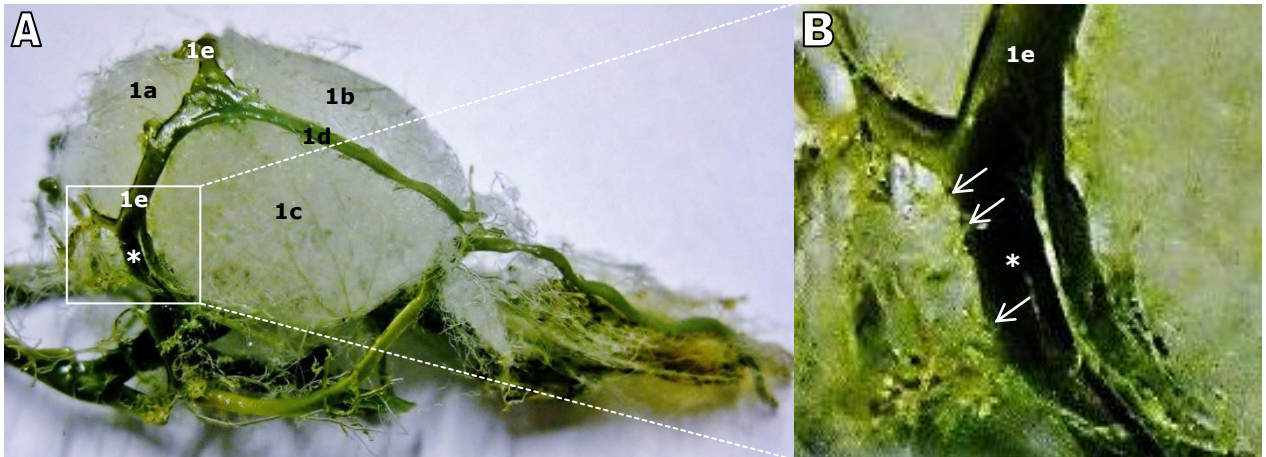


Figure 36: A, B: Macrographs of a cerebral VCC of rat specimen E, mounted on a flat stub. These images illustrate a network of bridging veins (arrows) and their tributaries, which drain into the right petrosquamous sinus (asterisk). Here, the cerebellum (1a); left cerebral hemisphere (1b); right cerebral hemisphere (1c); SSS (1d); and transverse sinuses (1e) are illustrated. These vessels are also illustrated in Figure 33 and Figure 34.

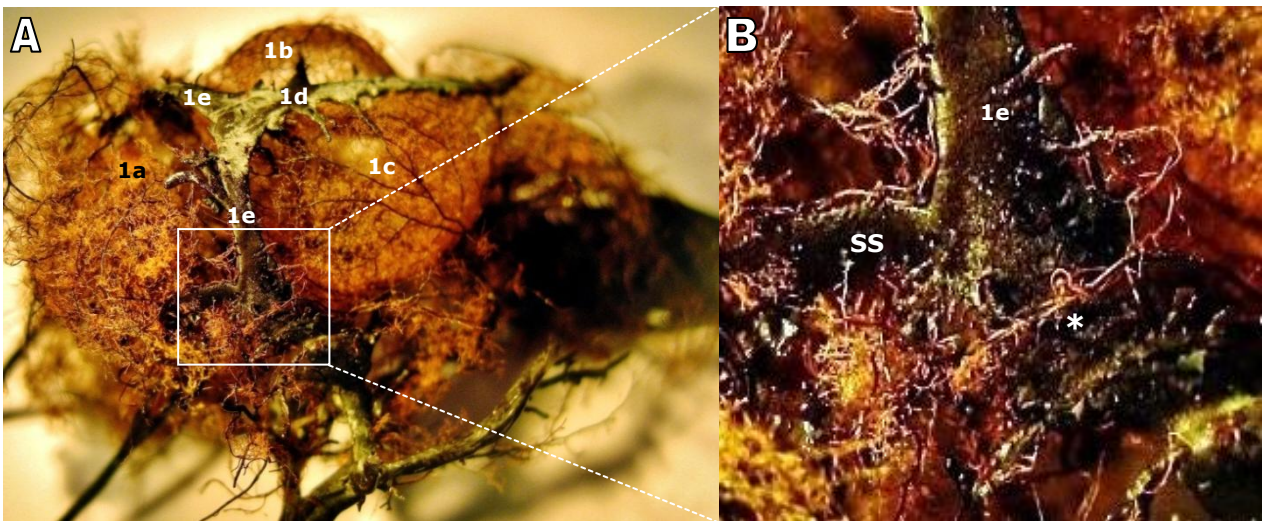


Figure 37: Macrographs of a cerebral VCC of rat specimen D2 (stained with OsO_4) mounted on a flat stub. **A:** Here, the cerebellum (1a); left cerebral hemisphere (1b); right cerebral hemisphere (1c); SSS (1d); and transverse sinuses (1e) are illustrated. **B:** A magnified image of a section of image A, illustrating a network of bridging veins and their tributaries, draining into the right transverse sinus (1e), the right petrosquamous sinus (asterisk), as well as the right sigmoid sinus (SS), to form a complex vascular network. ESEM images of these vessels are also illustrated in Figure 35.

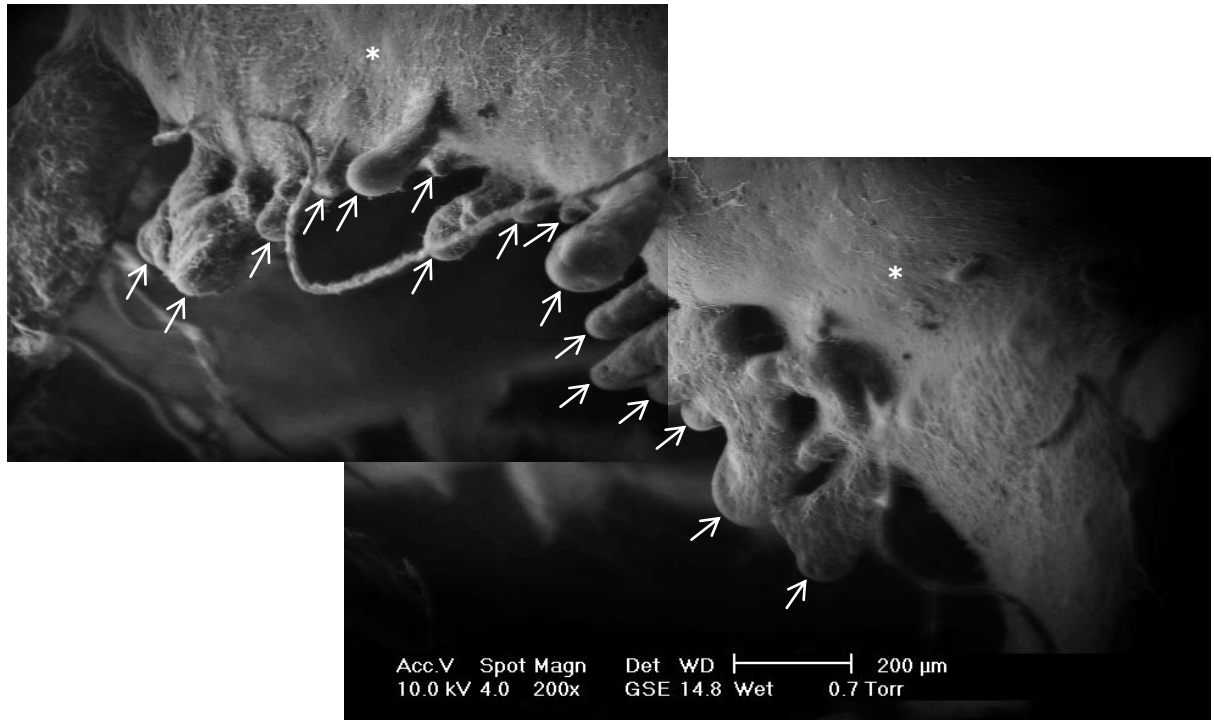


Figure 38: Photomontage of ESEM images of a cerebral VCC of rat specimen D2 mounted on a flat stub. The photomontage illustrates a network of bridging veins and their tributaries (arrows) which drain into the left petrosquamous sinus (asterisks). Macrographs of the same vessels are also illustrated in Figure 39. The location and structure of these vessels are similar to those found on the right hand side of the same VCC, near to the junction between the left petrosquamous and sigmoid sinus (Figure 35), as well as vessels seen in other rat VCCs (Figure 33, Figure 31, Figure 30 and Figure 29).

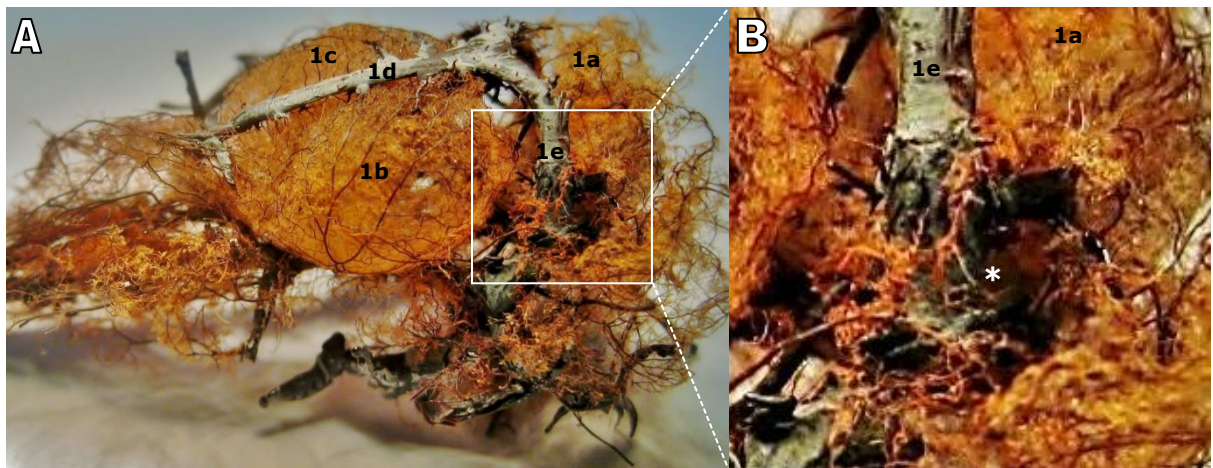
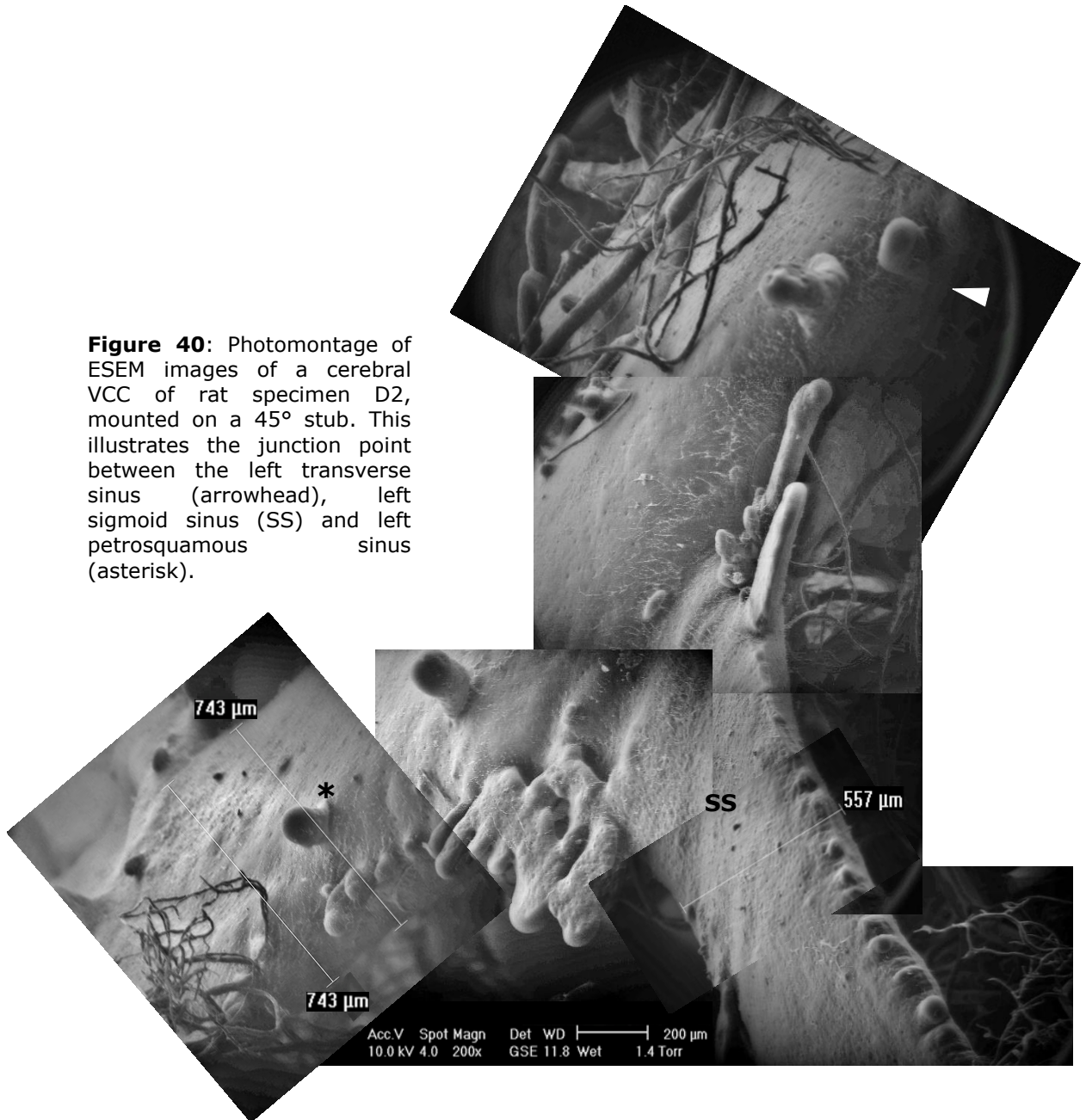


Figure 39: A, B: Macrographs of a cerebral VCC of rat specimen D2 mounted on a flat stub. These images illustrate a network of bridging veins and their tributaries, which drain into the left petrosquamous sinus (asterisk). Here, the cerebellum (1a); left cerebral hemisphere (1b); right cerebral hemisphere (1c); SSS (1d); and transverse sinuses (1e) are illustrated. ESEM images of these vessels are also illustrated in Figure 38.



2.3.2.2. ESEM Imaging of 1mm Coronal Sections of Resin Perfused Brain and Skull

ESEM images of 1mm coronal sections that were acquired from resin perfused rat brain specimens were able to illustrate the detailed structure of the different meningeal layers which lie in between the skull and surface of the brain. These include the outer endosteal dura mater layer which lies adjacent to the skull bone, as well as the inner meningeal layer of the dural membrane. The subdural space can also be seen (artificially created through the process of cardiac perfusion fixation), which lies adjacent to the arachnoid membrane which encloses the subarachnoid vessels. Adjacent to this lies the SAS, which is situated next to the brain tissue. An intradural vessel can also be seen enclosed in between the endosteal and meningeal layers of the dura mater in Figure 41.

Figure 42B and Figure 42C illustrate the great number of subarachnoid vessels that can be seen to lie in the SAS. The size of these subarachnoid vessels differs greatly, with measurements ranging from 45 μm to 121 μm in diameter in these particular images. Importantly, Figure 42A also illustrates a subdural vessel which is approximately 110 μm in diameter, which can be seen to traverse across the SDS to the dural membrane. This vessel can be seen to drain directly into the meningeal layer of the dural membrane, which presumably traverses across the intradural space, before then draining into a venous sinus directly or indirectly via a bridging vein.

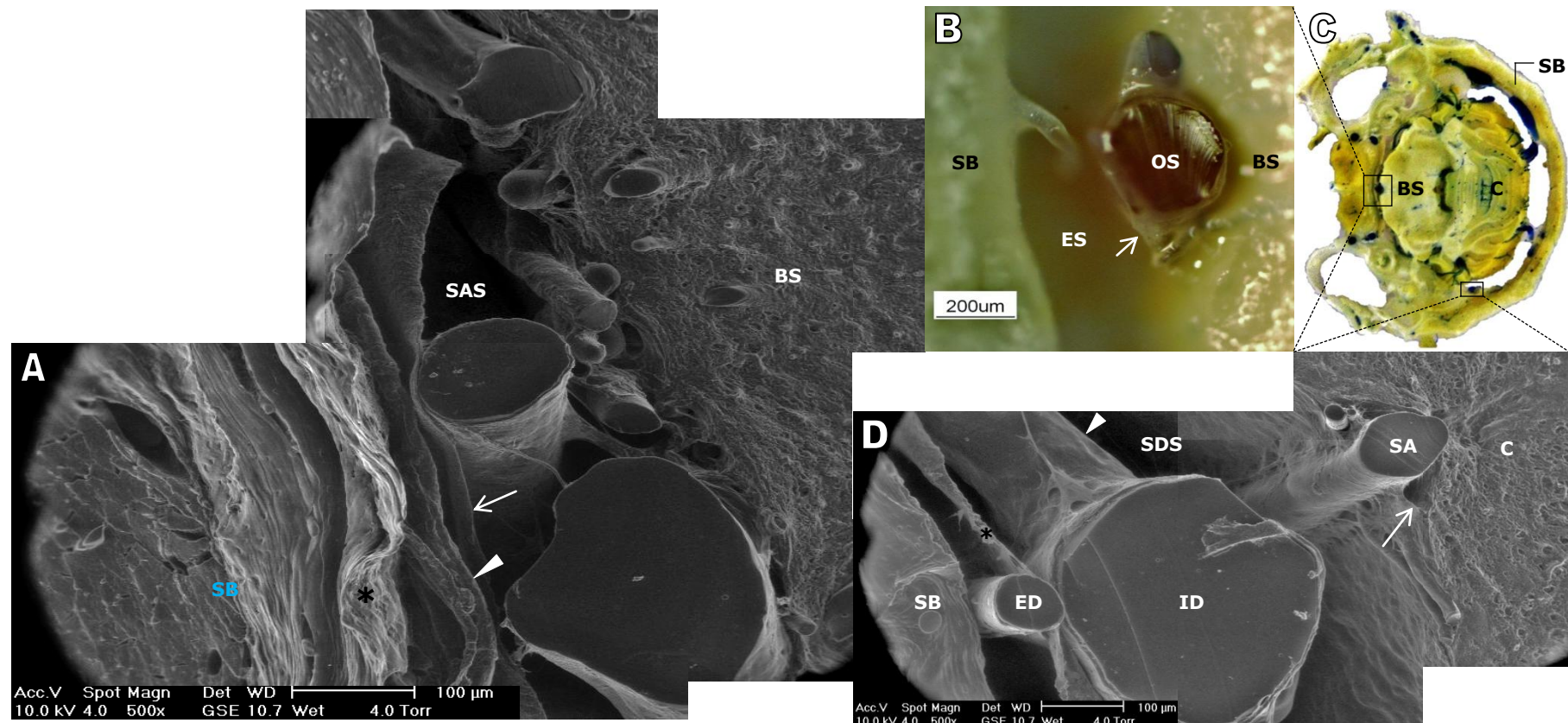


Figure 41: Images of a resin perfused 1mm thick section of Wistar rat D3 brain and skull specimen. These images illustrate the structure of the different meningeal layers which lie in between the skull and surface of the brain. **A:** Photomontage of ESEM images illustrating the skull bone (SB) on the left hand side of the image. Both the endosteal dura mater layer (asterisk) and the meningeal layer (arrowhead) of the dura mater can be seen, situated adjacent to a thin arachnoid membrane (arrow), which can be seen folded around vessels situated within the subarachnoid space (SAS). The brainstem (BS) can also be seen on the right hand side of the image. **B:** Macrograph illustrating the skull bone which lies on the left hand side of the image, with the epidural space (ES) which can be seen adjacent to the occipital sinus (OS) and other surrounding vessels, which are enclosed between the outer periosteal and inner meningeal layers of the dural membrane (arrow). The brainstem can be seen on the right hand side of the image. **C:** Macrograph of a coronal section of resin perfused rat specimen D3. Here, the brainstem; cerebellum (C); and skull bone are illustrated. **D:** ESEM image illustrating the skull bone which can be seen on the left hand side of an epidural vessel (ED) which is enclosed by the endosteal dural membrane. On the right hand side of this, an intradural vessel (ID) can also be seen enclosed in between the endosteal and meningeal layers of the dura mater. Adjacent to this, the subdural space can be seen, which is situated to the left of a subarachnoid vessel (SA), enclosed by the arachnoid membrane. The cerebellum can also be seen on the right hand side of the image.

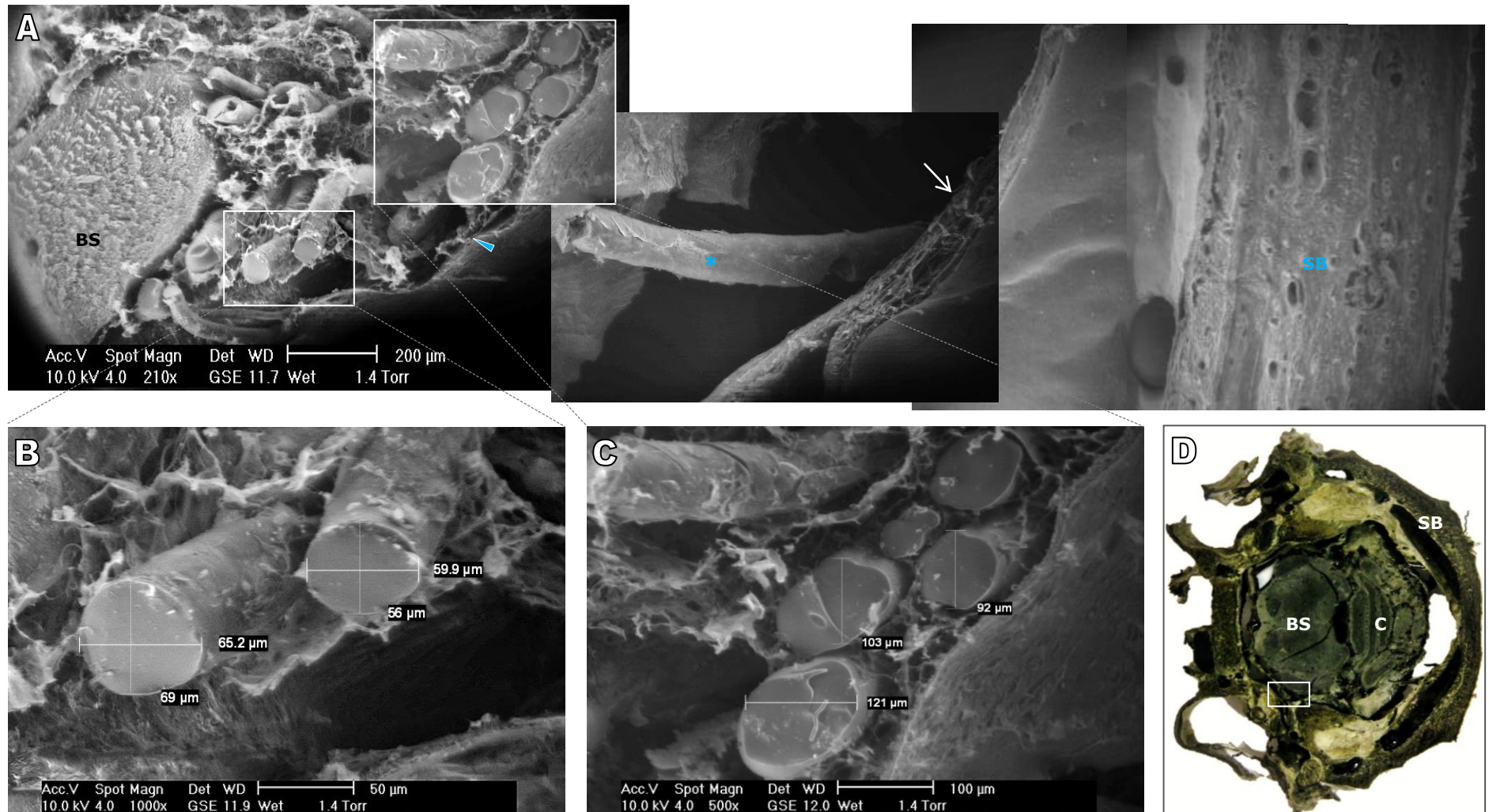


Figure 42: ESEM images of a 1mm thick coronal slice of resin perfused rat specimen C3 section. **A:** A photomontage illustrating the brainstem (BS) seen on the left hand side of the image, as well as the SAS containing vessels of different sizes, covered by the arachnoid membrane (arrowhead). A subdural vessel (asterisk) can also be seen traversing across the SDS to the dural membrane (arrow) and the skull bone (SB). **B, C:** Magnified ESEM images of areas of image A, illustrating the diameter of some of the vessels within the SAS. **D:** Macrograph of rat C3 section. The white box indicates the location in which the structures shown in image A lie in relation to the surrounding anatomy. Here, the brainstem (BS); cerebellum (C); and skull bone (SB) are illustrated.

2.3.3. Histology and Fluorescence Microscopy (FM) Imaging

FM was used to analyse Wistar rat brain tissue perfused with resin containing fluorescent powder, whereby the fluorescent images produced were overlaid onto histological images of H&E stained and DPX mounted 10µm thick histological sections. Figure 43A shows an image of a whole cross-section of a resin-perfused rat brain whereby the fluorescent PU4ii resin which has perfused into the cerebral vessels, can be seen in the fluorescence microscopy image (650nm wavelength), overlaid onto a bright field (BF) microscopy image of the same histological specimen (Leica DM IRB Fluorescence Microscope). Figure 43B shows a magnified image of the area indicated in Figure 43A, which illustrates the general histology of the dural membrane (asterisk), and the various layers of the skull bone (arrows). Figure 43C, Figure 43D and Figure 43E show the same histological specimen at progressively higher magnifications. The fluorescent microscopy images of the resin-perfused vessels (650nm wavelength) are overlaid onto BF microscopy images (510nm wavelength) of the same histological section (Leica DMRB Fluorescence Microscope). Analysis of the anatomical location of the resin perfused vessels (red) show that they appear to be located within the dura mater layer, as the meningeal layer lies immediately medial to the compact (arrows) and spongy (asterisk) layers of the skull bone.

Figure 44A and Figure 44B show a similar result, produced using a fluorescence microscopy (650nm wavelength) image overlaid onto a BF microscopy (grey scale) histological image, however this time using differential interference contrast (DIC) (Leica DM IRB Fluorescence Microscope) in order to obtain a clearer histological image with more of a 3D appearance. Again the resin perfused cerebral vessels seem to be located within the dura mater layer.

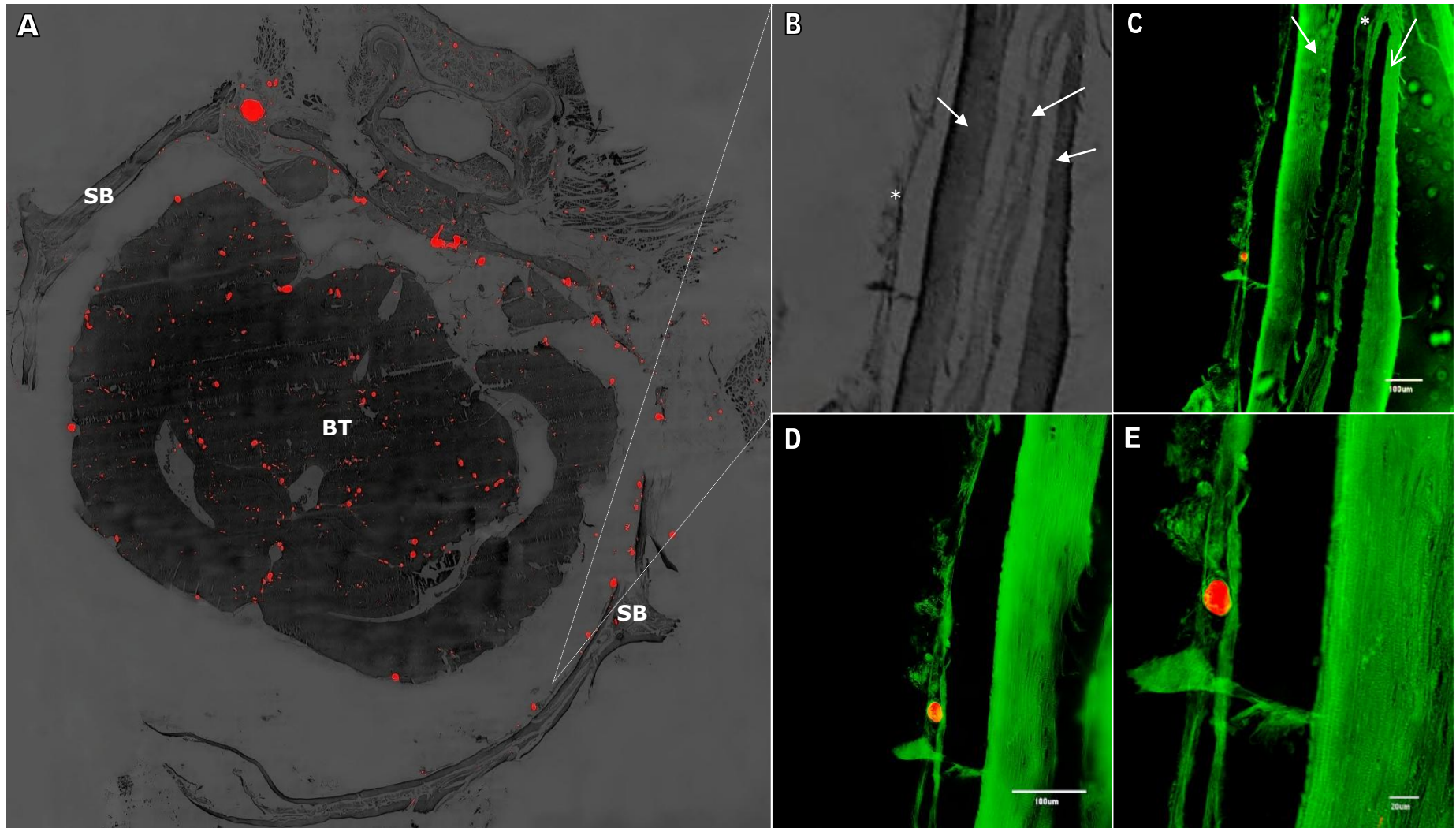


Figure 43: Fluorescent microscopy (FM) images of fluorescent powder-containing resin perfused vessels, overlaid onto histological images of H&E stained, DPX mounted histological sections (10µm thick) of resin perfused Wistar *Rat Specimen Y* skull and brain tissue. **A:** Whole map (coronal section) of the brain tissue (BT) and skull bone (SB) of a PU4ii resin perfused Wistar rat. FM image (red channel) is overlaid onto a BF microscopy (grey scale) histological image (Leica DM IRB Fluorescence Microscope). **B:** Magnified image of the area indicated in image A, illustrating general histology of the dura mater (asterisk) and layers of the skull (arrows). **C:** (x10) FM image (red channel) overlaid onto a BF microscopy (green channel) histological image (Leica DMRB Fluorescence Microscope) of the same area as seen in image B. The resin perfused vessel (red) is located within the dura mater layer, as the meningeal layer lies medial to the compact (arrows) and spongy (asterisk) layers of the skull bone. **D:** Higher (x20) magnification of structures seen in image C. **E:** Higher (x40) magnification of structures seen in image D.

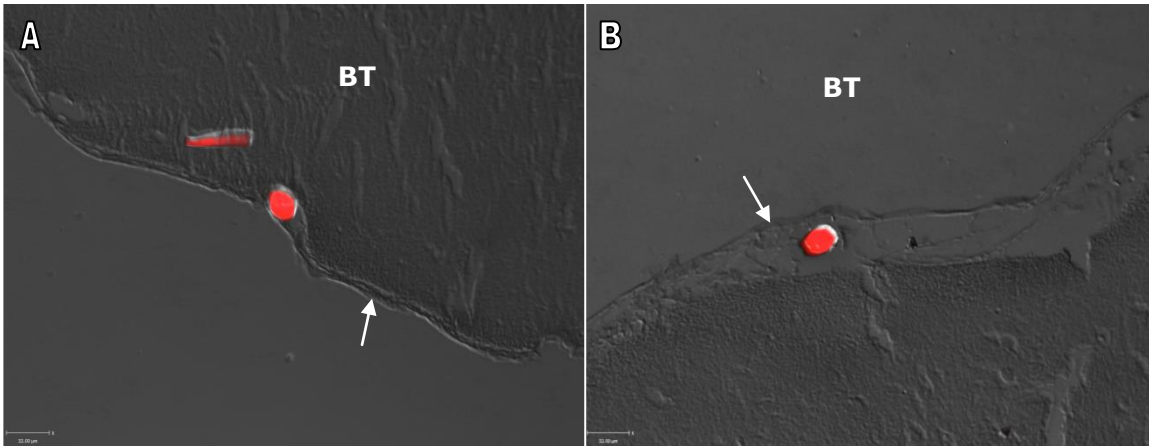


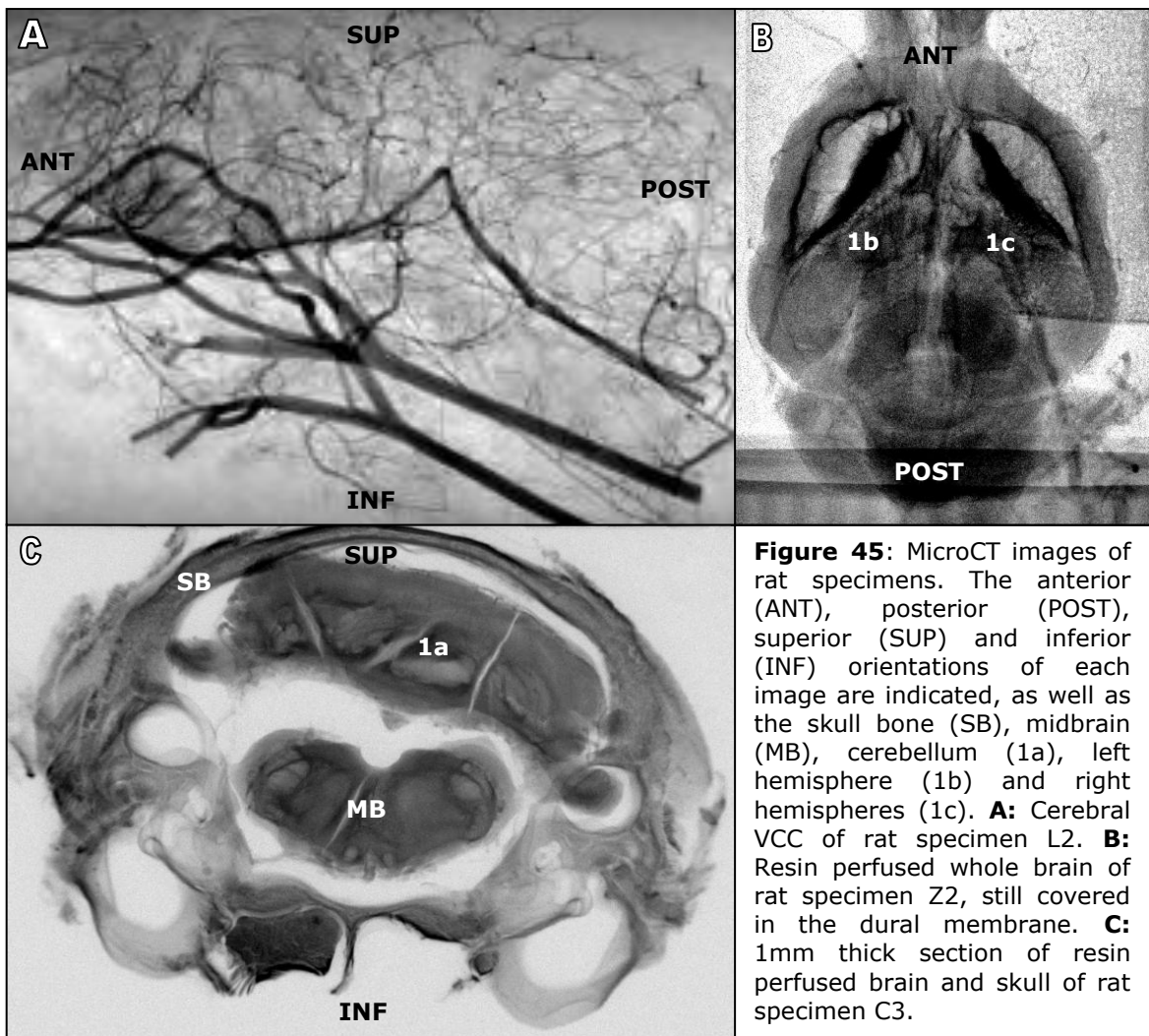
Figure 44: A, B: (x20) Fluorescence microscopy (red channel) image overlaid onto BF microscopy (grey scale) histological image using DIC (Leica DM IRB Fluorescence Microscope) of Wistar *rat specimen Y*. Here the brain tissue (BT) and dural membrane (arrow) are illustrated.

2.3.4. Confocal Microscopy of Resin Perfused Tissue

CM imaging of 1mm thick sections of resin perfused rat brain specimens were carried out using a Leica SP2 confocal laser-scanning microscope (CLSM). However, it was found that even at the maximum capacity of the confocal microscope, the maximum thickness of brain tissue that could be imaged at any one time was too small for purposes required for this project. The machine was therefore unable to facilitate the detailed analysis of the exact morphology and branching patterns of the vessels being investigated; therefore CM as an analysis technique was not pursued any further.

2.3.5. MicroCT Imaging

Figure 45A is a microCT image (SkyScan 1174, Bruker) taken from the imaging dataset of the cerebral VCC of a rat specimen. These microCT projection images were then reconstructed into a video (software provided for SkyScan-1174v2) which provided a 360° view of the whole resin cast specimen. Similar trial microCT scans were also carried out on resin perfused whole rat brain samples still covered in the dural membrane layer (Figure 45B), as well as 1mm thick sections of resin perfused rat skull and brain tissue (Figure 45C).



As can be seen, the most detailed and therefore most suitable microCT scans that were acquired for further analyses were of the macerated cerebral VCCs (Figure 45A). Further microCT scanning of these resin casts were therefore carried out, while altering parameters for further refinement of the microCT imaging protocol, to allow optimisation of the images acquired. These microCT images were then further processed using volume rendering and data analysis techniques, explained further in section 2.3.6.

As can be seen, the microCT scans of the resin perfused whole brain (Figure 45B) and the resin perfused brain sections (Figure 45C) were not particularly successful in terms of being able to depict the finer resin perfused vessels of the brain. This was due to the density of the tissue surrounding the resin cast making it more difficult for the x-rays emitted from the microCT scanner to penetrate through the specimen, and image the resin cast itself. As imaging of these types of samples

was unable to illustrate the fine cerebral vessels in as much detail as was required for this project, these processing techniques for producing non-macerated tissue samples for microCT scanning were pursued no further.

2.3.6. Volume Rendering and Approximating Vessel Size from microCT Imaging Datasets

Figure 46A is a microCT projection image produced from the imaging dataset of the VCC of rat specimen J2. Figure 46B illustrates a 3D reconstructed image of a section of the VCC of the same rat specimen, whereby the 'Simple Neurite Tracer' plug-in for the computer software Image J (NIH) was used for volume rendering of the microCT scanning dataset. The same software was then used to approximate the local thicknesses of the cerebral vessels and categorise them by colour. These measurements are illustrated through use of a calibration bar (Figure 46B), which shows that the larger the vessel diameter, the lighter the colour of the vessel that is indicated in the image. From the measurements taken directly from the microCT projection images, it can be calculated that each increase in one unit on this calibration bar represents an increase in approximately 65 μ m in the vessel diameter.

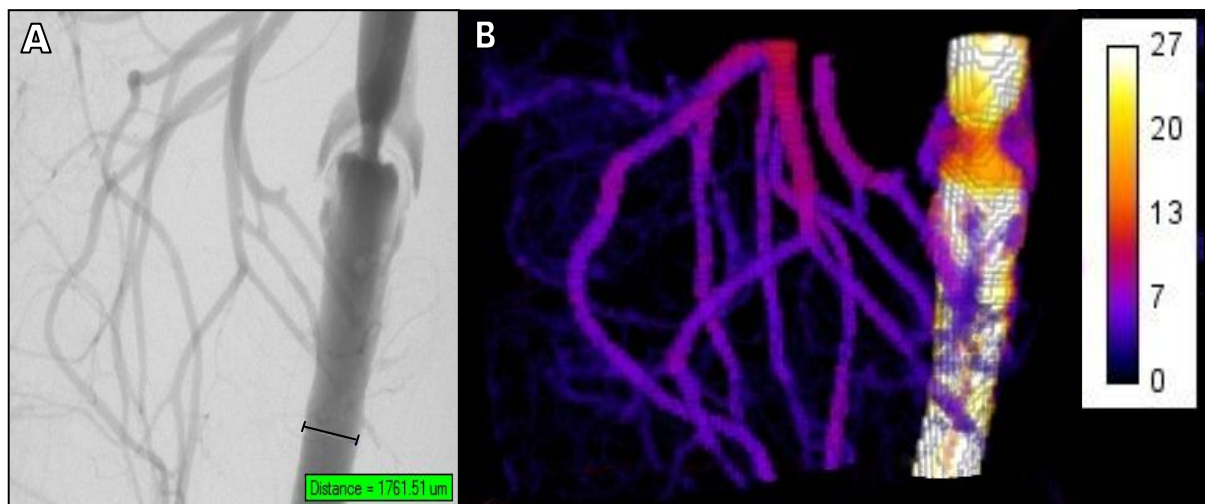


Figure 46: Images of a small section of the VCC of Rat Specimen J2. **A:** MicroCT projection image of a rat VCC. **B:** 3D reconstructed image produced from the microCT imaging dataset of the same rat VCC shown in image A, alongside a calibration bar (whereby 27 on the scale represents a vessel diameter of approximately 2mm, and 0 represents 0mm) indicating the approximate sizes of all the cerebral vessels.

Although this quantitative data is relatively simple, the preliminary results demonstrate that it is possible for further computer analysis of the microCT datasets to be carried out, with further development and application of improved

algorithms enabling further small vein segmentation and detailed analysis of the cerebral vasculature. Details regarding optimisation of these analysis methods are further discussed in section 4.4.

2.4. Discussion

The brain is thought to be one of the most challenging vascular structures to replicate (Lametschwandtner et al., 1984). However, high quality luminal surface replication of the cerebral vasculature was produced by refining the vascular casting protocol described in various other rat VCC studies (Inokuchi et al., 1989; Krucker et al., 2006; Murakami et al., 1992; Szabó, 1995). These PU4ii resin vascular casts were durable enough to withstand maceration using KOH as well as further processing, whilst still maintaining their detailed microvascular structure to allow further imaging and analysis (Giuvarasteanu, 2007; Krucker et al., 2006).

Characteristic features of the resin cast surfaces allowed the larger arterial and venous vessels to be easily differentiated (Giuvarasteanu, 2007; Reina-De La Torre et al., 1998). Venules have a distinctive flattened appearance in contrast to the smoother more rounded appearance of the arterioles (Harrison et al., 2002; Nakai et al., 1981; Reina-De La Torre et al., 1998). Another distinctive feature of arterioles is that the endothelial nuclei leave elongated ovoid depressions in the VCC of the vessels and run parallel along the vessel axis, whereas endothelial nuclei of venous casts consist of more round depressions which are not very well orientated in comparison (Krucker et al., 2004; Nakai et al., 1980; Toribatake et al., 1997). These morphological findings were consistent with the ESEM images acquired from the VCCs as illustrated in Figure 23.

However, although examining vessel morphology is a good indicator for distinguishing between larger arterioles and venules, this does not necessarily apply to the small calibre vessels being investigated in this study. The vascular casting protocol used for this project involved filling the entire vascular bed with resin by perfusing it from the arterial vessels into the venous system via the capillaries. Due to the lack of spatial orientation, it was difficult to differentiate between the smaller arterioles and venules using only morphology, as well as distinguishing the point at which the arterial vessels became part of the venous vasculature. It is for this reason that this project took a multimodal approach to analysis of the venous anatomy of the brain, involving MRI imaging, microCT and 3D XRM, gross tissue dissection, histological analysis, FM, CM and EM imaging.

These methods all facilitated the analysis of the cerebral vascular anatomy from a gross morphological perspective, down to a microscopic and ultrastructural scale.

2.4.1. Intradural and Subdural Vessels

BF and FM images were acquired from histological coronal cross-sections taken from fluorescent resin perfused Wistar rat skull and brain specimens (Figure 43 and Figure 44). These images were clearly able to show the anatomical location of the specific (fluorescent) resin perfused vessels located within the layers of the dura mater.

Gross dissection of resin perfused rat material as shown in Figure 20 also illustrates the presence of both intradural as well as subdural vessels in rat specimens.

Furthermore, the ESEM images acquired from the rat vascular corrosion casts (section 2.3.2.) illustrate countless networks of small venules that drain directly into the bridging veins, which then drain into the various different venous sinuses. Bridging veins in this case are described as veins which drain the superficial cerebral vessels, traverse across the pia, arachnoid and dura mater layers, before then draining either directly or indirectly into the cerebral venous sinuses.

As bridging veins traverse across from the surface of the brain to eventually drain into the venous sinuses, they are composed of both a subarachnoid and subdural part as they traverse across the various meningeal layers (Yamashima and Friede, 1984). From the ESEM images, it can be seen that the small venules that drain into the bridging veins are present along the majority of the whole vein. It is likely that these fine venules drain into the bridging veins at both their subarachnoid and subdural parts, thereby implying the existence of both subarachnoid and also subdural veins. However, due to the fact that the meninges have been macerated away in order to allow ESEM imaging of the VCC specimens, this cannot be confirmed using ESEM alone. The multimodal approach used in this study allowing analysis of the same vessels in different animal species, has proven the existence of subdural veins which either drain directly or indirectly into the venous sinuses via bridging veins.

2.4.2. ESEM Imaging of VCCs

One notable finding on analysis of the ESEM images of the rat VCCs was that constrictions could be seen in the walls of some of the venules at the junction point where they drained into either the bridging veins or the dural venous sinuses themselves. These findings are consistent with a number other studies of vessel morphology involving SEM of cerebral VCCs, whereby the features that could be seen were characteristic of vascular sphincters (Anderson and Anderson, 1978; Nakai et al., 1981; Nakai et al., 1989; Reina-De La Torre et al., 1998; Vignes et al., 2007). These constrictions have been found to be more frequent at branching points of arterioles; however they have also been observed in capillaries and venules (Nakai et al., 1981).

It has been suggested that these vascular sphincter-like constrictions are a result of vascular pericytes. These are perivascular cells that wrap around the endothelial cells of capillaries and other small blood vessels, which help to sustain the blood-brain barrier (BBB) (Harrison et al., 2002). It has been suggested that these pericytes have a role in vascular vasoconstriction and it is now widely assumed that these sphincter-like constrictions are involved in fine control of blood flow in cortical capillary beds (Harrison et al., 2002; Kojimahara and Ooneda, 1980).

Aminergic nerve terminals located adjacent to the basement membranes of cerebral blood vessels and capillaries have been illustrated using EM (Itakura et al., 1977). It has been suggested that a possible regulatory mechanism may therefore involve the vascular endothelium detecting local changes in blood flow, which would trigger the release of local chemical factors or metabolic factors (Reina-De La Torre et al., 1998) controlling vasoconstriction. These substances would then target the pericytes or smooth muscles within the vessel walls, which would induce vascular constriction or relaxation, thereby controlling vessel calibre and blood flow (Toribatake et al., 1997). As pericytes have been shown to be located primarily at the site of branching in capillaries it has been suggested that pericytes therefore control vasoconstriction in a similar way to smooth muscle cells in the arterioles (Gaudio et al., 1990). This suggests that in addition to arterioles, both cerebral capillaries and venules are able to alter their diameter in order to control cerebral blood flow (Nakai et al., 1981).

SEM and ESEM images of the rat VCCs consistently showed incompletely filled bridging veins as well as their tributaries. This is unlikely to be due to a flaw in the resin perfusion process causing incomplete filling of the vessels, as much finer

vascular networks had been perfused with resin in the same experiments. One explanation is that activation of the sympathetic nervous system (SNS) immediately before, or during resin perfusion into the vascular system could activate the vasoconstriction mechanism described above, therefore preventing adequate perfusion through the bridging veins and their tributaries to produce complete vascular casts. This may also explain why in some experiments, the venous sinuses in particular were not filled with resin, while surrounding fine calibre vascular networks had been perfused completely.

It is important to note however that this same mechanism may also mean that the fine subdural vessels hypothesised to be the source of SDH in cases of NAHI could also vasoconstrict in response to SNS activation following vessel rupture, and therefore limit bleeding, at least for a time. This may contribute to the reason why during surgical procedures, accidental tearing of a bridging vein commonly leads to a substantial amount of bleeding; however manual dissection into the subdural space around the occipital lobe and cerebellum does not always cause significant haemorrhaging (MacArthur, 2014). Considering the large number of fine subdural venules that have shown to be present in these areas, significantly more haemorrhaging might be anticipated following dissection into the SDS, however this vasoconstrictive mechanism may help to further explain the small volume of thin-film blood often seen in cases of NAHI.

Chapter 3. Investigating Venous Anatomy in the Human (*Homo sapiens*)

3.1. Introduction

Further investigation into the cerebral venous anatomy of the human is critical. This is because any anatomical information that is discovered in the other species investigated in this project such as rats, marmosets or macaques will always be referred back to, and compared with that of the human. The reason for this, is that vital information regarding the anatomical location of the source of intracranial bleeding in cases of accidental and NAHIs, as well as information regarding exact morphology of the structures involved, can only ultimately be answered through a human model. Humans are the species in which it is most important to establish a well-defined mechanism for the causation of intracranial haemorrhaging found in cases of traumatic head injuries.

Due to the common occurrence of intracranial bleeding caused by traumatic head injuries, investigation into the mechanism that explains this haemorrhaging is on-going, and has been of public as well as scientific concern for many years. Detailed investigation into the cerebral venous anatomy through the use of human material has the potential to have a particular benefit in possible infantile abuse cases, however also has the prospect of impacting upon societal health as a whole, thereby encompassing people of all ages.

3.2. Materials and Methods

Ethical approval was obtained in accordance with the Human Tissue Act 2004, for the use of cadaveric material in investigating the human anatomical structure of the venous drainage of the brain, as part of this project.

3.2.1. Perfusion Fixation and PU4ii Resin Perfusion of Fresh Cadaveric Material

3.2.1.1. Calculation of the Cerebral Blood Volume (CBV) of an Adult Human

The total cerebral blood volume (including water) of an adult human can be calculated using the following equations:

2.85±0.97 ml/100g (Elwell et al., 1994) or **3.05±0.77 ml/100g** (Leung et al., 2006).

The upper limit of the total CBV calculated from both equations is 3.82ml/100g. Given that the brain is approximately 1500g in weight, it can be calculated that perfusion of a minimum volume of 57.3ml of resin into the cerebral vessels should completely fill the cerebral vasculature of the cadaveric specimen.

However the resin that would perfuse into the skin, muscles and skull, as well as some of the blood vessels in the neck had to be taken into account. This is reflected in the volume of PU4ii resin used during perfusion of the cadaveric head. The calculated CBV was increased by a factor 6, so 360ml of PU4ii resin was perfused into the specimen.

3.2.1.2. Perfusion Fixation and PU4ii Resin Perfusion of Fresh Cadaveric Material

Perfusion Fixation

Decreasing the post-mortem interval to as little as possible before tissue fixation, as well as excluding individuals affected by traumatic or degenerative cerebrovascular conditions, should decrease the amount of artefact found within the cadaveric tissue. Therefore cadaveric material (obtained within 7 days of death and whereby the cause of death was not due to traumatic head injury or cerebral degenerative causes) was immediately fixed with embalming fluid for a duration of 24 hours, while making sure to fix the brain thoroughly. This was done by carefully cannulating the common carotid arteries bilaterally and perfusing the fixative into the cerebral vasculature at high pressure (10-15 psi).

PU4ii Resin Perfusion

The methodology for carrying out PU4ii resin perfusion in the cadaver was similar to that carried out in the rat specimens. However as fixation of the tissue had already been carried out, the apparatus used for resin perfusion was a lot more simple than that illustrated in Figure 19. Two World Precision Instrument AL-1010 Dual Pumps were connected via silicone tubing to two cannulas, which were inserted into each carotid artery of the cadaver, before perfusion of 360ml of PU4ii resin (mixed with blue fluorescent powder) was carried out at a rate of 60ml/min. Following perfusion, the resin was then left to cure over a period of 48 hours at

room temperature. Further information regarding mixing of the resin components as well as the resin perfusion procedure is detailed in Figure 47.

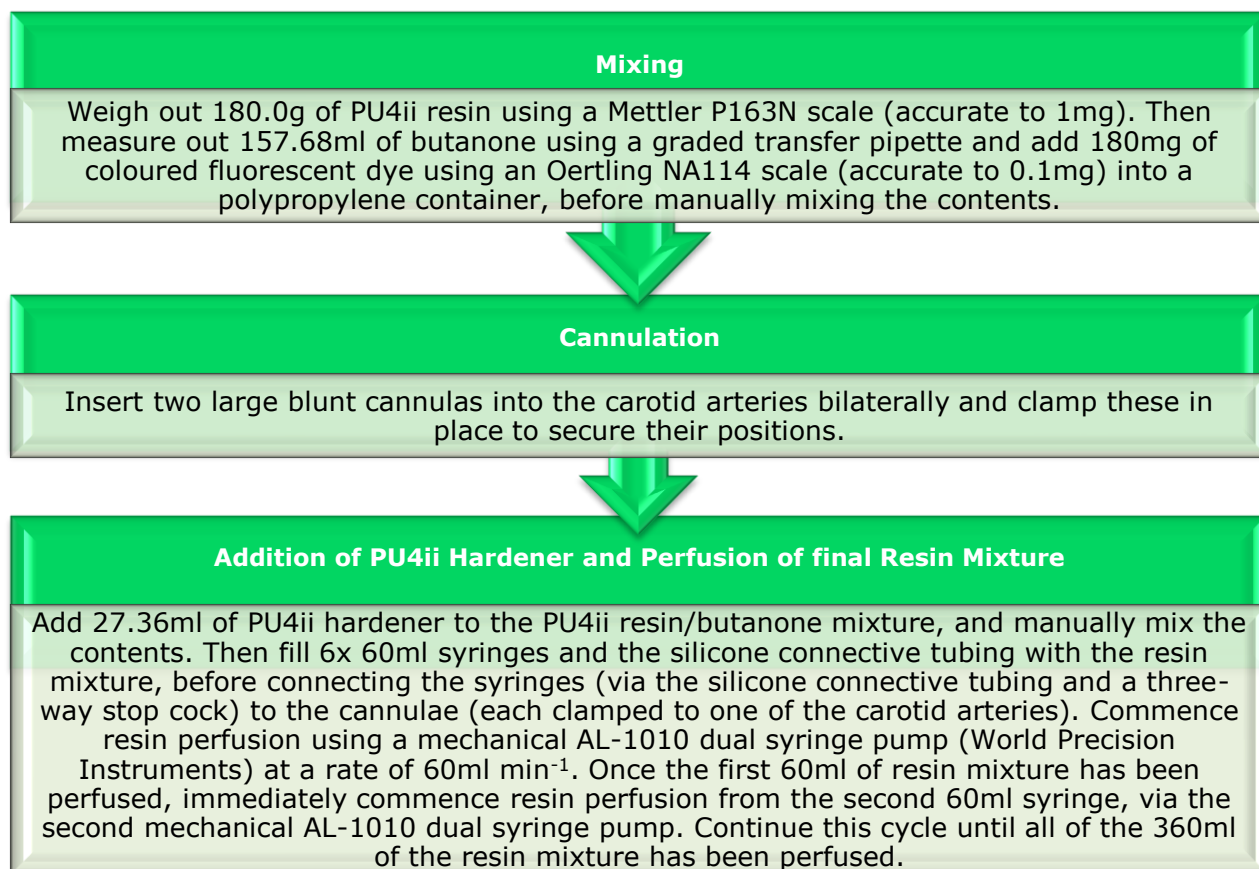


Figure 47: Method for PU4ii Resin Perfusion (containing coloured fluorescent dye) of a Cadaveric Specimen.

3.2.2. Gross Dissection of Cadaveric Material

Gross tissue dissection of the cerebral vessels was carried out on cadaveric material in order to determine the anatomical structure of the layers of the human skull, meninges and brain. This could then be correlated to the overall anatomy of the brain *in situ* from the MRI imaging data taken from a number of healthy volunteers.

3.2.3. Histological Evaluation of Prefixed and Resin Perfused Cadaveric Material

Although cadaveric material was adequately fixed for gross dissection, fixation of the tissue was not sufficient for the material to undergo further processing such as

EM imaging (see section 3.3.2.). However histological processing and analysis of the cadaveric material could be carried out using standard light microscopy (LM). This therefore allowed the same specimens to be imaged on a microscopic as well as a macroscopic scale.

Carefully selected and dissected out tissue samples were first embedded in wax before being sectioned into 15µm slices and stained with haematoxylin and eosin (H&E), to produce histological slides. Images of these whole slide sections were then acquired using a NanoZoomer Digital Slide Scanner (Hamamatsu) to obtain an overall view of the structure of the tissue samples. Higher magnification images of the same tissue samples were then taken using a Leica DM4000 B light microscope (Leica Microsystems), a digital camera (MicroPublisher 3.3 RTV, QImaging) and specialised software (Openlab), to allow further detailed analysis of these samples.

Further supplementary information regarding the protocol for tissue processing and wax embedding of pre-fixed tissue for histology; microtome sectioning of wax-embedded tissue; staining of tissue with H&E and cover-slipping prepared histology slides are detailed in Appendices 10, 11 and 12.

3.2.4. MRI Imaging of Pre-fixed Cadaveric Material

MRI imaging was carried out in order to gain a better understanding of the overall cerebral vascular anatomy in situ, in relation to the normal surrounding anatomical structures. Preliminary MRI scans of prefixed human cadaveric material, using an Achieva 7.0 Tesla MRI scanner (Philips), were first carried out to determine whether bridging veins or even smaller vessels than these could be detected in human cadaveric material. The advantage of using cadaveric material is that scans carried out using these specimens can be as long as is required, in order to produce optimal results. However, during *in vivo* scans, the length of time it takes for a patient to be scanned has to be carefully considered.

MRI images of a pre-fixed cadaveric head (removed from the body prior to scanning, to aid transportation from the site of fixation to the site of scanning) were first performed without further processing of the fixed tissue. However, there were issues with adequate visualisation of the fine vessels surrounding the meningeal layers of the brain, due to entry of air emboli into the tissue.

MRI scans were therefore repeated after injection of the MRI contrast medium Gadolinium (Gd) into the head, via the carotid arteries bilaterally. Six litres of fixative was also perfused prior to the Gd, through the cerebral vessels at high pressure in order to flush out as much residual air emboli as possible. The MRI scans produced were clearer than in previous scans. However due to enlargement of the subdural space (during the 1 year period in which the cadaveric material had been left to fix); complete removal of all of the air emboli, including air trapped within the expanded subdural space, was not possible. Furthermore, the lack of contrast between the Gd and the trapped air meant that vessels containing any air could not be seen.

Further scans were therefore carried out following flushing out of all of the previously injected contrast medium, and perfusing the vessels with distilled water. In theory the contrast produced between the water and the trapped air within the expanded subdural space should allow visualisation of the water-filled vessels and the surrounding air-filled subdural space. However, due to a combination of the vessels being filled with air emboli; interference of the fixed material with the MRI signals; and possible damage of some of the fine subdural vessels due to continued perfusion of fluid through the vascular system at high pressure, the quality of the MRI scans produced was not sufficient for use. Despite this in some of the MRI images that were produced, fine structures were seen to traverse what was thought to possibly be the subdural space. Therefore it was determined that carrying out MRI scans of the human head *in vivo* would circumvent these problems caused by tissue fixation and dissection of the scanned material.

3.2.5. MRI Imaging of the Human Head *in Vivo*

Various different imaging sequences were trialled during MRI scanning of a number of healthy volunteers (multiple scans were carried out on 5 different volunteers in total), in order to optimise the quality of images produced by specifically targeting the detection of small veins around the meningeal layers of the brain. Scans were carried out both in the prone and supine position, as well as a range of ages of volunteers scanned (age range: 22-87 years) so that the anatomical variations between younger and older individuals could be compared.

Scanning in the supine position was preferred over the prone position, as the movement of the chest during inhalation and exhalation caused excess movement of the head during scanning. Furthermore, additional discomfort caused during

scanning in the prone position meant that scan times could only be extended to 15 minutes or less, compared to scan times of 1 hour or more in the supine position.

MR imaging of a wide age range of volunteers was carried out, however it was determined that MRI scanning of elderly volunteers would allow images of fine intracranial surface vessels to be more easily identified and acquired. This is due to the fact that unlike many other animals (Sherwood et al., 2011) the volume of the normal human brain shrinks in size with increasing age (Raz et al., 2005; Sowell et al., 2003). This shrinkage in brain size as an individual grows older is caused by loss of brain tissue as a result of atrophy, which means that the space in between the skull and brain surface becomes larger as the brain gradually shrinks back from the surface of the skull. This is evident in MRI scans of older volunteers, where widening of sulci and an increase in CSF spaces can be seen around the brain, which means that the likelihood of detecting vessels traversing between the meningeal layers and surface of the brain should be greater.

3.2.6. Small Vein Segmentation using MRI Data

Segmentation algorithms focussing on small veins at the surface of the brain were applied to the *in vivo* human MRI data that was acquired. This was able to produce some preliminary results whereby the small cerebral surface vessels could be highlighted using an assigned colour, to allow these fine vessels to be more easily distinguished from similar surrounding structures.

Cadaver (<i>Homo sapiens</i>) Specimen	Gender (M/F)	Procedure	Investigation
A	F	MR Imaging of the sample perfused with fixative only. Vessels were then perfused with Gadolinium (Gd) and MR images of the sample were again acquired; vessels were then perfused with water, before scans were again repeated.	MRI (7.0 Tesla scanner). Gross dissection, photographs (macrographs).
B	M	Perfusion fixation followed by decalcification solution for 14 days at 37°C.	Gross dissection.
C	M	Perfusion fixation.	Gross dissection, photographs (macrographs and micrographs). Produced histology sections using a microtome, which were H&E stained and analysed using LM.
D	M	Perfusion fixation via the carotid arteries bilaterally, followed by resin perfusion.	Gross dissection, photographs (macrographs).

Table 2: Experimental cadaveric specimens used during the study. The main use of these specimens was to dissect out and therefore illustrate the anatomical structure of the cerebral anatomy, while demonstrating the similarities in anatomical structure with that of rat and primate material. The table also details how the tissues were further processed and analysed.

Homo sapiens specimen (in vivo)	Gender (M/F)	Age (Years)	Procedure
A	F	22	MRI imaging (7.0T scanner) – in the supine and prone positions. Various scans were tested.
B	F	48	MRI imaging (7.0T scanner) – in the prone position.
C	F	78	MRI imaging (7.0T scanner) – in the supine position.
D	F	87	MRI imaging (7.0T scanner) – in the supine position.
E	F	27	MRI imaging (7.0T scanner) – in the supine position.

Table 3: In vivo human (*homo sapiens*) volunteers used during the study. These volunteers were used for MRI imaging of the head and brain.

3.3. Results

3.3.1. Gross Dissection of Pre-fixed Cadaveric Material

Human cadaveric material (*Homo sapiens*) was dissected to illustrate bridging veins and subdural veins traversing the subdural space in between the right occipital lobe and the superior surface of the tentorium cerebelli (Figure 48A and Figure 48B) in *cadaveric specimen A*, as well as in between the inferior part of the tentorium cerebelli and the superior part of the cerebellum (Figure 48C and Figure 48D) in *cadaveric specimen C*.

The subdural vessels and bridging veins shown in Figure 48 can be seen traversing from the surface of the brain (indicated by 'ROL' in images A and B, and 'C' in images C and D) still covered in the arachnoid membrane, across the subdural space (SDS), before penetrating the tentorium cerebelli (TC) which is composed of the dural membrane. The subdural spaces in these specimens were created artefactually through a combination of factors including the fixation. This process initially caused the potential space to be opened up to form a SDS by the separation of the arachnoid membrane (which is still adherent to the pial membrane and surface of the brain) away from the dural membrane. This was due to shrinkage of the brain itself, caused by fixation of the tissue as well as lack of CSF present within the subarachnoid space which caused the arachnoid membrane to separate away from the dura. The vessels traversing the SDS were then further exposed via careful manual dissection of the tissue, to allow illustration of the vascular anatomy via macrographs as shown below (Figure 48 and Figure 49).

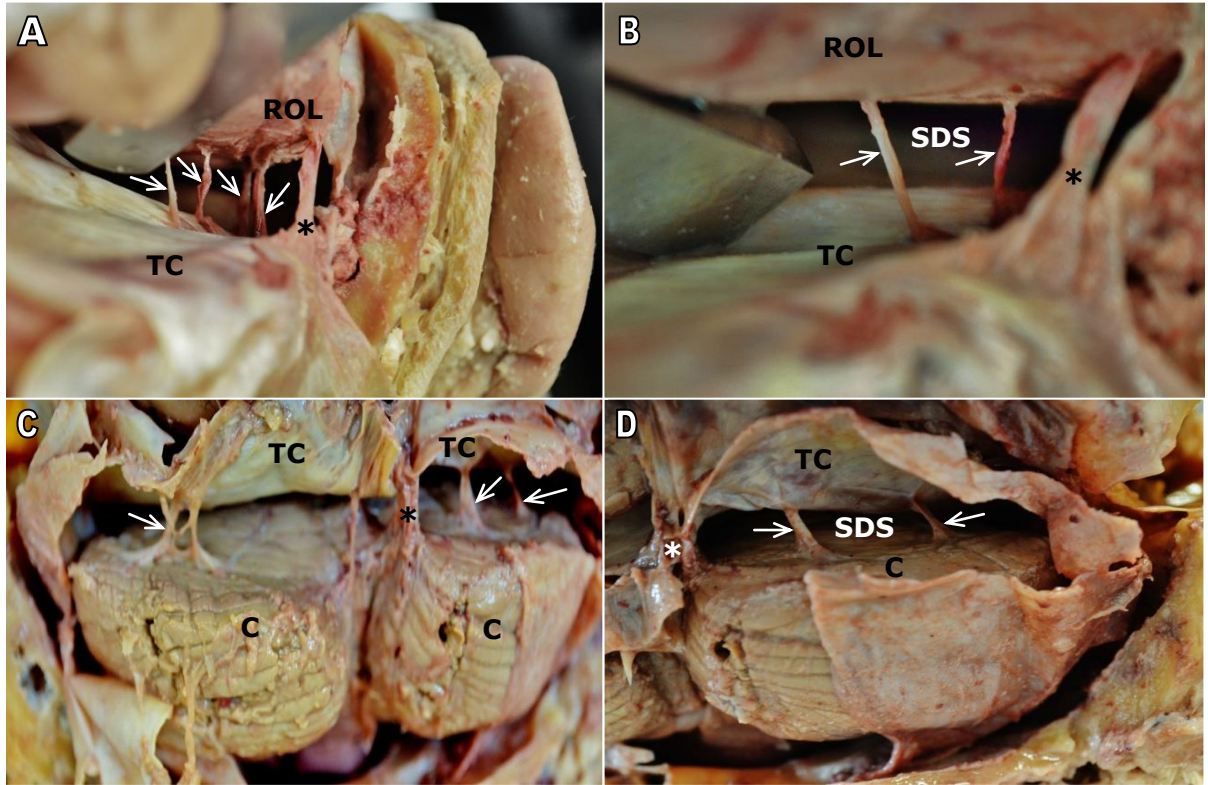


Figure 48: Human cadaveric material (*Homo sapiens*). Images A and B are taken from dissections of cadaveric specimen A, and images C and D are acquired from dissections of cadaveric specimen C. Bridging veins (asterisks) and subdural vessels (arrows) traversing the subdural space (SDS) are indicated in each image. **A:** Bridging veins and subdural vessels located in between the right occipital lobe (ROL) and the superior surface of the tentorium cerebelli (TC). **B:** Macrograph of the same subdural vessels as seen in image A. **C:** Bridging and subdural veins located in between the inferior part of the tentorium cerebelli (TC) and the superior part of the cerebellum (C). **D:** Macrograph of the same subdural vessels as seen in image C.

3.3.2. Resin Casting and Gross Dissection of Resin Perfused Cadaveric Material

Following perfusion fixation and PU4ii resin perfusion of cadaveric specimen D, although staining of the peripheries (such as the skin of the face and neck) with coloured fluorescent dye was evident, the resin did not seem to have penetrated the cerebral vasculature of the specimen as well as expected. This may have been due to the fixation process as, although the cadaveric specimen had been collected as soon as possible post-mortem (within 7 days) and immediately fixed with embalming fluid, this was still enough of a time lag for the tissues to start to undergo decomposition, as well as allowing the vessels to flatten and blood to clot within the vasculature. This is not usually an issue for the normal embalming process for cadaveric material, however, for purposes of this project, the time in between death and fixation of the specimen is critical in being able to produce high quality detailed vascular casts.

Resin perfusion of the cadaveric material was successful in penetrating the larger venous sinuses and bridging veins. However, the smaller vessels draining into these bridging veins (or draining directly into the dural membrane surrounding these bridging veins) that were shown via gross dissection were not filled with resin, and therefore this tissue could not undergo further microCT or FM analysis.

It may be possible to apply for ethical approval that will allow cadaveric specimens to be obtained immediately after death, and therefore overcome the fixative and resin perfusion issues faced in these experiments. In this project however, the issues that were faced regarding obtaining this material related to strict legal restrictions placed upon bodies donated for medical science and anatomical education, which had to be processed via a strict protocol. This meant that fresh cadaveric material was unable to be obtained immediately after death, due to restrictions of the licences of this project.

3.3.3. Histology - Prefixed and Resin Perfused Cadaveric Material

The cadaveric specimens that were dissected to reveal bridging and subdural veins (Figure 48 and Figure 49) were further processed for histological evaluation. Carefully selected and dissected out tissue samples were first embedded in wax, sectioned at 15 μ m and then stained with H&E to produce histological slides (See Appendices 10, 11 and 12). Images of these whole slide sections were then taken using a NanoZoomer Digital Slide Scanner (Hamamatsu) to obtain an overall view of the structure of the tissue samples (Figure 50A, D and G). Higher magnification images of the same samples (Figure 50B, C, E, F, H and I) were then taken using a light microscope (Leica DM4000 B, Leica Microsystems) to allow further detailed analysis of these samples.

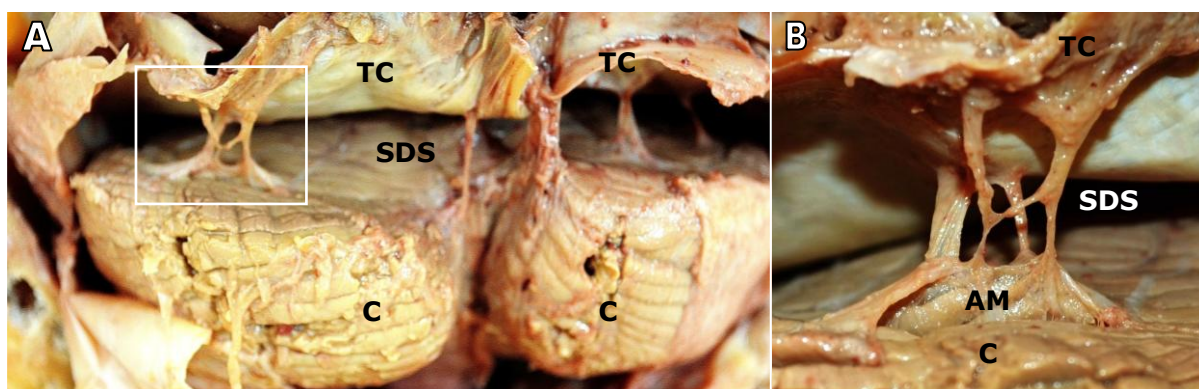


Figure 49: Macrograph of dissected cadaveric specimen C. **A:** A network of bridging veins and subdural vessels can be seen traversing across the subdural space (SDS), draining from the superior surface of the cerebellum (C) still covered by the arachnoid membrane (AM) indicated in image B, to the tentorium cerebelli superiorly (TC). **B:** A magnified image of the same vessels illustrated in image A (white box).

Each row of images illustrated in Figure 50 are micrographs of 3 different histological slices taken at different points through the serial section of the same tissue sample. A, B and C in Figure 50 are different magnification images of slide 111 (taken from serial histological sectioning from the same tissue sample), which illustrates the presence of the dural membrane as well as a network of bridging veins and subdural vessels. D, E and F are different magnification images of slide 101 which illustrate the presence of the bridging veins and subdural vessels without hardly any surrounding brain tissue or dura. G, H and I are different magnification images of slide 11, which illustrate the presence of the cerebellum as well as a network of bridging veins and subdural vessels. From this it can therefore be deduced that these bridging and subdural vessels must drain from the surface of the brain tissue (as seen in Figure 50G, H and I), before then

traversing across both the subarachnoid and subdural spaces (as seen in Figure 50D, E and F) and then finally entering into the dural membrane (Figure 50A, B and C) before draining into the dural venous sinuses.

Through careful histological evaluation of these tissues, it can also be seen that the vessels illustrated in Figure 50C, F and I are veins. Therefore, the vascular structures that were previously revealed via gross dissection of the cadaveric material (Figure 48) are vessels (specifically veins and venules), and not that of other structures such as fascia (connective tissue).

Generally, veins or venules can be distinguished from arteries or arterioles in that they tend to have larger diameters and thinner walls than that of accompanying arterial vessels. They are also often collapsed to varying degrees, compared to the often rounded and patent lumina seen in accompanying arterial vessels. The vessels identified in Figure 50 below are categorised as venules due to their relatively small size and shape (lumen diameter of post capillary venules are often between 5-10 μm , collecting venules between 10-50 μm and small muscular venules between 50-200 μm), as well as the particular layered structure of their walls. The inner endothelial layer (tunica intima) composed of squamous endothelial cells can be seen, along with the thin/almost non-existent middle layer of muscle and elastic tissue (tunica media), and a thin outer layer of connective tissue (tunica adventitia). Arterioles in comparison have a much more developed and thicker muscular tunica media, from which they can be distinguished.

Further analysis of Figure 50 illustrates that the average diameter of the small venule (asterisk) illustrated in Figure 50C is 76 μm (the smallest measurable diameter being 52 μm ; the largest measurable diameter being 100 μm). There are also a number of either small venules or post-capillary venules illustrated in Figure 50F, whereby the average diameter of the vessel indicated by F1 is 57 μm (2 μm ; 112 μm), and the average diameters of F2, F3 and F4 are 177 μm (6 μm ; 348 μm), 52 μm (24 μm ; 80 μm), and 16 μm (8 μm ; 24 μm) respectively. Another small venule (asterisk) with an average diameter of 75 μm (16 μm ; 134 μm) is also illustrated in Figure 50I. All of these veins illustrated in Figure 50 are much smaller in calibre than the diameter of vessels traditionally defined as bridging veins (which drain directly into the venous sinuses) and the thickness of the walls of these standard size bridging veins have been shown to be nearly as thick as the whole diameters of some of the venules illustrated in these images. It can therefore be argued that veins such as these are more likely to be the source of SDH found in cases of

traumatic head injury, rather than the traditionally defined much larger bridging vein structures. This is further discussed in more detail in section 3.4.

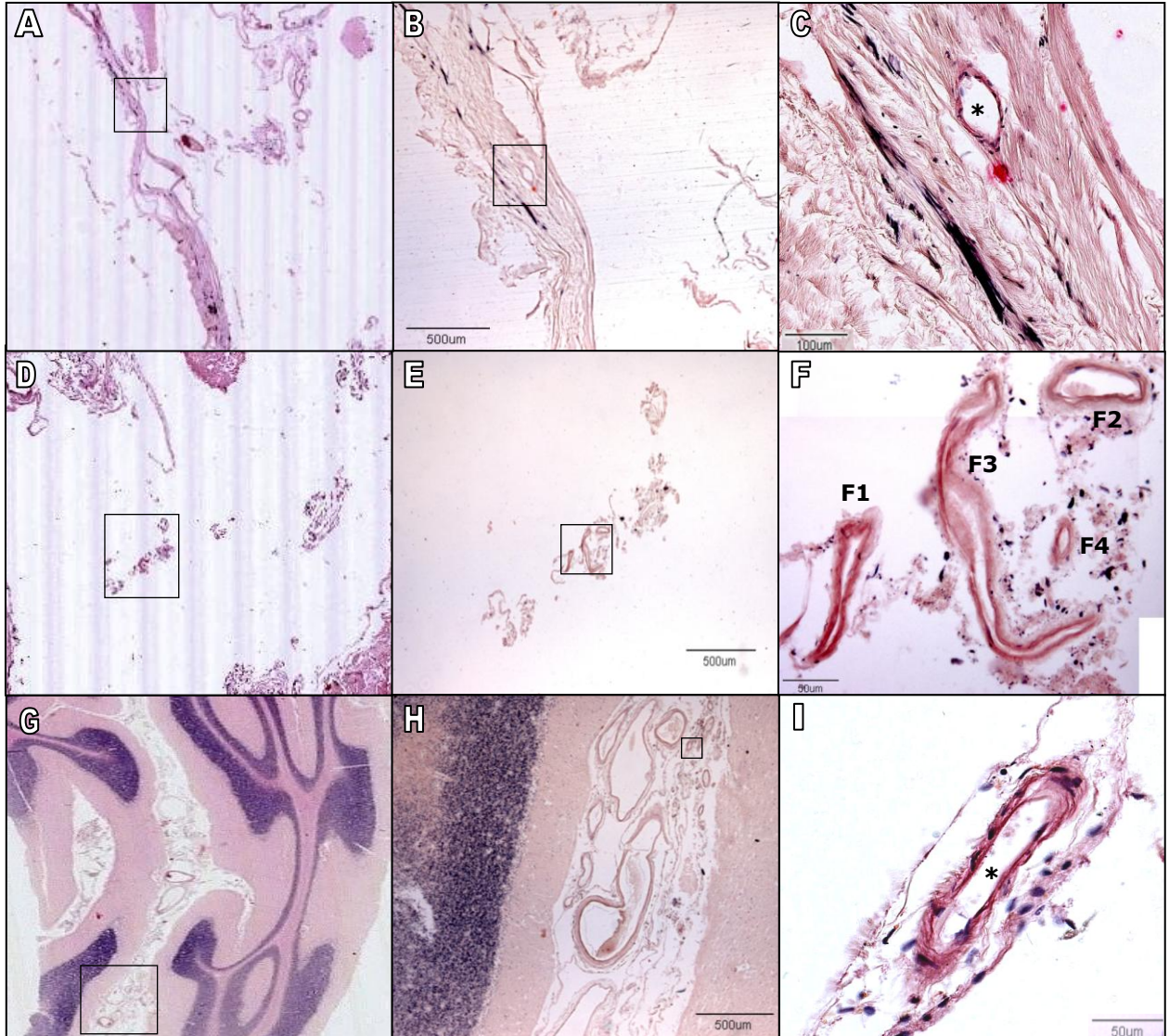


Figure 50: Histological images of cadaveric specimen C (illustrated in the white box in Figure 49) where network of bridging veins and subdural vessels can be seen, traversing across the subdural space from the superior surface of the cerebellum to the tentorium cerebelli superiorly. **A:** Macrograph of the dura and surrounding vessels, Slide 111. **B, C:** LM image of the dura and vessels, Slide 111: x2.5 (area indicated by the black box in image A) and x10 (area indicated by the black box in image B) respectively. **D:** Macrograph of the bridging veins and subdural vessels without surrounding brain tissue or dura, Slide 101. **E, F:** LM image of the bridging veins and subdural vessels, Slide 101: x2.5 (area indicated by the black box in image D) and x20 (area indicated by the black box in image E) respectively. F1-F4 indicate 4 different vessel lumina. **G:** Macrograph of the cerebellum and surrounding vessels, Slide 11. **H, I:** LM image of the cerebellum and surrounding vessels, Slide 11: x2.5 (indicated by black box in image G) and x20 (indicated by black box in image H) respectively.

3.3.4. MRI Imaging of the Human Head in Vivo

Various MRI images of the human (*Homo sapiens*) head *in vivo* were acquired using an Achieva 7.0 Tesla Scanner (Philips), at various different image sequences. MRI scans were carried out on volunteers across a wide age range (between 22 and 87) so that the anatomical variations between younger and older individuals could be compared.

As the volume of the normal human brain shrinks in size with increasing age, MRI scans of older volunteers show how the space in between the skull and brain surface is larger compared to those seen in younger individuals. This is because as the brain atrophies, it gradually shrinks back from the surface of the skull, creating larger CSF spaces around the brain. This is clearly shown in the MRI images that were acquired from scanning of a number of volunteers, a selection of which are illustrated below (Figure 51). Figure 51 illustrates the extent to which the brain has atrophied with increasing age as seen in image C (a 78 year old individual), as compared to image B (a 22 year old individual). Figure 51A is a sagittal section of the brain to show the anatomical point at which both the transverse sections in Figure 51B and C were acquired.

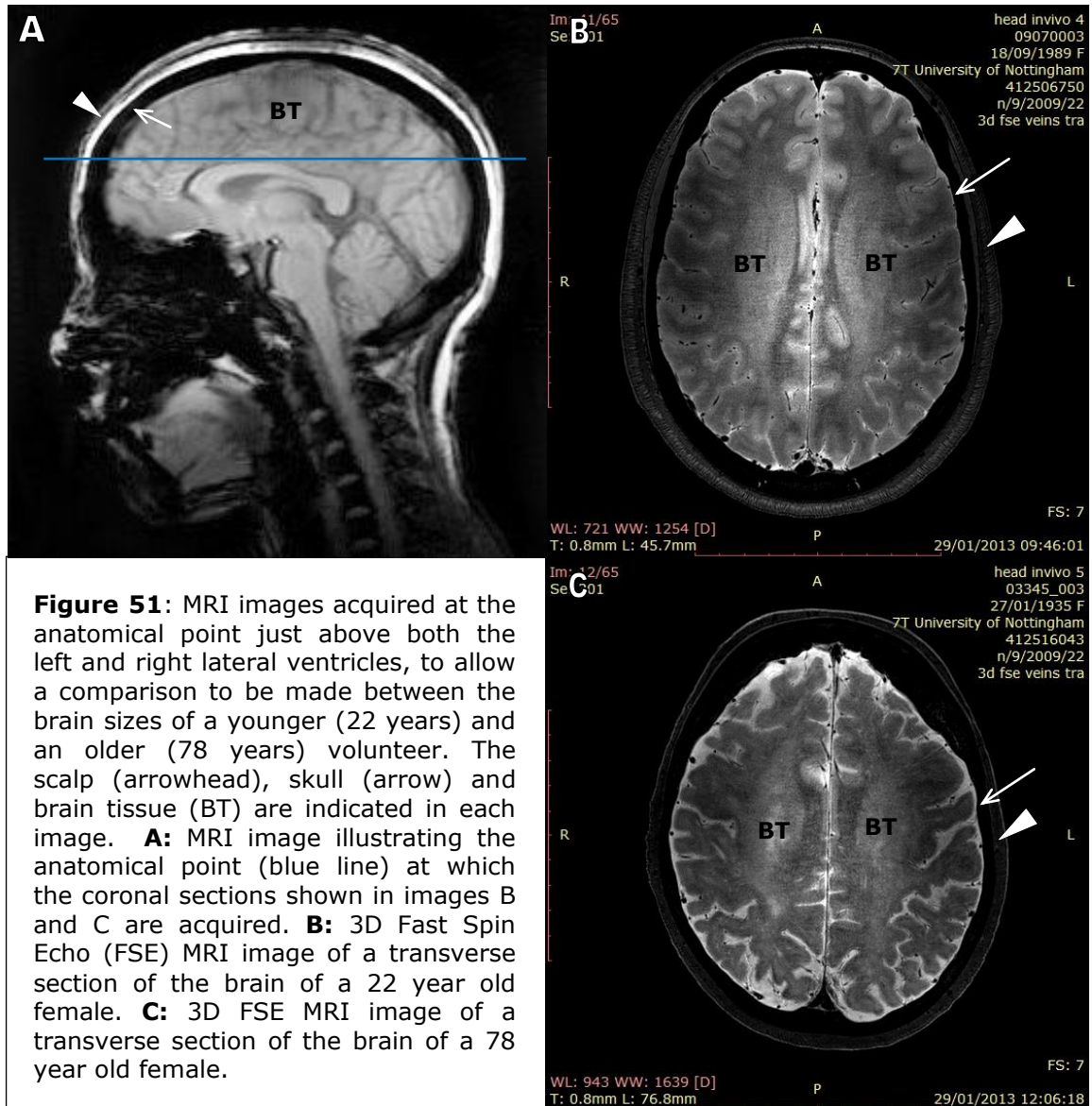


Figure 52 and Figure 53 below show a selection of images that were acquired from a 22 year old individual, whereby 3D Fast Spin Echo (3D FSE) (Figure 52A and Figure 53) and Fast Low Angle Shot (FLASH) (Figure 52B, C and D) MRI sequence imaging were used. These illustrate possible bridging veins, as well as other smaller vessels that are seen to both drain into the SSS, as well as traverse across the meningeal layers (although each individual meningeal membrane cannot be differentiated in these MR images).

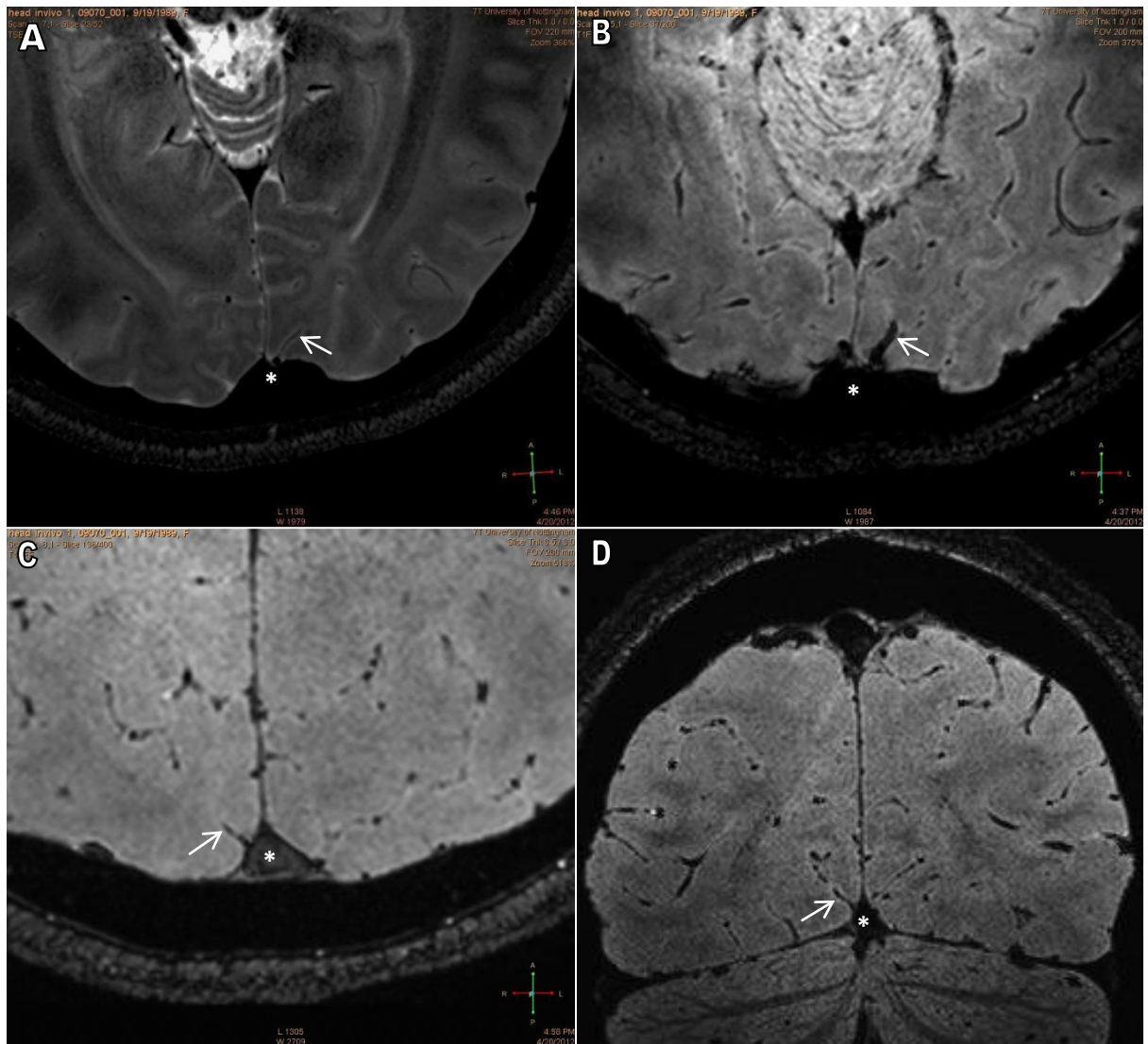


Figure 52: MRI Scan of a human (*Homo sapiens*) head *in vivo* (7.0 Tesla Scanner) of a 22 year old individual. **A:** 3D Fast Spin Echo (FSE) Magnetic resonance imaging (MRI) sequence image of a transverse section of the head illustrating a small calibre vein (arrow) draining into the SSS (asterisk). **B:** Fast Low Angle Shot (FLASH) MRI sequence image of a transverse section of the head illustrating the same small calibre vein (arrow) as seen in image A. **C:** FLASH MRI sequence image of a transverse section of the head illustrating a very small vein (arrow) draining into the SSS (asterisk). **D:** FLASH MRI sequence image of a coronal section of the head illustrating a small calibre vein (arrow) draining into the SSS (asterisk).

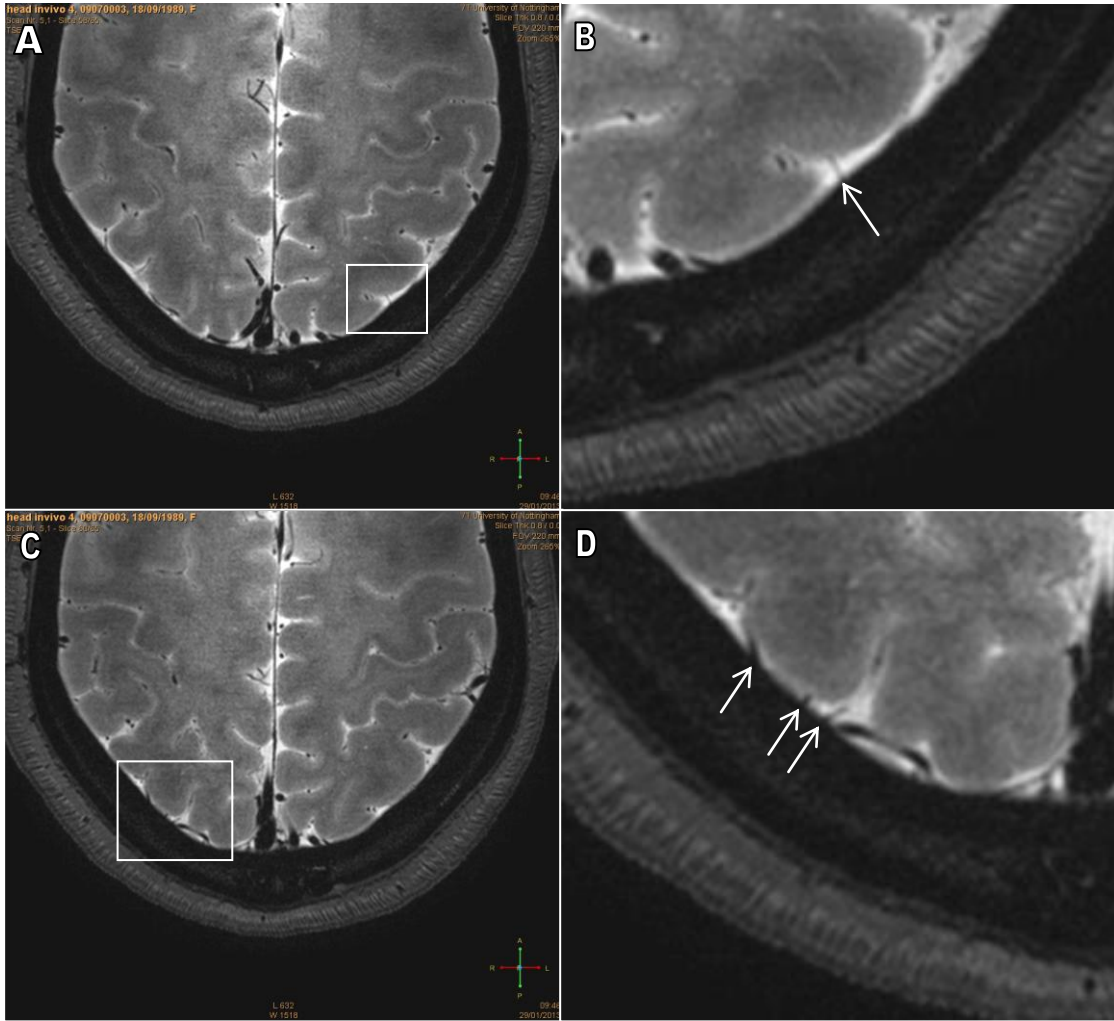


Figure 53: Transverse MRI Scan sections of a human (*Homo sapiens*) head in vivo (7.0 Tesla Scanner) of a 22 year old individual. **A:** 3D FSE MRI sequence image illustrating a fine calibre vessel (white box) seen to traverse across from the cerebral surface through the subarachnoid space to enter the dura. **B:** The same fine vessel (arrow) as illustrated in A. **C:** 3D FSE MRI sequence image illustrating fine calibre vessels (white box) seen to also traverse the subarachnoid space to enter the dura. **D:** The same fine vessels (arrows) as illustrated in C.

Similar vascular structures to those illustrated in Figure 52 and Figure 53 were also found in MRI scans that were carried out on 78 and 87 year old individuals. Figure 54A clearly illustrates a fine vessel that traverses across from the cerebellar tissue and enters the tentorium cerebelli, as has already been shown in previously illustrated grossly dissected cadaveric specimens. Figure 54B shows a venous plexus and bridging vein surrounded by a dural membrane layer, with a small calibre vein draining into this venous plexus inferiorly. Another fine venule is shown to traverse across an arachnoid granulation before draining into the venous plexus, illustrating that this vessel must cross both the arachnoid and dural membranes in order for this to occur. Additionally Figure 54C illustrates a small calibre vessel entering directly into the SSS through the dural membrane, similar to those vessels demonstrated in Figure 52.

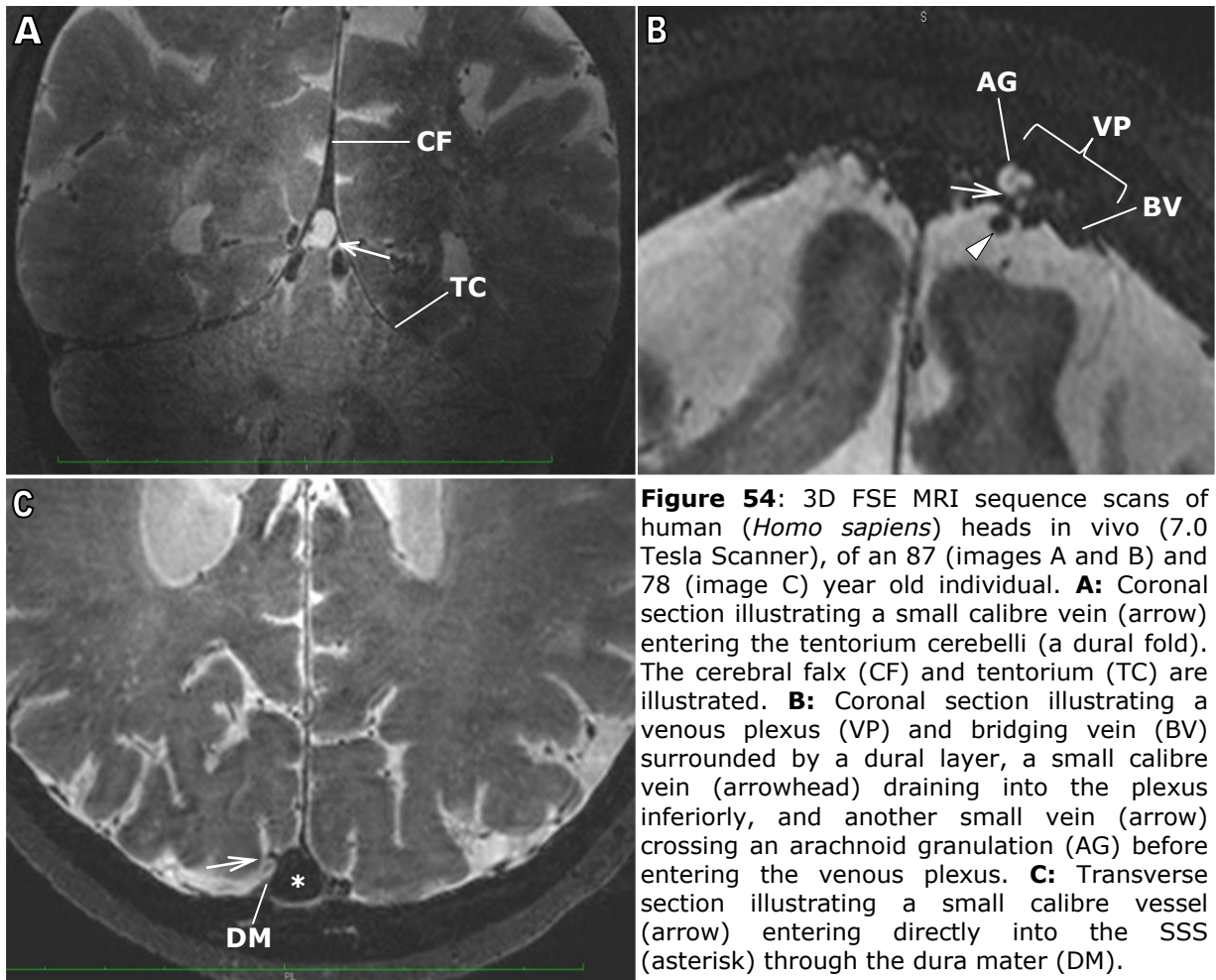


Figure 54: 3D FSE MRI sequence scans of human (*Homo sapiens*) heads in vivo (7.0 Tesla Scanner), of an 87 (images A and B) and 78 (image C) year old individual. **A:** Coronal section illustrating a small calibre vein (arrow) entering the tentorium cerebelli (a dural fold). The cerebral falx (CF) and tentorium (TC) are illustrated. **B:** Coronal section illustrating a venous plexus (VP) and bridging vein (BV) surrounded by a dural layer, a small calibre vein (arrowhead) draining into the plexus inferiorly, and another small vein (arrow) crossing an arachnoid granulation (AG) before entering the venous plexus. **C:** Transverse section illustrating a small calibre vessel (arrow) entering directly into the SSS (asterisk) through the dura mater (DM).

3.3.5. Small Vein Segmentation using MRI Data

Segmentation algorithms focussing on small veins at the surface of the brain were applied to the *in vivo* human MRI data that was acquired to produce some preliminary results. These contrast based algorithms allowed the fine cerebral surface vessels to be highlighted using an assigned colour, to allow them to be more easily distinguished from similar surrounding structures.

The left hand column in Figure 55 displays images acquired from different views (sagittal, coronal and transverse sections from top to bottom) of the same original MRI head scan dataset. The right hand column illustrates the results of small vein segmentation after non-local means filtering (removal of any background noise whilst maintaining contrast in the areas of interest, in this case the veins) was applied to the same MRI data as shown in the left hand column. The segmented small veins are shown in red. In these filtered images it can also be seen that a relatively well-defined thin red band is segmented all around the brain. This may indicate a large number of localised fine veins in this area; however it may also be an artefact. This is not yet known due to the nature of these newly developed algorithms; however this is an area in which further work and fine-tuning of the protocol could be carried out in order to determine this.

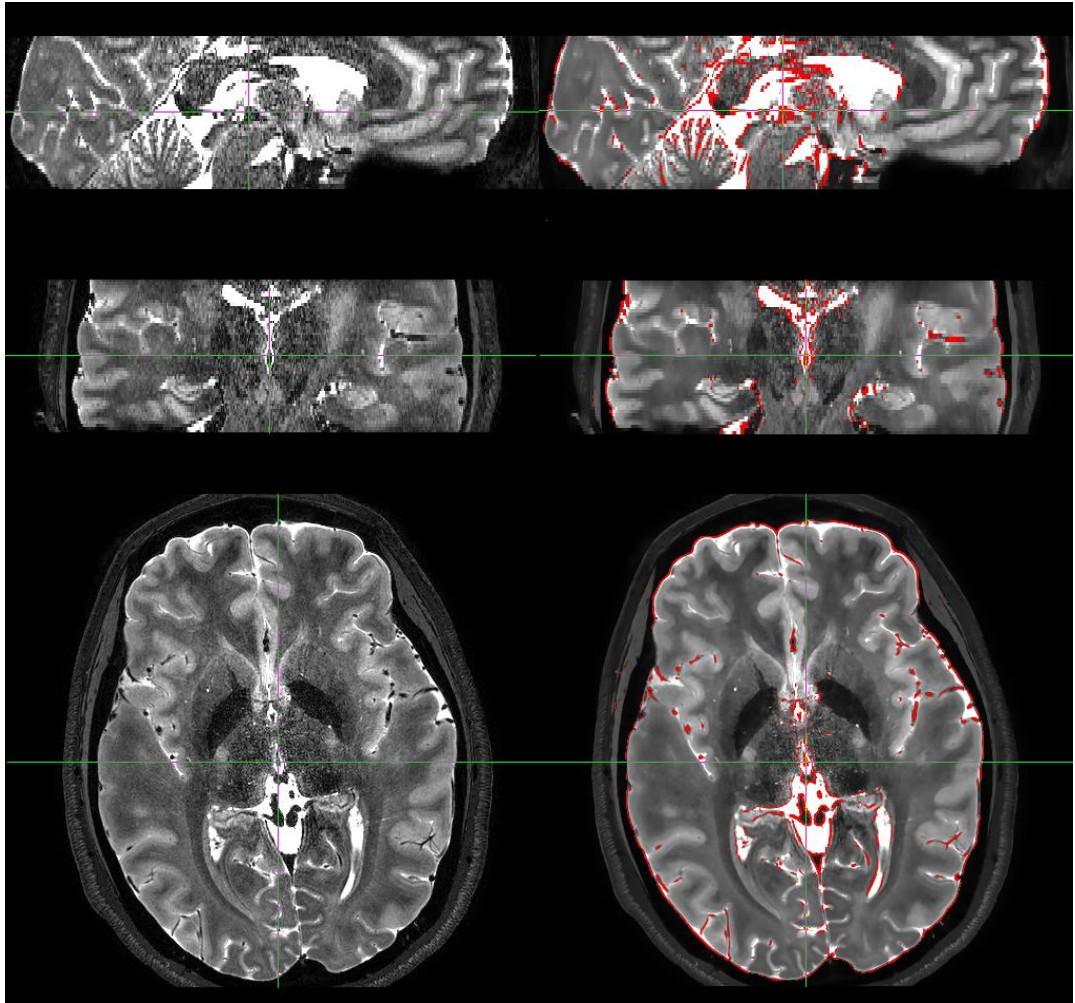


Figure 55: T2 weighted MR images (acquired in the axial plane and reformatted in the sagittal and coronal planes from bottom to top) of the same unaltered MRI head scan dataset (left hand column), compared to the results of small vein segmentation (right hand column) and non-local means filtering that was applied to the same MRI data as shown in the left hand column.

3.4. Discussion

There have been many previous studies that have carried out vascular resin casting of cadaveric cerebral vessels (Brockmann et al., 2012; Han et al., 2007; Reina-De La Torre et al., 1998). However the vascular casts that were produced in these studies were unable to perfuse the fine cerebral vessels to the extent that has been possible using the vascular casting technique that has been developed throughout this project.

Gross dissections of these resin perfused human cadaveric specimens (as well as other non-resin perfused cadaveric specimens) were able to macroscopically illustrate the existence of networks of subdural vessels and bridging veins, which could be seen traversing the subdural space.

The same tissues were then further histologically processed and analysed using LM, which allowed confirmation of the macroscopic findings on a microscopic scale. Images acquired from these histological sections sampled from the same tissue block, show that there are fine vessels present among the cerebral tissue, in between the brain surface and dural membrane (including the SDS), as well as within the dural membrane itself (Figure 48 and Figure 49). It can therefore be shown from these images that there are complex networks of both fine venules and arterioles that traverse the SDS from the surface of the brain and into the dura mater, through which the venules either drain directly or indirectly (via bridging veins) into the venous sinuses (Figure 50). Furthermore, analysis of these micrographs clearly shows that many of these vessels that are seen to traverse across the SDS are in fact venules. This can be determined from the size and shape of the vessel, as well as the composition of the vascular walls, and thereby again illustrates the presence of both fine subdural veins and bridging veins within the SDS. Although other studies have also histologically demonstrated bridging veins crossing the subdural space (Nierenberger et al., 2013), there are no documented studies that illustrate much finer networks of vessels traversing the subdural space in the same way.

The upper and lower limits of the documented sizes of bridging veins taken from a number of different studies show an average diameter range of 1.69-3.11mm (Baeck et al., 2012; Chen et al., 2012; Ehrlich et al., 2003; Yu et al., 2010). The sizes of the subdurally located venules illustrated in Figure 50 have diameters ranging from 16-177 μ m and are therefore much smaller in calibre compared to

the aforementioned size range of the conventionally defined bridging veins. It can therefore be argued that vessels such as these fine subdurally located veins are more vulnerable and thus more likely to be damaged in cases of NAHI, in comparison to traditionally defined much larger and more robust bridging vein structures. Due to their smaller diameter, it is reasonable to suggest that these finer veins could be the source of the thin-film subdural haemorrhaging often seen in MRI scans of NAHIs.

Higher numbers of these subdural vessels were particularly found to be located both immediately above and immediately below the tentorium cerebelli as illustrated in the gross tissue dissections shown in Figure 48 and Figure 49; as well as in the MR images shown in Figure 52 and Figure 54. Due to the continuity that exists between the cranial and spinal dural membranes, it is plausible that cranial subdural haemorrhaging originating from these supratentorial and infratentorial regions of the brain could dissect downwards to form a spinal SDH, a feature which is in fact commonly found in MRI scans of NAHIs (Choudhary et al., 2012; Koumellis et al., 2009).

In addition to the anatomical findings described above, high quality MRI images that were acquired using a 7.0 Tesla scanner were able to illustrate *in vivo* the presence of a wide spectrum of vessel sizes, ranging from the larger major bridging veins (2-4mm in diameter), to much smaller calibre (<0.5mm in diameter) vessels. These vessels have been shown to traverse across from the surface of the brain to the venous sinuses, and this has been illustrated in both young and elderly subjects (Figure 52, Figure 53 and Figure 54).

A number of different studies have carried out MRI imaging of bridging veins and other intracranial cerebral vessels in the past (Kirchhof et al., 2002; Kiyosue et al., 2008; Si et al., 2008). However the superior spatial resolution of the 7.0T scanner generated by a higher signal-to-noise ratio, in combination with the refined methodology for imaging of superficial cerebral vessels in this project, has made it possible to illustrate fine anatomical detail that would not be visible with other lower field systems and imaging techniques (Dammann et al., 2010; Li et al., 2006; Lupo et al., 2011).

However despite these positive outcomes, there was still a relative lack of success in the MR imaging part of this study than was initially expected. This was partly because MR imaging of the cadaveric material was consistently complicated by the

absence of subarachnoid fluid around the surface of the brain which normally acts as a natural contrast medium, allowing visualisation of structures over the surface of the brain. Additionally, the absence of blood flow may have also impaired vessel detection on imaging sequences that are dependent upon flow related enhancement of the MRI signals that allow detection of vessels.

Whilst the spatial resolution of MR imaging undertaken in both the young adults and elderly subjects was considerably superior to that obtained at the lower field strength clinical imaging MR systems, there is as yet insufficient sensitivity to be able to reliably and consistently detect the very small calibre blood vessels that are the subject of this study. However future work employing specially adapted multi-channel surface imaging coils, and the use of specific sequences that were not able to be fully assessed during the course of the project could potentially overcome this issue.

During this study, it was not possible to obtain human cadaveric material that could be perfused with resin immediately after death due to licence restrictions, although ethical approval could be applied for to allow for future cadaveric work to be carried out. Additionally, for logistical, practical and ethical reasons, it was not possible to undertake *in vivo* MRI at 7.0T in infants, therefore removing the possibility of obtaining high resolution imaging of the venous anatomy at this crucial and relevant age. This therefore highlights the importance of the experimental results obtained through the use of the primate (marmoset and macaque) material, as illustrated in the next chapter.

Chapter 4. Investigating Venous Anatomy in the Primate (*Callithrix jacchus* and *Macaca mulatta*)

4.1. Introduction

As has been described, rat specimens were used to first develop the PU4ii resin perfusion and vascular casting protocol in order to try to illustrate the existence of the subdural vessels we hypothesise to be the cause of SDH in NAHI. However for the purposes of this project, it is important to also illustrate this in a more closely related species to humans than that of the rat.

It has been shown that scientific procedures carried out on non-human primates are still vital in the biomedical field of research, taking into the account the present state of scientific knowledge that is available. The use of non-human primates however is difficult due to public concern regarding ethical issues. This is because their genetic proximity to humans means that they have highly developed social skills and general awareness in addition to the many biological similarities to humans (Roth et al., 2004). Therefore, use of non-human primates is only permitted in research deemed to be of a great benefit to humans, and for which there are no alternative options available (European Directive 2010/63/EU, 2011).

In the case of this project, the genetic homology between humans (Figure 56) and primates of approximately 92.5-95.0% (Roth et al., 2004) means that the anatomical structure of the human brain would be most accurately represented through analysis of the primate brain, and therefore is an essential component of this investigation. Further highlighting the need for primate work is the continuing discrepancies in the validity of the theories as to the cause of SDH in NAHI that have been put forward over the years. Experimental animal models such as mice alone are not sufficient with regards to accuracy and applicability of results in humans. These factors, as well as the continuing requirement for further research in possible cases of child abuse, illustrate how it is essential that primate work is carried out in order to ascertain vital information regarding fine anatomical structure of the microvasculature of the brain.

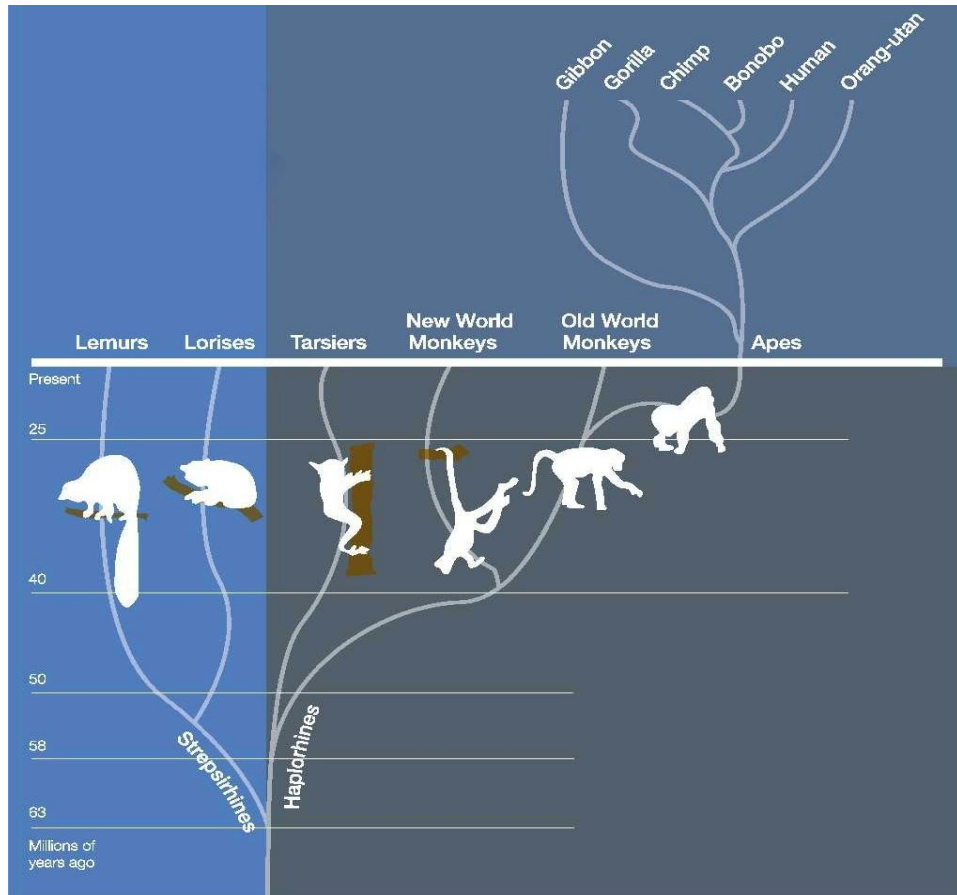


Figure 56: The Primate Family Tree: shows the points at which different evolutionary lineages split off from a common ancestor. Images are not to scale (MRC and The Wellcome Trust, 2006, with permission requested).

Experimental laboratory work was therefore carried out at the Kunming Institute of Zoology, Chinese Academy of Sciences, involving rhesus macaque (*Macaca mulatta*) specimens (old world monkeys). The Institution is an internationally recognised biodiversity research centre (Cyranski, 2004) which was able to provide primate specimens specific to the requirements of this project, as well as allowing access to all required scientific equipment and providing expert guidance (Kunming Institute of Zoology Chinese Academy of Sciences, 2012).

As well as looking at the anatomy of a more developed macaque brain, it was determined that it would be essential to investigate further the cerebral anatomical structure of an infant macaque, equivalent to approximately 6 months of age in a human. This is because this is the age in which cases of traumatic intracranial injuries in humans are most common. This is possibly due to the fact that between birth and 6 months, the single layer of cortical bone that forms the new-born's skull begins to differentiate structurally into a mature skull (Margulies

and Thibault, 2000). Additionally, it has also been shown that the cerebral and dural venous network undergoes many anatomical changes, and is thought to become less vascularized with increasing age from about 6 months after birth.

As well as using primate material supplied by the Kunming Institute of Zoology, previously obtained pre-fixed adult and infant marmoset specimens (new world monkeys) were also used for the purposes of this investigation. Processing of this marmoset material was carried out in a similar way to that of the human cadaveric material, so that the similarities between the cerebral anatomical structures of the human and marmoset could be illustrated.

4.2. Materials and Methods

Ethical approval was granted by the University of Nottingham Animal Welfare and Ethical Review Body (AWERB) for research involving primate material for the specific purposes of this project. All marmoset (*Callithrix jacchus*) material that was used had already been sacrificed and pre-fixed in accordance with Schedule I approved criteria for the humane killing of animals of the Animals Act 1986), under License Number: PL 40/1937. All procedures involving macaque (*Macaca mulatta*) material were also conducted in accordance with the same act as part of the institutional, UK and international regulations and standards of animal welfare. These sacrifices were carried out by a trained veterinary surgeon at the Kunming Institute of Zoology in China.

4.2.1. Marmoset (*Callithrix jacchus*)

4.2.1.1. PU4ii Resin Perfusion

The methodology for carrying out vascular resin casting of the prefixed marmoset material was similar to that carried out in the rat specimens. However as fixation of the tissue had already been carried out, the apparatus used for resin perfusion was simpler than illustrated in Figure 19. A World Precision Instrument AL-1010 Dual Pump was connected via plastic tubing to a 19G metal needle, which was inserted into the opening of the superior vena cava of the heart. Perfusion of 60ml of PU4ii resin (mixed with blue fluorescent powder) was subsequently carried out at a rate of 60ml/min. Following perfusion, the resin was then left to cure over a period of 48 hours at room temperature. Further information regarding mixing of

the resin components as well as the resin perfusion procedure is detailed in Figure 57.

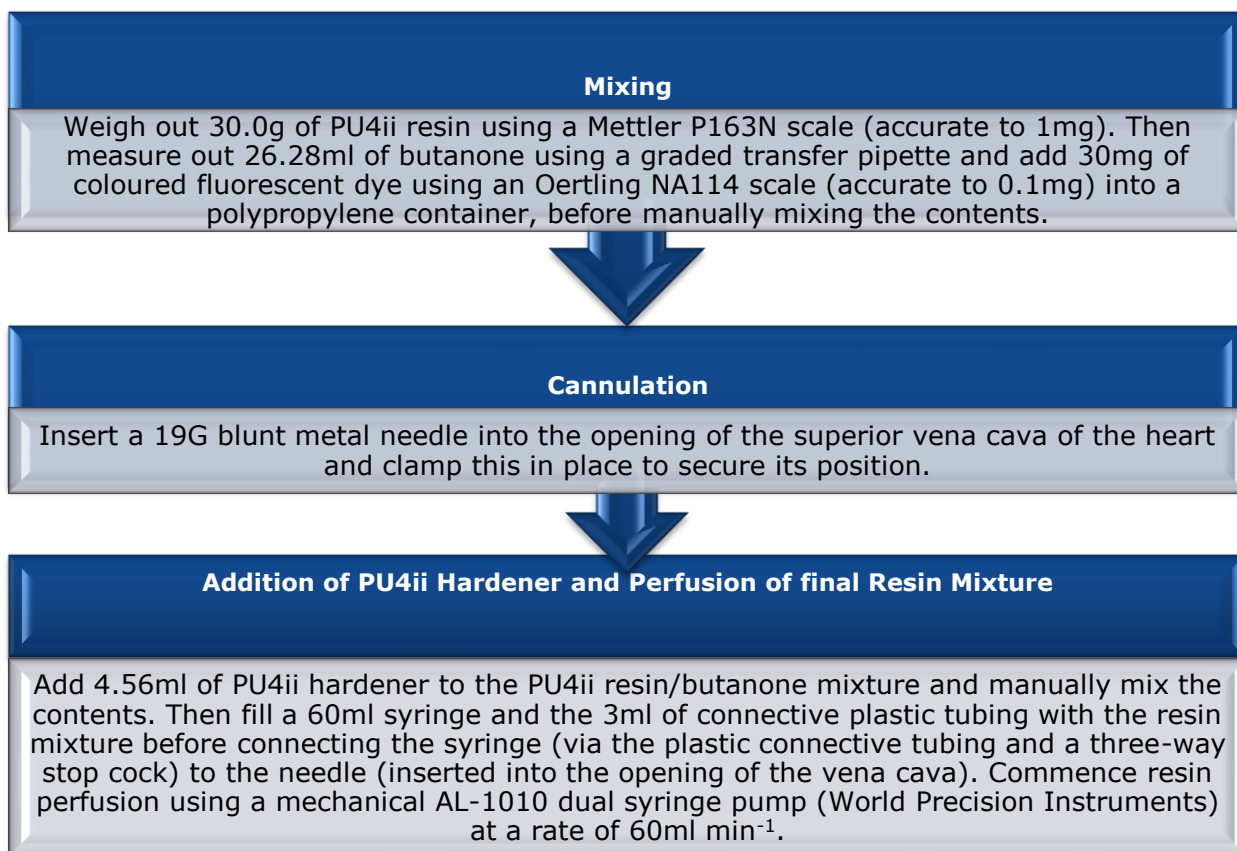


Figure 57: Method for PU4ii Resin Perfusion (containing coloured fluorescent dye) of a prefixed marmoset specimen.

Tissue Processing

Following perfusion of the macaque specimen, the resin was left to cure over a period of 48 hours at room temperature.

4.2.1.2. Gross Dissection and Decalcification

The skin and soft tissue of the marmoset head was dissected off to expose the underlying skull bone. This was submerged in decalcification solution Biocal C (Biostain Ready Reagents) for 3 days at 37°C in an incubator, to allow the bone to soften via decalcification and demineralisation.

4.2.1.3. Dissection

Pre-fixed marmoset material was processed and decalcified in the same way as described in section 4.2.1.2., before careful dissection of the specimens was performed using a Nikon dissecting microscope. Both macrographs and micrographs of the dissected material were acquired to allow documentation of results (in a similar way to that of the macaque material), before then dissecting out sections of the marmoset material for further tissue analysis to be carried out.

4.2.1.4. Maceration

The decalcified skull bone and soft tissue surrounding the previously resin perfused sample was fully macerated in 10% KOH solution in a 37°C incubator under constant agitation for 24 days, until all the surrounding tissue had been dissolved. The revealed VCC was then washed before undergoing further processing in preparation for ESEM and microCT imaging and analysis.

4.2.1.5. Osmocation and Lyophilisation (Freeze-drying)

The VCC was first osmicated in 1% OsO₄ solution for 24 hours, before being thoroughly washed in distilled water. Lyophilisation was then carried out using a similar method to that described for lyophilisation of rat VCC specimens in section 2.2.2.3. However due to the larger size of the marmoset VCC compared to the rat, the sample was submerged in 150ml of distilled deionised water before undergoing lyophilisation for a duration of 3 days.

Tissue Analysis

Following gross dissection of the prefixed infant and adult marmoset specimens, relevant material, such as bridging veins, subdural vessels, and their surrounding tissues were dissected out from the rest of the specimen, to undergo further processing and analysis.

4.2.1.6. Macroscopy

Specimens were imaged using professional imaging software ScopeImage DynamicPro as described in section 2.2.3.1. as well as a Canon PC1271 Powershot Digital Camera, in order to take detailed photographs of the marmoset tissue at various different stages of tissue processing.

4.2.1.7. Environmental Scanning Electron Microscopy (ESEM)

Following soft tissue maceration, osmocation and lyophilisation, the vascular resin cast was then prepared for ESEM imaging. The marmoset VCC was mounted onto a metal stub using conductive graphite paint (carbon cement) to secure the specimen during imaging. Electron micrographs were then acquired using a Philips XL30 FEG ESEM machine (Oxford Instruments INCA Microanalysis System).

4.2.1.8. Histology: LM and TEM Imaging

Following dissection of marmoset specimens A and B, tissues requiring further analysis were dissected away from the rest of the specimen. These were then embedded in Araldite resin in preparation for further processing for TEM imaging (further supplementary information regarding the protocol for processing tissue and embedding in Araldite resin for TEM is detailed in Appendix 5).

An alternative water-soluble resin called Durcupan was also trialled due to its potential of minimising damage caused to the tissues during the resin embedding process (further supplementary information regarding the protocol for resin embedding samples in Durcupan for TEM is detailed in Appendix 6). Durcupan was used to embed the whole brain of marmoset specimen C; however this resin was not very successful in penetrating the brain tissue sufficiently, as well as failing to harden sufficiently. The final resin colour was also very dark, therefore making it difficult to orientate the tissue itself for further processing. It was therefore concluded that Araldite would be used for all further resin embedding required for TEM imaging during this project.

Once embedded in Araldite resin, the tissue samples were then cut into semi-thin 1µm thick sections using a Leica Ultracut Ultramicrotome (Leica Microsystems) and glass knives. These were then stained with Toluidine Blue O before being analysed using a light microscope (Leica DM 4000B). LM mages were acquired

using Openlab software (PerkinElmer) and a MicroPublisher 3.3 RTV camera (QImaging). This was to gain an overall idea as to the anatomical structures present in the sections, as well as to aid identification of a ROI that would be further analysed with TEM. Further supplementary information regarding the protocol for staining of semi-thin sections with Toluidine Blue O is detailed in Appendix 7.

The same marmoset tissue samples as described above were then cut into 80nm thick ultra-thin sections using a Leica Ultracut Ultramicrotome (Leica Microsystems) and diamond knife. These samples were stained before then undergoing TEM imaging using a Tecnai G2 12 Biotwin TEM (FEI). Further supplementary information regarding the protocol for staining of ultra-thin tissue sections is detailed in Appendix 8.

4.2.1.9. Magnetic Resonance Imaging (MRI)

MRI images of prefixed infant and adult marmoset (sealed within air-tight plastic bags, to prevent leakage of fluid into the machine during scanning) were acquired using a 2.35T Bruker BioSpec Avance Animal MRI System (Bruker).

4.2.1.10. MicroCT Imaging of Vascular Casts

The freeze-dried and osmicated VCC of *marmoset E* sample was placed into a 60ml polypropylene universal tube which was attached to the stage of the microCT scanner using a carbon adhesive tab, in order to minimise drift as much as possible during the scanning process. MicroCT scanning of the VCC specimen was then carried out using a SkyScan 1174 machine (Bruker).

4.2.1.11. Computer-Aided Analysis of MicroCT Imaging Datasets

The microCT imaging datasets that were acquired from scanning of the marmoset cerebral VCC were used to generate 3D volumetric reconstructions using specialised SkyScan-1174v2 software (Bruker). These microCT projection images were then restructured using the same software, to create a video providing a 360° view of the whole VCC of the marmoset specimen.

Primate Specimen	Species/ Gender (M/F)	Age (Weeks)	Weight (g)	Procedure	Method of Perfusion	Needle size (G)	Resin Perfusion Rate (ml/min)	Decalcification (Days); Temperature (°C)	Tissue Processing and Analysis
A	Common Marmoset (<i>Callithrix jacchus</i>)/M	65 (Adult)	320	Fixation, resin perfusion, gross dissection, histology and TEM	Entrance to the Ascending Aorta	16 Cannula	1.5	73 ; 21	Gross dissection of the specimen, before it was photographed (macrographs and micrographs). Histological sections of the sample were then produced using a microtome (H&E stained). Further dissected out tissue samples which were processed for TEM (PFA and glutaraldehyde fixation, OsO ₄ staining, Araldite CY212 resin embedding). Then produced semi- and ultra-thin sections which underwent LM and TEM imaging.
B	Common Marmoset (<i>Callithrix jacchus</i>)/M	5 (Infant)	160	Fixation, gross dissection, histology and TEM	N/A	N/A	N/A	2 ; 37	Gross dissection of the specimen, before it was photographed (macrographs and micrographs). Produced histological sections of tissues embedded in agarose using a microtome, followed by H&E staining of samples for LM . Further dissected out tissue samples which were processed for TEM (PFA and glutaraldehyde fixation, OsO ₄ staining, Araldite CY212 resin embedding). Then produced semi- and ultra-thin sections which underwent LM and TEM imaging.
C	Common Marmoset (<i>Callithrix jacchus</i>)/M	5 (Infant)	160	Fixation, gross dissection	N/A	N/A	N/A	2 ; 37	Gross dissection of the specimen, before it was photographed (macrographs and micrographs).
D	Common Marmoset (<i>Callithrix jacchus</i>)/M	65 (Adult)	320	Fixation, gross dissection	N/A	N/A	N/A	24 ; 21	Embedded sample in agarose and sectioned into 1mm slices .
E	Common Marmoset (<i>Callithrix jacchus</i>)/M	65 (Adult)	320	Fixation, resin perfusion	Entrance to the superior vena cava	19 Blunt needle	60.0	3 ; 37	Scanned in an animal MRI scanner. Tissue was then macerated , osmicated , and dried before it was photographed (macrographs), and underwent microCT and ESEM imaging.
F	Common Marmoset (<i>Callithrix jacchus</i>)/M	5 (Infant)	160	Fixation, resin perfusion	Entrance to the ascending aorta	19 Blunt needle	60.0	4 ; 37	Embedded in agarose and sectioned into 1mm slices which were photographed (macrographs). Samples were then osmicated and freeze-dried, before photomicrographs and ESEM images were taken of these sections. Scanned in an animal MRI scanner.

Table 4: Experimental primate specimens (Common Marmosets: *Callithrix jacchus*) used during the study. The main use of these specimens was to dissect out and therefore illustrate the anatomical structure of the cerebral anatomy, while demonstrating the similarities in anatomical structure with that of rat and cadaveric material. The table also details how the tissues were further processed and analysed.

4.2.2. Rhesus Macaque (*Macaca Mulatta*)

4.2.2.1. Cardiac Perfusion Fixation and PU4ii Resin Vascular Casting

During the laboratory visit to the Kunming Institute of Zoology in China, various perfusion experiments were carried out using 4 rhesus macaque specimens. The age of these rhesus macaques ranged between 1.5 and 4 months old, as this correlates with the relative age range of 6-12 months in humans, when most cerebral anatomical changes are thought to occur.

The first perfusion experiment involved perfusion fixation only, using a mixture of 1% glutaraldehyde and 4% PFA fixative solution in order to thoroughly fix the tissue in preparation for EM analysis. The second perfusion experiment involved perfusion fixation with 4% PFA solution, before then perfusing the specimen with PU4ii resin mixed with fluorescent dye. The third experiment also involved perfusion fixation with 4% PFA solution, however the specimen was then perfused with PU4ii resin mixed with fluorescent dye and a low concentration of gold nanoparticles, to allow enhancement of the resin contrast for 3D XRM imaging. The fourth experiment similarly involved perfusion fixation with 4% PFA solution, followed by perfusion of PU4ii resin mixed with fluorescent dye and the normal calculated concentration of gold nanoparticles to allow for maximum contrasting effect with 3D XRM scanning.

In this way, each perfusion experiment was comprised of slightly different components that would allow the material to be processed in different ways. This facilitated the multimodal approach in which analysis could be carried out on these specimens, and is essential for an overall understanding of the gross morphology, microscopic and ultrastructural anatomy of the vessels that are being investigated.

Primate Specimen	Species/ Gender (M/F)	Age (Days)	Weight (g)	Procedure	Method of Perfusion	Needle size (G)	Resin Perfusion Rate (ml/min)	Decalcification (Days); Temperature (°C)	Tissue Processing and Analysis
A	Rhesus monkey (<i>Macaca mulatta</i>)/M	58	780	Fixation	Entrance to the Ascending Aorta	16 Needle	N/A	7 ; 37	Gross dissection. Samples were also photographed (macrographs).
B	Rhesus monkey (<i>Macaca mulatta</i>)/M	72	820	Fixation, Resin perfusion (blue fluorescent dye)	Entrance to the Ascending Aorta	16 Needle	60	7 ; 37	Gross dissection. Samples were also photographed (macrographs).
C	Rhesus monkey (<i>Macaca mulatta</i>)/M	100	520	Fixation, low concentration Gold nanoparticle and Resin perfusion (blue fluorescent dye)	Entrance to the Ascending Aorta	16 Needle	60	2 ; 37	Maceration to produce a whole brain VCC. Sample was then photographed (macrographs). Osmocated VCC in OsO ₄ before freeze- drying and imaging using ESEM and 3D XRM.
D	Rhesus monkey (<i>Macaca mulatta</i>)/M	66	860	Fixation, Gold nanoparticle and Resin perfusion (blue fluorescent dye)	Entrance to the Ascending Aorta	16 Needle	60	9 ; 37	Gross dissection. Samples were also photographed (macrographs). Wax embedding of select samples for microtome sectioning, H&E staining and imaging using LM and FM/CM.

Table 5: Experimental primate specimens (Rhesus monkeys: *Macaca mulatta*) used during the study. The main use of these specimens was to illustrate the anatomical structure of the cerebral anatomy using as many different tissue processing, imaging and analysis techniques as possible, while demonstrating the similarities in the cerebral anatomical structure of the primate, with that of the rat and human.

Experiment 1: Rhesus Macaque **A** (58 days/ 1.9 months old) (Figure 58)

Perfuse 1.5 litres of prewash solution at high pressure (200mmHg), followed by 600ml of a mixture of 1% glutaraldehyde and 4% PFA fixative solution at low pressure (20mmHg) for a duration of 20 minutes, to allow thorough fixation of the tissue in preparation for EM analysis.

Experiment 2: Rhesus Macaque **B** (72 days/ 2.4 months old) (Figure 59)

Perfuse 1.5 litres of prewash solution followed by 1.5 litres of 4% paraformaldehyde solution, both at high pressure (200mmHg), to allow fixation of the tissue. Then perfuse 120ml of PU4ii (polyurethane) resin (VasQtec, Switzerland) mixed with fluorescent powder, at a rate of 60ml/min, into the specimen via the heart.

Experiment 3: Rhesus Macaque **C** (100 days/ 3.3 months old) (Figure 60)

Perfuse 1.5 litres of prewash solution followed by 1.5 litres of 4% paraformaldehyde solution, both at high pressure (200mmHg), to allow fixation of the tissue. Then perfuse 120ml of PU4ii (polyurethane) resin (VasQtec, Switzerland) mixed with fluorescent powder and a low concentration (40mg) of gold nanoparticles (Nanoprobes, Inc., USA) at a rate of 60ml/min, into the specimen via the heart. These particles allow vessels to be detected using 3D XRM imaging.

Experiment 4: Rhesus Macaque **D** (66 days/ 2.2 months old) (Figure 61)

Perfuse 1.5 litres of prewash solution followed by 1.5 litres of 4% paraformaldehyde solution, both at high pressure (200mmHg), to allow fixation of the tissue. Then perfuse 120ml of PU4ii (polyurethane) resin (VasQtec, Switzerland) mixed with fluorescent powder and a normal concentration (160mg) of gold nanoparticles (Nanoprobes, Inc., USA) at a rate of 60ml/min, into the specimen via the heart.

Information regarding the methodology for conducting these experiments is detailed in the following flow charts (Figure 58, Figure 59, Figure 60 and Figure 61). Supplementary information regarding the protocol for anaesthesia and Schedule 1 killing of the rhesus macaques is detailed in Appendix 9.

4.2.2.1.1. Calculation of the Relative Age between the Rhesus macaque and the Human

At the age of 6 months, the anatomy of the human infant dura and venous drainage begins to alter, and it has been shown that the cerebral venous network present in infants gradually diminishes in size with increasing age (Browder et al., 1975). This is why the dural venous anatomy of rhesus macaques of an age equivalent to 6-12 human months, needs to be more closely examined.

The rate of aging in a rhesus macaque is approximately 3-4 times as fast compared to that of the human (O'Dell and Boothe, 1997; Roth et al., 2004). Therefore the equivalent of 6 and 12 human months in a rhesus macaque can be calculated as 1.5-2 months (45-60 days) and 3-4 months (90-120 days) respectively. The age of the rhesus macaques that were used in the perfusion experiments carried out at the Kunming Institute of Zoology were therefore between 1.5 and 4 months old, as this correlated with the relative age range of 6-12 months in humans, when most cerebral anatomical changes are thought to occur.

4.2.2.1.2. Calculation of the Blood Volume of the Rhesus Macaque

Calculation of the total blood volume of the Rhesus macaque allows the volume of each solution required for cardiac perfusion fixation, as well as gold nanoparticle and PU4ii resin perfusion to be determined. This is done by extrapolating the volumes of the solutions used in the protocol developed for cardiac perfusion fixation and PU4ii resin perfusion of the Wistar rat in previous vascular casting experiments, by comparing the relative total blood volumes between the Rhesus macaque and the Wistar rat.

The blood volume of the rhesus macaque has been shown to be approximately 60.9ml/kg (Bender, 1955). Therefore using the average weight of 745g (calculated from the weights of all the Rhesus macaques used for the perfusion experiments carried out at the Kunming Institute of Zoology), the total blood volume can be calculated from this weight to be 45.37ml.

4.2.2.1.3. Rhesus macaque: Perfusion Experiment Volume Calculations

Since the total blood volume of a 250g rat is approximately 15.77ml, the volumes of prewash, fixative and resin required for a rhesus macaque weighing 745g are 2.9 times that of a 250g rat.

As a 250g rat (with a total blood volume of 15.77ml) would normally require 500ml of prewash and 500ml of fixative for complete fixation, it can be calculated that a 745g rhesus macaque (with a total blood volume of 45.37ml) would require approximately 1450ml of prewash and 1450ml of fixative for complete fixation.

Experiment 1

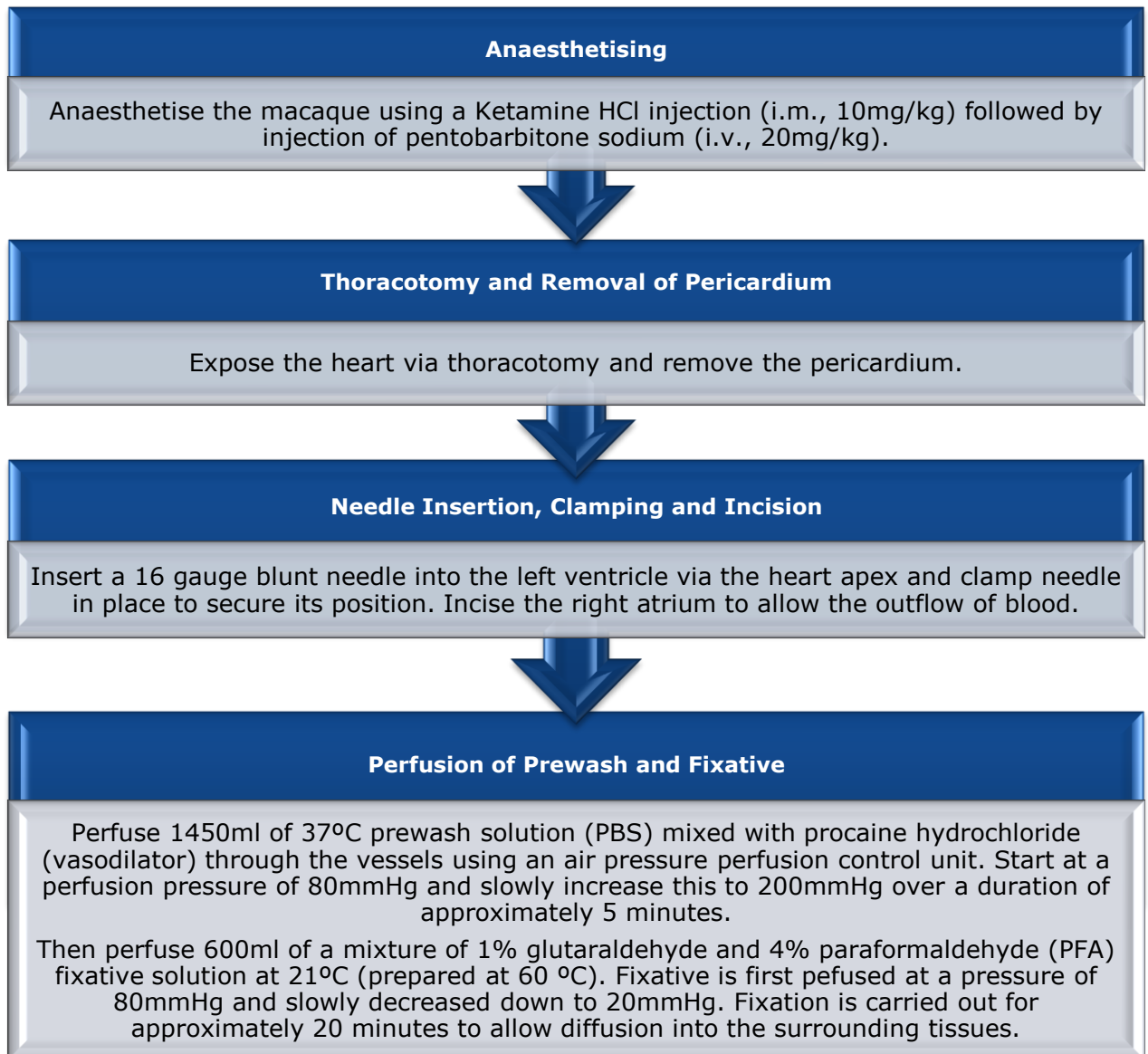


Figure 58: Method for Cardiac Perfusion Fixation (1% Glutaraldehyde and 4% PFA) of a 745g rhesus macaque, in preparation for EM analysis.

Experiment 2

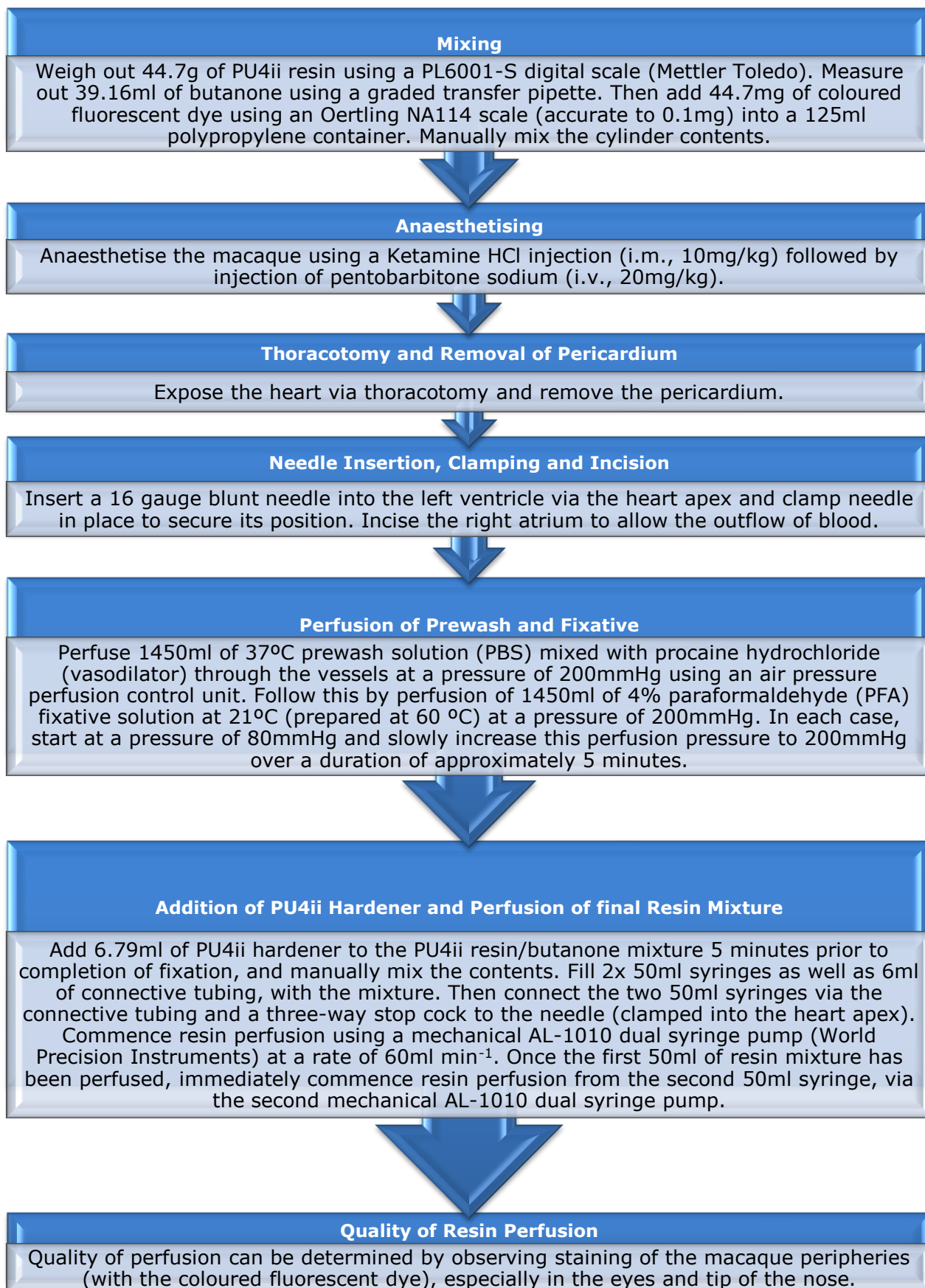


Figure 59: Method for Cardiac Perfusion Fixation (4% PFA) and PU4ii Resin Perfusion (containing coloured fluorescent dye) of a 745g rhesus macaque.

Experiment 3

Perfusion experiments 3 and 4 both involve perfusion of gold nanoparticles (mixed with PU4ii resin and fluorescent dye) into the cerebral vasculature. This newly developed CT contrast medium will enable better visualisation of the cerebral vessels *in situ* during 3D XRM imaging of the macaque specimens.

Experiment 3 uses a quarter of the concentration of gold nanoparticles (40mg/kg) suggested to be the optimal concentration (160mg/kg) as used in Experiment 4 (Powell, 2012). This is because unlike other investigations using these gold nanoparticles, 3D XRM scanning in these experiments will be carried out on perfused dead animal material. This means that longer scanning sequences can be used that will increase the amount of exposure, which should mean that a lower concentration of gold nanoparticles is required compared to that needed when scanning live specimens, for acquisition of high quality imaging data.

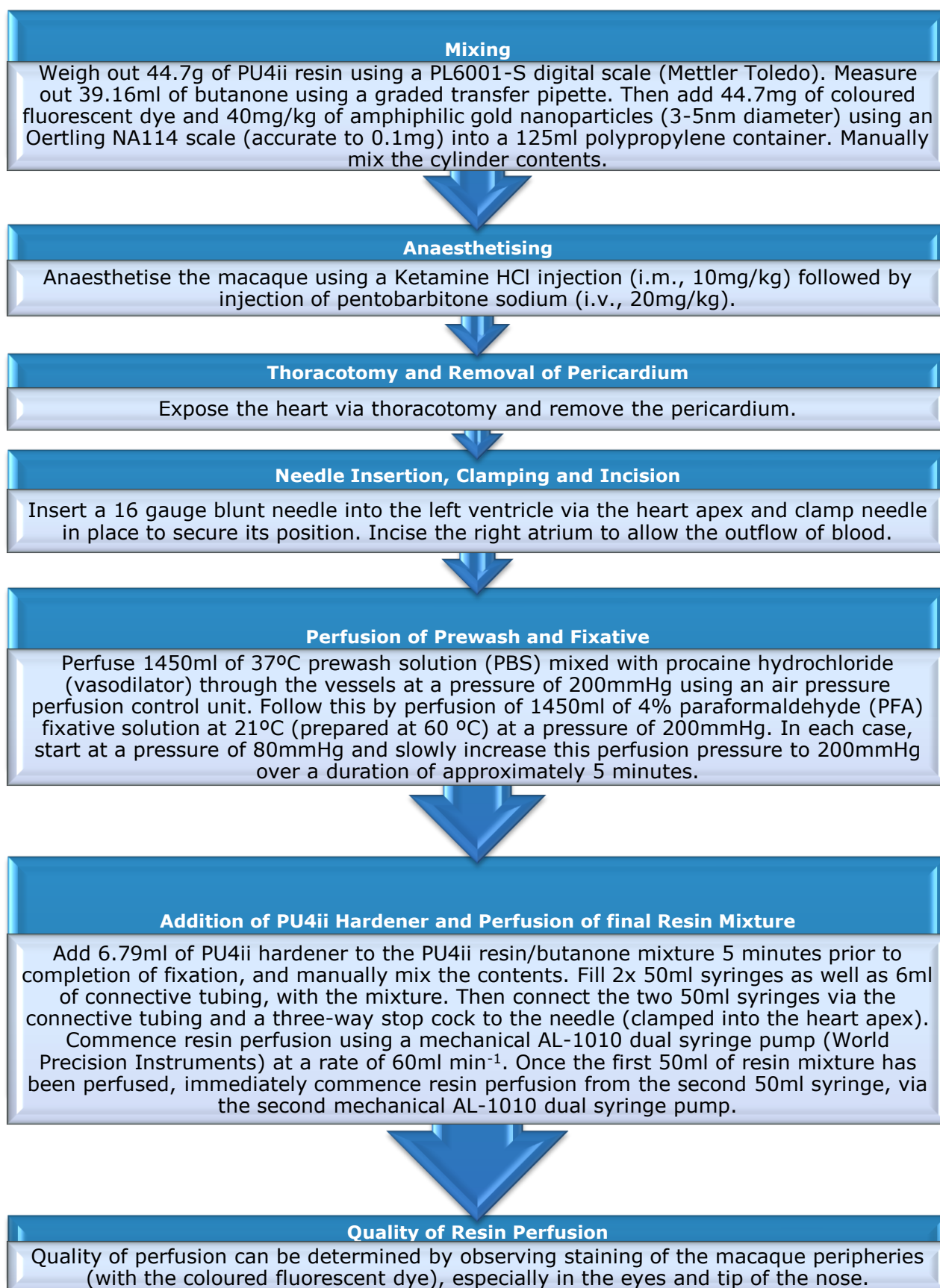


Figure 60: Method for Cardiac Perfusion Fixation (4% PFA) and PU4ii Resin Perfusion (containing coloured fluorescent dye and 40mg/kg of amphiphilic gold nanoparticles) of a 745g rhesus macaque.

Experiment 4

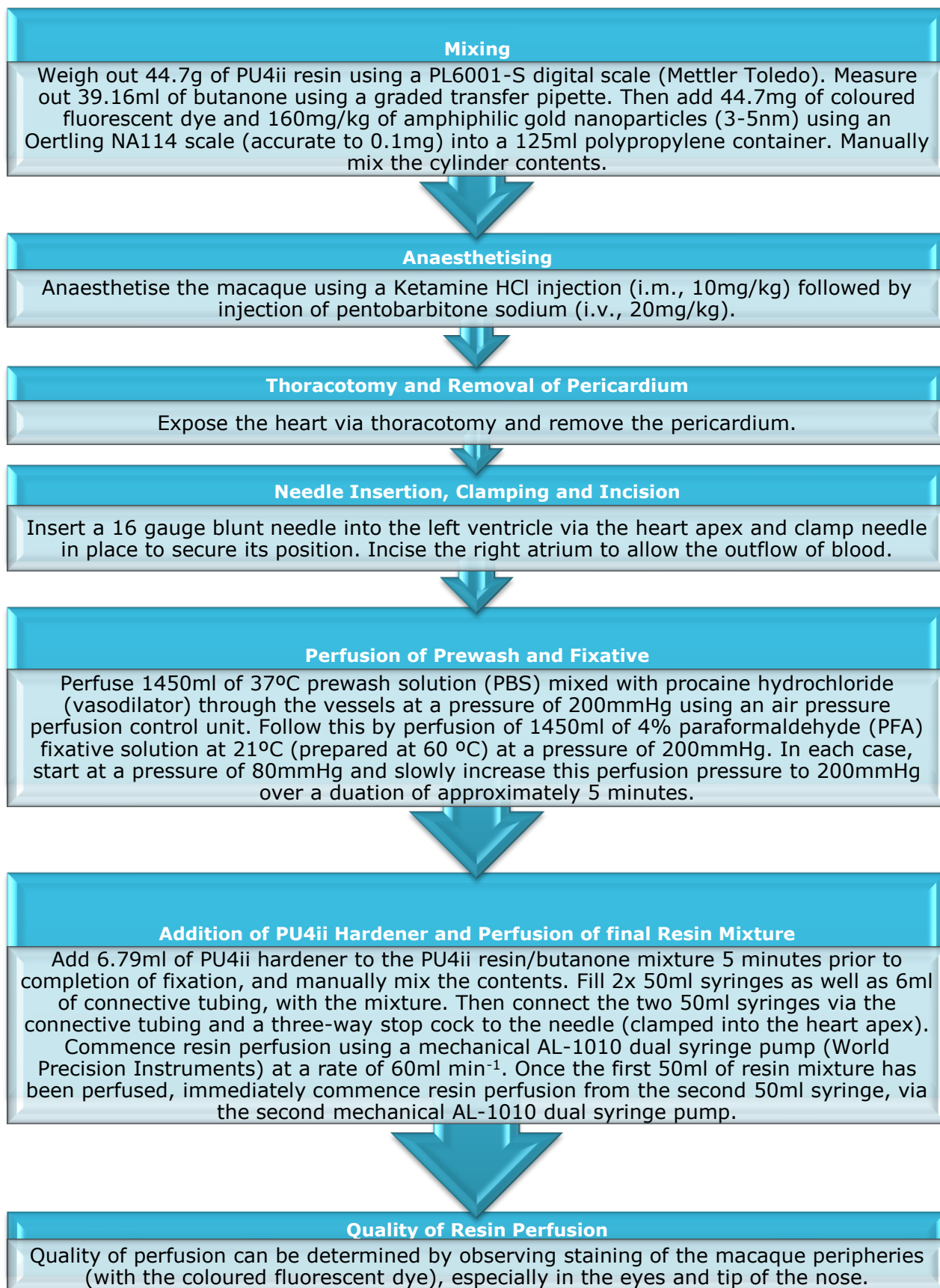


Figure 61: Method for Cardiac Perfusion Fixation (4% PFA) and PU4ii Resin Perfusion (containing coloured fluorescent dye and 160mg/kg of amphiphilic gold nanoparticles) of a 745g rhesus macaque.

Tissue Processing

4.2.2.2. Gross Dissection and Decalcification

Following perfusion of the macaque specimens, the resin was left to cure over a period of 48 hours at room temperature. The tissue surrounding the macaque heads was then removed using gross dissection to expose the underlying skull bone. The tissue was then submerged in decalcification solution Biocal C (Biostain Ready Reagents) for at least 7 days at 37°C in an incubator, to allow the bone to soften via decalcification and demineralisation. Following decalcification, macaque specimens either went on to be further dissected, processed and analysed; or underwent maceration to produce whole brain VCCs which were then further processed and analysed.

4.2.2.3. Dissection

Careful dissection of both resin perfused and non-resin perfused fixed macaque material was then performed using a Nikon dissecting microscope. Both macrographs and micrographs of the dissected material were taken in order to document what was found (in a similar way to that of the marmoset material), before then dissecting out the most important sections of the macaque material, to allow further tissue analysis.

4.2.2.4. Maceration

Skull bone and soft tissue surrounding the previously resin-perfused sample was fully macerated in 40% KOH solution in a 37°C incubator, under constant agitation for 15 days, until all the surrounding tissue had been dissolved. The revealed VCC (Figure 77) was then washed before undergoing further processing in preparation for ESEM and 3D XRM imaging and analysis.

4.2.2.5. Osmocation and Lyophilisation (Freeze-drying)

The VCC was first osmicated in 1% OsO₄ solution for 24 hours, before being thoroughly washed in distilled water. Lyophilisation was then carried out using a similar method to that described for lyophilisation of rat VCC specimens in section 2.2.2.3. However due to the significantly larger size of the macaque VCC, the

sample was submerged in 200ml of distilled deionised water before undergoing lyophilisation for a duration of 5 days.

Tissue Analysis

Following tissue processing, various different forms of imaging and analysis were performed on the macaque material.

4.2.2.6. Macroscopy

Specimens were imaged using professional imaging software ScopeImage DynamicPro as described in section 2.2.3.1. as well as a Canon PC1271 Powershot Digital Camera, in order to take detailed photographs of the macaque tissue at various different stages of tissue processing.

4.2.2.7. Environmental Scanning Electron Microscopy (ESEM)

Following soft tissue maceration, osmocation and lyophilisation, the vascular resin cast was then prepared for ESEM imaging. Carefully identified sections of the macaque VCC were first carefully dissected away, in order to reveal the underlying structures to be scanned with ESEM. The Macaque VCC was then mounted onto a metal stub using conductive graphite paint (carbon cement) to completely secure the specimen during imaging. Electron micrographs were acquired using a Philips XL30 FEG ESEM machine (Oxford Instruments INCA Microanalysis System).

4.2.2.8. 3D XRM of VCCs

As well as using ESEM to illustrate any subdural vessels that were present, 3D X-Ray Microscopy (XRM) was also used to obtain morphometrical data of the vessels *in situ*.

In order to obtain as much contrast as possible, a newly developed CT contrast medium (Nanoprobe Inc., 1992) in the form of gold nanoparticles (Nanoprobe, Inc., USA) was perfused into the cerebral vascular system in combination with the PU4ii resin mixture, using the vascular resin casting methodology previously described. 3D XRM imaging was then carried out on these resin-perfused macaque specimens, using a VersaXRM-500 (Xradia) machine with a true submicron spatial resolution of $<0.7\mu\text{m}$. 3D XRM is an essential analysis technique as it allows for

much larger sample imaging than is possible with a microCT scanner, and it also allows digital reconstructions of the VCCs to be produced in 3D in much greater detail than is possible with either microCT or MRI imaging (Shearing et al., 2013).

4.2.2.9. Computer-Aided Analysis of 3D XRM Imaging Datasets

Volume Rendering

Coronal (XY) serial section images of the macaque VCC were constructed from the 3D XRM dataset acquired from the resin cast specimen. These images were then processed using volume rendering software CTvox (Bruker) and reconstructed into a 3D format. Specific thresholds were then applied to the dataset to filter out any extraneous noise. Although this method of volume rendering was useful for the rapid production of relatively detailed 3D reconstructed images from the 3D XRM data, the CTvox software was unable to determine the size of each individual vessel, as well as carry out other detailed forms of analysis.

Approximating Vessel Size from 3D XRM Imaging Datasets

Volume rendering of the 3D XRM imaging dataset acquired from the VCC of macaque C was carried out using the 'Simple Neurite Tracer' plug-in for the computer software Image J (NIH). After reconstructing a 3D image of the scanning dataset, using the same plug-in, the local thicknesses of the macaque cerebral vessels were then categorised by colour, which was indicated by a calibration bar. Further supplementary information regarding the protocol for volume rendering an image dataset and illustrating the local thicknesses of the cerebral vessels is detailed in Appendix 4.

4.2.2.10. Histology and FM Imaging

Following dissection of macaque specimens A and D, carefully selected vessels requiring further analysis were dissected away from the rest of the tissue to be further processed. These specimens were first wax-embedded and then cut into 15µm sections using a SLEE CUT 4060 (Mainz) Rotary Microtome (Mainz) with a 4689 Accu-Edge Low-Profile Blade, in preparation for further processing and histological analysis including LM and FM. Further supplementary information regarding the protocol for wax embedding and microtome sectioning is detailed in Appendix 10 and Appendix 11 respectively).

The most detailed FM images that were produced from previous experiments involving resin perfused (rat) specimens were acquired from imaging of H&E stained sections, which were mounted onto aminopropyltriethoxy-silane (APES) coated microscope slides using DPX. However in this case, due to the larger size of the macaque vessels in comparison to the rat, the larger luminal resin sections became detached from the histology slides during the process of de-waxing and H&E staining. This was due to the lack of remaining support around the resin sections once the infiltrated wax had been dissolved in xylene. Further supplementary information regarding the protocol for H&E staining is detailed in Appendix 12.

Various other processing techniques were therefore trialled, including mounting the tissue sections in either DPX or non-fluorescent mounting medium, without first de-waxing the specimens. However analysis of these slides with a fluorescent microscope showed that the results were not optimal as the fluorescence that was detected from these specimens was minimal. Another technique of placing the wax embedded specimens into xylene for a shorter amount of time, to allow partial de-waxing of the specimen, was also trialled. However the resin perfused into the lumina of the larger cerebral vessels once again floated off from the histology slides almost instantaneously. To aid bonding of tissue samples to histology slides and therefore decrease the likelihood of detachment during processing, tissues are often mounted onto Leica X-tra microscope slides, in addition to placing the mounted samples into a 60°C oven for 12 hours following sectioning. However in this case, due to the relatively dense yet elastic nature of the resin which was perfused into the very fine vessels of the brain, it is very unlikely that these methods would maintain bonding of the tissue to the slides during further processing.

Overall, it was decided that although some resin would be lost during processing of the tissue, the remaining specimens should be de-waxed, H&E stained and mounted in DPX as this protocol produces the highest quality images. This is even after taking into account the given technical constraints discussed above.

Once prepared, FM was then used to analyse the macaque brain specimens that were perfused with resin mixed with fluorescent powder. The FM images that were acquired (red channel) were overlaid onto BF histological images (green channel) of the same histological sections (H&E stained, DPX mounted). This was so that

the fluorescence detected within the resin-perfused vessels would allow easy identification of the cerebral vessels in relation to their surrounding histological structures. The exact protocol as to acquiring BF and FM images and combining these into a single image is described in section 2.2.3.6. In this case, special care was taken to ensure that the specimens underwent as little agitation as possible during processing, to allow retention of as much resin within the vessel lumina as possible.

4.3. Results

The hypothesis of this project is that there are fine subdural venules which surround or drain into the bridging veins (which in turn drain into the venous sinuses) that are the cause of subdural bleeding found in cases of accidental and non-accidental traumatic head injuries. This project focuses exclusively upon research into the structure of these fine venules so that their existence can be proven, and to therefore allow the origin of haemorrhaging caused by non-accidental head injuries (NAHI) to be more accurately located.

Through various different analysis techniques (encompassing gross tissue dissection; vascular resin casting; microCT and 3D XRM scanning; ESEM imaging; histological techniques including LM, FM and TEM; as well as MRI and different forms of data reconstruction), a detailed examination of primate (marmoset and macaque) material was performed. This was to first of all illustrate the existence of subdural vessels in primates as well as in humans and rats (so as to demonstrate their existence across different species) as well as to investigate further their morphological structure. This could then act as vital evidence supporting the proposed theory that subdural vessels are the source of intracranial bleeding seen in cases of accidental and non-accidental traumatic head injuries.

4.3.1. Marmoset (*Callithrix jacchus*)

4.3.1.1. Gross Dissection of Prefixed Marmoset Material

Careful dissection of prefixed marmoset material was carried out to reveal bridging veins (Figure 62) draining directly into the venous sinuses, as well as other subdurally located fine vessels (Figure 63). Macrographs were taken of these specimens, before dissecting them out to further process and analyse them using histological techniques such as light microscopy and TEM.

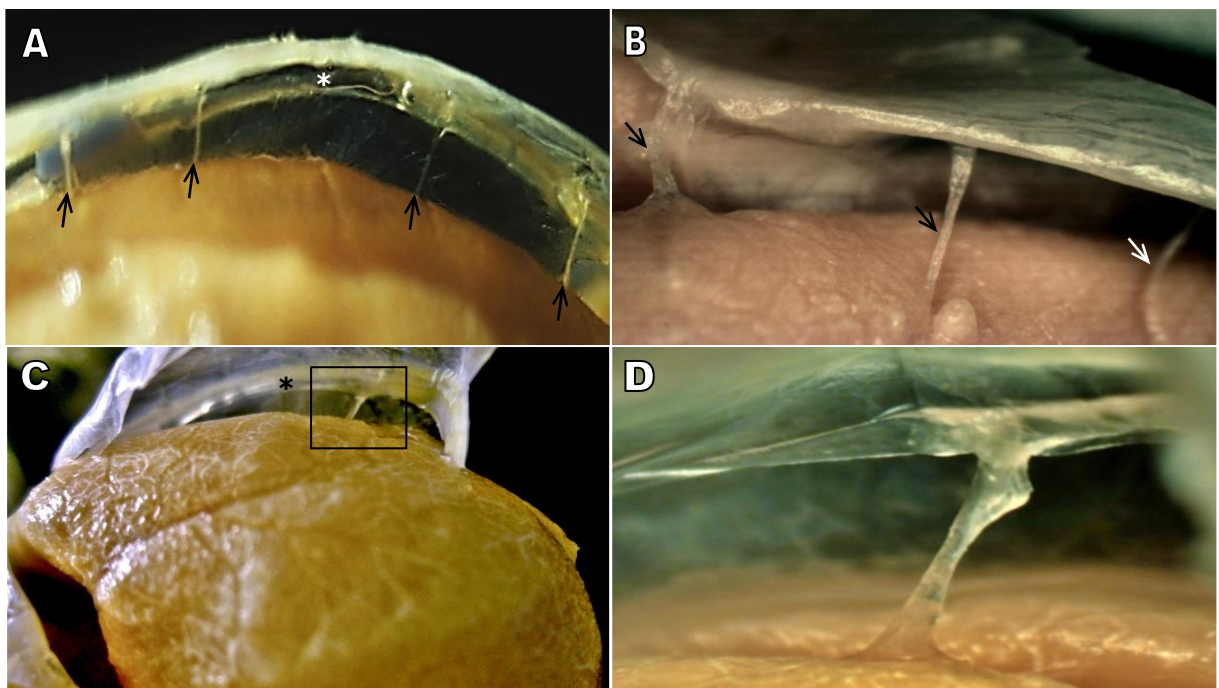


Figure 62: Macrographs of adult (A, B) and infant (C, D) common marmoset (*Callithrix jacchus*) specimens taken in the sagittal plane, which were dissected to illustrate bridging veins draining directly into the superior sagittal sinus (SSS). **A:** Macrograph of bridging veins (arrows) draining into the SSS (asterisk). **B:** Higher magnification image of the same bridging veins (arrows) as illustrated in image A. **C:** Macrograph of a bridging vein (black box) draining into the SSS (asterisk). **D:** Higher magnification image of the same bridging vein as illustrated in image C.

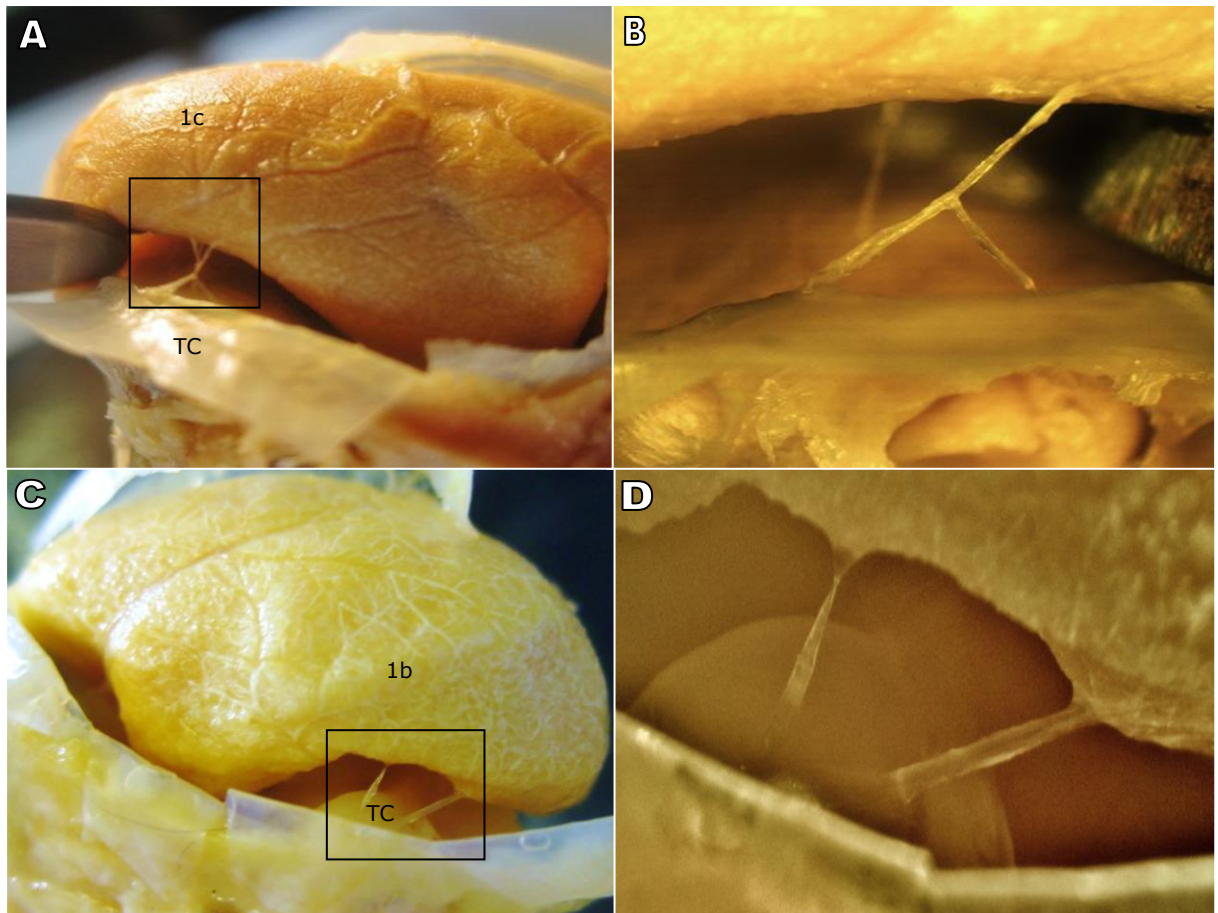


Figure 63: Macrographs of adult (A, B) and infant (C, D) common marmoset (*Callithrix jacchus*) specimens, dissected to illustrate subdurally located veins. **A:** Subdural vessels (black box) draining from the surface of the right cerebral hemisphere (1c), to the tentorium cerebelli (TC) below. **B:** Higher magnification image of the same subdural veins as seen in image A. **C:** Subdural vessels (black box) draining from the left cerebral hemisphere (1b) of the brain, to the tentorium (TC) cerebelli covering the cerebellum below. **D:** Higher magnification image of the same vessels as seen in image C.

4.3.1.2. Vascular Resin Casting and ESEM Imaging of VCCs

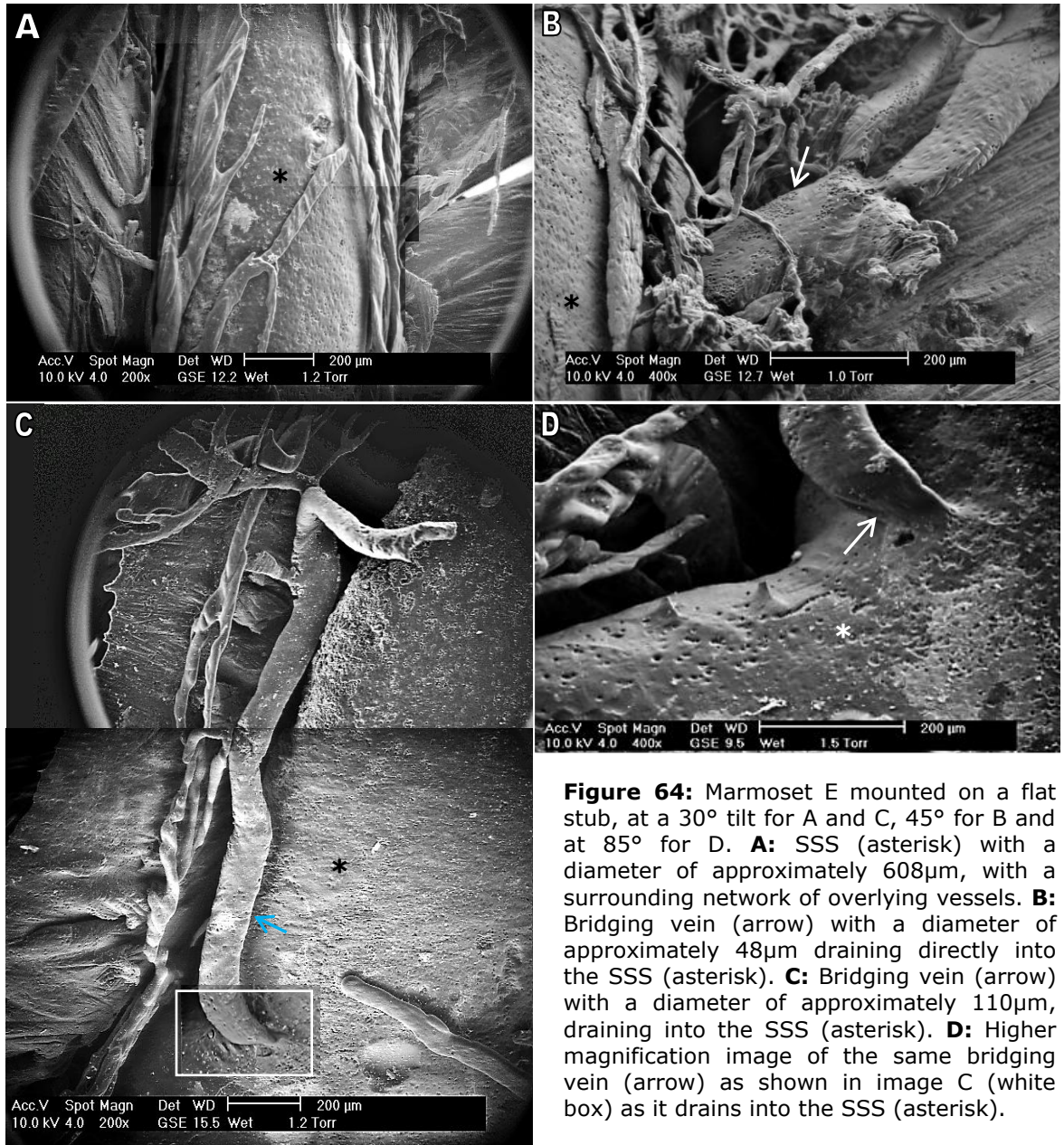
Following soft tissue maceration, osmocation and lyophilisation of the resin perfused marmoset specimen, the VCC was then imaged using ESEM.

Images illustrating the general size and diameter of a number of different venous sinuses, as well as vascular networks of bridging veins and their tributaries draining into these sinuses are shown below. These include ESEM images of the SSS (Figure 64), TS (Figure 65, Figure 66 and Figure 70), SS (Figure 67 and Figure 70) and PS (Figure 68, Figure 69 and Figure 70).

Although the quality of the resin perfused marmoset specimen meant that all the cerebral vessels were not filled with resin, a general pattern regarding the size and distribution of the vessels draining into the various venous sinuses can be identified. For example, the bridging veins and tributaries that drain into the sigmoid and petrosquamous sinuses seem to be smaller in diameter while being larger in number, compared to the vessels that drain into larger venous sinuses sizes such as the superior sagittal or transverse sinuses. It should be noted that although the size as well as the manner and extent of branching of the bridging veins and their tributaries can be seen to differ slightly, even between the vessels which drain into the same venous sinuses, this can be attributed to normal anatomical variation.

Additionally, narrowing of the bridging veins at the junction point where they drain into the venous sinuses can also be clearly seen in many of the images of these marmoset specimens (Figure 64D, Figure 65D, Figure 66B and Figure 69C). Overall, these ESEM results correlate well with similar findings established through ESEM imaging of resin perfused rat specimens (Section 2.3.2.).

The Superior Sagittal Sinus (SSS)



The Transverse Sinus (TS)

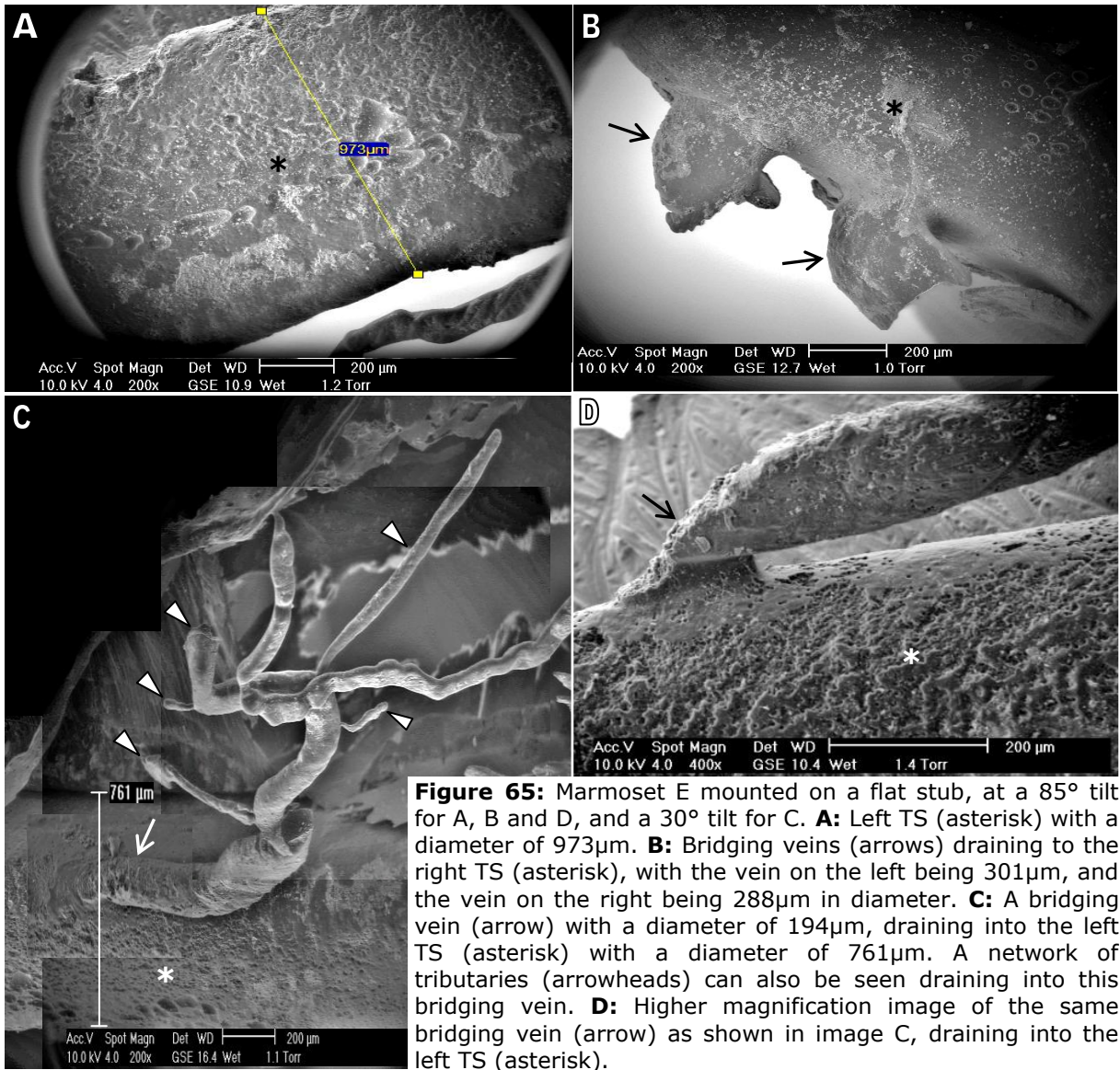


Figure 65: Marmoset E mounted on a flat stub, at a 85° tilt for A, B and D, and a 30° tilt for C. **A:** Left TS (asterisk) with a diameter of 973μm. **B:** Bridging veins (arrows) draining to the right TS (asterisk), with the vein on the left being 301μm, and the vein on the right being 288μm in diameter. **C:** A bridging vein (arrow) with a diameter of 194μm, draining into the left TS (asterisk) with a diameter of 761μm. A network of tributaries (arrowheads) can also be seen draining into this bridging vein. **D:** Higher magnification image of the same bridging vein (arrow) as shown in image C, draining into the left TS (asterisk).

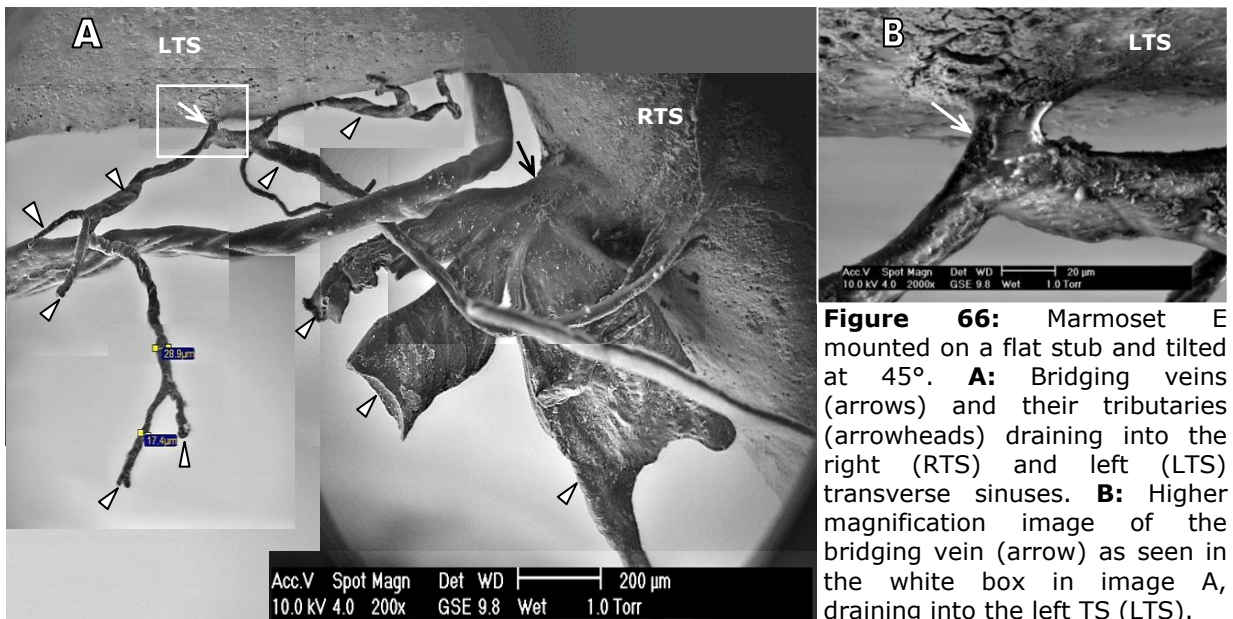
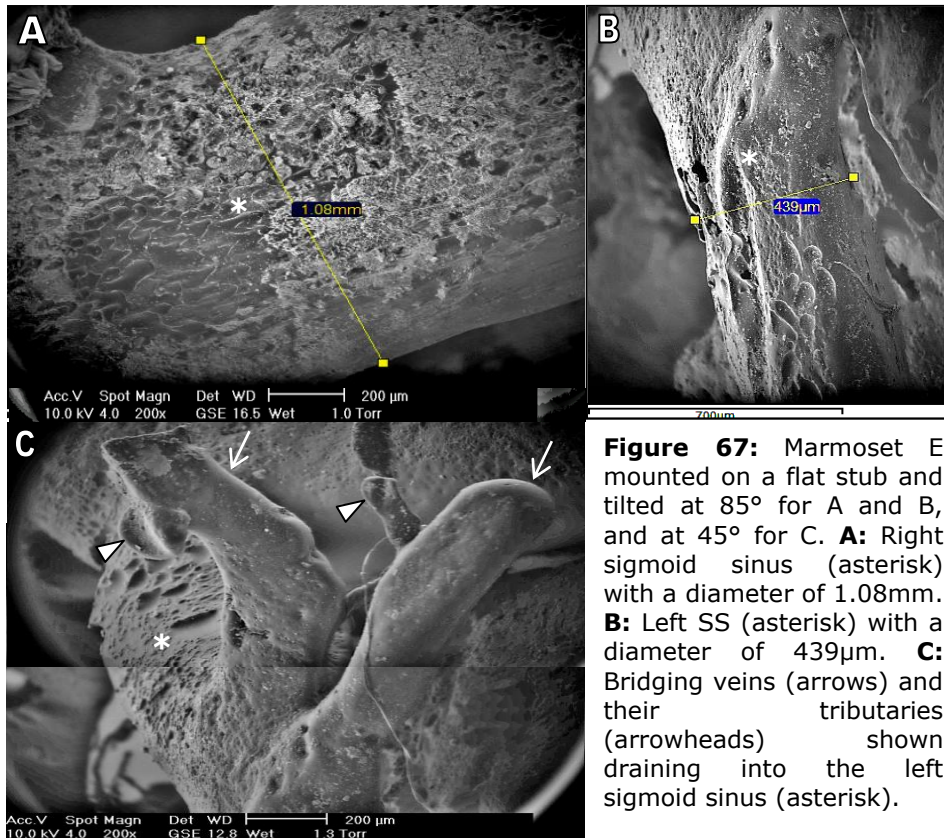
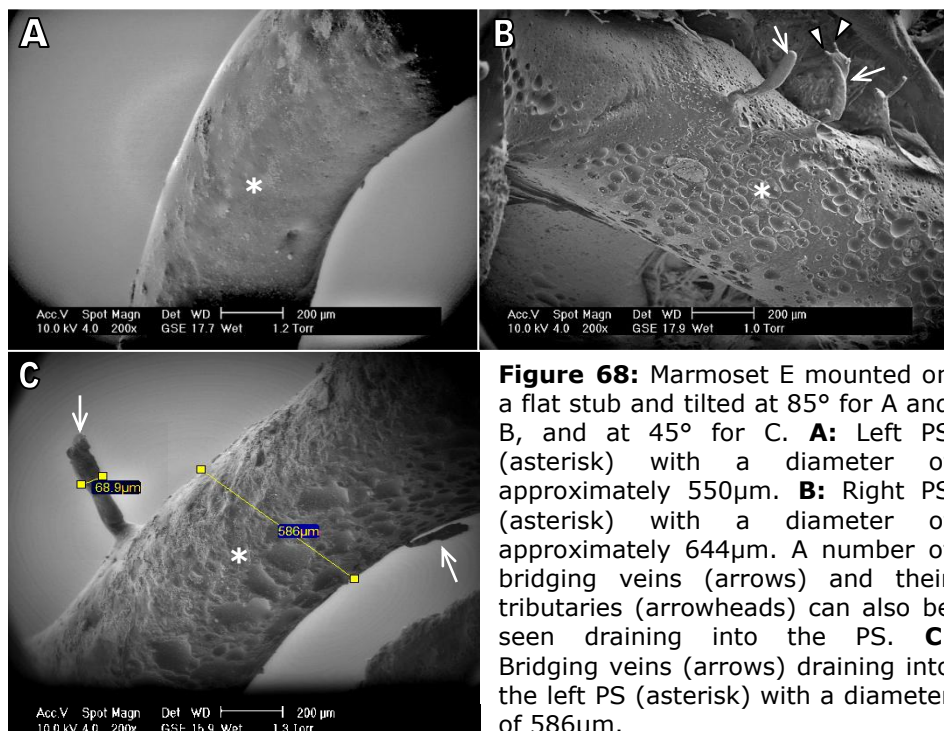


Figure 66: Marmoset E mounted on a flat stub and tilted at 45°. **A:** Bridging veins (arrows) and their tributaries (arrowheads) draining into the right (RTS) and left (LTS) transverse sinuses. **B:** Higher magnification image of the bridging vein (arrow) as seen in the white box in image A, draining into the left TS (LTS).

The Sigmoid Sinuses (SS)



The Petrosquamous Sinus (PS)



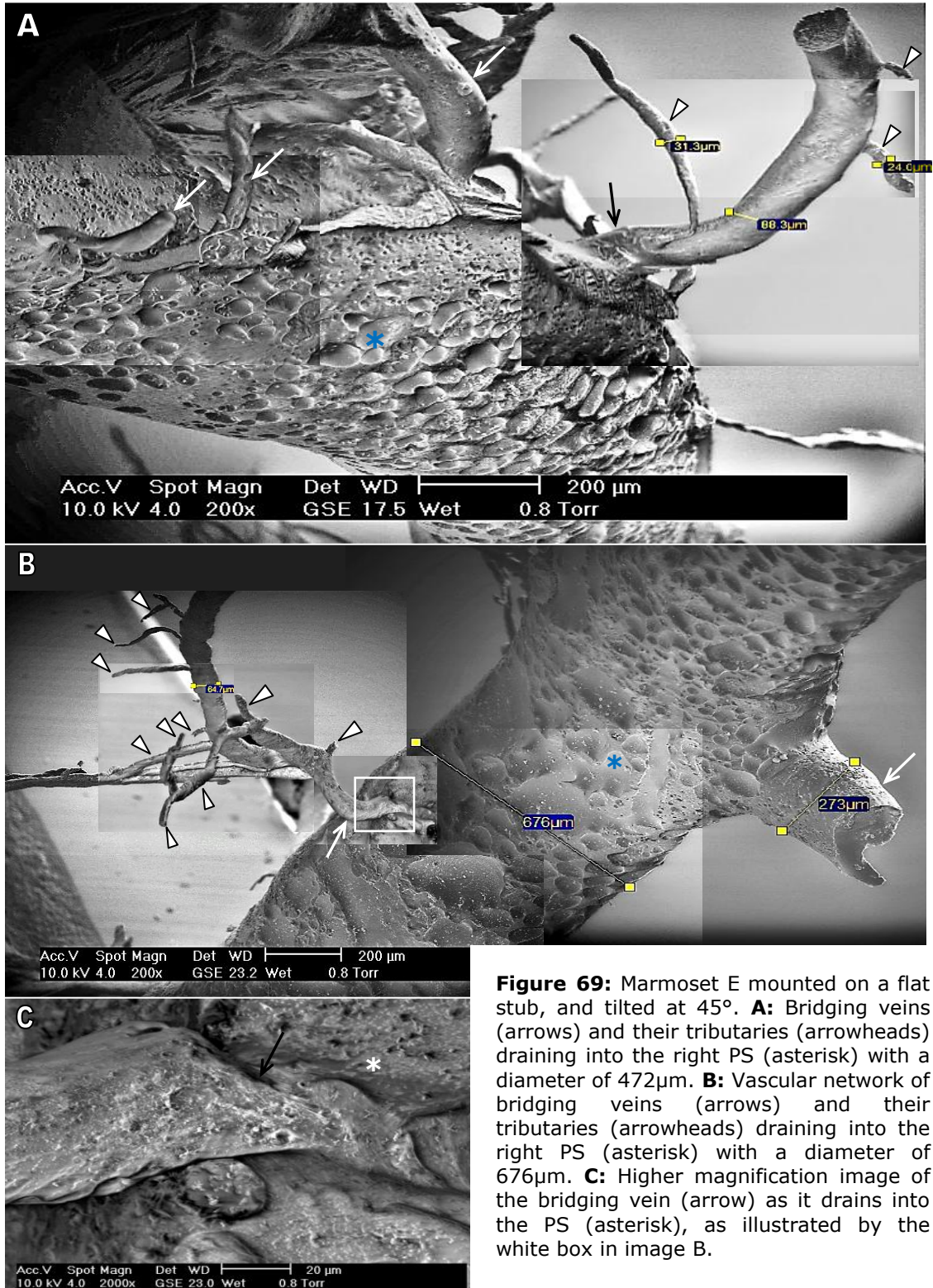


Figure 69: Marmoset E mounted on a flat stub, and tilted at 45°. **A:** Bridging veins (arrows) and their tributaries (arrowheads) draining into the right PS (asterisk) with a diameter of 472µm. **B:** Vascular network of bridging veins (arrows) and their tributaries (arrowheads) draining into the right PS (asterisk) with a diameter of 676µm. **C:** Higher magnification image of the bridging vein (arrow) as it drains into the PS (asterisk), as illustrated by the white box in image B.

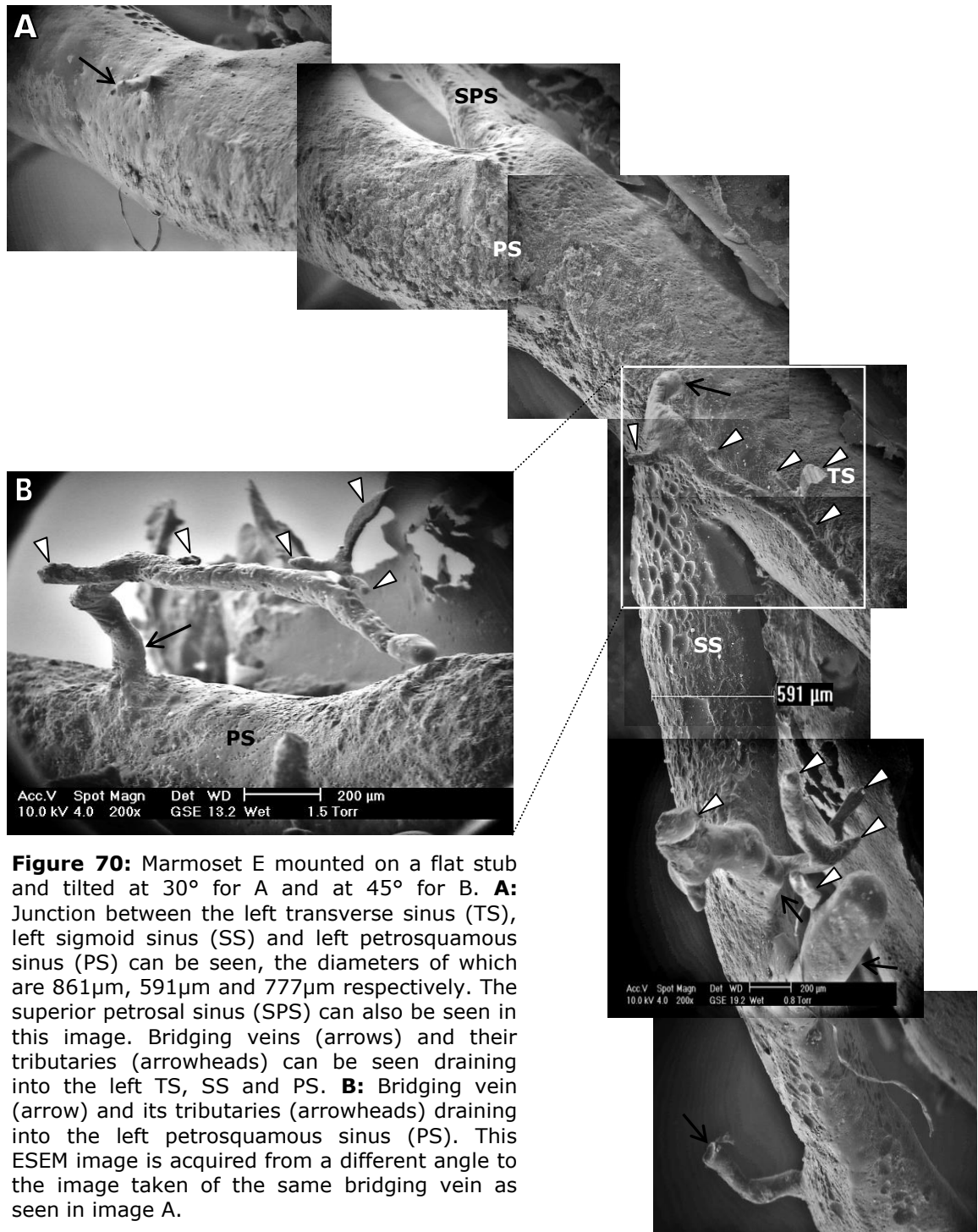


Figure 70: Marmoset E mounted on a flat stub and tilted at 30° for A and at 45° for B. **A:** Junction between the left transverse sinus (TS), left sigmoid sinus (SS) and left petrosquamous sinus (PS) can be seen, the diameters of which are 861 μ m, 591 μ m and 777 μ m respectively. The superior petrosal sinus (SPS) can also be seen in this image. Bridging veins (arrows) and their tributaries (arrowheads) can be seen draining into the left TS, SS and PS. **B:** Bridging vein (arrow) and its tributaries (arrowheads) draining into the left petrosquamous sinus (PS). This ESEM image is acquired from a different angle to the image taken of the same bridging vein as seen in image A.

ESEM Imaging of 1mm Coronal Sections of Resin Perfused Brain and Skull

Images of 1mm coronal sections of resin perfused marmoset specimens were acquired using ESEM. This was to try to illustrate the detailed structure of the different meningeal layers which lie in between the skull and surface of the brain, in relation to any cerebral vessels traversing across these layers. However due to incomplete filling of the vessels, ESEM images obtained were insufficient to allow for any further analysis of the specimen.

4.3.1.3. Histology: LM and TEM Imaging of Pre-fixed Marmoset Material

Following careful dissection of the marmoset specimens, tissues requiring further examination were sampled for further processing and analysis involving LM and TEM imaging.

Once embedded in resin, the tissue samples were cut into 1 μ m thick semi-thin sections and stained with Toluidine Blue O before being analysed using LM (Figure 71A and B; Figure 72B, C and D). This was to obtain an overall image of the whole specimen and to gain an idea as to the anatomical structures present in the sections. It also enabled identification of regions of interest that could be further analysed with TEM. Once these areas were identified via LM, the same resin embedded samples were then cut into 80nm thick ultra-thin sections and stained before undergoing TEM imaging (Figure 71C, D and E; Figure 73).

Images in Figure 71 were acquired from a sample of the SSS of a marmoset specimen. Figure 71A demonstrates an overall picture as to the structure of the SSS, whereas the TEM images in Figure 71C, D and E illustrate the ultrastructure of the dural membrane layers which make up the dural venous sinuses. In these TEM images of the SSS, there are large numbers of collagen fibrils (CT1 and CT2) orientated in different directions, as well as endothelial cells (EC), endothelial cell nuclei (EN) and pericytes (PC). There are also a number of intradural vessels (ID) seen situated in between the outer endosteal layer and inner meningeal layer of the dural membrane.

Figure 72A illustrates a bridging vein (black box) with an average lumen diameter of 118 μ m (the smallest measurable diameter being 2 μ m and the largest measurable diameter being 233 μ m), which traverses across the subdural space (SDS) from the surface of the brain (BT) still covered by the pia and arachnoid membranes, to the dura mater layer above (DM). An overall view of the bridging vein alongside the dural membrane can be seen in image B, as well as a higher magnification image of the same vessel in image D. The histological structure of the layers of the vessel wall, as well as the vessel shape, confirms that this is a vein (and not an artery) (Figure 72B and D). The vessel walls are thin and composed of an inner endothelial layer (tunica intima), a thin middle layer of muscular and elastic tissue (tunica media), as well as a thin outer layer of connective tissue (tunica adventitia), in comparison to a thicker and more developed muscular tunica media often seen in arteries. The shape of the vessel is

also elongated and irregular, distinguishing it from the often rounded regular shape of the lumina of accompanying arterial vessels. The detailed ultrastructure of the wall of this same vessel is illustrated in the TEM images shown in Figure 73. The image illustrated in Figure 73A is an overall photomontage image of the whole vessel, whereas higher magnification TEM images of the vessel wall are illustrated in images B and C. The ultrastructure of wall of this bridging vein is composed of numerous collagen fibrils (CT1 and CT2) orientated in different directions, as well as many other structures including endothelial cells (EC), endothelial cell nuclei (EN) and pericytes (PC), which are all indicated in Figure 73.

Alongside the vessel in Figure 72B is the dural membrane (through which the bridging vein penetrates) that contains many intradural veins (Figure 72C). The size of these vessels varies from an average diameter of 22.5 μ m (19 μ m; 26 μ m) to 147.5 μ m (45 μ m; 250 μ m); some of the layers of the walls of these vessels can also be distinguished (as described above).

Unfortunately, although macrographic images of fine subdural veins (that do not drain directly into the venous sinuses like traditionally defined bridging veins) of the marmoset material were acquired, further histological analysis such as LM and TEM imaging of the fine subdural vein specimens in particular could not be carried out. This was due to the quality of this prefixed material, which made it difficult to dissect out the fine venules without causing them to rupture.

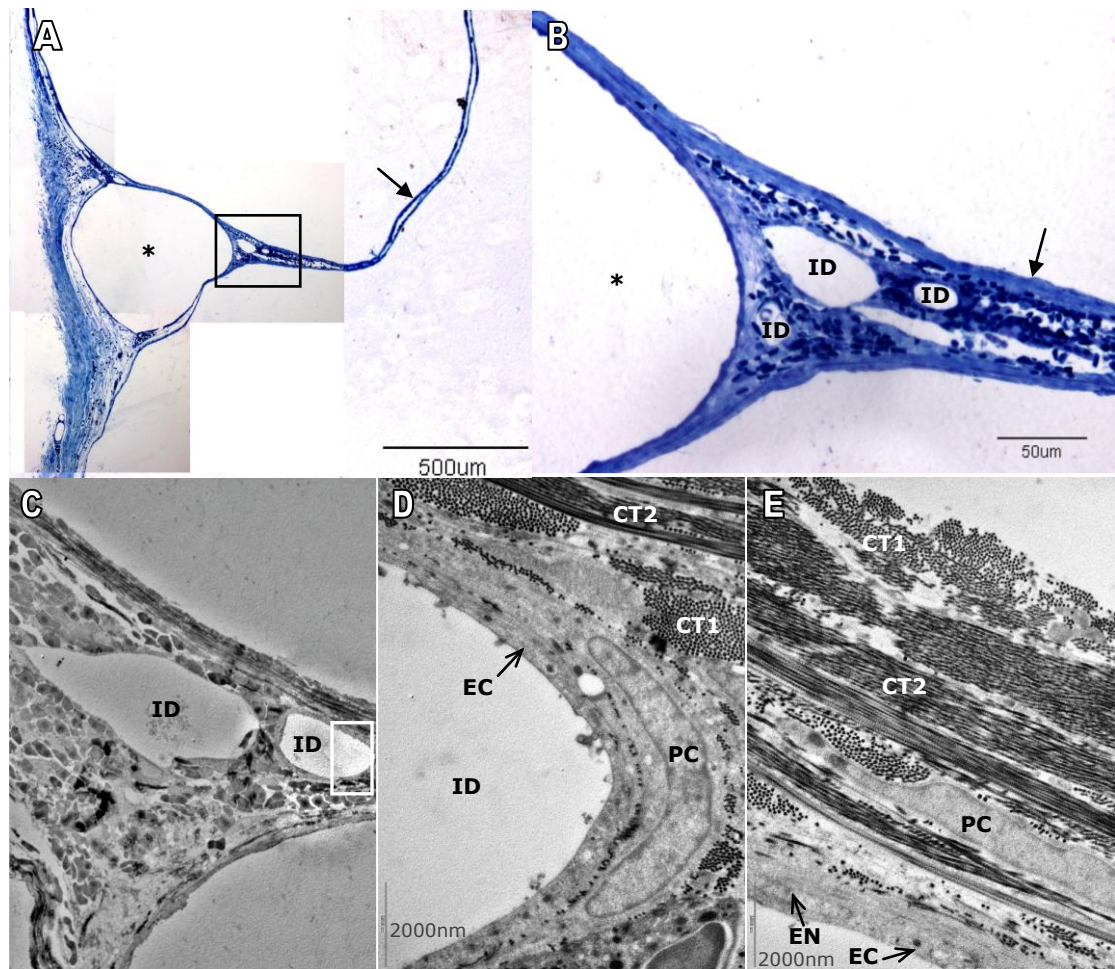


Figure 71: LM and TEM images of a cross section of the SSS of an infant *Marmoset B*. **A, B:** LM images of a semi-thin section ($1\mu\text{m}$) of a marmoset SSS, at magnifications of $\times 2.5$ and $\times 20$ respectively. The venous sinus lumen (asterisks), falx cerebri (arrows), and intradural vessels (ID) are indicated. **C, D, E:** TEM images at magnifications of $\times 610$, $\times 8200$ and $\times 8200$ respectively. Transverse (CT1) and longitudinal (CT2) sections of collagen fibrils, as well as endothelial cells (EC), endothelial cell nuclei (EN) and pericytes (PC) are indicated.

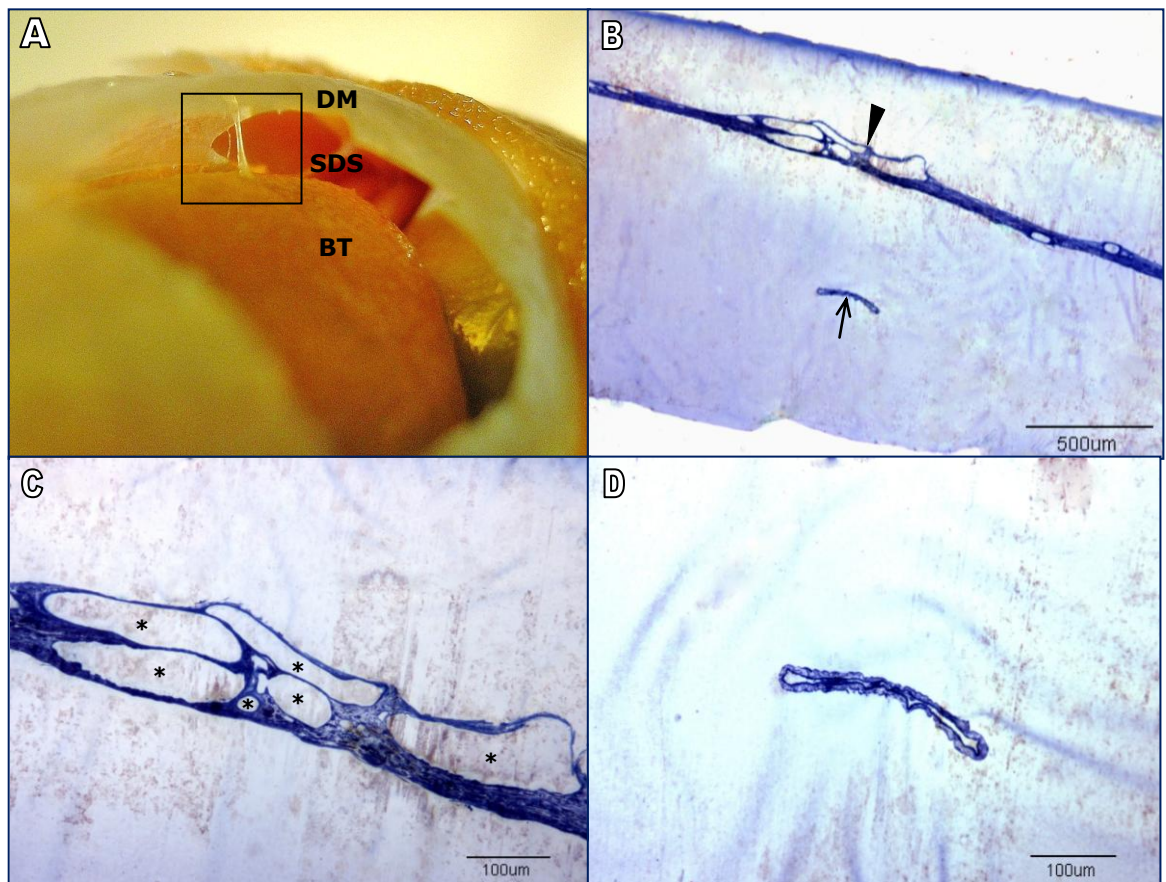


Figure 72: Images of a cross section of a bridging vein and the dural membrane of an adult *marmoset*. **A:** Macrograph of a bridging vein (black box) traversing across the subdural space (SDS) from the surface of the right hemisphere of the brain (BT), through the dura mater layer (DM), and into the SSS above. **B:** LM image (x2.5) of a semi-thin (1µm thick) section of the bridging vein (arrow) as seen in image A, and the dural membrane (arrowhead) into which the vessel ultimately drains. **C:** Higher (x10) magnification image of the dural membrane shown in image B. Here, many intradural vessels can be seen (asterisks). **D:** Higher (x10) magnification image of the bridging vein shown in image B.

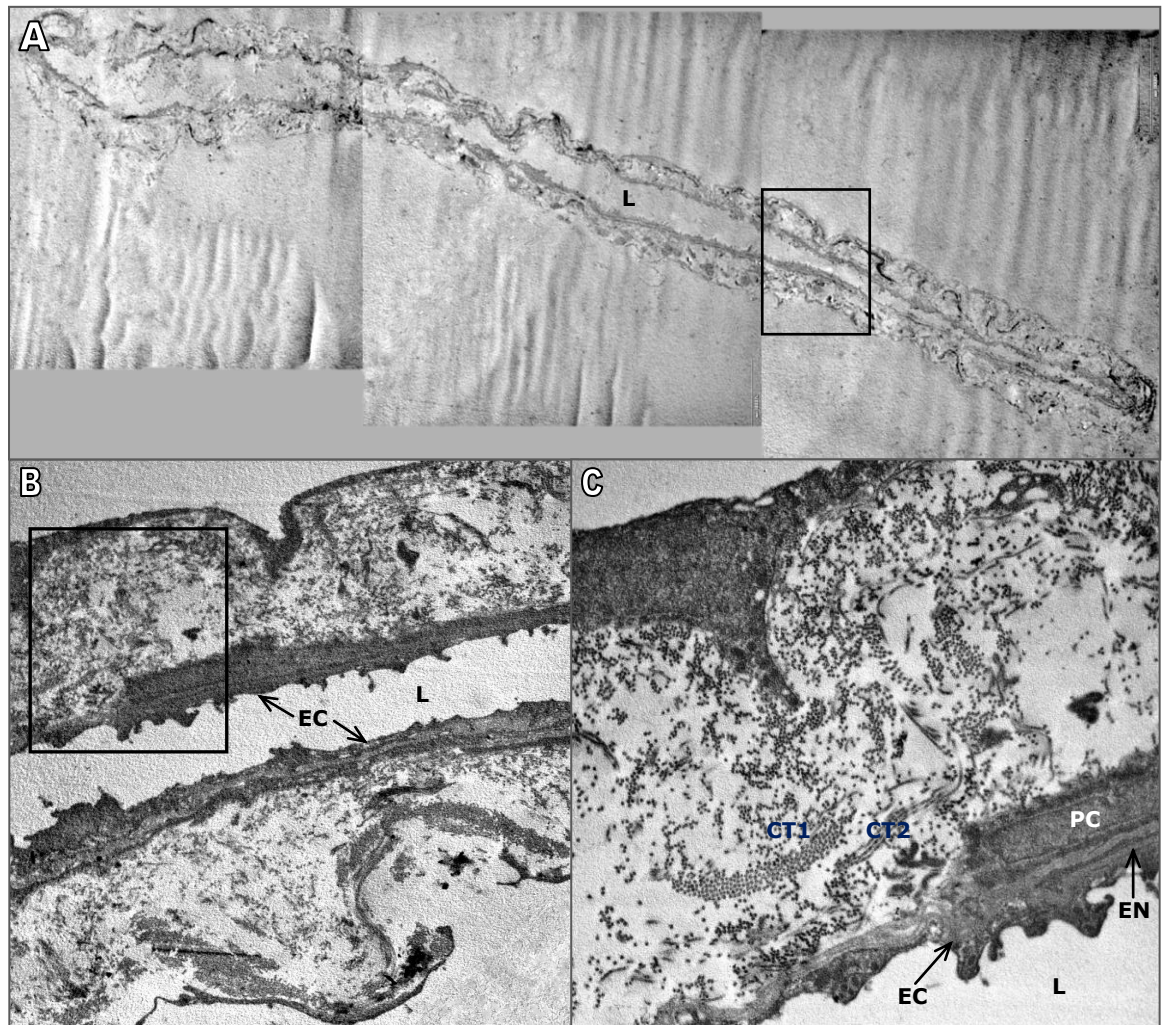


Figure 73: TEM images of an ultra-thin 70nm thick section of an adult *marmoset A* specimen (also illustrated in Figure 72). **A:** TEM image (x790) photomontage of the same bridging vein as illustrated in Figure 72D. **B:** Higher magnification image (x2550) of the bridging vein illustrated in image A (black box). **C:** Higher magnification image (x8200) of the bridging vein illustrated in image B (black box). Transverse (CT1) and longitudinal (CT2) sections of collagen fibrils, as well as endothelial cells (EC), endothelial cell nuclei (EN) and pericytes (PC) are indicated. The vessel lumen (L) is also indicated in each case.

4.3.1.4. Magnetic Resonance Imaging (MRI)

MRI scanning of prefixed adult and infant (*Marmoset E* and *Marmoset F* respectively) primate samples was carried out using a specialised 2.35T animal MRI machine (Bruker). However the images that were acquired were not very clear. This was due to interference of the MRI signals caused by the fixative within the tissues, as well as entry of air emboli into the vasculature during tissue preparation, meaning that imaging of small calibre vessels surrounding the meningeal layers could not be carried out effectively.

Although it was determined that submersion of the fixed tissue in PBS solution for a number days may remove excess fixative solution and air emboli, and therefore decrease signal distortion, it was decided that the quality of MRI scans that could be produced would not be sufficient for use in this particular project. After these preliminary MRI scans, it was also determined that this particular MRI machine would be unlikely to be able to produce images of the cerebral vessels at a high enough resolution required for the purposes of this project.

4.3.1.5. MicroCT Imaging

MicroCT scanning of the VCC of marmoset specimen E (Figure 74) was carried out using a SkyScan 1174 machine (Bruker). As can be seen, resin perfusion of this pre-fixed marmoset material did not produce vascular casts as complete as those produced in previous experiments involving resin perfusion of rat specimens, whereby the resin was perfused into the vascular system immediately after death.

During the resin perfusion process of the macaque specimen, there was a build-up of a significant amount of back-pressure which made the procedure extremely difficult. This was most likely due to the long duration of time in between the initial fixation of the tissue and subsequent perfusion of resin into the vasculature, leading to a decrease in the elasticity of the vessels to occur over time. However in this case, as the resin was perfused into the vascular system via the superior vena cava (as opposed to the entrance to the ascending aorta in previous rat perfusion experiments) the resin was able to perfuse into the majority of the venous sinuses and their tributaries, which are the most important areas for further analysis in this project.

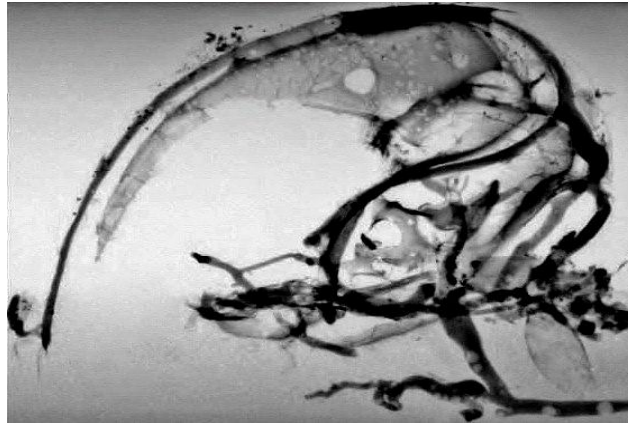


Figure 74: Projection image from the microCT scan data of the VCC of *Macaque E* specimen.

In view of these results, regarding the methodology for resin casting in general, it is essential for perfusion of pre-wash, fixative and resin to be carried out immediately after the killing of the animal to allow production of complete and detailed resin casts of the cerebral vasculature. Although it would be ideal for perfusion to be carried out via the superior vena cava, as was done in the marmosets, it has been shown that it is more important that resin perfusion is carried out as soon after death of the animal as possible in order to produce well perfused vascular casts. This is an important consideration since a significant amount of time would be spent isolating and cannulating the superior vena cava.

4.3.1.6. Computer-Aided Analysis of MicroCT Imaging Datasets

The microCT imaging datasets that were acquired from scanning of the cerebral VCC of marmoset specimen E were used to generate a 3D volumetric reconstruction of the resin cast using specialised software (SkyScan-1174v2, Bruker). These microCT projection images were then restructured using the same software to create a video providing a 360° view of the whole VCC specimen.

The VCC of this particular marmoset specimen was not detailed enough for further volume rendering and analysis of the data to be particularly useful for the purposes of this project. However it would be possible to carry out detailed analysis (such as approximating vessel size) of microCT imaging datasets of more complete VCCs using the same methods as described in section 4.2.2.11.

4.3.2. Macaque (*Macaca mulatta*)

4.3.2.1. Gross Dissection of Macaque Material

Careful dissection of both resin perfused and fixed macaque material was performed to reveal both bridging veins (Figure 75A and B; Figure 76A, B and C) draining directly into the venous sinuses, as well as other subdurally located fine vessels (Figure 75C and D; Figure 76C and D). Macrographs were taken of these specimens, before dissecting them out to further process and analyse using histological techniques such as LM and FM.

Figure 75A illustrates a macrograph of a grossly dissected resin perfused macaque specimen which shows fine networks of small subdural veins which are situated within the subdural space. These vessels can be seen draining directly into bridging veins, which in turn drain into the right transverse sinus of the brain. This shows that even on a macrographic scale, fine subdural veins can be seen, which drain directly into the bridging veins as they traverse across the SDS and into the venous sinuses. Similar structures to these networks of subdural veins have also been found through gross dissection of both marmoset and human cadaveric material.

Further examples of bridging veins are illustrated in Figure 76A, which shows a number of bridging veins that traverse the SDS and drain directly into the SSS. Figure 75C and D, as well as Figure 76D illustrate fine subdural vessels which also traverse the SDS, however do not drain directly into the venous sinuses (unlike traditional bridging veins) but penetrate the inner meningeal layer of the dura mater and presumably traverse along the intradural space before either draining into a venous sinus directly or indirectly via a bridging vein.

Figure 76C further illustrates both bridging veins and subdural vessels which pass through the SDS and traverse from the brain surface above to the tentorium cerebelli below, whereas similar veins illustrated in Figure 75B and Figure 76B this time traverse the SDS between the tentorium cerebelli above, and the cerebellar surface below. These images therefore illustrate the existence of bridging veins and subdural vessels that traverse the SDS both above and below the tentorium cerebelli (which is an inner reflection of the dura mater layer).

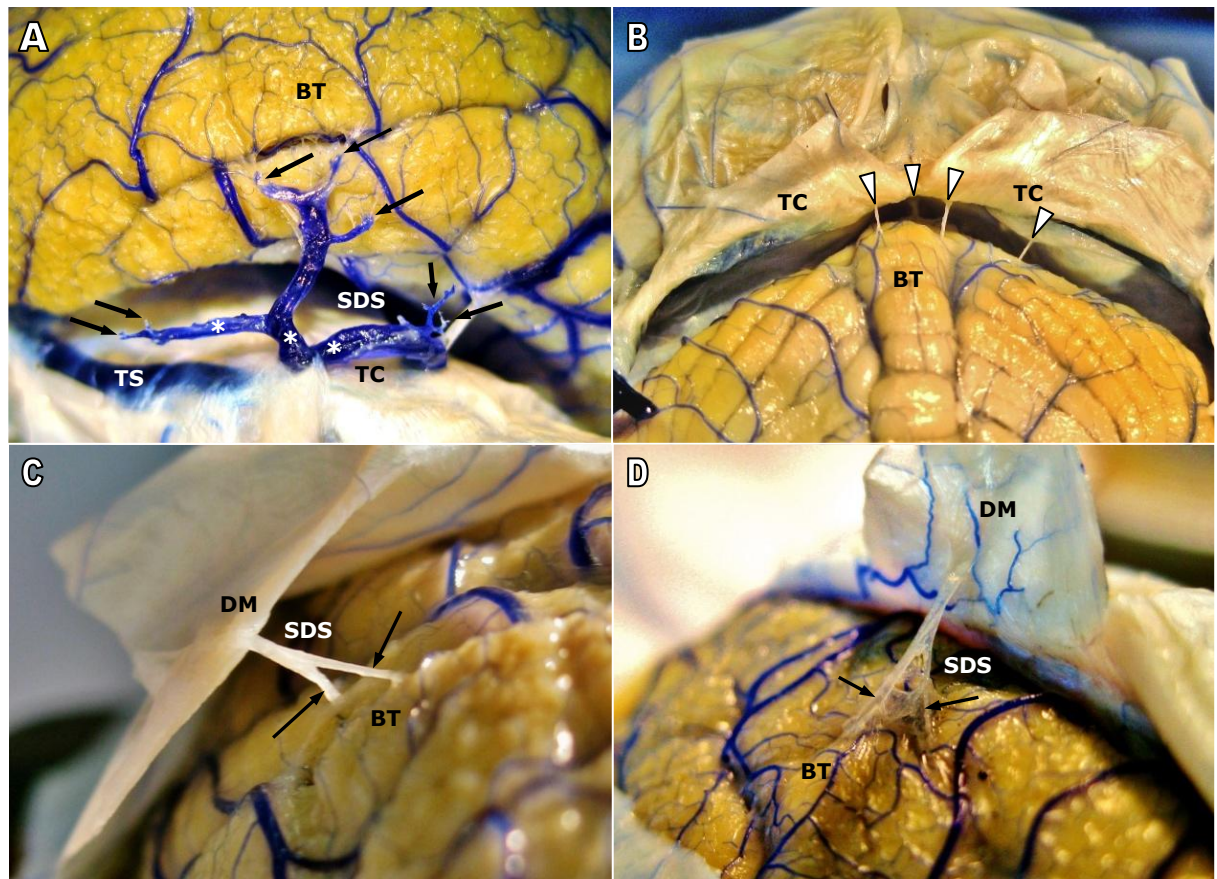


Figure 75: Grossly dissected resin perfused cerebral vessels of *Macaque D*. **A:** Resin perfused macaque sample illustrating the right transverse sinus (TS), into which a number of converging bridging veins (asterisks) can be seen to drain. There are further networks of smaller subdural veins (arrows), situated within the subdural space (SDS), which can be seen then draining into the bridging veins of the transverse sinus. **B:** Bridging and subdural veins (they cannot be differentiated with certainty from this image alone) (arrowheads) traversing across from the cerebellar brain surface (BT) to the tentorium cerebelli (TC) above. **C, D:** Subdural vessels (arrows) traversing across the subdural space (SDS) from the arachnoid membrane covering the brain tissue (BT) below, to the dural membrane (DM) above.

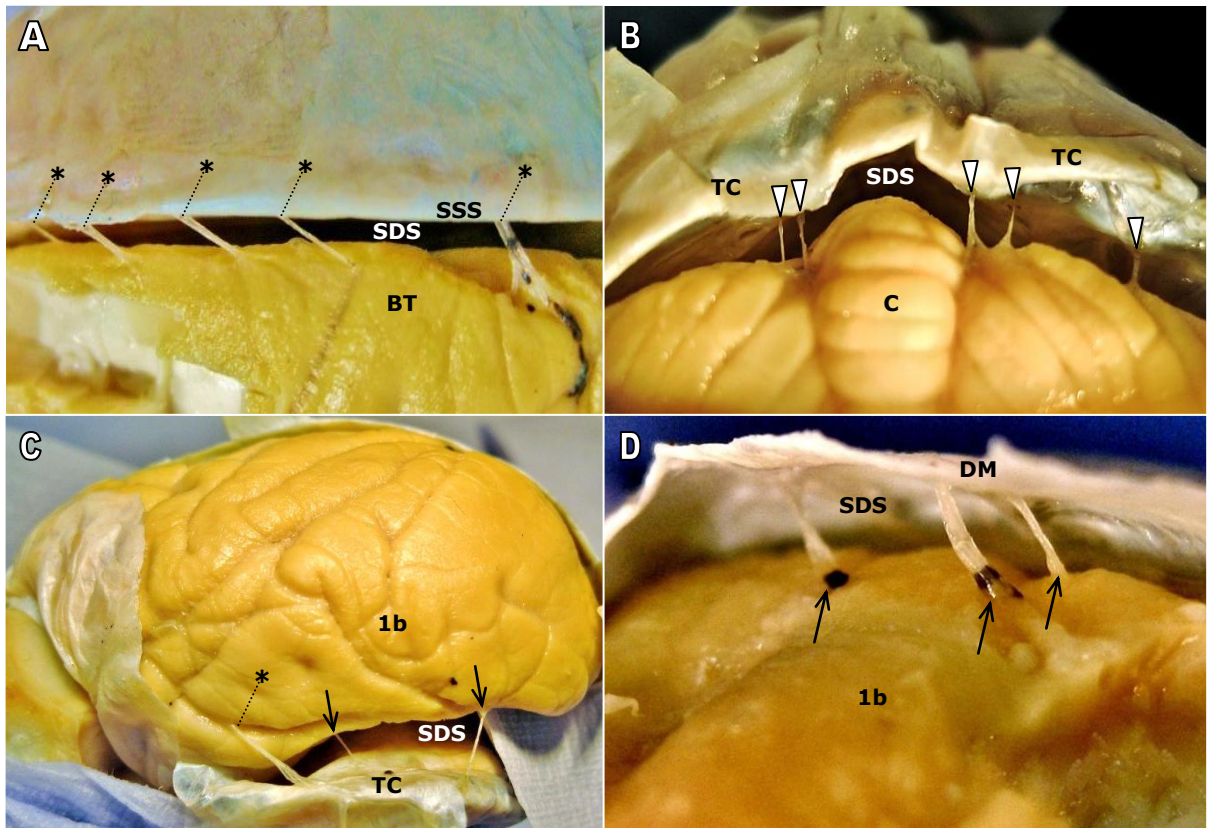


Figure 76: Grossly dissected *Macaque A* sample, illustrating the cerebral vessels of the brain. **A:** Bridging veins (asterisks) draining from the arachnoid membrane covering the brain tissue (BT), across the subdural space (SDS), and into the superior sagittal sinus (SSS) above which is situated within the 2 layers of the dural membrane. **B:** Bridging and subdural veins (they cannot be differentiated with certainty from this image alone) (arrowheads) traversing across from the cerebellar surface (C) to the tentorium cerebelli (TC) above. **C:** A bridging vein (asterisk) and subdural vessels (arrows) traversing across the subdural space (SDS) from the left cerebral hemisphere (1b), down to the tentorium cerebelli (TC) inferiorly. **D:** Subdural vessels (arrows) traversing across the subdural space (SDS) from the left cerebral hemisphere (1b) to the dural membrane (DM) above.

4.3.2.2. Vascular Resin Casting and ESEM Imaging

Following soft tissue maceration, osmocation and lyophilisation of the resin perfused macaque C, the VCC was then imaged using ESEM.

ESEM images of the macaque VCC shown in Figure 77 were acquired using a Philips XL30 FEG ESEM machine (Oxford Instruments INCA Microanalysis System), to allow more detailed analysis of the morphology of the cerebral vessels; particularly the venous sinuses, bridging and subdural veins, and their surrounding vessels.

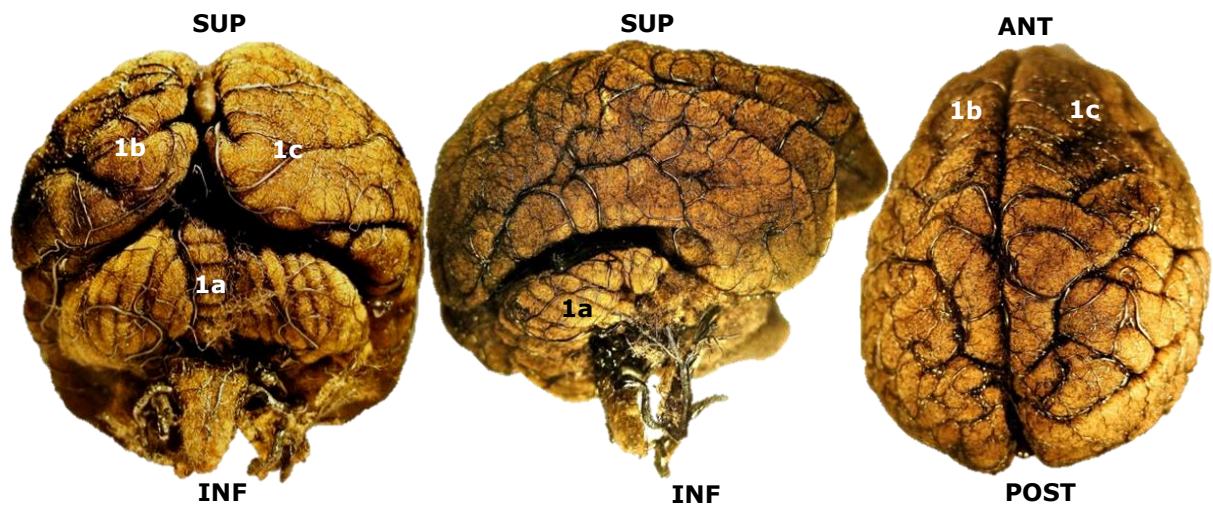
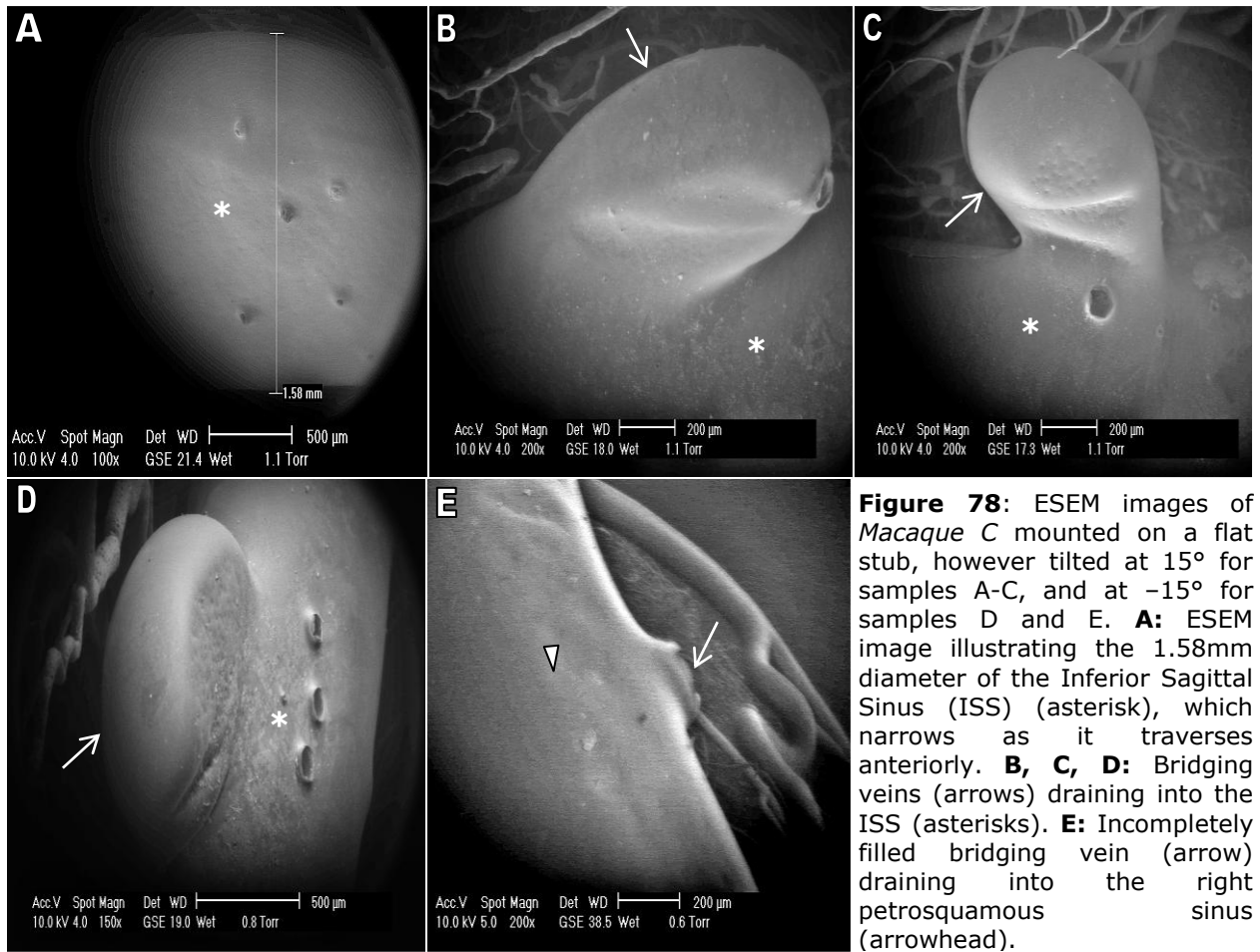


Figure 77: Macrographs of the VCC of Macaque specimen C, illustrating the posterior, lateral and superior views of the cast (from left to right). The superior (SUP), inferior (INF), anterior (ANT) and posterior (POST) orientations of each image are indicated, as well as the cerebellum (1a), left hemisphere (1b) and right hemisphere (1c).

ESEM images of the macaque VCC illustrate the large (1.58mm) diameter of the inferior sagittal sinus (ISS), as well as the size and shape of the bridging veins seen draining into this sinus. The diameter of bridging veins illustrated in Figure 78B, C and D are 800 μ m, 650 μ m and 1395 μ m respectively. As was seen with ESEM imaging of the rat and marmoset VCC specimens, distinct narrowing of the bridging veins can be seen at the junction point as the vessel drains into the venous sinus. A smaller bridging vein draining into the petrosquamous sinus (PS) with a diameter of 258 μ m is also illustrated in Figure 78E.



ESEM imaging of the VCC of macaque C also shows that there were a number of incompletely filled bridging veins draining into the ISS (Figure 79A, B and C). This is not thought to be due to incomplete filling of the fine vasculature of the specimen in general, as other fine cerebral vessels of up to 3µm in diameter, were successfully perfused and imaged in the same VCC (Figure 79D). This incomplete filling of the vessels is thought to be possibly due to a reactive mechanism of the vessels as the specimen is being perfused. Possible mechanisms regarding this incomplete filling will be further discussed in Chapter 5.

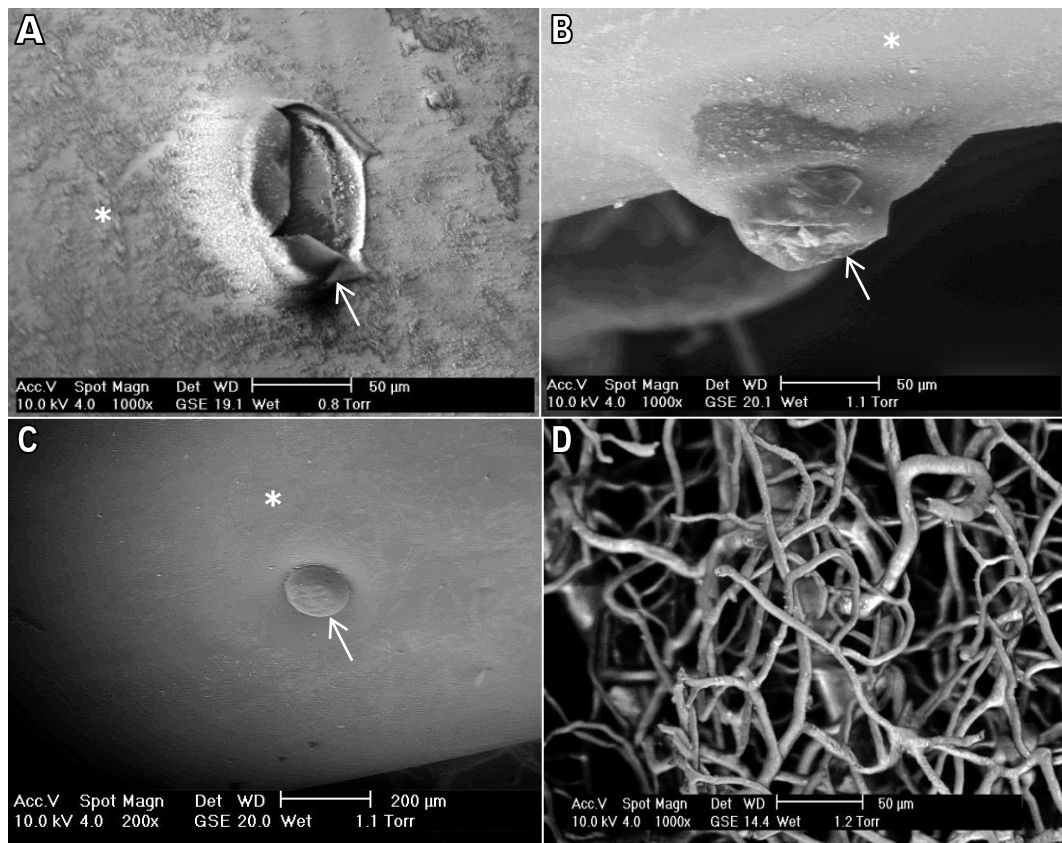
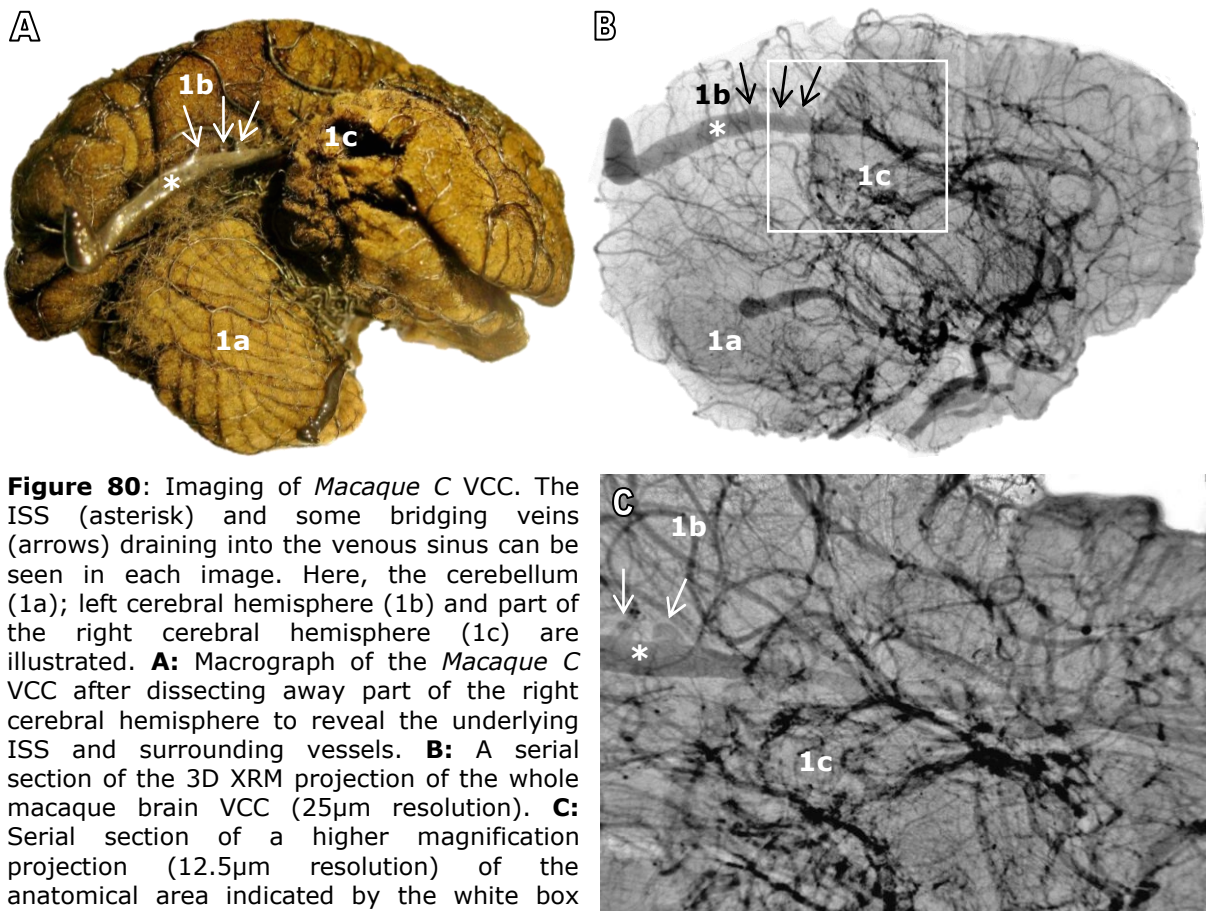


Figure 79: ESEM images of *macaque C* VCC. **A, B, C:** Incompletely filled bridging veins (arrows), draining into the ISS (asterisks). This specimen was mounted on a flat stub and tilted at -15° in image A, and at $+15^\circ$ in images B and C. **D:** ESEM image illustrating complete filling of resin into other much finer cerebral vessels, in contrast to images A, B and C acquired from the same VCC.

Due to incomplete filling of a number of the venous sinuses of *macaque C*, unfortunately not enough data could be acquired to allow further statistical analysis of the vessels, particularly regarding size range and distribution of bridging veins and their tributaries draining into the venous sinuses.

4.3.2.3. 3D XRM and Computer-Aided Analysis of Imaging Datasets

The vascular corrosion cast of *Macaque C* was scanned with a 3D XRM scanner (VersaXRM-500, Xradia). This microscope works in a similar way to that of the microCT scanner however allows further magnification of the specimen at a larger working distance than is possible with the conventional microCT scanner. Therefore, this was ideal for imaging of the comparatively larger macaque VCC sample compared to that of the rat, while also capable of 3D imaging of the sample at a much higher spatial resolution ($<0.7\mu\text{m}$) than is possible with a microCT scanner. A 3D XRM scan of a macaque VCC was first carried at a low resolution of $25\mu\text{m}$ (Figure 80B) which was necessary to allow the whole vascular cast to be captured in the same field of view. A region of interest (ROI) was then selected from the dataset and this area was then scanned at a higher resolution of $12.5\mu\text{m}$ (Figure 80C) to obtain more detailed information regarding the finer vascular structures.



From the original dataset of the 3D XRM scans of the *macaque E* cerebral VCC, coronal (XY) serial section images were constructed (one of these sections is illustrated in Figure 81A). These images were then processed using volume rendering software CTvox (Bruker) and reconstructed into a 3D format. Specific thresholds were then applied to the dataset to filter out any extraneous noise, such as the container in which the sample was scanned, to produce the image illustrated below in Figure 81B. The main issue with applying thresholds to filter out extraneous noise from these scanning datasets was that sometimes the very fine vessels that were being analysed were also removed along with the background noise due to their small size. This is therefore an important area in which further improvement in the processing technique is required, and hence in which future work will be carried out. This will be further discussed in section 4.4.

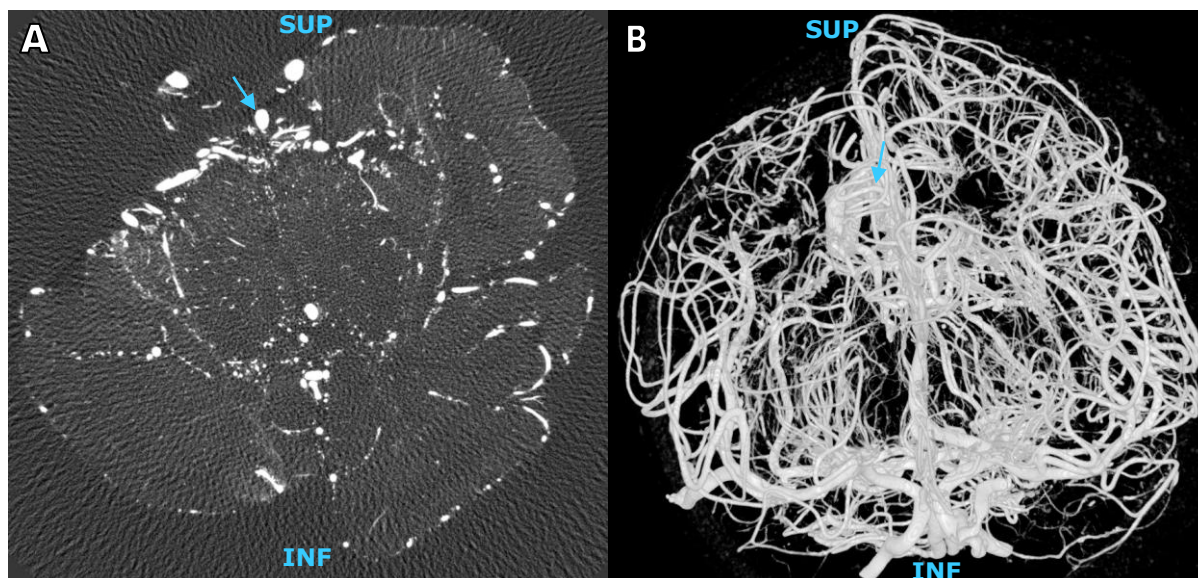


Figure 81: **A:** A coronal section from the 3D XRM scanned dataset of Macaque C VCC. **B:** 3D reconstruction of the 3D XRM scanning dataset of macaque C cerebral VCC. The superior (SUP) and inferior (INF) parts of the resin cast, as well as the ISS (arrows) are indicated in both images **A** and **B**.

Although the 3D reconstruction of the scanning data (Figure 81) using volume rendering software CTvox (Bruker) was able to produce relatively detailed 3D images of the VCCs, the software was unable to determine the size of the individual vessels. Therefore the 'Simple Neurite Tracer' plug-in for the computer software Image J (NIH) was used for volume rendering of the 3D XRM scanning dataset, approximating the local thicknesses of the macaque cerebral vessels and categorising them by colour. These measurements were illustrated via a

calibration bar (Figure 82), in which the larger the vessel diameter, the lighter the colour that was indicated in the image. Each increase by one unit on this calibration bar represents an increase in approximately 65 μ m in the vessel diameter.

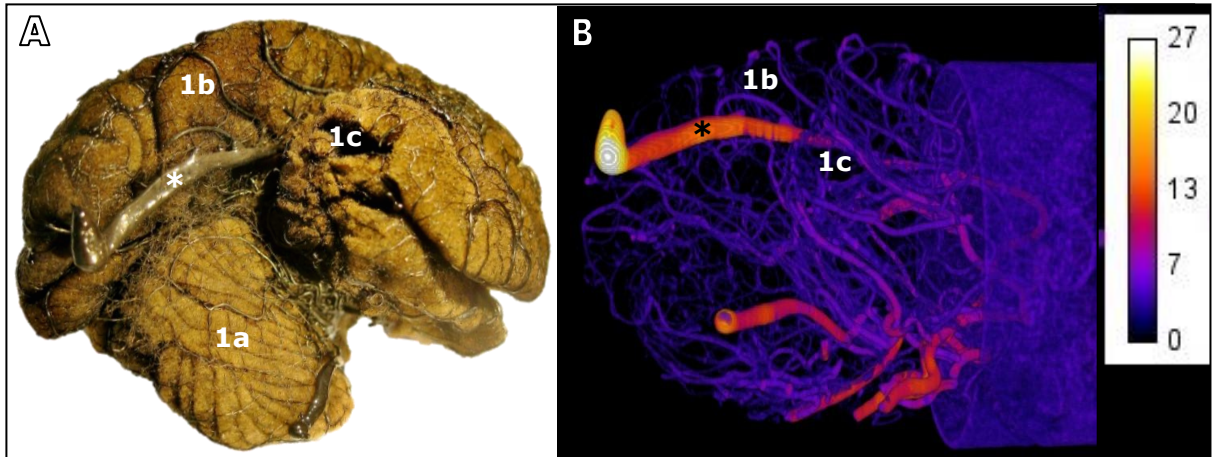


Figure 82: Images of the VCC of *Macaque C* with the ISS (asterisk), cerebellum (1a); left cerebral hemisphere (1b) and right cerebral hemisphere (1c) being illustrated. **A:** Macrograph of the *Macaque C* VCC after dissecting away part of the right cerebral hemisphere to reveal the underlying ISS and surrounding vessels. **B:** 3D reconstructed image from the 3D XRM dataset of the same macaque VCC shown in image A, alongside a calibration bar (whereby 27 on the scale represents a vessel diameter of approximately 2mm, and 0 represents 0mm) indicating the approximate sizes of all the cerebral vessels.

Although these preliminary results extracted from the 3D XRM imaging data are relatively simple, they illustrate that it is possible for these methods of segmentation, volume rendering and further analysis to be carried out, as well as further improved. Further information regarding how these methodological improvements will be carried out will be discussed in section 4.4.

4.3.2.4. Gold Nanoparticles and 3D XRM Imaging

Macaque experiments involving perfusion of gold nanoparticles into the cerebral vasculature (along with PU4ii resin) were carried out, in the hope of improving quality of the images acquired via 3D XRM.

Figure 80B shows an example of the 3D XRM images produced from scanning of macaque C following perfusion with a low dose (40mg) of gold nanoparticles. Reviewing the results, the use of gold nanoparticles was found to improve the

quality of the 3D XRM images acquired when compared to microCT images produced from similar VCCs without perfused gold nanoparticles (Figure 45A). In each case, both machines were set at a similar scanning resolution to allow a fair comparison between the results.

However, further information regarding relative improvement in the quality of the images acquired between different concentrations of gold nanoparticles could not be accurately investigated in these experiments. This is due to the differing success as to the extent of resin perfusion into the fine vasculature of each macaque perfusion experiment (described in section 4.2.2.1.), which meant that macaque specimens C and D were perfused more completely than macaque specimen B for example. This meant that although ideally macaque D should have also been processed and scanned using 3D XRM imaging (as it had been perfused with a normal dose of 160mg of gold nanoparticles), instead it was determined that more useful results were more likely be obtained through gross dissection and further micrographic analysis of the tissues. Macaque D therefore did not undergo 3D XRM imaging. However, further work involving vascular perfusion of different concentrations of gold nanoparticles into macaque specimens (followed by 3D XRM imaging) could be carried out if ethical approval for the use of further macaque material could be obtained.

4.3.2.5. Histology and FM Imaging

FM was used to carry out analysis of macaque brain tissue that was perfused with resin mixed with fluorescent powder. The FM images that were acquired were overlaid onto BF images of the same histological sections (H&E stained, DPX mounted), so that the fluorescence detected within the resin perfused vessels would allow easy identification of the cerebral vessels in relation to their surrounding histological structures.

Figure 83A is a FM image of a histological section of a resin perfused macaque bridging vein (a macrograph of the same vessel is illustrated in Figure 75A). The section was not de-waxed or mounted onto a coverslip, as the image was acquired immediately after wax embedding and microtome sectioning of the tissue sample. This meant that the resin perfused into the vessel lumen remained *in situ* (as the surrounding supporting wax was still present), however fluorescence emitted from the tissue during FM imaging was minimal. Therefore artificial colour (red) was

added after acquisition of the image (GIMP 2 software), to allow clearer identification of the location of the resin contained within vessel lumina.

As well as being prepared using the method described above, other similar histological sections were prepared via de-waxing, H&E staining and mounting in DPX, before undergoing FM imaging. The most notable difference that can be seen in Figure 83 between the FM images of wax embedded specimens and de-waxed specimens is that resin is still present within the bridging vein (asterisk) and subarachnoid vessels (arrows) in the wax embedded specimens (Figure 83A), as opposed to the empty vessel lumina of the same vessels in de-waxed specimens (Figure 83B and C).

Figure 83B shows slide 61 from the serial cross-sections that were cut from macaque D. These sections were collected starting from the dural membrane layer down to the brain tissue. Figure 83C shows slide 96 from the same set of macaque serial sections. This image illustrates a bridging vein (asterisk) draining from the surface of the brain tissue (BT), traversing across the subarachnoid and subdural spaces (SDS) before then draining into the dural membrane (DM). Importantly, in this image a smaller vein (white box) can be clearly seen draining directly into the bridging vein, which shows that smaller branches of bridging veins do exist. The diameter of the bridging vein in Figure 83C at its largest point is approximately 3733 μm , while the diameter of the smaller vein draining into the bridging vein is approximately 978 μm at its largest point. Notably, the junction point between these two vessels becomes noticeably constricted (the diameter at this junction being approximately 111 μm) which is highly likely to be a structural weak point.

The same fine vein can also be clearly seen draining directly into a bridging vein, in a macrograph of the same sample (Figure 75A) from which Figure 83C (white box) was acquired. These BF and FM images of the macaque specimen validate the aforementioned macroscopic findings, as they show the same vascular structures, but on a histological scale. The fluorescent images prove that the lumina in which the resin lies must be that of vessels (and not other structures) as resin has only been perfused into the vascular system. Additionally the surrounding histology then proves that both these bridging veins and the smaller veins which drain into the bridging veins, cross the subdural space which is situated between the dural membrane (DM) and the arachnoid membrane lining the brain surface. This histological confirmation of the macrographic evidence

demonstrated through gross dissection of tissue further reinforces the information found in ESEM imaging of marmoset and rat cerebral VCCs, whereby smaller vessels which drain into bridging veins (which then drain into the venous sinuses) have been found to exist. The way in which the smaller vessels constrict at the junction point between the smaller vessels and the bridging veins also correspond with these ESEM findings.

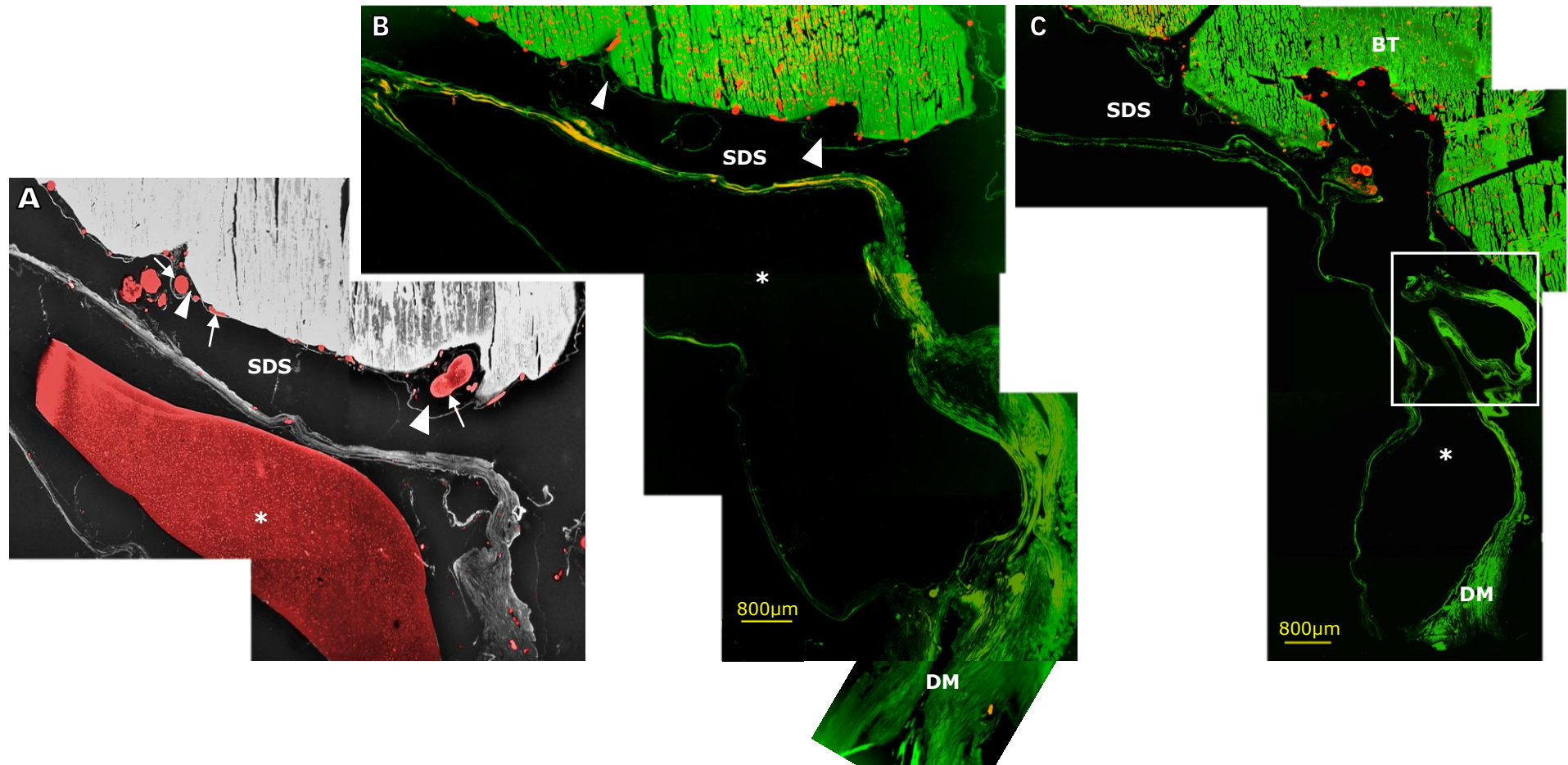


Figure 83: Histological sections of *macaque D* specimen. **A:** FM image (x2.5) of slide 55 from the serial sections that were cut from macaque D specimen. Artificial colour (red) was added to the already acquired FM image due to lack of fluorescence emitted from the tissue sample. The image illustrates the presence of resin located within the lumen of a bridging vein (asterisk) seen at the bottom of the image, as well as resin located within the lumina of subarachnoid vessels (arrows) which are located within the subarachnoid space (arrowheads). These structures are situated just superior to the subdural space (SDS), in which the bridging vein lies. **B:** An overlay of BF and FM images of the same H&E stained and DPX mounted histological specimen (slide 61). A bridging vein (asterisk) draining into the dural membrane (DM) can be seen, as well as subarachnoid vessels located within the SAS (arrowheads). This bridging vein and subarachnoid vessels are the same as those vessels illustrated in image A, however without the perfused luminal resin. **C:** Slide 96 (x2.5). Similar structures as described in image B. The bridging vein (asterisk) can be seen draining from the surface of the brain (BT), traversing across the subarachnoid and subdural spaces (SDS) before draining into the dural membrane (DM). Additionally, a smaller vein (white box) can be seen draining directly into the bridging vein, showing again that branches of the bridging veins do exist.

4.4. Discussion

This project encompasses numerous different components, allowing thorough analysis of the anatomy of the venous drainage of the brain, and in particular, the subdural vessels which are hypothesised to be the source of intracranial bleeding often found in cases of traumatic head injuries. A multimodal approach was conducted to first of all prove the existence of these fine subdural veins as well as to also allow analysis of the exact morphological structure of the vessels on a microscopic as well as an ultrastructural scale.

Due to the complexity of the human physiology, biological models that were more phylogenetically similar to the human than that of rats were essential for the purposes of this project. Because of the high genetic homology between humans and primates, experimental results obtained from macaque and marmoset material (unable to be carried out using cadaveric material due to ethical reasons) were used to allow credible conclusions to be drawn regarding the anatomical structure of the human brain.

4.4.1. Gross Dissection

Gross dissection of both pre-fixed and resin perfused marmoset and macaque specimens were able to macroscopically illustrate the existence of fine vascular networks of both subdural and bridging veins traversing across the SDS (Figure 62, Figure 63, Figure 75 and Figure 76).

Subdural veins were seen draining directly into the bridging veins within the SDS, which then drained into the venous sinuses. However in some cases these fine vessels were seen to traverse across the SDS before penetrating directly into the inner meningeal layer of the dura mater. Presumably these vessels then traverse along the intradural space before then either draining into a venous sinus directly, or indirectly via a bridging vein. Similar structures to these networks of subdural veins have also been found through gross dissection of human cadaveric material.

From observations made from gross dissection of these primate specimens as well as previously dissected human cadaveric material, a similar pattern regarding distribution of these networks of subdural vessels can be seen. Higher numbers of subdural vessels can be found located around the tentorium cerebelli, either draining from the superior cerebellar brain surface to the tentorium, or from the

inferior surface of the temporal and occipital lobes of the brain to the tentorium cerebelli.

4.4.2. Histological Analysis

Following gross tissue dissection, histological analysis of prefixed marmoset specimens including LM and TEM, as well as LM and FM of resin perfused macaque specimens, was able to further illustrate the morphological structure of these vessels on a micrographic scale, as well as identify their location within the SDS.

4.4.3. LM and TEM of Marmoset Specimens

As previously discussed, although macrographic images of the superficial cerebral networks of venules revealed through dissection of marmoset material were acquired, further histological analysis of the fine subdural vessel specimens in particular could not be carried out. This was due to the quality of the prefixed material, which made it difficult to dissect out the much finer subdural venules without causing them to rupture.

Therefore, although the subdural vessels could not be further histologically analysed, LM and TEM analyses of the marmoset venous sinuses, bridging veins and dura mater were able to further micrographically illustrate these other important anatomical structures in more detail.

No muscle content was found within the vessel walls of the marmoset bridging veins that were imaged using LM and TEM. Due to their comparatively small size, it is highly likely that the walls of the fine subdural veins in question would therefore also lack muscular fibre content, increasing their vulnerability to rupturing in cases of traumatic head injuries.

Additionally, numerous intradural vessels of different calibres that can be seen grouped together at different points along the dural membrane of the marmoset specimens (Figure 72C) could indicate an intradural vascular network. In a number of cases, intradural vessels were found particularly in parts of the dural membrane that were in close proximity to bridging veins. An example of this is pictured in Figure 72B. This indicates that these intradural vessels may be involved in some way with the drainage of the bridging veins and subdural vessels. The involvement of an intradural vascular plexus in cases of accidental and NAHIs

has already been briefly discussed in section 1.4.9. However further investigation into this area would be required in order to validate this supposition, which would include additional work involving histological processing and analysis of further primate specimens.

4.4.4. LM and FM of Macaque Specimens

Fine venules have been clearly shown draining directly into much larger bridging veins in some of the LM and FM images of the macaque specimens (Figure 83). This shows that fine venular tributaries that drain directly into bridging veins as they traverse across from the surface of the brain to the venous sinuses do exist.

This information is vital, as these finer veins are much more likely to be the source of subdural bleeding found in cases of traumatic head injuries due to their small calibre, compared to the bridging veins themselves. Rupturing of these fine venules is also more likely to result in much smaller volumes of thin-film subdural bleeding than would occur with the rupture of the much larger bridging veins, as is often found in cases of NAHI. Additionally, noticeable constrictions at the junction points between the bridging veins and their venular tributaries (similarly illustrated in ESEM images of macaque and rat VCC specimens) are also likely to be further structural weak points, increasing vulnerability to rupturing of the vessels on application of a certain amount and type of force.

Similar anatomical structures to those described above have been consistently illustrated both macrographically and micrographically in primate, human and rat material.

4.4.5. Further Work

4.4.5.1. Resin Casting and Histological Processing of Tissue

Due to their fragile nature, dissecting out the fine subdural vessels of the marmoset samples proved to be very difficult, particularly those singular vessels traversing across the SDS that penetrated directly into the dural membrane (without first joining with a bridging vein). Microscopy of these subdural vessels could therefore not be carried out for use in this project. In addition to this, it is these same subdural vessels that were often found to be incompletely perfused with resin. However this was unlikely to be due to a flaw in the resin perfusion

process causing incomplete vessel filling, as much finer capillary networks had also been perfused with the resin in the same experiments. One possible explanation for these findings involving reflex vasoconstriction of the vessels due to SNS activation in response to vascular perfusion has already been discussed in section 2.4.2. Future work could therefore include further resin casting and histological processing of the macaque subdural venules to allow further investigation into the exact micrographic structure of these vessels.

4.4.5.2. MicroCT, 3D XRM and Further Analysis

As previously mentioned, ESEM images acquired from the vascular casts of both marmoset and macaque specimens reinforce the anatomical findings of the rat VCC ESEM results illustrated in section 2.3.2. However, due to the quality of the microCT scans which were then generated from these same marmoset VCCs, further analysis of the microCT datasets was not possible.

It was possible for the 3D XRM images acquired from the macaque VCC to be further processed using various computer-aided analyses of the imaging datasets. These analysis techniques included volume rendering of the sample images, as well as approximation and representation of the local thicknesses of the cerebral vessels, demonstrating the potential for further computer analysis to be carried out in future work. Further analysis could contribute towards determining the type and amount of force required for these vessels to rupture as a result of a traumatic injury to the head, and would therefore be an important aspect of any future work.

Therefore, to allow for further more detailed analysis of the microCT and 3D XRM images of the various cerebral VCCs, a collaboration has been set up with a research group led by Dr Bai Li, which specialises in medical image analysis and modelling. This research group are looking further into image segmentation of the scanned datasets by designing specific algorithms that can then be used for volume rendering and therefore reconstruction of 3D images of the vessels. This will allow further analysis and quantification of the cerebral vascular structure, including measurement of the vessel diameters which will allow them all to be grouped and categorised, as well as detailed analysis of the branching patterns relating vessel size and frequency, according to their anatomical location.

As it is possible for this 3D XRM scanning technique to acquire much higher resolution images (down to $<0.7\mu\text{m}$) than were obtained during these trial experiments, further more detailed scans will be carried out once the above mentioned algorithms are perfected and can be applied to this scanning data for further analysis.

4.4.5.3. MRI Scanning

The issues regarding MRI signal distortion due to fixative and air emboli in the prefixed marmoset material were the same as those faced when carrying out MRI scans of human cadaveric material. It would therefore be preferable to scan live primates in order to obtain the required results, by adapting the current MRI scanning technique applied to cerebral surface vessel scanning of humans *in vivo*, to that of primate specimens. This is on the basis that much higher quality MRI images were acquired when human *in vivo* head scans were carried out as opposed to scans of cadaveric material, as well as the fact that scans carried out *in vivo* better represent the cerebral anatomy without the possible structural changes that are known to occur post-mortem. Further scanning of primate material would be invaluable in correlating anatomical data of the meningeal layers and surrounding regions of the brain with other species. This is therefore an area in which further work should be considered, although this was not possible during this project due to licence restrictions.

Chapter 5. Concluding Discussion

5.1. Main Findings of the Thesis

5.1.1. Conclusions

This project aimed to prove the existence of fine subdural veins hypothesised to be the source of subdural bleeding often seen in cases of accidental and NAHIs, and consequently illustrate their anatomical structure. This was important in contributing towards establishing the causal mechanism for traumatic intracranial bleeding, and was particularly applicable in unexplained traumatic head injuries in cases of possible child abuse.

Results from a number of experiments involving rat, primate and human material have all illustrated the existence of subdurally located vessels shown in all of these species. The existence of these vessels has been illustrated through the use of various scientific and imaging techniques that have allowed analysis to be carried out in many different ways, from macroscopic to an ultrastructural scale.

Future work will be carried out so as to aid determination of the normal functionality of these vessels, and to try to gain a better understanding as to whether they could be damaged during traumatic head injuries.

5.1.2. Discussion

5.1.2.1. Summary of Project Findings

In light of current scientific knowledge and literature, results shown throughout this project prove that there are very fine subdurally located vessels present that could be the source of subdural bleeding found in cases of accidental and non-accidental traumatic head injuries. These vessels are thought to either first traverse between the dural layers before draining into larger calibre bridging veins, or drain into the subdural part of the bridging veins directly. The similarities that have been observed between the cerebral vascular anatomical structures of the different species that were analysed during this investigation show that not only do subdural vessels exist, but also indicate that they may be present across many species.

The existence of bridging veins, venous tributaries of these bridging veins, as well as other fine calibre subdural veins was confirmed through various forms of tissue processing and analysis, followed by further investigation of their morphological structures. ESEM imaging of both rat (section 2.3.2.) and primate VCCs (section 4.3.1.2.) was able to clearly show complex networks of venous vessels draining into bridging veins on an ultrastructural scale. The vessels were also illustrated macrographically via gross dissection of rat (Figure 20B), cadaveric (Figure 48 and Figure 49), marmoset (Figure 63) and macaque material (Figure 75 and Figure 76). One particular resin perfused bridging vein (shown to drain directly into a venous sinus) of a macaque specimen illustrated macroscopically a network of vessels draining directly into the bridging veins (Figure 75A). These structures were then further investigated using FM and LM of the same vessels (Figure 83), clearly illustrating the same structures on a micrographic scale. Similar vessels have also been shown histologically in cadaveric specimens (Figure 50).

Through application of appropriate biomechanical modelling techniques, this data will hopefully allow determination of the type and amount of force that would be required to cause these vessels to rupture, and to allow a better understanding as to why they may lead to haemorrhaging into the subdural space in cases of traumatic head injury.

5.1.2.2. Anatomy of the PS and SS

The existence of a PS has often been described as a rare finding in the adult human (Chell, 1991). It was only recently confirmed by numerous studies that the PS is in fact neither a rare nor an abnormal finding (San Millán Ruíz et al., 2006), although this has been suggested to be the case since the 1800s (Bell and Bell, 1816; Cheatele, 1899; Knott, 1881). It is now thought that it is the rule rather than the exception for the PS to be present as part of the normal adult venous system (San Millán Ruíz et al., 2006).

It has been suggested that reorientation of the venous anatomy that occurs during embryonic development and early childhood in the human leads to the regression of the PS, and replacement by the SS to become the major outflow pathway of the TS in the adult (Conroy, 1982; Padget, 1957). In contrast to this, in animals with a lesser telencephalic development such as the rat, the PS is likely to be retained as the major outflow pathway of the TS due to the persistent verticality of the TS (San Millán Ruíz et al., 2006; Szabó, 1995). These anatomical

venous sinus structures found in the rat should therefore be similar to the cerebral venous sinus anatomy seen in a human during embryonic and early childhood development before retraction in the size of the PS (Butler, 1957).

This difference in anatomy between infants and adults can clearly be seen in Figure 84 below (Padget, 1957; Padget, 1956). This figure illustrates the presence of a prominent PS in the infant on the left, while the venous anatomy of the adult, on the right, depicts the PS as a remnant of the previously existing larger vessel in the infant. However recent research shows that the PS is in fact a normal feature of the adult venous system, as previously discussed, although the venous sinus is not likely to be as prominent in the adult as it is in an infant.

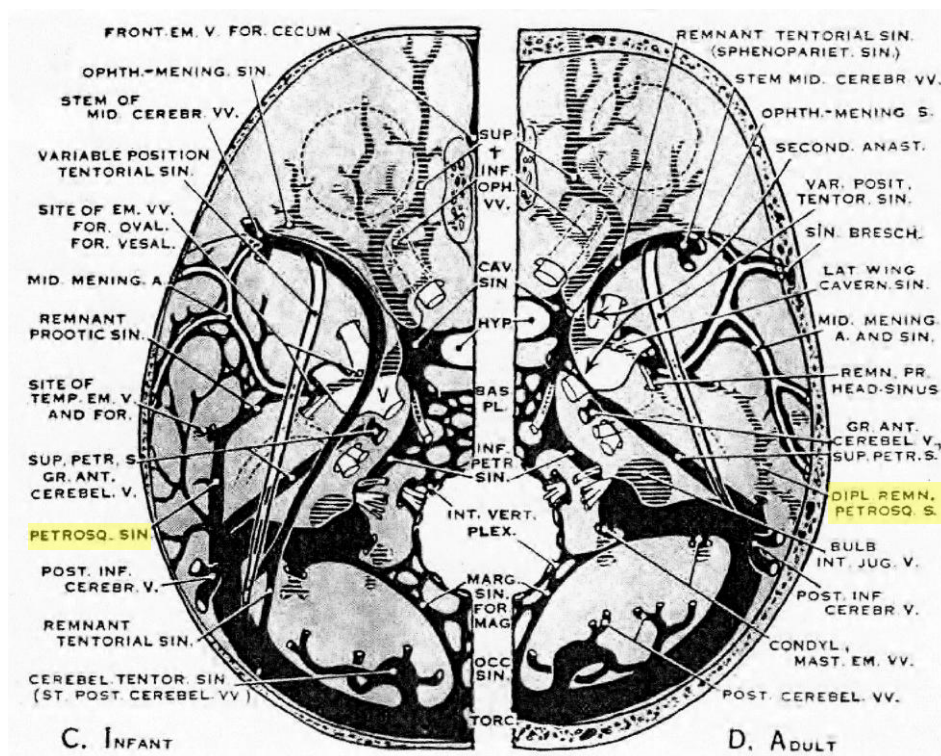


Figure 84: Illustration comparing the anatomical differences in the venous anatomy between an infant (left) and an adult (right) (Padget, 1957, with permission).

This project was able to demonstrate a wide variety of veins of a range of different sizes draining directly into the venous sinuses. ESEM images of the VCCs of the rat specimens in particular were able to demonstrate complex venous networks entering the venous sinuses, with the majority being very small in diameter and a few larger calibre vessels. The size of the bridging veins and their

tributaries depended upon the size of the venous sinus into which the vessels drained. In general, the diameter of the bridging veins and tributaries that drain into the SS and PS seem to be smaller than vessels that drain into larger venous sinuses sizes such as the SSS or TS. Additionally, the range in diameter of the bridging veins and tributaries were also found to be wider in the larger SSS and TS, as opposed to the SS and PS, which in comparison have a larger number, but narrower range of smaller vessels draining into the venous sinuses. The aforementioned complex venous networks were also found to be most numerous particularly around the SS and PS.

The presence of a larger number of smaller calibre vessels draining into the SS and PS compared to the SSS and TS is crucial. This finding may be especially relevant to birth related SDHs as well as SDHs in NAHI. These fine calibre vessels could be the potential source of the SDHs, rather than due to rupturing of much larger bridging veins, and their distinctive distribution may in part explain the more common localisation of SDHs in the peri-tentorial region and posterior fossa in cases of both NAHIs and birth-related traumas.

Differences in size and shape between the right and left SS have been documented, although this has not yet been researched for the PS as studies have only recently found that the PS exists more frequently than first thought, as previously discussed. It has been found that SS are subject to lateral dominance, with the right side being frequently more developed than the left side (Ichijo et al., 1993; Solter and Paljan, 1973). This is consistent with the results of this project in terms of the venous sinus calibre, as well as the fact that the right SS and PS were found to be associated with more bridging veins and tributary venous networks compared to the left hand side of the brain. These findings are particularly evident in the ESEM images of the rat and primate VCCs.

Despite this however one study suggests that chronic SDHs are more frequent on the left hand side of the head (MacFarlane et al., 2009). However this is likely to be due to fewer cases of right sided lesions being diagnosed as right hemispheric (non-dominant) lesions are less likely to cause severe functional impairment such as communication difficulties, or impairment of the functioning of the individual's dominant hand (although this is mainly shown in adults, as the age group of infants commonly subjected to NAHIs and are not necessarily able to talk yet, and may have not yet established hand dominance). They are instead associated with more subtle symptoms and therefore more difficult to diagnose. It has also been shown that this left sided tendency has not been found specifically in either acute

or sub-acute cases. This illustrates that although lateralisation of SDHs is a theoretical possibility this as yet has not been born out in clinical practice. If anything, due to the higher number of fine venous networks seen to be draining into the right SS and PS, lateralisation of ASDHs on the right side of the brain may in fact be more likely, although further work will have to be done in this area in order to determine this.

5.1.2.3. Bridging Veins, Venous Tributaries and Subdural Vessels

As previously mentioned, the terminology used in the past to describe the vessels traditionally called 'bridging veins' is imprecise, as it only addresses the presence of large veins that enter the major venous sinuses. Despite being mentioned in a great number of studies as a potential source of the SDHs often found in cases of NAHIs, no accurate description as to their number and distribution, histological factors or a clearly defined size range currently exists which allows them to be differentiated from smaller venous tributaries and subdural veins.

Histology

Regarding some of the currently known histological data concerning bridging veins, one study showed that the thickness of bridging veins varies greatly between the subdural portion of the vessel whereby the thinnest section was found to be 10µm, whereas the subarachnoid section of the bridging vein had a thickness of 50-200µm (Yamashima and Friede, 1984). Further EM examination also showed that the bridging vein walls within the subarachnoid portion of the vessel consisted of compact collagen, while the subdural portion of the vein was composed of loosely woven collagen fibres lacking in outer reinforcement by arachnoid trabecules. All of these factors contribute towards the subdural section of the bridging vein being more fragile than its subarachnoid section, indicating a relatively greater vulnerability to mechanical injury and therefore an increased likelihood of rupturing of the vessels as they cross the subdural space.

Although other studies have also histologically demonstrated bridging veins crossing the subdural space (Nierenberger et al., 2013), there are no documented studies that illustrate much finer vessels traversing the subdural space in the same way as illustrated throughout this project in multiple animal species (Figure 50 and Figure 83). However, further histological work regarding exact morphology of the smaller calibre venous tributaries and subdural veins illustrated in this

project still needs to be carried out. Nonetheless there are anatomical similarities that can already be determined between the traditionally described bridging veins and these fine calibre venules. This includes structural weakness caused by lack of outer reinforcement within the subdural portion of the vessels, which may contribute towards the increased likelihood of venular rupture particularly at the subdural portion of the small veins that traverse both the subarachnoid and subdural spaces. This may therefore further explain the commonly found subdural location of resultant haematomas (Yamashima and Friede, 1984) often following mechanical head injury.

Vessel Size

Histological sections of the cadaveric specimen shown in Figure 50 illustrates cross-sections of a number of vessels fitting the description of traditionally defined bridging veins as they traverse across the pia, arachnoid and dura mater layers, before then draining either directly or indirectly into the cerebral venous sinuses. However the width of the walls of some of the largest venules are larger than the whole vessel diameters of some of the other venules within the same network of vessels (as seen in Figure 49) that were all shown traversing across the subdural space.

The range in diameter of these subdurally located networks of vessels also varies greatly from 16 μ m-177 μ m. They are however still much smaller in calibre compared to the mean size range (1.69-3.11mm) of many conventionally defined bridging veins (Baeck et al., 2012; Chen et al., 2012; Ehrlich et al., 2003; Yu et al., 2010). It could therefore be argued that these subdurally located smaller calibre vessels are more vulnerable and thus more likely to be damaged in cases of NAHI, in comparison to traditionally defined much larger and more robust bridging vein structures. It may also be reasonable to suggest that due to their smaller diameter, these smaller calibre vessels (as illustrated in Figure 50) could be the source of the thin-film subdural haemorrhaging often seen in cases of NAHIs. This therefore further demonstrates the need for more work to be carried out in order to allow bridging veins to be more accurately defined, and to allow a differentiation to be made between traditionally described bridging veins, and the smaller venous tributaries and subdural veins.

Number and Distribution

A higher number of vessels crossing the subdural space were found to be particularly located over the more posterior parts of the brain, particularly immediately above and immediately below the tentorium cerebelli, as illustrated in gross dissections of both primate (Figure 63, Figure 75 and Figure 76) and cadaveric material (Figure 48 and Figure 49). The highest number of small venous networks was found to drain into the bridging veins of the SS and PS which are also located posteriorly. This is clearly demonstrated in the ESEM images acquired from both rat and primate VCC specimens. Due to the continuity that exists between the cranial and spinal dural membranes, it is therefore possible that cranial subdural haemorrhaging originating from these regions of the brain could dissect downwards to form a spinal SDH, a feature which is commonly found in MRI scans of NAHIs (Choudhary et al., 2012; Koumellis et al., 2009).

5.2. Future Directions

This investigation has contributed to the knowledge base of the intracranial venous drainage system and underlined the necessity for further research into the structure of the venous drainage system of the brain. However exploration of this subject matter is still far from complete. Therefore this section suggests possible improvements that could be made to existing methodology, and discusses future directions in which work could be carried out in addition to the possible future work that has already been described and discussed in previous chapters.

5.2.1. Vascular Perfusion

ESEM imaging of the macaque VCC illustrated in Figure 79 shows a number of incompletely filled bridging veins and other networks of vessels draining into the ISS. This is not due to incomplete filling of the fine vasculature of the specimen in general, as other fine cerebral vessels of up to 3µm in diameter, were successfully perfused and imaged in the same VCC (Figure 79D). Similar incomplete filling of vessels draining into the venous sinuses was also found during ESEM analysis of the VCCs of the rat and marmoset specimens. This is also not due to incomplete vascular filling in general, as other much finer cerebral vessels were successfully perfused in other areas of the same vascular cast samples.

This incomplete filling of the vessels may have been due to a reactive mechanism of the vessels as the specimen was being perfused. One possible explanation is that flow through the vessels was being cut off as the result of a reflex action,

causing the junction points at which the vessels entered into the venous sinuses to constrict. This could have been in response to pressure changes, changes in blood flow, or osmotic changes caused by the perfusion process. The presence of sphincter-like constrictions in the walls of some of the venules at the junction points as they drain into either the bridging veins or the dural venous sinuses themselves has already been discussed in section 2.4.2. These sphincters may cause reflexive constriction of the vessel junctions in response to the perfusion process as previously mentioned, therefore causing incomplete filling of some of the vessels seen in various different specimens. The mechanism by which this is likely to have occurred has already been discussed in detail in section 2.4.2. Possible ways to prevent this from reoccurring in future may be to increase the concentration of procaine hydrochloride perfused into the vessels to further counteract vasoconstriction occurring in response to the perfusion process. Additionally injection of heparin, a venodilator and an anticoagulant, into the vascular system prior to vascular perfusion could also prevent vasoconstriction and possible coagulation of the blood which could be causing obstruction of the vessels at these narrowed junction points.

5.2.2. Vessel Morphology

There is a diverse amount of methodological variety in the vascular casting procedures used in different studies. These include use of different resin types, processing techniques, routes of access to vasculature as well as different rates of perfusion. However there are so far no other studies that have used vascular casting to focus exclusively upon investigating the structure of subdural vessels that could be the cause of intracranial bleeding found in cases of accidental and NAHI. Development of the vascular casting protocol for purposes of this project was therefore essential to allow future replication of good quality, complete vascular casts which in turn will allow further analysis of the vascular architecture of the vessels under investigation on an ultra-structural scale. Future work should therefore include use of the now fine-tuned vascular casting technique to allow further examination of the exact orientation and structure of the fine venules under investigation, to allow their exact morphology to be determined. New information regarding the size, location and structural detail of these fine calibre veins traversing the subdural space will provide the opportunity to radically re-evaluate biomechanical modelling techniques that have traditionally focused upon the larger bridging veins as the source of subdural bleeding. This will allow further

elucidation of the underlying mechanism behind SDH formation in NAHI as these factors will affect how vessel walls are damaged.

5.2.3. Correlating morphological findings with Clinical MR Imaging

As previously mentioned, bridging veins, smaller venous tributaries and other subdural veins traversing the subdural space were found to be distributed across most areas of the brain. However the largest numbers that were consistently found in each of the species investigated in this project were found to be located in the posteroinferior parts of the brain, particularly supratentorially and infratentorially, as well as adjacent to the SS and PS.

MRI scans of cases of NAHIs undertaken at the acute stage of presentation typically demonstrate subdural bleeding that is predominantly located posteriorly (over the posterior surfaces of the cerebral hemispheres, alongside the posterior cerebral falx, both sides of the tentorium as well as the posterolateral surfaces of the cerebellar hemispheres). Blood from the posterior fossa may sometimes be shown to be contiguous with subdural blood in the rostral spinal canal, as well as tracking down into the lower thoracic and lumbar regions. If SDH is found to originate from disruption of small subdural vessels in the areas described above, as the cranial dural membrane is continuous with the spinal dural membrane, it makes sense that there may be dissection of blood from the cranial SDS (created due to subdural vessel rupture and bleeding) into the spine, thereby creating another artificial SDS in the spine.

Although the exact morphology of the vessels under investigation cannot yet be defined, a lot of new and vital information has been discovered throughout this investigation. This includes first of all proving the existence of fine subdural veins, as well as ascertaining further information regarding their general structure (both macroscopically and microscopically), their size, number and overall distribution.

Important future work could involve collection of further data regarding the exact morphology of these vessels via use of the newly developed resin casting technique described, in conjunction with various imaging techniques to allow analysis of the vessels *in situ*. This information could then be correlated to MRI images of the brain revealing SDH, which may allow the source of SDHs in cases of NAHIs to be accurately traced and pin-pointed. Knowledge gained from this could then hopefully be applied to a clinical setting, when presented with patients

with signs of possible NAHI. This may help to allow accidental and non-accidental cases to be differentiated, particularly so that cases of NAHI can be quickly recognised and appropriately treated. This is crucial as MRI is routinely used in clinical settings because it is a form of imaging that is more accessible and non-invasive in comparison to many other imaging techniques.

5.2.4. Volume Rendering of Imaging Datasets

Although small vein segmentation of the MRI data collected during this project has already been carried out, further work involving production of more highly detailed volume rendering and 3D reconstructions of the cerebral vessels using the imaging data could be carried out to allow more detailed analysis of these MRI datasets.

Additionally, to allow further more detailed analysis of the microCT and 3D XRM images of the various cerebral VCCs, volume rendering of these imaging datasets could also be carried out. This rendering could be carried out using specialised imaging software and algorithms, and conducted through collaboration with a computer sciences research group (led by Dr Bai Li, as previously described) to produce detailed 3D reconstructions of the imaging datasets obtained throughout this project. Although other studies have been carried out which have processed imaging data in a similar way (Vasquez et al., 2011), this collaboration will allow computer analysis of the vast network of subdurally located vessels that have been found, in finer detail than has been possible in other studies thus far. As it is possible for the 3D XRM scanning technique to acquire images of resolutions down to $<0.7\mu\text{m}$, further more detailed scans will be carried out once the specialised algorithms are perfected, which can then be applied to this scanning data to allow further data analysis.

5.2.5. Macaque Work

There are a number of studies that have carried out resin casting of the macaque vascular system using similar techniques to those described in this project (Ohkuma and Ryan, 1983). These have looked at both the venous system (Hegedus and Shackelford, 1965) as well as the cerebral vasculature of the brain in general (Weber et al., 2008; Weinstein and Hedges, 1962). However these studies have not been able to examine the fine anatomical structure of the superficial venous system in as much detail as was possible in this project, owing

to the careful fine-tuning of the resin casting methodology in combination with the high quality imaging facilities available and techniques that were employed to obtain the final results of this project.

However, future additional work involving macaque material is still essential for further more detailed results regarding the superficial cerebral venous anatomy to be obtained. If ethical approval for the use of additional macaque material can be obtained, further work involving vascular perfusion of different concentrations of gold nanoparticles using the previously described resin perfusion technique could be carried out. This will allow further detailed analysis of the vessels to be carried out *in situ* via imaging techniques such as high field MRI and microCT imaging of the tissue, as well as histology and EM imaging of the primate material which will allow the vessels to be analysed further on an ultrastructural scale.

5.2.6. Cadaveric Work

It has been shown that from the age of 6 months, the anatomy of the human dura and cerebral venous drainage begins to alter as the cerebral venous network present in infants gradually diminishes in size with increasing age (Browder et al., 1975). Therefore in addition to the work which has already been carried out involving dissection and processing of cadaveric material as well as MR imaging of the human head *in vivo*; comparison of the anatomy of the venous drainage of the brain between adults and infants should also be carried out in a similar way, due to the differences in structure in both groups.

Another possible route for further investigation into this subject matter is via the production of vascular casts of post-mortem cadavers (San Millán Ruíz et al., 2002) ideally within 24 hours after death, and if ethical approval permits, aborted fetuses, stillborn neonates or post-mortem infants. Following observation of the post-mortem of a 3 month old infant that was carried out 24 hours after death, although ethical approval would not allow macrographs to be taken at this stage in the project, it was evident that further work involving use of post-mortem infants would be vital for further progression in this subject area. Work involving improvement of existing methods of imaging and dissection at post-mortem examinations has already been carried out (Stein et al., 2006). However further improvements in these techniques are still required if fragile structures such as the fine calibre vessels shown to traverse the subdural spaces are to be preserved during these examinations. This is so that the source of SDH found in cases of

possible NAHIs can be accurately located, as this information could be used to help to explain the mechanism leading to intracranial haemorrhaging seen in cases of SBS and possible child abuse.

5.2.7. Biomechanical Modelling

All biomechanical modelling of the venous structures involved in SDH formation in primates and humans has so far been based on the larger diameter bridging veins that have traditionally been considered to be the source of bleeding in cases of NAHI. Results of this research project will hopefully act as the basis for further biomechanically related research to re-evaluate the mechanisms for SDH formation in early life. Further work to allow determination of the exact anatomy and morphology of the surface vessels over the brain (particularly as they cross the subdural space) could act as the basis for future biomechanical modelling in this field of medicine. This could then be used to more accurately replicate the acceleration and deceleration forces subjected to an infant's head during a shaking motion, using either calculated models, or by physical reproduction of a representative model using these scientifically determined parameters.

References

- 2005, R v Harris and Other Appeals, EWCA Crim, p. 2-52.
- ACR, 2009, American College of Radiology Appropriateness Criteria®: Suspected Physical Abuse - Child.
- Adamsbaum, C., S. Grabar, N. Mejean, and C. Rey-Salmon, 2010, Abusive Head Trauma: Judicial Admissions Highlight Violent and Repetitive Shaking: Pediatrics.
- Adhiyaman, V., M. Asghar, K. Ganeshram, and B. Bhowmick, 2002, Chronic subdural haematoma in the elderly: Postgraduate Medical Journal, v. 78, p. 71-75.
- Agid, R., I. Shelef, J. N. Scott, and R. I. Farb, 2008, Imaging of the Intracranial Venous System: The Neurologist, v. 14, p. 12-22.
- Alan, C., and B. Clemetson, 2004, Is it "Shaken Baby," or Barlow's Disease Variant? : Journal of American Physicians and Surgeons, v. 9, p. 78-80.
- Alexander, R., D. Schor, and W. Smith Jr, 1986, Magnetic resonance imaging of intracranial injuries from child abuse: The Journal of Pediatrics, v. 109, p. 975-979.
- Allen, R., ed., 2004, *English Dictionary*. 2nd ed.: London, Penguin Books Ltd.
- Altman, R., M. Kutscher, and D. Brand, 1998, The "Shaken-Baby Syndrome": New England Journal of Medicine, v. 339, p. 1329-1330.
- Anderson, B., and W. Anderson, 1978, Scanning electron microscopy of microcorrosion casts; intracranial and abdominal microvasculature in domestic animals: American Journal of Anatomy, v. 153, p. 523-536.
- Andres, K., and M. During, 1981, General Methods for Characterization of Brain Regions, *Techniques in Neuroanatomical Research*: Berlin, Springer-Verlag.
- Auer, L. M., N. Ishiyama, K. C. Hodde, R. Kleinert, and R. Pucher, 1987, Effect of intracranial pressure on bridging veins in rats: Journal of neurosurgery, v. 67, p. 263-8.
- Baeck, K., A. Asiminei, E. Verbeken, J. Goffin, and J. Sloten, 2012, Experimental characterization of the mechanical properties of the superior sagittal sinus: bridging vein complex: Proceedings of the Institution of Mechanical Engineers, Part P: Journal of Sports Engineering and Technology, v. 226, p. 165-169.
- Baile, E. M., G. G. King, N. L. Muller, Y. D'Yachkova, E. E. Coche, P. D. Pare, and J. R. Mayo, 2000, Spiral computed tomography is comparable to angiography for the diagnosis of pulmonary embolism: Am J Respir Crit Care Med, v. 161, p. 1010-5.

- Bandak, F., 2005, Shaken baby syndrome: A biomechanics analysis of injury mechanisms: *Forensic science international*, v. 151, p. 71-79.
- Barlow, K., and R. Minns, 2000, Annual incidence of shaken impact syndrome in young children: *The Lancet*, v. 356, p. 1571-1572.
- Barlow, K. M., R. J. Gibson, M. McPhillips, and R. A. Minns, 1999, Magnetic resonance imaging in acute non-accidental head injury: *Acta paediatrica (Oslo, Norway : 1992)*, v. 88, p. 734-40.
- Barnes, P. D., and M. Krasnokutsky, 2007, Imaging of the central nervous system in suspected or alleged nonaccidental injury, including the mimics, *Top Magn Reson Imaging*, v. 18: United States, p. 53-74.
- Beckmann, N., A. Schuler, T. Mueggler, E. P. Meyer, K. H. Wiederhold, M. Staufenbiel, and T. Krucker, 2003, Age-dependent cerebrovascular abnormalities and blood flow disturbances in APP23 mice modeling Alzheimer's disease, *J Neurosci*, v. 23: United States, p. 8453-9.
- Bell, E., M. Shouldice, and A. Levin, 2011, Abusive head trauma: A perpetrator confesses: *Child Abuse & Neglect*, v. 35, p. 74-77.
- Bell, J., and C. Bell, 1816, *The Anatomy and Physiology of the Human Body*, v. II: London, Longman.
- Bender, M., 1955, Blood Volume of the Rhesus Monkey: *Science*, v. 122, p. 156-156.
- Billmire, M., and P. Myers, 1985, Serious Head Injury in Infants: Accident or Abuse?: *Pediatrics*, v. 75, p. 340-342.
- Biron, D., and D. Shelton, 2005, Perpetrator accounts in infant abusive head trauma brought about by a shaking event: *Child Abuse & Neglect*, v. 29, p. 1347-1358.
- Bolay, H., U. Reuter, A. Dunn, Z. Huang, D. Boas, and M. Moskowitz, 2002, Intrinsic brain activity triggers trigeminal meningeal afferents in a migraine model: *Nature Medicine*, v. 8, p. 136-142.
- Brockmann, C., S. Kunze, P. Schmiedek, C. Groden, and J. Scharf, 2012, Variations of the superior sagittal sinus and bridging veins in human dissections and computed tomography venography, *Clin Imaging*, v. 36: United States, A 2012 Elsevier Inc, p. 85-9.
- Browder, J., H. A. Kaplan, and A. J. Krieger, 1975, Venous lakes in the suboccipital dura mater and falx cerebelli of infants: surgical significance: *Surg Neurol*, v. 4, p. 53-5.
- Brown, J., and R. Minns, 2008, Non-Accidental Head Injury, with Particular Reference to Whiplash Shaking Injury and Medico-Legal Aspects: *Developmental Medicine and Child Neurology*, v. 35, p. 849-869.

- Buhimschi, C., I. Buhimschi, A. Malinow, G. Saade, R. Garfield, and C. Weiner, 2003, *The Forces of Labour: Fetal and Maternal Medicine Review*, v. 14, p. 273-307.
- Butler, H., 1957, *The development of certain human dural venous sinuses: J Anat*, v. 91, p. 510-26.
- Buttram, H., and E. Yazbak, 2004, *Shaken baby syndrome (SBS) or vaccine-induced encephalomyelitis? the story of Baby Alan: Medical Veritas*, v. 1, p. 34-44.
- Byard, R. W., P. Blumbergs, G. Ruddy, J. Sperhake, J. Banner, and H. F. Krous, 2007, *Lack of evidence for a causal relationship between hypoxic-ischemic encephalopathy and subdural hemorrhage in fetal life, infancy, and early childhood: Pediatr Dev Pathol*, v. 10, p. 348-50.
- Caffey, J., 1957, *Some traumatic lesions in growing bones other than fractures and dislocations: clinical and radiological features: Br J Radiol*, v. 30, p. 225-38.
- Caffey, J., 1972, *On the theory and practice of shaking infants. Its potential residual effects of permanent brain damage and mental retardation: American journal of diseases of children (1960)*, v. 124, p. 161-9.
- Caffey, J., 1974, *The Whiplash Shaken Infant Syndrome: Manual Shaking by the Extremities With Whiplash-Induced Intracranial and Intraocular Bleedings, Linked With Residual Permanent Brain Damage and Mental Retardation: Pediatrics*, v. 54, p. 396-403.
- Case, M., 2007, *Abusive head injuries in infants and young children: Legal Medicine*, v. 9, p. 83-87.
- Casey, S. O., R. A. Alberico, M. Patel, J. M. Jimenez, R. R. Ozsvath, W. M. Maguire, and M. L. Taylor, 1996, *Cerebral CT venography: Radiology*, v. 198, p. 163-170.
- Cassot, F., F. Lauwers, C. Fouard, S. Prohaska, and V. Lauwers-Cances, 2006, *A novel three-dimensional computer-assisted method for a quantitative study of microvascular networks of the human cerebral cortex: Microcirculation*, v. 13, p. 1-18.
- Cater, C. W., 1963, *The Evaluation of Aldehyde and other Difunctional Compounds as cross-linking agents for collagen.: Lab. Rep. Br. Leath. Mfrs' Res. Ass.*, v. 62, p. 69-84.
- Chadwick, D., S. Chin, C. Salerno, J. Landsverk, and L. Kitchen, 1991, *Deaths from falls in children: how far is fatal?: J Trauma*, v. 31, p. 1353-5.
- Chakeres, D. W., P. Schmalbrock, M. Brogan, C. Yuan, and L. Cohen, 1991, *Normal venous anatomy of the brain: demonstration with gadopentetate*

- dimeglumine in enhanced 3-D MR angiography: *AJR Am J Roentgenol*, v. 156, p. 161-72.
- Cheatle, A., 1899, On the Anatomy and pathological importance of the petrosquamosal sinus: *The Lancet*, v. 154, p. 611-612.
- Chell, J., 1991, The squamoso-petrous sinus: a fetal remnant: *J Anat*, v. 175, p. 269-71.
- Chen, J., X. Wang, L. Luan, B. Chao, B. Pang, H. Song, and Q. Pang, 2012, Biological characteristics of the cerebral venous system and its hemodynamic response to intracranial hypertension: *Chin Med J (Engl)*, v. 125, p. 1303-9.
- Choudhary, A., R. Bradford, M. Dias, G. Moore, and D. Boal, 2012, Spinal Subdural Hemorrhage in Abusive Head Trauma: A Retrospective Study: *Radiology*, v. 262, p. 216-223.
- Christie, K. N., and P. J. Stoward, 1974, A quantitative study of the fixation of acid phosphatase by formaldehyde and its relevance to histochemistry: *Proceedings of the Royal Society of London. Series B, Containing papers of a Biological character*. Royal Society (Great Britain), v. 186, p. 137-64.
- Cohen, M. C., and I. Scheimberg, 2009, Evidence of occurrence of intradural and subdural hemorrhage in the perinatal and neonatal period in the context of hypoxic Ischemic encephalopathy: an observational study from two referral institutions in the United Kingdom, *Pediatr Dev Pathol*, v. 12: United States, p. 169-76.
- Connie, H., H. Dallas, O. Matthias, and W. Ewald, 2010, An Official Research Policy Statement of the American Thoracic Society/European Respiratory Society: Standards for Quantitative Assessment of Lung Structure *Am J Respir Crit Care Med*, v. 181, p. 394-418.
- Conroy, C., 1982, A Study of Cerebral Vascular Evolution in Primates, *in* E. Armstrong, and D. Falk, eds., *Primate Brain Evolution*, Springer US, p. 247-261.
- Cory, C. Z., and B. M. Jones, 2003, Can shaking alone cause fatal brain injury? A biomechanical assessment of the Duhaime shaken baby syndrome model: *Medicine, science, and the law*, v. 43, p. 317-33.
- Cradock, G., 2011, Thinking Goudge: Fatal child abuse and the problem of uncertainty: *Current Sociology*, v. 59, p. 362-378.
- Craig, W. S., 1938, Intracranial Haemorrhage in the new-born: A study of diagnosis and differential diagnosis based upon pathological and clinical findings in 126 cases: *Archives of disease in childhood*, v. 13, p. 89-124.

- Cushing, H., 1905, Concerning Surgical Intervention for the Intracranial Hemorrhages of the Newborn: *Am J Med Sci*, v. 130, p. 563-581.
- Cwavusa, 2012, Education SBS, Photobucket Corporation.
- Cyranoski, D., 2004, China takes steps to secure pole position in primate research: *Nature*, v. 432, p. 3-3.
- Daly, S. E., and S. M. Connor, 2001, Seasonal variations in the incidence of suspected shaken baby syndrome: *International journal of trauma nursing*, v. 7, p. 124-8.
- Dammann, P., M. Barth, Y. Zhu, S. Maderwald, M. Schlamann, M. Ladd, and U. Sure, 2010, Susceptibility weighted magnetic resonance imaging of cerebral cavernous malformations: prospects, drawbacks, and first experience at ultra-high field strength (7-Tesla) magnetic resonance imaging: *Neurosurg Focus*, v. 29, p. E5.
- Dashti, S. R., D. D. Decker, A. Razzaq, and A. R. Cohen, 1999, Current patterns of inflicted head injury in children, *Pediatr Neurosurg*, v. 31: Switzerland, 2000 S. Karger AG, Basel., p. 302-6.
- Datta, S., N. Stoodley, S. Jayawant, S. Renowden, and A. Kemp, 2005, Neuroradiological aspects of subdural haemorrhages: *Archives of disease in childhood*, v. 90, p. 947-51.
- De Leeuw, M., and W. Jacobs, 2007, Shaken baby syndrome: the classical clinical triad is still valid in recent court rulings: *Critical Care*, v. 11, p. P416.
- Di Pietro, M., A. Brody, C. Cassady, P. Kleinman, J. Wyly, K. Applegate, B. Wood, J. Zerlin, M. Mercado-Deane, J. Seibert, and A. Stolic, 2009, Diagnostic Imaging of Child Abuse: *Pediatrics*, v. 123, p. 1430-1435.
- Donohoe, M., 2003, Evidence-based medicine and shaken baby syndrome: part I: literature review, 1966-1998: *Am J Forensic Med Pathol*, v. 24, p. 239-42.
- Drake, R., W. Vogl, and A. Mitchell, 2005, *Gray's Anatomy for Students*: Philadelphia, Elsevier Saunders.
- Duhaime, A., C. Christian, L. Rorke, and R. Zimmerman, 1998, Nonaccidental Head Injury in Infants — The "Shaken-Baby Syndrome": *New England Journal of Medicine*, v. 338, p. 1822-1829.
- Duhaime, A. C., T. A. Gennarelli, L. E. Thibault, D. A. Bruce, S. S. Margulies, and R. Wiser, 1987, The shaken baby syndrome. A clinical, pathological, and biomechanical study: *Journal of neurosurgery*, v. 66, p. 409-15.
- Durham, S. R., R. R. Clancy, E. Leuthardt, P. Sun, S. Kamerling, T. Dominguez, and A. C. Duhaime, 2000, CHOP Infant Coma Scale ("Infant Face Scale"): a novel coma scale for children less than two years of age: *J Neurotrauma*, v. 17, p. 729-37.

- Dykstra, M., and L. Reuss, 2003, *Techniques, Biological Electron Microscopy*, Springer US, p. 190-196.
- Ehrlich, E., H. Maxeiner, and J. Lange, 2003, Postmortem radiological investigation of bridging vein ruptures: *Legal Medicine*, v. 5, p. S225-S227.
- Eisenbrey, A. B., 1979, Retinal hemorrhage in the battered child: *Childs Brain*, v. 5, p. 40-4.
- Ellis, G., 1990, Subdural hematoma in the elderly: *Emerg Med Clin North Am*, v. 8, p. 281-94.
- Elwell, C., M. Cope, A. Edwards, J. Wyatt, D. Delpy, and E. Reynolds, 1994, Quantification of adult cerebral hemodynamics by near-infrared spectroscopy: *Journal of Applied Physiology*, v. 77, p. 2753-2760.
- Emerson, M., D. Pieramici, K. Stoessel, J. Berreen, and R. Gariano, 2001, Incidence and rate of disappearance of retinal hemorrhage in newborns: *Ophthalmology*, v. 108, p. 36-39.
- Epstein, H. M., H. W. Linde, A. R. Crampton, I. S. Ciric, and J. E. Eckenhoff, 1970, The vertebral venous plexus as a major cerebral venous outflow tract: *Anesthesiology*, v. 32, p. 332-7.
- European Directive 2010/63/EU, 2011, UK implementation of European directive 2010/63/EU on the protection of animals used for scientific purposes, *in* H. Office, ed., *Directive 2010/63/EU*, Official Journal of the European Union, p. 33-79.
- Flow Tech Inc., 1999, Microfil, < <http://www.flowtech-inc.com/microfil.htm> >, Carver, Massachusetts.
- Fogelholm, R., O. Heiskanen, and O. Waltimo, 1975, Chronic subdural hematoma in adults. Influence of patient's age on symptoms, signs, and thickness of hematoma: *J Neurosurg*, v. 42, p. 43-6.
- Forbes, B. J., C. W. Christian, A. R. Judkins, and K. Kryston, 2004, Inflicted childhood neurotrauma (shaken baby syndrome): ophthalmic findings: *J Pediatr Ophthalmol Strabismus*, v. 41, p. 80-8; quiz 105-6.
- Fox, R. J., A. H. Walji, B. Mielke, K. C. Petruk, and K. E. Aronyk, 1996, Anatomic details of intradural channels in the parasagittal dura: a possible pathway for flow of cerebrospinal fluid: *Neurosurgery*, v. 39, p. 84-90; discussion 90-1.
- Fuchs, S., M. J. Barthel, A. M. Flannery, and K. K. Christoffel, 1989, Cervical spine fractures sustained by young children in forward-facing car seats: *Pediatrics*, v. 84, p. 348-54.
- Funk, R., and J. W. Rohen, 1987, SEM studies on the functional morphology of the rabbit ciliary process vasculature: *Exp Eye Res*, v. 45, p. 579-95.

- Gabaeff, S. C., 2011, Challenging the Pathophysiologic Connection between Subdural Hematoma, Retinal Hemorrhage and Shaken Baby Syndrome: The western journal of emergency medicine, v. 12, p. 144-58.
- Gaudio, E., L. Pannarale, A. Caggiati, and G. Marinozzi, 1990, A three-dimensional study of the morphology and topography of pericytes in the microvascular bed of skeletal muscle: Scanning microscopy, v. 4, p. 491-9; discussion 499-500.
- Geddes, J. F., A. K. Hackshaw, G. H. Vowles, C. D. Nickols, and H. L. Whitwell, 2001a, Neuropathology of inflicted head injury in children. I. Patterns of brain damage: Brain : a journal of neurology, v. 124, p. 1290-8.
- Geddes, J. F., and J. Plunkett, 2004, The evidence base for shaken baby syndrome: BMJ, v. 328, p. 719-720.
- Geddes, J. F., and D. G. Talbert, 2006, Paroxysmal coughing, subdural and retinal bleeding: a computer modelling approach: Neuropathol Appl Neurobiol, v. 32, p. 625-34.
- Geddes, J. F., R. C. Tasker, A. K. Hackshaw, C. D. Nickols, G. G. Adams, H. L. Whitwell, and I. Scheimberg, 2003, Dural haemorrhage in non-traumatic infant deaths: does it explain the bleeding in 'shaken baby syndrome?': Neuropathology and applied neurobiology, v. 29, p. 14-22.
- Geddes, J. F., G. H. Vowles, A. K. Hackshaw, C. D. Nickols, I. S. Scott, and H. L. Whitwell, 2001b, Neuropathology of inflicted head injury in children. II. Microscopic brain injury in infants: Brain : a journal of neurology, v. 124, p. 1299-306.
- Giugarasteanu, I., 2007, Scanning electron microscopy of vascular corrosion casts--standard method for studying microvessels, Rom J Morphol Embryol, v. 48: Romania, p. 257-61.
- Glauser, J., 2004, Head injury: which patients need imaging? Which test is best?: Cleve Clin J Med, v. 71, p. 353-7.
- Gray, H., 2003, Gray's Anatomy: East Molesey, Senate, 1248 p.
- Gray, H., 2008, Gray's Anatomy - The Anatomical Basis of Clinical Practice: London, Elsevier Limited.
- Greenes, D., and S. Schutzman, 1999, Clinical indicators of intracranial injury in head-injured infants: Pediatrics, v. 104, p. 861-7.
- Greenes, D. S., and S. A. Schutzman, 1997, Infants with isolated skull fracture: what are their clinical characteristics, and do they require hospitalization?, Ann Emerg Med, v. 30: United States, p. 253-9.
- Greenwald, M. J., A. Weiss, C. S. Oesterle, and D. S. Friendly, 1986, Traumatic retinoschisis in battered babies: Ophthalmology, v. 93, p. 618-25.

- Guthkelch, A. N., 1971, Infantile subdural haematoma and its relationship to whiplash injuries: *British medical journal*, v. 2, p. 430-1.
- Hainfeld, J., D. Slatkin, T. Focella, and H. Smilowitz, 2005, In Vivo Vascular Casting: Microscopy and Microanalysis, v. 11, p. 1216-1217
M3 - 10.1017/S143192760550847X.
- Hainfeld, J. F., D. N. Slatkin, T. M. Focella, and H. M. Smilowitz, 2006, Gold nanoparticles: a new X-ray contrast agent: *British Journal of Radiology*, v. 79, p. 248-253.
- Hall, J. R., H. M. Reyes, M. Horvat, J. L. Meller, and R. Stein, 1989, The mortality of childhood falls: *J Trauma*, v. 29, p. 1273-5.
- Han, H., W. Tao, and M. Zhang, 2007, The dural entrance of cerebral bridging veins into the superior sagittal sinus: an anatomical comparison between cadavers and digital subtraction angiography: *Neuroradiology*, v. 49, p. 169-75.
- Hannah, J., 1936, The Aetiology of Subdural Hematoma (An Anatomical and Pathological Study): *The Journal of Nervous and Mental Disease*, v. 84, p. 169-186.
- Harada, K., T. Orita, S. Abiko, and H. Aoki, 1989, Coagulation and fibrinolysis in chronic subdural hematoma. Measurement of fibrinopeptides: *Neurologia medico-chirurgica*, v. 29, p. 113-6.
- Harrison, R., N. Harel, J. Panesar, and R. Mount, 2002, Blood Capillary Distribution Correlates with Hemodynamic-based Functional Imaging in Cerebral Cortex: *Cerebral Cortex*, v. 12, p. 225-233.
- Haviland, T. N., and L. C. Parish, 1970, A brief account of the use of wax models in the study of medicine: *J Hist Med Allied Sci*, v. 25, p. 52-75.
- Hegedus, S. A., and R. T. Shackelford, 1965, A Comparative Anatomical Study of the Cranio-Cervical Venous Systems in Mammals, with Special Reference to the Dog: Relationship of Anatomy to Measurements of Cerebral Blood Flow: *Am J Anat*, v. 116, p. 375-86.
- Heinzer, S., T. Krucker, M. Stampanoni, R. Abela, E. P. Meyer, A. Schuler, P. Schneider, and R. Müller, 2006, Hierarchical microimaging for multiscale analysis of large vascular networks: *NeuroImage*, v. 32, p. 626-36.
- Heinzer, S., G. Kuhn, T. Krucker, E. Meyer, A. Ulmann-Schuler, M. Stampanoni, M. Gassmann, H. Marti, R. Müller, and J. Vogel, 2008, Novel three-dimensional analysis tool for vascular trees indicates complete micro-networks, not single capillaries, as the angiogenic endpoint in mice overexpressing human VEGF165 in the brain: *NeuroImage*, v. 39, p. 1549-1558.

- Helfer, R., T. Slovis, and M. Black, 1977, Injuries Resulting When Small Children Fall Out of Bed: *Pediatrics*, v. 60, p. 533-535.
- Hinman, F., D. Morison, and R. Lee-Brown, 1923, Methods of Demonstrating the Circulation in General: As applied to a Study of the Renal Circulation in Particular: *JAMA: The Journal of the American Medical Association*, v. 81, p. 177-184.
- Hoia, D., and A. Micheau, 2010, *e-Anatomy: human anatomy, medical imaging and illustrations*, Montpellier, IMAIOS SAS, www.imaios.com.
- Hobbs, C., 1984, Skull fracture and the diagnosis of abuse: *Arch Dis Child*, v. 59, p. 246-52.
- Hobbs, C., A. M. Childs, J. Wynne, J. Livingston, and A. Seal, 2005, Subdural haematoma and effusion in infancy: an epidemiological study: *Archives of Disease in Childhood*, v. 90, p. 952-955.
- Holbourn, A. H. S., 1943, Mechanics of Head Injuries: *The Lancet*, v. 242, p. 438-441.
- Holland, E., 1922, Cranial Stress in the Fœtus during Labour and on the effects of Excessive Stress on the Intracranial Contents; with an analysis of eighty-one cases of Torn Tentorium Cerebelli and Subdural Cerebral Hamorrhage.1: *BJOG: An International Journal of Obstetrics & Gynaecology*, v. 29, p. 549-571.
- Hopwood, D., 1967, Some aspects of fixation with glutaraldehyde. A biochemical and histochemical comparison of the effects of formaldehyde and glutaraldehyde fixation on various enzymes and glycogen, with a note on penetration of glutaraldehyde into liver: *Journal of anatomy*, v. 101, p. 83-92.
- Hudetz, A., A. Greene, G. Feher, D. Knuese, and A. Cowley, Jr., 1993, Imaging system for three-dimensional mapping of cerebrocortical capillary networks in vivo: *Microvasc Res*, v. 46, p. 293-309.
- Hurley, M., R. Dineen, C. Padfield, S. Wilson, T. Stephenson, H. Vyas, N. McConachie, and T. Jaspán, 2010, Is there a causal relationship between the hypoxia-ischaemia associated with cardiorespiratory arrest and subdural haematomas? An observational study: *British Journal of Radiology*, v. 83, p. 736-743.
- Hymel, K., 2004, Traumatic intracranial injuries can be clinically silent: *The Journal of Pediatrics*, v. 144, p. 701-702.
- Hymel, K., K. Makoroff, A. Laskey, M. Conaway, and J. Blackman, 2007, Mechanisms, Clinical Presentations, Injuries, and Outcomes From Inflicted

- Versus Noninflicted Head Trauma During Infancy: Results of a Prospective, Multicentered, Comparative Study: *Pediatrics*, v. 119, p. 922-929.
- Hymel, K., C. Rumack, T. Hay, J. Strain, and C. Jenny, 1997, Comparison of intracranial computed tomographic (CT) findings in pediatric abusive and accidental head trauma: *Pediatr Radiol*, v. 27, p. 743-7.
- Ichijo, H., M. Hosokawa, and H. Shinkawa, 1993, Differences in size and shape between the right and left sigmoid sinuses: *European Archives of Oto-Rhino-Laryngology*, v. 250, p. 297-299.
- Ichord, R. N., M. Naim, A. N. Pollock, M. L. Nance, S. S. Margulies, and C. W. Christian, 2007, Hypoxic-ischemic injury complicates inflicted and accidental traumatic brain injury in young children: the role of diffusion-weighted imaging: *Journal of neurotrauma*, v. 24, p. 106-18.
- Innis, M., 2006, Vaccines, Apparent Life-Threatening Events, Barlow's Disease, and Questions about "Shaken Baby Syndrome": *Journal of American Physicians and Surgeons*, v. 11.
- Inokuchi, T., R. Yokoyama, H. Satoh, M. Hamasaki, and R. Higashi, 1989, Scanning electron microscopic study of periendothelial cells of the rat cerebral vessels revealed by a combined method of corrosion casting and KOH digestion: *J Electron Microsc (Tokyo)*, v. 38, p. 201-13.
- Itakura, T., K. Yamamoto, M. Tohyama, and N. Shimizu, 1977, Central dual innervation of arterioles and capillaries in the brain: *Stroke*, v. 8, p. 360-5.
- Ito, H., T. Komai, and S. Yamamoto, 1975, Fibrin and fibrinogen degradation products in chronic subdural hematoma: *Neurol Med Chir (Tokyo)*, v. 15 pt 1, p. 51-5.
- Ito, H., T. Komai, and S. Yamamoto, 1978, Fibrinolytic enzyme in the lining walls of chronic subdural hematoma: *Journal of neurosurgery*, v. 48, p. 197-200.
- Ito, H., S. Yamamoto, T. Komai, and H. Mizukoshi, 1976, Role of local hyperfibrinolysis in the etiology of chronic subdural hematoma: *Journal of neurosurgery*, v. 45, p. 26-31.
- Jaspan, T., 2008, Current controversies in the interpretation of non-accidental head injury: *Pediatric radiology*, v. 38 Suppl 3, p. S378-87.
- Jaspan, T., P. D. Griffiths, N. S. McConachie, and J. A. G. Punt, 2003, Neuroimaging for Non-Accidental Head Injury in Childhood: A Proposed Protocol: *Clinical Radiology*, v. 58, p. 44-53.
- Jenny, C., K. Hymel, A. Ritzen, S. Reinert, and T. Hay, 1999, Analysis of Missed Cases of Abusive Head Trauma: *JAMA: The Journal of the American Medical Association*, v. 281, p. 621-626.

- Karnovsky, M. J., 1965, A Formaldehyde-Glutaraldehyde Fixative of High Osmolality for Use in Electron Microscopy, v. 27, p. 137-8A.
- Kasim, M., I. Cheah, and H. Shafie, 1995, Childhood deaths from physical abuse: Child Abuse & Neglect, v. 19, p. 847-854.
- Kawakami, Y., M. Chikama, T. Tamiya, and Y. Shimamura, 1989, Coagulation and fibrinolysis in chronic subdural hematoma: Neurosurgery, v. 25, p. 25-9.
- Kellogg, N., 2007, Evaluation of Suspected Child Physical Abuse: Pediatrics, v. 119, p. 1232-1241.
- Kempe, C., F. Silverman, B. Steele, W. Droegemueller, and H. Silver, 1962, The Battered-Child Syndrome: JAMA: The Journal of the American Medical Association, v. 181, p. 17-24.
- Kfolio, 2012a, Shaken Baby - Brain Damage, Stockmedicalart.com.
- Kfolio, 2012b, Shaken Baby Comparison, Stockmedicalart.com.
- Kiernan, J., 2000, Formaldehyde, formalin, paraformaldehyde and glutaraldehyde: What they are and what they do: Microscopy Today, v. 00, p. 8-12.
- Kiessling, F., D. Razansky, and F. Alves, 2010, Anatomical and microstructural imaging of angiogenesis: European journal of nuclear medicine and molecular imaging, v. 37 Suppl 1, p. S4-19.
- Kilic, T., and A. Akakin, 2008, Anatomy of cerebral veins and sinuses: Frontiers of neurology and neuroscience, Basel, Karger, v. 23, p. 4-15.
- Kirchhof, K., T. Welzel, O. Jansen, and K. Sartor, 2002, More Reliable Noninvasive Visualization of the Cerebral Veins and Dural Sinuses: Comparison of Three MR Angiographic Techniques: Radiology, v. 224, p. 804-810.
- Kiyosue, H., S. Tanoue, Y. Sagara, Y. Hori, M. Okahara, J. Kashiwagi, H. Nagatomi, and H. Mori, 2008, The anterior medullary-anterior pontomesencephalic venous system and its bridging veins communicating to the dural sinuses: normal anatomy and drainage routes from dural arteriovenous fistulas: Neuroradiology, v. 50, p. 1013-23.
- Klinich, D., G. Hulbert, and L. Schneider, 2002, Estimating infant head injury criteria and impact response using crash reconstruction and finite element modeling: Stapp Car Crash J, v. 46, p. 165-94.
- Knott, J., 1881, On the Cerebral Sinuses and their Variations: J Anat Physiol, v. 16, p. 27-42.
- Kogushi, M., S. Nakamura, Y. Kishi, S. Kim, and K. Takahashi, 1988, A study of leukocyte extravasation in early inflammatory changes in the pulp: Journal of Endodontics, v. 14, p. 475-481.

- Kojimahara, M., and G. Ooneda, 1980, Ultrastructural observations on bifurcations in rat cerebral arteries. 1. Young and aging rats: *Virchows Archiv. B, Cell pathology including molecular pathology*, v. 34, p. 21-32.
- Kondo, S., 1998, Microinjection methods for visualization of the vascular architecture of the mouse embryo for light and scanning electron microscopy: *Journal of Electron Microscopy*, v. 47, p. 101-113.
- Koumellis, P., N. S. McConachie, and T. Jaspan, 2009, Spinal subdural haematomas in children with non-accidental head injury: *Archives of disease in childhood*, v. 94, p. 216-9.
- Kraus, J. F., D. Fife, P. Cox, K. Ramstein, and C. Conroy, 1986, Incidence, severity, and external causes of pediatric brain injury: *Am J Dis Child*, v. 140, p. 687-93.
- Kristof, R. A., J. M. Grimm, and B. Stoffel-Wagner, 2008, Cerebrospinal fluid leakage into the subdural space: possible influence on the pathogenesis and recurrence frequency of chronic subdural hematoma and subdural hygroma: *Journal of neurosurgery*, v. 108, p. 275-80.
- Krucker, T., A. Lang, and E. P. Meyer, 2006, New polyurethane-based material for vascular corrosion casting with improved physical and imaging characteristics: *Microscopy research and technique*, v. 69, p. 138-47.
- Krucker, T., A. Schuler, E. P. Meyer, M. Staufenbiel, and N. Beckmann, 2004, Magnetic resonance angiography and vascular corrosion casting as tools in biomedical research: application to transgenic mice modeling Alzheimer's disease: *Neurological research*, v. 26, p. 507-16.
- Kunming Institute of Zoology Chinese Academy of Sciences, 2012, Kunming Institute of Zoology, Chinese Academy of Sciences.
- Lametschwandtner, A., U. Lametschwandtner, and T. Weiger, 1984, Scanning electron microscopy of vascular corrosion casts--technique and applications: *Scan Electron Microsc*, p. 663-95.
- Laskey, A., M. Holsti, D. Runyan, and R. Socolar, 2004, Occult head trauma in young suspected victims of physical abuse: *The Journal of pediatrics*, v. 144, p. 719-722.
- Lauer, B., E. ten Broeck, and M. Grossman, 1974, Battered child syndrome: review of 130 patients with controls: *Pediatrics*, v. 54, p. 67-70.
- Laurent-Vannier, A., M. Nathanson, F. Quiriau, E. Briand-Huchet, J. Cook, T. Billette de Villemeur, J. Chazal, C. Christophe, S. Defoort-Dhellemmes, G. Fortin, C. Rambaud, J. S. Raul, C. Rey-Salmon, F. Sottet, E. Vieux, M. Vinchon, and R. Willinger, 2011, A public hearing "Shaken baby syndrome: Guidelines on establishing a robust diagnosis and the procedures to be

- adopted by healthcare and social services staff". Guidelines issued by the Hearing Commission: *Annals of Physical and Rehabilitation Medicine*, v. 54, p. 600-625.
- Lee, H., and M. Blaufox, 1985, Blood Volume in the Rat: *Journal of Nuclear Medicine*, v. 26, p. 72-76.
- Lee, H., M. Wintermark, A. D. Gean, J. Ghajar, G. T. Manley, and P. Mukherjee, 2008, Focal lesions in acute mild traumatic brain injury and neurocognitive outcome: CT versus 3T MRI: *J Neurotrauma*, v. 25, p. 1049-56.
- Lee, M. C., and R. C. Haut, 1989, Insensitivity of tensile failure properties of human bridging veins to strain rate: implications in biomechanics of subdural hematoma: *J Biomech*, v. 22, p. 537-42.
- Lee, S. I., S. Y. Lee, K. H. Yoon, K. S. Choi, K. Y. Jang, W. H. Yoo, S. H. Kim, T. H. Choi, and J. G. Park, 2009, Molecular MR imaging for visualizing ICAM-1 expression in the inflamed synovium of collagen-induced arthritic mice: *Korean J Radiol*, v. 10, p. 472-80.
- Leestma, J., 2006, "Shaken Baby Syndrome": Do Confessions by Alleged Perpetrators Validate the Concept? : *Journal of American Physicians and Surgeons*, v. 11.
- Leestma, J. E., 2005, Case analysis of brain-injured admittedly shaken infants: 54 cases, 1969-2001: *The American journal of forensic medicine and pathology*, v. 26, p. 199-212.
- Leung, T., I. Tachtsidis, M. Smith, D. Delpy, and C. Elwell, 2006, Measurement of the absolute optical properties and cerebral blood volume of the adult human head with hybrid differential and spatially resolved spectroscopy: *Physics in Medicine and Biology*, v. 51, p. 703.
- Levin, A., 2010, Retinal Hemorrhage in Abusive Head Trauma: *Pediatrics*, v. 126, p. 961-970.
- Levin, A. V., M. R. Magnusson, S. E. Rafto, and R. A. Zimmerman, 1989, Shaken baby syndrome diagnosed by magnetic resonance imaging: *Pediatr Emerg Care*, v. 5, p. 181-6.
- Li, T., P. van Gelderen, H. Merkle, L. Talagala, A. Koretsky, and J. Duyn, 2006, Extensive heterogeneity in white matter intensity in high-resolution T2*-weighted MRI of the human brain at 7.0 T: *Neuroimage*, v. 32, p. 1032-40.
- Liau, L., M. van Buchem, A. Spilt, F. de Bruijne, R. van den Berg, J. Hermans, and M. Wasser, 2000, MR Angiography of the Intracranial Venous System: *Radiology*, v. 214, p. 678-682.
- Lipton, J. M., 1972, Superior sagittal sinus as a chronic venous route in the rat: *Journal of applied physiology*, v. 32, p. 701-2.

- Lloyd, D. A., H. Carty, M. Patterson, C. K. Butcher, and D. Roe, 1997, Predictive value of skull radiography for intracranial injury in children with blunt head injury, *Lancet*, v. 349: England, p. 821-4.
- Looney, C., J. Smith, L. Merck, H. Wolfe, N. Chescheir, R. Hamer, and J. Gilmore, 2006, Intracranial Hemorrhage in Asymptomatic Neonates: Prevalence on MR Images and Relationship to Obstetric and Neonatal Risk Factors¹: *Radiology*, v. 242, p. 535-541.
- Lopez, J. P., J. Roque, J. Torres, and A. V. Levin, 2010, Severe retinal hemorrhages in infants with aggressive, fatal *Streptococcus pneumoniae* meningitis, *J AAPOS*, v. 14: United States, Inc, p. 97-8.
- Lupo, J., Y. Li, C. Hess, and S. Nelson, 2011, Advances in ultra-high field MRI for the clinical management of patients with brain tumors: *Curr Opin Neurol*, v. 24, p. 605-15.
- MacArthur, D., 2014, Personal Communication, Nottingham University Hospitals, NHS Trust.
- MacFarlane, M., Y. Weerakkody, and Y. Kathiravel, 2009, Chronic subdural haematomas are more common on the left than on the right: *J Clin Neurosci*, v. 16, p. 642-4.
- Mack, J., W. Squier, and J. T. Eastman, 2009, Anatomy and development of the meninges: implications for subdural collections and CSF circulation: *Pediatric radiology*, v. 39, p. 200-10.
- Maguire, S., N. Pickerd, D. Farewell, M. Mann, V. Tempest, and A. M. Kemp, 2009, Which clinical features distinguish inflicted from non-inflicted brain injury? A systematic review: *Archives of disease in childhood*, v. 94, p. 860-7.
- Majno, P., P. Loubeyre, G. Mentha, P. Morel, C. Becker, and J. Fasel, 2005, Segmental Anatomy of the Liver, in R. Lencioni, D. Cioni, and C. Bartolozzi, eds., *Focal liver lesions: detection, characterization, ablation*: Germany, Springer, p. 53-62.
- Malkusch, W., M. Konerding, B. Klapthor, and J. Bruch, 1995, A simple and accurate method for 3-D measurements in microcorrosion casts illustrated with tumour vascularization: *Anal Cell Pathol*, v. 9, p. 69-81.
- Manelli, A., S. Sangiorgi, E. Binaghi, and M. Raspanti, 2007, 3D analysis of SEM images of corrosion casting using adaptive stereo matching: *Microscopy Research and Technique*, v. 70, p. 350-354.
- Margulies, S. S., and K. L. Thibault, 2000, Infant skull and suture properties: measurements and implications for mechanisms of pediatric brain injury: *J Biomech Eng*, v. 122, p. 364-71.

- Markowitz, S., K. Saito, and M. A. Moskowitz, 1987, Neurogenically mediated leakage of plasma protein occurs from blood vessels in dura mater but not brain: *J Neurosci*, v. 7, p. 4129-36.
- Martin, E., ed., 2007, *Oxford Concise Medical Dictionary*. 7th ed. : Oxford, Oxford University Press.
- Masters, S., P. McClean, J. Arcarese, R. Brown, J. Campbell, H. Freed, G. Hess, J. Hoff, A. Kobrine, D. Koziol, J. Marasco, D. Merten, H. Metcalf, J. Morrison, J. Rachlin, J. Shaver, and J. Thornbury, 1987, Skull X-Ray Examinations after Head Trauma: *New England Journal of Medicine*, v. 316, p. 84-91.
- Matschke, J., B. Herrmann, J. Sperhake, F. Korber, T. Bajanowski, and M. Glatzel, 2009a, Shaken baby syndrome: a common variant of non-accidental head injury in infants: *Deutsches Arzteblatt International*, v. 106, p. 211-7.
- Matschke, J., K. Püschel, and M. Glatzel, 2009b, Ocular pathology in shaken baby syndrome and other forms of infantile non-accidental head injury: *International Journal of Legal Medicine*, v. 123, p. 189-197.
- Matsumoto, M., N. Kodama, J. Sakuma, S. Sato, M. Oinuma, Y. Konno, K. Suzuki, T. Sasaki, K. Suzuki, T. Katakura, and F. Shishido, 2005, 3D-CT Arteriography and 3D-CT Venography: The Separate Demonstration of Arterial-Phase and Venous-Phase on 3D-CT Angiography in a Single Procedure: *AJNR Am J Neuroradiol*, v. 26, p. 635-641.
- McKinnon, S. G., 1998, Anatomy of the cerebral veins, dural sinuses, sella, meninges, and CSF spaces: *Neuroimaging clinics of North America*, v. 8, p. 101-17.
- Merten, D., D. Osborne, M. Radkowski, and J. Leonidas, 1984, Craniocerebral trauma in the child abuse syndrome: radiological observations: *Pediatr Radiol*, v. 14, p. 272-7.
- Meyer, E., G. Beer, A. Lang, M. Manestar, T. Krucker, S. Meier, D. Mihic-Probst, and P. Groscurth, 2007, Polyurethane elastomer: A new material for the visualization of cadaveric blood vessels: *Clinical Anatomy*, v. 20, p. 448-454.
- Meyer, E., and T. Krucker, 2007, New polyurethane based casting material with improved imaging and physical characteristics: *Advances in Vascular Casting*.
- Miller, J., and R. Nader, 2013, Acute subdural hematoma from bridging vein rupture: a potential mechanism for growth: *J Neurosurg*.
- Miller, R., and M. Miller, 2010, Overrepresentation of males in traumatic brain injury of infancy and in infants with macrocephaly: further evidence that

- questions the existence of shaken baby syndrome: *Am J Forensic Med Pathol*, v. 31, p. 165-73.
- Minnich, B., H. Leeb, E. Bernroider, and A. Lametschwandtner, 1999, Three-dimensional morphometry in scanning electron microscopy: a technique for accurate dimensional and angular measurements of microstructures using stereopaired digitized images and digital image analysis: *Journal of Microscopy*, v. 195, p. 23-33.
- Minns, R. A., and A. Busuttil, 2004, Patterns of presentation of the shaken baby syndrome: Four types of inflicted brain injury predominate: *BMJ*, v. 328, p. 766.
- Morad, Y., Y. Kim, D. Armstrong, D. Huyer, M. Mian, and A. Levin, 2002, Correlation between retinal abnormalities and intracranial abnormalities in the shaken baby syndrome¹ 1 InternetAdvance publication at ajo.com May 29, 2002: *American journal of ophthalmology*, v. 134, p. 354-359.
- Morad, Y., Y. Kim, M. Mian, D. Huyer, L. Capra, and A. Levin, 2003, Nonophthalmologist accuracy in diagnosing retinal hemorrhages in the shaken baby syndrome: *The Journal of Pediatrics*, v. 142, p. 431-434.
- Morison, C., and R. Minns, 2005, The Biomechanics of Shaking, *in* R. Minns, and J. Brown, eds., *Shaking and other non-accidental head injuries in children*: London, Mac Keith Press, p. 142-143.
- MRC, and The Wellcome Trust, 2006, *Primates in Medical Research*, Medical Research Council (MRC) & the Wellcome Trust, p. 1-21.
- Muhlfeld, C., B. Rothen-Rutishauser, D. Vanhecke, F. Blank, P. Gehr, and M. Ochs, 2007, Visualization and quantitative analysis of nanoparticles in the respiratory tract by transmission electron microscopy: *Particle and fibre toxicology*, v. 4, p. 11.
- Murakami, T., 1971, Application of the scanning electron microscope to the study of the fine distribution of the blood vessels: *Arch Histol Jpn*, v. 32, p. 445-54.
- Murakami, T., T. Fujita, and H. Hinenoya, 1992, A modified method for vascular casting and scanning electron microscopy: its utility in the demonstration of rat pancreatic insulo-acinar and other blood vascular systems: *Arch Histol Cytol*, v. 55 Suppl, p. 233-8.
- Murakami, T., S. Hitomi, A. Ohtsuka, T. Taguchi, and T. Fujita, 1997, Pancreatic insulo-acinar portal systems in humans, rats, and some other mammals: scanning electron microscopy of vascular casts: *Microscopy research and technique*, v. 37, p. 478-88.

- Nabeshima, S., T. S. Reese, D. M. Landis, and M. W. Brightman, 1975, Junctions in the meninges and marginal glia: *J Comp Neurol*, v. 164, p. 127-69.
- Nakagawa, T., and E. Conway, 2004, Shaken baby syndrome: Recognizing and responding to a lethal danger: *Contemporary Pediatrics*.
- Nakai, K., H. Imai, I. Kamei, T. Itakura, N. Komai, H. Kimura, T. Nagai, and T. Maeda, 1980, Scanning Electron Microscopic Investigation on the Plastic Cast Model of Small Cerebral Blood Vessels: *Neurologia medico-chirurgica*, v. 20, p. 155-161.
- Nakai, K., H. Imai, I. Kamei, T. Itakura, N. Komari, H. Kimura, T. Nagai, and T. Maeda, 1981, Microangioarchitecture of rat parietal cortex with special reference to vascular "sphincters". Scanning electron microscopic and dark field microscopic study: *Stroke*, v. 12, p. 653-659.
- Nakai, K., Y. Naka, H. Yokote, T. Ikatura, H. Imai, N. Komai, and T. Maeda, 1989, Vascular "sphincter" and microangioarchitecture in the central nervous system: constriction of intraparenchymal blood vessels following a treatment of vasoconstrictive neurotransmitter: *Scanning Microsc*, v. 3, p. 337-41.
- Nanoprobes Inc., 1992, Nanoprobes Gold Nanoparticles: NanoGold Labels for Imaging.
- Narat, J. K., J. A. Loef, and M. Narat, 1936, On the preparation of multicolored corrosion specimens: *The Anatomical Record*, v. 64, p. 155-160.
- Netter, F., 2006, *Atlas of Human Anatomy*: Pennsylvania, Elsevier Saunders.
- Nierenberger, M., R. Wolfram-Gabel, S. Decock-Catrin, N. Boehm, Y. Remond, J. L. Kahn, and S. Ahzi, 2013, Investigation of the human bridging veins structure using optical microscopy: *Surg Radiol Anat*, v. 35, p. 331-7.
- Nimityongskul, P., and L. D. Anderson, 1987, The likelihood of injuries when children fall out of bed: *J Pediatr Orthop*, v. 7, p. 184-6.
- O'Dell, C., and R. Boothe, 1997, The development of stereoacuity in infant rhesus monkeys: *Vision Research*, v. 37, p. 2675-2684.
- Ohkuma, H., and S. Ryan, 1983, Vascular casts of experimental subretinal neovascularization in monkeys: *Investigative Ophthalmology & Visual Science*, v. 24, p. 481-490.
- Ommaya, A. K., F. Faas, and P. Yarnell, 1968, Whiplash injury and brain damage: an experimental study: *JAMA*, v. 204, p. 285-9.
- Ommaya, A. K., W. Goldsmith, and L. Thibault, 2002, Biomechanics and neuropathology of adult and paediatric head injury: *Br J Neurosurg*, v. 16, p. 220-42.

- Orlowski, J., and D. Szpilman, 2001, Drowning: Rescue, Resuscitation, and Reanimation: *Pediatric Clinics of North America*, v. 48, p. 627-646.
- Oshita, K., M. Oshima, Y. H. Gao, K. H. Lee, and S. Motomizu, 2002, Adsorption behavior of mercury and precious metals on cross-linked chitosan and the removal of ultratrace amounts of mercury in concentrated hydrochloric acid by a column treatment with cross-linked chitosan: *Anal Sci*, v. 18, p. 1121-5.
- Padget, D., 1957, *The development of the cranial venous system in man, from the viewpoint of comparative anatomy*: Washington.
- Padget, D. H., 1956, The cranial venous system in man in reference to development, adult configuration, and relation to the arteries: *American Journal of Anatomy*, v. 98, p. 307-355.
- Pang, D., and I. F. Pollack, 1989, Spinal cord injury without radiographic abnormality in children--the SCIWORA syndrome: *J Trauma*, v. 29, p. 654-64.
- Papaiconomou, C., A. Zakharov, N. Azizi, J. Djenic, and M. Johnston, 2004, Reassessment of the pathways responsible for cerebrospinal fluid absorption in the neonate: *Childs Nerv Syst*, v. 20, p. 29-36.
- Plunkett, J., 2001, Fatal pediatric head injuries caused by short-distance falls: *Am J Forensic Med Pathol*, v. 22, p. 1-12.
- Pollanen, M., 2011, Subdural hemorrhage in infancy: keep an open mind: *Forensic Science, Medicine, and Pathology*, v. 7, p. 298-300.
- Powell, R., 2012, Personal Communication, Nanoprobos.
- Prange, M. T., B. Coats, A. C. Duhaime, and S. S. Margulies, 2003, Anthropomorphic simulations of falls, shakes, and inflicted impacts in infants: *J Neurosurg*, v. 99, p. 143-50.
- Provenzale, J., 2010, Imaging of Traumatic Brain Injury: A Review of the Recent Medical Literature: *Am. J. Roentgenol.*, v. 194, p. 16-19.
- Quayle, K., D. Jaffe, N. Kuppermann, B. Kaufman, B. Lee, T. Park, and W. McAlister, 1997, Diagnostic Testing for Acute Head Injury in Children: When Are Head Computed Tomography and Skull Radiographs Indicated?: *Pediatrics*, v. 99, p. e11.
- Rafaat, K., R. Spear, C. Kuelbs, K. Parsapour, and B. Peterson, 2008, Cranial computed tomographic findings in a large group of children with drowning: diagnostic, prognostic, and forensic implications: *Pediatr Crit Care Med*, v. 9, p. 567-72.
- Raz, N., U. Lindenberger, K. Rodrigue, K. Kennedy, D. Head, A. Williamson, C. Dahle, D. Gerstorf, and J. Acker, 2005, Regional Brain Changes in Aging

- Healthy Adults: General Trends, Individual Differences and Modifiers: *Cerebral Cortex*, v. 15, p. 1676-1689.
- RCPATH, 2009, Report of a Meeting on the Pathology of Traumatic Head Injury in Children, London.
- RCPCH, and RCOphth, 2013, Abusive Head Trauma and the Eye in Infancy, London, The Royal College of Paediatrics and Child Health & The Royal College of Ophthalmologists, Clinical Guidelines, p. 1-106.
- Reiber, G. D., 1993, Fatal falls in childhood. How far must children fall to sustain fatal head injury? Report of cases and review of the literature: *Am J Forensic Med Pathol*, v. 14, p. 201-7.
- Reina-De La Torre, F., A. Rodriguez-Baeza, and J. Sahuquillo-Barris, 1998, Morphological characteristics and distribution pattern of the arterial vessels in human cerebral cortex: a scanning electron microscope study: *Anat Rec*, v. 251, p. 87-96.
- Renton, P., 2004, Medical Imaging an Illustrated Colour Text: London, Elsevier Churchill Livingstone.
- Riew, C., and R. Smith, 1971, Modified osmium tetroxide stain for the microscopy of rubber-toughened resins: *Journal of Polymer Science Part A-1: Polymer Chemistry*, v. 9, p. 2739-2744.
- Rogers, C. B., H. H. Itabashi, U. Tomiyasu, and E. T. Heuser, 1998, Subdural neomembranes and sudden infant death syndrome: *J Forensic Sci*, v. 43, p. 375-6.
- Romano, C., T. Brown, and T. Frewen, 1993, Assessment of pediatric near-drowning victims: Is there a role for cranial CT?: *Pediatric Radiology*, v. 23, p. 261-263.
- Rooks, V. J., J. P. Eaton, L. Ruess, G. W. Petermann, J. Keck-Wherley, and R. C. Pedersen, 2008, Prevalence and evolution of intracranial hemorrhage in asymptomatic term infants: *AJNR. American journal of neuroradiology*, v. 29, p. 1082-9.
- Rosenberg, K., and W. Trevathan, Bipedalism and human birth: The obstetrical dilemma revisited.
- Roth, G., J. Mattison, M. Ottinger, M. Chachich, M. Lane, and D. Ingram, 2004, Aging in Rhesus Monkeys: Relevance to Human Health Interventions: *Science*, v. 305, p. 1423-1426.
- Roth, S., J.-S. Raul, B. Ludes, and R. Willinger, 2007, Finite element analysis of impact and shaking inflicted to a child: *International Journal of Legal Medicine*, v. 121, p. 223-228.

- Royal College of Surgeons in Ireland, 2014, Anatomical Society Summer Meeting 2013: Form and Function in Regenerative Medicine & The Dark Art of Learning Outcomes: *Journal of Anatomy*, v. 224, p. 228-249.
- Rubin, D., C. Christian, L. Bilaniuk, K. Zazyczny, and D. Durbin, 2003, Occult Head Injury in High-Risk Abused Children: *Pediatrics*, v. 111, p. 1382-1386.
- San Millán Ruíz, D., P. Gailloud, D. Rufenacht, J. Delavelle, F. Henry, and J. Fasel, 2002, The craniocervical venous system in relation to cerebral venous drainage: *AJNR Am J Neuroradiol*, v. 23, p. 1500-8.
- San Millán Ruíz, D., P. Gailloud, H. Yilmaz, F. Perren, J. Rathgeb, D. Rufenacht, and J. Fasel, 2006, The petrosquamosal sinus in humans: *J Anat*, v. 209, p. 711-20.
- Sane, S., P. Kleinman, R. Cohen, M. Di Pietro, J. Seibert, B. Wood, and M. Zerlin, 2000, Diagnostic imaging of child abuse: *Pediatrics*, v. 105, p. 1345-8.
- Sangiorgi, S., A. Manelli, C. Dell'Orbo, and T. Congiu, 2006, A new method for the joint visualization of vascular structures and connective tissues: Corrosion casting and 1 N NaOH maceration: *Microscopy Research and Technique*, v. 69, p. 919-923.
- Sato, Y., W. T. C. Yuh, W. L. Smith, R. C. Alexander, S. C. S. Kao, and C. J. Ellerbe, 1989, Head Injury in Child Abuse - Evaluation with MR Imaging: *Radiology*, v. 173, p. 653-657.
- Saulsbury, F. T., and B. A. Alford, 1982, Intracranial bleeding from child abuse: the value of skull radiographs: *Pediatr Radiol*, v. 12, p. 175-8.
- Schachenmayr, W., and R. Friede, 1978, The origin of subdural neomembranes. I. Fine structure of the dura-arachnoid interface in man: *Am J Pathol*, v. 92, p. 53-68.
- Schneider, P., T. Krucker, E. Meyer, A. Ulmann-Schuler, B. Weber, M. Stampanoni, and R. Muller, 2009, Simultaneous 3D visualization and quantification of murine bone and bone vasculature using micro-computed tomography and vascular replica: *Microsc Res Tech*, v. 72, p. 690-701.
- Schultz, A. H., 1949, Sex differences in the pelves of primates: *Am J Phys Anthropol*, v. 7, p. 401-23.
- Schutzman, S., and D. Greenes, 2001, Pediatric minor head trauma: *Annals of emergency medicine*, v. 37, p. 65-74.
- Shearing, P., D. Eastwood, R. Bradley, J. Gelb, S. Cooper, F. Tariq, D. Brett, N. Brandon, P. Withers, and P. Lee, 2013, Exploring electrochemical devices using X-ray microscopy: 3D microstructure of batteries and fuel cells, *Microscopy and Analysis*, London, John Wiley & Sons Ltd, p. 19-22.

- Sherwood, C., A. Gordon, J. Allen, K. Phillips, J. Erwin, P. Hof, and W. Hopkins, 2011, Aging of the cerebral cortex differs between humans and chimpanzees: *Proceedings of the National Academy of Sciences*, v. 108, p. 13029-13034.
- Si, Z., L. Luan, D. Kong, G. Zhao, H. Wang, K. Zhang, T. Yu, and Q. Pang, 2008, MRI-based investigation on outflow segment of cerebral venous system under increased ICP condition: <http://ukpmc.ac.uk/abstract/MED/18499557>, v. 13, p. 121-6.
- Solter, M., and D. Paljan, 1973, Variations in shape and dimensions of sigmoid groove, venous portion of jugular foramen, jugular fossa, condylar and mastoid foramina classified by age, sex and body side: *Zeitschrift für Anatomie und Entwicklungsgeschichte*, v. 140, p. 319-335.
- Sowell, E., B. Peterson, P. Thompson, S. Welcome, A. Henkenius, and A. Toga, 2003, Mapping cortical change across the human life span: *Nat Neurosci*, v. 6, p. 309-315.
- Squier, W., 2009, Shaken Baby Syndrome, *Wiley Encyclopedia of Forensic Science*, John Wiley & Sons, Ltd.
- Squier, W., and J. Mack, 2009, The neuropathology of infant subdural haemorrhage: *Forensic science international*, v. 187, p. 6-13.
- Starling, S., J. Holden, and C. Jenny, 1995, Abusive Head Trauma: The Relationship of Perpetrators to Their Victims: *Pediatrics*, v. 95, p. 259-262.
- Starling, S. P., S. Patel, B. L. Burke, A. P. Sirotnak, S. Stronks, and P. Rosquist, 2004, Analysis of perpetrator admissions to inflicted traumatic brain injury in children, *Arch Pediatr Adolesc Med*, v. 158: United States, p. 454-8.
- Stein, K., K. Ruf, M. Ganten, and R. Mattern, 2006, Representation of cerebral bridging veins in infants by postmortem computed tomography: *Forensic Science International*, v. 163, p. 93-101.
- Stolz, E., 2006, Cerebral veins and sinuses: *Frontiers of neurology and neuroscience*, v. 21, p. 182-93.
- Stoodley, N., 2005, Neuroimaging in non-accidental head injury: if, when, why and how: *Clinical Radiology*, v. 60, p. 22-30.
- Streeter, G. L., 1915, The development of the venous sinuses of the dura mater in the human embryo: *American Journal of Anatomy*, v. 18, p. 145-178.
- Stroobandt, G., P. Evrard, and C. Laterre, 1978, [Pathogenesis of persistent subdural effusions in infants (author's transl)]: *Neurochirurgie*, v. 24, p. 47-51.

- Szabó, K., 1995, The cranial venous system in the rat: anatomical pattern and ontogenetic development: II. Dorsal drainage: *Annals of Anatomy*, v. 177, p. 313-322.
- Takaku, T., D. Malide, J. Chen, R. Calado, S. Kajigaya, and N. Young, 2010, Hematopoiesis in 3 dimensions: human and murine bone marrow architecture visualized by confocal microscopy: *Blood*, v. 116, p. e41-e55.
- Tarantino, C. A., M. D. Dowd, and T. C. Murdock, 1999, Short vertical falls in infants: *Pediatr Emerg Care*, v. 15, p. 5-8.
- Taylor, S., R. Quencer, B. Holzman, and T. Naidich, 1985, Central nervous system anoxic-ischemic insult in children due to near-drowning: *Radiology*, v. 156, p. 641-646.
- Tompsett, D., 1969, 'Anatomical Injections' Arnott Demonstration at the Royal College of Surgeons of England on 23rd April 1969: Arnott Demonstration.
- Toribatake, Y., K. Tomita, N. Kawahara, H. Baba, H. Ohnari, and S. Tanaka, 1997, Regulation of vasomotion of arterioles and capillaries in the cat spinal cord: role of alpha actin and endothelin-1: *Spinal Cord*, v. 35, p. 26-32.
- Towner, D., M. A. Castro, E. Eby-Wilkens, and W. M. Gilbert, 1999, Effect of Mode of Delivery in Nulliparous Women on Neonatal Intracranial Injury: *New England Journal of Medicine*, v. 341, p. 1709-1714.
- Trachsel, S., K. Purkabiri, O. Loup, H. Jenni, B. Eberle, M. Ochs, and A. Kadner, 2011, High-quality lung fixation by controlled closed loop perfusion for stereological analysis in a large animal model: *The Journal of surgical research*, v. 166, p. e97-102.
- Trenchs, V., A. Curcoy, J. Pou, M. Morales, and A. Serra, 2005, Retinal haemorrhages as proof of abusive head injury: *The Journal of Pediatrics*, v. 146, p. 437-438.
- Tuerkheimer, D., 2009, The Next Innocence Project: Shaken Baby Syndrome and the Criminal Courts: *Washington University Law Review*, Vol. 87, No. 1, 2009.
- Uddin, M. A., T. U. Haq, and M. Z. Rafique, 2006, Cerebral venous system anatomy: *JPMA. The Journal of the Pakistan Medical Association*, v. 56, p. 516-9.
- Ulmann-Schuler, A., T. Krucker, and E. Meyer, 2007, PU4ii vascular casting combined with histological staining methods: *Advances in Vascular Casting*.
- Uscinski, R. H., 2006, Shaken baby syndrome: an odyssey: *Neurologia medico-chirurgica*, v. 46, p. 57-61.

- Uscinski, R. H., and D. K. McBride, 2008, The shaken baby syndrome: an odyssey. II Origins and further hypotheses: *Neurologia medico-chirurgica*, v. 48, p. 151-5; discussion 155-6.
- VasQtec, 2004, VasQtec.
- Vasquez, S., F. Gao, F. Su, V. Grijalva, J. Pope, B. Martin, J. Stinstra, M. Masner, N. Shah, D. Weinstein, R. Farias-Eisner, and S. Reddy, 2011, Optimization of MicroCT Imaging and Blood Vessel Diameter Quantitation of Preclinical Specimen Vasculature with Radiopaque Polymer Injection Medium: *PLoS ONE*, v. 6, p. e19099.
- Verli, F. D., T. R. Rossi-Schneider, F. L. Schneider, L. S. Yurgel, and M. A. de Souza, 2007, Vascular corrosion casting technique steps: *Scanning*, v. 29, p. 128-32.
- Vežina, G., 2009, Assessment of the nature and age of subdural collections in nonaccidental head injury with CT and MRI: *Pediatric Radiology*, v. 39, p. 586-590.
- Vignes, J. R., A. Dagain, J. Guerin, and D. Liguoro, 2007, A hypothesis of cerebral venous system regulation based on a study of the junction between the cortical bridging veins and the superior sagittal sinus. Laboratory investigation: *Journal of neurosurgery*, v. 107, p. 1205-10.
- Vinchon, M., I. Delestret, S. DeFoort-Dhellemmes, M. Desurmont, and N. Noulé, 2010a, Subdural hematoma in infants: can it occur spontaneously? Data from a prospective series and critical review of the literature: *Child's Nervous System*, v. 26, p. 1195-1205.
- Vinchon, M., M. Desurmont, G. Soto-Ares, and S. De Foort-Dhellemmes, 2010b, Natural history of traumatic meningeal bleeding in infants: semiquantitative analysis of serial CT scans in corroborated cases: *Child's Nervous System*, v. 26, p. 755-762.
- Watson, E. A., and M. J. Monteiro, 2009, Advise use of rear facing child car seats for children under 4 years old: *BMJ*, v. 338, p. b1994.
- Weber, B., A. Keller, J. Reichold, and N. Logothetis, 2008, The Microvascular System of the Striate and Extrastriate Visual Cortex of the Macaque: *Cerebral Cortex*, v. 18, p. 2318-2330.
- Wedro, B., 2012, Coma Symptoms, Causes, Treatment - Bleeding (Hemorrhage), *in* W. J. Shiel, ed., *MedicineNet*, Inc. ©2012, WebMD, LLC. All rights reserved.
- Weiger, T., A. Lametschwandtner, and P. Stockmayer, 1986, Technical parameters of plastics (Mercox CL-2B and various methylmethacrylates)

- used in scanning electron microscopy of vascular corrosion casts: *Scan Electron Microsc*, p. 243-52.
- Weinstein, J. D., and T. R. Hedges, Jr., 1962, Studies of intracranial and orbital vasculature of the rhesus monkey (*Macaca mulatta*): *Anat Rec*, v. 144, p. 37-41.
- Whitby, E. H., P. D. Griffiths, S. Rutter, M. F. Smith, A. Sprigg, P. Ohadike, N. P. Davies, A. S. Rigby, and M. N. Paley, 2004, Frequency and natural history of subdural haemorrhages in babies and relation to obstetric factors: *Lancet*, v. 363, p. 846-51.
- Williams, R., 1991, Injuries in infants and small children resulting from witnessed and corroborated free falls: *J Trauma*, v. 31, p. 1350-2.
- Wilson, M., P. Enevoldson, and B. Menezes, 2008, Intracranial dural arterio-venous fistula: *Practical Neurology*, v. 8, p. 362-369.
- Wyganski-Jaffe, T., Y. Morad, and A. V. Levin, 2009, Pathology of retinal hemorrhage in abusive head trauma: *Forensic Sci Med Pathol*, v. 5, p. 291-7.
- Yamashima, T., and R. Friede, 1984, Why do bridging veins rupture into the virtual subdural space?: *J Neurol Neurosurg Psychiatry*, v. 47, p. 121-7.
- Yamashima, T., S. Yamamoto, and R. L. Friede, 1983, The role of endothelial gap junctions in the enlargement of chronic subdural hematomas: *Journal of neurosurgery*, v. 59, p. 298-303.
- Yarnell, P., and A. K. Ommaya, 1969, Experimental cerebral concussion in the rhesus monkey: *Bulletin of the New York Academy of Medicine*, v. 45, p. 39-45.
- Yu, Y., J. Chen, Z. Si, G. Zhao, S. Xu, G. Wang, F. Ding, L. Luan, L. Wu, and Q. Pang, 2010, The Hemodynamic Response of the Cerebral Bridging Veins to Changes in ICP: *Neurocritical Care*, v. 12, p. 117-123.
- Zagorchev, L., P. Oses, Z. Zhuang, K. Moodie, M. Mulligan-Kehoe, M. Simons, and T. Couffinhal, 2010, Micro computed tomography for vascular exploration: *Journal of Angiogenesis Research*, v. 2, p. 7.

Appendices

Appendix 1: Brief History of Resins and VCC

Casting methods have been present for over 500 years as Leonardo da Vinci first made wax casts by injecting into cerebral ventricles (Haviland and Parish, 1970). Current methods of VCC are based on a study carried out by Jan Swammerdam, who used carefully adjusted mixtures that solidified and remained flexible when cold so that casts did not become brittle, however, melted at relatively low temperatures (Tompsett, 1969). In 1882, Paul Schiefferdecker introduced celloidin dissolved in ether for casting media, which was then improved by Storch in 1899 who used celluloid instead of celloidin and therefore increased resistance of casts after drying (Narat et al., 1936).

In 1903, Krassuskaja found that addition of camphor can strengthen the casts as well as increasing the rate at which they harden (Narat et al., 1936). A similar mixture was then used by Hinman in 1923 who found that decreasing the injection mass viscosity would allow perfusion of smaller vessels (Hinman et al., 1923). Resin products such as polyester and acrylic resins as well as silicone were used in the 1950s which greatly improved VCC methods (Kondo, 1998).

In 1971, Takuro Murakami introduced a low viscosity semi-polymerised methyl methacrylate medium which could be analysed using SEM. This was a great advancement in VCC as it allowed rapid perfusion of small capillaries (Murakami et al., 1997). It combined superior characteristics such as resistance to corrosion, dissection and further processing, electron conductivity with electron bombardment resistance and rapid but even polymerisation. It has therefore been the most widely used resin for producing vascular casts. Methyl methacrylate resins can be either laboratory prepared or are commercially available (Giuvarasteanu, 2007). These include Mercoc (Sangiorgi et al., 2006), Clear Flex 95 (Krucker et al., 2006) and Baston's compound (Baile et al., 2000). However Baston 17 has lower vessel penetrability with no difference in resistance to electron accelerating voltage (Verli et al., 2007).

Although Mercoc (a commercialised form of the low viscosity semi-polymerised methyl methacrylate medium) can produce detailed vascular casts (Murakami et al., 1997), it has been found to have a minimum shrinkage of 8.018% (Weiger et al., 1986). More recently a new polyurethane based resin, PU4ii has been

developed which has shown to be superior to other resins. It is highly elastic, low in viscosity, resistant to corrosion and causes little shrinkage (Heinzer et al., 2006; Krucker et al., 2006; Meyer and Krucker, 2007).

Appendix 2: Protocol for Optical Clearing of Tissue using Scaleview-A2

A case for making a mouse brain transparent:

1. Transcardially perfuse an anaesthetised mouse with 4% paraformaldehyde (PFA)/PBS.
2. Remove the whole brain and subject it to post-fixation in 4% PFA/PBS at 4°C for 10 hours and cryo-protect in 20% sucrose/PBS at 4°C for 24 hours.
3. Embed the sample in OCT compound and freeze it.
4. Thaw and rinse the sample in PBS, and fix it again with 4% PFA/PBS for 20 minutes at room temperature.
5. Clear the sample by incubation in Scaleview-A2.
 - a. More than 30ml of Scaleview-A2 is required for an adult mouse brain.
 - b. A full week of incubation may be necessary for transparency.
 - c. During incubation, stir slowly using an orbital shaker.
 - d. Exchanging Scaleview-A2 each day accelerates the transparency process.
 - e. The sample might be expanded 10-30% in one direction after incubation.
6. Perform deep imaging of the transparent brain using an appropriate dipping objective lens. Use Scaleview-A2 as the immersion medium. If necessary, immobilize the sample to the bottom of the imaging vessel with agarose.
7. The transparent brain can be stored for a long time in Scaleview-A2.

Caution: If the solution comes into contact with your skin, this may cause dermatitis. In these cases, please take the following treatment immediately:

- For skin: wash with water and soap.
- For eyes: Rinse with fresh water for 15 minutes or more.
- If the appearance of skin or eyes is altered or pain persists, see your doctor immediately.
- For accidental ingestion: induce vomiting, rinse out mouth with fresh water and consult with a doctor immediately.

Appendix 3: Solutions required for transcardiac perfusionPre-wash solution: for 1 litre

Sodium barbitone	5.9g
Sodium acetate trihydrate	3.9g
N/10HCl	120ml
Distilled H ₂ O	880ml
NaCl	9.0g
KCl	0.3g
CaCl ₂ ·H ₂ O	0.2g
MgCl ₂	0.05g
Dextran 60	40g
Dextran 40	60g
Procaine hydrochloride	1g

Fixative for Histology/Immunocytochemistry: 1 litre

Paraformaldehyde powder	40g
Distilled H ₂ O	500ml
0.2M PBS	500ml

Note on fixative preparation: Heat to 60°C (becomes insoluble above 70°C) to dissolve powder and when cloudy add a couple of drops of 1M NaOH to clear solution. Add 0.2M PBS to give final concentration of 4% PFA in 0.1M PBS.

Post Fixative Wash: 1 Litre

PBS	1000ml
Sucrose	75.2g

Starting Solution temperatures

- Pre-wash - place in water bath at 37°C
- Fixative - Keep on ice final temperature approximately 21°C (room temperature)

Note: all solutions for perfusion fixation must be filtered through 0.4µm Millipore filter before use. All solutions should be stored at 4°C.

Equipment

- 2 bottles connected to each other in series for gas flow and fluid delivery
- 3-way stop cocks
- Source of compressed N₂
- In line pressure gauge reading mmHg
- Needle: 16G

Procedure

Anaesthetic: Sodium pentobarbitone (60mg/kg) administered IP. Once the toe stretch reflex lost (reflex pathway shared with spinothalamic tract) the animal is ready for surgery.

Surgery

1. Spray thorax with 70% ethanol to prevent hair entering the thorax when surgical incision is made
2. Using toothed forceps (surgical) to hold the skin, cut through at the level of the costal angle
3. Find costal angle and cut through the muscle and lower edge of the rib cage with a rounded tip scissors - take care to raise the cage using the forceps and always cutting upward avoiding damage to the thoracic contents i.e. heart and vessels below.
4. Extend the cut to just above the sternum and place a small protractor into the space between the cut ribs and expand and click into position.
5. With fine toothed forceps and scissors dissect away the pericardium to reveal the apex beat of the left ventricle and the right atrium.
6. Ensure that warm pre-wash solution (37°C) has been taken up into the delivery tube with needle (16G). Gently pierce the apex beat with the needle securing it with a small clip taking care not to push the needle too far (you can see position of the needle by gently raising the needle to "see" it through the heart wall). If you push too far the needle will enter the right atrium and the perfusion short-circuited. Another point to observe is to ensure that the clip holding the needle in position does not clamp the opening of the

- needle.
7. Immediately cut the right atrium taking care not to damage the left atrium by cutting too far.
 8. Turn on the perfusion fluid and slowly increase the perfusion pressure until it reaches 200mmHg. Perfuse 500ml of prewash solution at this high pressure (keep at 37°C throughout).
 9. Turn on the fixative solution, which is kept at approximately 21°C (room temperature) while the prewash solution is turned off simultaneously. Slowly increase the perfusion pressure until it reaches 200mmHg for a duration of approximately 5 minutes, and continue to perfuse a total of 500ml of fixative solution. Note that successful perfusion will be indicated by the rapid contraction of the skeletal muscles as the fixative reaches the periphery.
 10. At the end of this procedure the rat is completely fixed and the tissue does not need to be further submerged in fixative. Store fixed tissue at 4°C until required.

Note: after perfusion wash out all the tubes with distilled water to prevent any bacterial growth.

Appendix 4: Procedure for Volume Rendering and Approximating Vessel Size from microCT and 3D XRM Imaging Datasets

Open the required dataset in Image J (NIH) and use the 'Simple Neurite Tracer' plug-in for volume rendering of the scanned images taken via either microCT or 3D XRM imaging. This is done by carrying out the following basic steps:

1. File → Open → (Dataset to be analysed in the form of an '.nii' volumetric file)
2. Analyze → Local Thickness → Local Thickness (complete process) → OK
3. Plugin → 3D Viewer → OK

Using the same plug-in, the local thicknesses of the cerebral vessels can then then be categorised by colour, and this is indicated by a calibration bar:

4. Analyze → Tools → Calibration Bar Menu

Appendix 5: Procedure for Processing Tissue and Embedding in Araldite Resin for Transmission Electron Microscopy

Reagents

- 2% aqueous osmium tetroxide
- 1% glutaraldehyde and 4% PFA fixative solution
- 0.2M Phosphate/Cacodylate buffer
- Grades of ethanol
- Propylene oxide (Propox)
- Araldite resin

Procedure

- Cut tissue to small size (1mm³ is ideal). Fix tissue overnight.
- Wash in 0.1M phosphate/cacodylate buffer, prepared by mixing equal volumes of 0.2M buffer stock solution and distilled water
- Post fix tissue in 1% osmium tetroxide for 1-2 hours
- Wash for 1 x 5min in distilled water
- Dehydrate in graded ethanol series.
 1. 2 x 15 min - 50% ethanol
 2. 2 x 15 min - 70% ethanol
 3. 2 x 15 min - 90% ethanol
 4. 3 x 20 min - Absolute ethanol
 5. 2 x 15 min - 100% propylene oxide (propox) – it may be necessary to use acetone in some circumstances e.g. with cell inserts.
- Infiltrate with resin (see procedure below)
 1. 4 hours in 3:1 propox : resin
 2. Overnight in 1:1 propox : resin – leave lids off the bottles
 3. In fresh bottles, 3 x 2.5 hours in 100% resin
- Embed in an appropriate plastic mould and polymerise

Procedure for preparing resins

- Add 25ml Araldite CY212 resin, 15ml Agar 100 resin and 55ml DDSA to a 'tripour' beaker
- Stir well
- Add 2ml Dibutyl phthalate and 1.5ml DMP 30 (use only if opening date is less than 6 months ago)
- Stir well until there are no striations and bubbles are evenly distributed

- Stir occasionally to keep above conditions, colour should change from red-orange to orange
- Cover with tin foil when leaving the resin to limit exposure and spillage chance
- Polymerise for 48 hours at 60°C

Always wear gloves and a lab coat when working with resin and keep it in a fume cupboard. Resins are TOXIC when unpolymerised (resin dust, from polymerised blocks, is also toxic).

Appendix 6: Protocol for Resin Embedding Samples for TEM: using Durcupan (a water soluble embedding medium)

1. Fixing and Dehydrating:

Fix the tissue in osmium tetroxide, potassium permanganate, or 10% formaldehyde (with Veronal buffer, pH 7-7.5). Dehydrate through various concentrations of Component A on a shaker, with the concentration of Component A increasing in consecutive stages, as shown in the following table:

Dehydration bath:

1 st Tray	50% Component A with 50% water*	30 minutes
2 nd Tray	70% Component A with 30% water*	45 minutes
3 rd Tray	90% Component A with 10% water*	45 minutes
4 th Tray	100% Component A	90 minutes
5 th Tray	100% Component A	90 minutes

*Aqueous solution of the following contrast agents may be added to the contents of these trays: Osmium tetroxide, phosphotungstic acid, uranyl acetate. Do not add lead hydroxide (see section on Contrasting below).

2. Embedding

The dehydrated tissue is now placed in a polymerisation mixture of the following composition:

Component	Volume	Miscibility with water
A	5ml	All proportions
B	11.7ml	Nil
C	1.0-1.2ml (very critical*)	Limited
D	0.2-0.4ml	nil

*Insufficient component C: the block becomes too soft. Excess of component C: the block becomes granular.

Leave the tissue overnight at 4-5 °C in this comparatively viscous mixture on a shaker is possible.

3. Polymerisation

Then fill the gelatine capsules with freshly prepared polymerisation mixture of the same composition and charge them with tissue specimens. Polymerisation occurs at 37-45°C and takes 3-4 days.

Contrasting

The tissue fixed with formaldehyde showed very low contrast in the electron microscope, an advantage for certain histochemical investigations. However, for purely morphological investigations, contrasting agents must be used. The following heavy-metal compounds are suitable for this purpose: osmium tetroxide, phosphotungstic acid, lead hydroxide and uranyl acetate. Contrasting can be carried out in two ways: Either let the mount mesh covered with ultrathin specimens float for about an hour on a solution of these heavy-metal compounds, or add the aqueous heavy-metal compound solution (but not lead hydroxide) to the dehydration bath trays marked*.

The blocks obtained following this embedding method are mostly softer than methacrylate blocks and present certain difficulties in the preparation of ultrathin sections, particularly because of the chatter, a frequent occurrence. Ordinary glass knives or knives made of the harder Tempax glass are suitable for ultra-microtomy (diamond knives did not produce any better results than glass knives). The sections can be caught in a solution of 20-50°C acetone in water.

If the Durcupan blocks are too soft, try to cut the tissue out and re-embed it in pre-polymerised methacrylate. Such Durcupan/methacrylate blocks are usually much easier to cut.

Caution: Take great care when working with Durcupan, as this substance may cause skin irritation and allergic reactions. Always wear gloves. Immediately wash off droplets on the skin with 3% boric acid solution. Wash hands, arms, and face frequently in lukewarm soap water.

Appendix 7: Procedure for Staining Semi-thin Sections with Toluidine Blue O

Applications and Objectives

This procedure is used to stain 0.25 to 0.5 μm epoxide or acrylic resin sections for light microscopy and to impart the originally low-contrast semi-thin sections of these resin-embedded materials.

Materials Needed

- 1% aqueous sodium borate
- 1% Toluidine blue O
- Storage bottle for stain solution
- 10ml plastic syringe with 0.45mm pore size filter attached
- Hot plate
- DPX
- Glass microscope slides
- Glass coverslips
- Distilled water
- Transfer loop

Procedure

Stain Preparation. Dissolve 0.25g of sodium borate in 25ml of distilled water. Add 0.25g of toluidine blue O and stir. Store at room temperature. Fill a 10ml syringe with some of the stain and affix a 0.45 μm filter to the syringe.

Section Staining

- Pick up semi-thin sections (cut at 1 μm thickness using a Leica Microsystem Ultracut machine) with a transfer loop and transfer to a drop of distilled water

on a glass microscope slide. The droplet should be approximately 1-1.5cm in diameter and should be applied just before the sections are added.

- Immediately place the slide on a hot plate at approximately 60°C and wait until the drop of water has totally evaporated.
- Add just enough of the toluidine blue O staining solution to cover sections.
- When the edge of the stain drop just begins to turn to a metallic gold colour (15-30 seconds), quickly remove the slide from the hot plate and direct a stream of distilled water from a squeeze bottle just above the stain drop so that the stain is quickly and completely washed from the slide into a waste beaker.
- Wipe any water from the bottom of the slide, circle the area containing sections (on the bottom of the slide) with a permanent marker pen and put the slide back onto the hot plate until totally dry.
- Place 1-2 drops of DPX onto the sections and carefully place a coverslip onto the slide to minimize any bubbles in the DPX. Examine with a light microscope.

Results Expected

Sections should be wrinkle- and dirt-free, with different components of the sample exhibiting different shades of blue (Dykstra and Reuss, 2003).

Appendix 8: Procedure for Staining Ultra-Thin Sections for TEM

Applications and Objectives

This procedure is meant to impart contrast to resin-embedded ultra-thin sections. The stained ultra-thin sections should have sufficient contrast to be easy to visualize on a TEM viewing screen.

Materials Needed

Uranyl acetate

Lead nitrate

Sodium citrate

Distilled water

100% methanol

Parafilm™

Petri-dishes

Forceps

Ultrathin (60-90 nm thick) sections on grids

Filter paper

1 N NaOH

50ml volumetric flask with a plastic snap-cap

20 to 50ml brown glass storage container (or foil-wrapped glass container)

50ml disposable beakers

Procedure

Stain Preparation:

- *Methanolic Uranyl acetate*: Add 1.25g Uranyl acetate to 25ml of absolute or 50% methanol in a brown glass bottle or storage container wrapped in aluminium foil to protect from light. Sonicate the solution until little precipitate is visible. Store the solution at room temperature. It is ready to use after standing overnight. A small amount of precipitate in the bottom of the container is acceptable, since the solution is essentially saturated. The solution may be stored for about 1 month and used until it has evidence of precipitate or stained grids have noticeable Uranyl acetate crystals (needle-like dirt) when viewed with the TEM.
- *Reynolds' (1963) lead citrate*: To a 50ml volumetric flask with a plastic snap cap add the following in the order listed:
 - 30ml of distilled water
 - 1.33g of $Pb(NO_3)_2$ (lead nitrate)
 - 1.76g of $Na_3(C_6H_3O_7)H_2O$ (sodium citrate)
- Shake the flask continuously for 1 minute and then allow to stand with intermittent shaking for an additional 30 minutes. Then add 0.32g of NaOH pellets. The previously milky solution should change quickly to an absolutely clear solution with no evidence of precipitate. Dilute to a final volume of 50ml with distilled water. The final pH is approximately 12. The stain can be stored at 4°C for 1-3 months. If it becomes cloudy, or any precipitate is visible, discard the solution.

Staining Resin Sections

- Prepare a square of Parafilm™ slightly smaller than a plastic petri-dish and attach it to the bottom of the dish by applying pressure to the four corners of the Parafilm™ square with the blunt end of a pair of forceps.
- Place 1 drop of methanolic uranyl acetate on to the Parafilm™. Touch the section-side (shiny side) of a grid to the drop, turn grid over, and leave the grid section-side up at the bottom of the drop. Cover the petri-dish staining chamber and leave for 5 minutes.

- Retrieve the grid from the drop of uranyl acetate with forceps and quickly dip three times in each of a series of three 50ml disposable beakers containing distilled or deionized water, pH 6.0-7.5. Enter the first rinse beaker gently and do not agitate excessively as this may wrinkle or dislodge the sections.
- Blot the grid dry by touching a piece of filter paper to the edge of the grid where it is held by the forceps. Repeat on the opposite side of the forceps. Blot the grid on clean filter paper in a petri-dish on both sides, and then slide a fresh part of the filter paper between the forceps blades and use it to push the grid out of the forceps and onto a clean and dry piece of the filter paper in the petri-dish.
- Using the same chamber, put one drop of Reynolds' lead citrate on the Parafilm™ and insert grid as previously described. Quickly cover the dish and leave for 8 minutes.
- While the grid is staining, empty the rinse beakers and wash them thoroughly with deionized water. Refill with distilled or deionized water, pH 6.0-7.5. After the grids have been stained for 8 minutes, rinse and blot dry as above. They are now ready for examination with the TEM.

Results Expected

The grids should have sufficient contrast to be seen easily on the TEM screen, with membranes, ribosomes, DNA in the nucleus, glycogen, and proteinaceous elements clearly defined.

Appendix 9: Protocol for Anaesthesia of the Rhesus macaque (*Macaca mulatta*)

The Schedule 1 killing procedure will be carried out as follows:

1. Premedication with ketamine HCl (i.m., 10mg/kg)
2. The rhesus macaque is then transferred to the surgical table after becoming unconscious and after exhibiting loss of protective reflexes.
3. The rhesus macaque will then be injected with barbitone (i.v., 20mg/kg).
4. Heart rate, respiratory rate and pupil dilation are monitored to confirm death. After death of the animal is confirmed by the veterinary surgeon, the rhesus macaque will be fixed via transcatheter perfusion.
5. No adverse effects apply as all surgical procedures will be carried out post-mortem. These are standard methods of material preservation.

Appendix 10: Protocol for tissue processing and wax embedding of pre-fixed brain tissue for histology

Macroscopically cut the tissues so that areas of interest can be placed into a standard histological processing cassette, before placing them into an automatic tissue processor. An automatic tissue processor has a series of pots containing ethanol of increasing strengths to remove the water content of the tissue, which are then followed by pots containing a solvent which acts as a link between the ethanol and the final molten wax baths.

Tissues are processed in the following solutions (under vacuum) for a total of 17 hours 30 minutes:

70% Ethanol	1 hour 30 minutes
80% Ethanol	1 hour 30 minutes
95% Ethanol	1 hour 30 minutes
Absolute Ethanol	1 hour
Absolute Ethanol	1 hour
Absolute Ethanol	1 hour
Chloroform	3 hours
Chloroform	3 hours
Paraffin wax	2 hours
Paraffin wax	2 hours

Once the tissues are processed, transfer tissue into a metal mould before filling with molten wax (approximately 65°C). Then place a labelled processing cassette on top of the tissue. Place the mould onto a cold plate to allow the tissue to set. The processing cassette will act as a firm base which will be used to allow the wax tissue block to be clamped to a microtome, ready for sectioning.

Appendix 11: Protocol for Microtome Sectioning of Wax-embedded Tissue

1. Clamp the base of the wax block into a microtome (Leica).
2. Each time the microtome handle is turned, it advances the specimen by 15µm, allowing thin sections of tissue to be cut via a ribbon.
3. Float tissue sections onto a water bath (approximately 40°C) to smooth out the wax sections.

4. Carefully pick up the smoothed out tissue sections from the surface of the water using an APES coated microscope slide.
5. Drain slides of any excess water and dry on a hotplate (set at approximately 50°C). This allows the tissue to stick to the slide prior to staining.

Appendix 12: Procedure for Staining tissue with Haematoxylin and Eosin (H&E) and Cover-slipping Prepared Histology Slides

Dehydrate wax sections through:

Xylene	5 minutes
Xylene	5 minutes
Absolute Ethanol	30 seconds
Absolute Ethanol	30 seconds
90% Ethanol	30 seconds
70% Ethanol	30 seconds
50% Ethanol	30 seconds
Running Tap Water	30 seconds

1. Submerge slides for 5 minutes in Harris Haematoxylin.
2. Wash in a bath of running tap water until the water clears.
3. Dip in Acid Alcohol for 5-10 seconds.
4. Wash in a bath of running tap water until the water clears.
5. Dip in Lithium Carbonate/ Scott's Tap Water for 1 minute.
6. Wash in a bath of running tap water until the water clears.
7. Check the samples have gone blue using the microscope.
8. Submerge slides for 5 minutes in 1% Eosin.
9. Quickly rinse in a bath of running tap water (Note: Eosin is removed by water and ethanol).
10. Dip into the 50%, 70%, 90% and 100% ethanol solutions for 10 seconds each.
11. Dip into fresh Xylene for 2 minutes.
12. Dip into Finishing Xylene for 2 minutes.
13. Remove slide and wipe excess xylene from around the section.
14. Add a few drops of DPX (mounting medium) to an appropriately sized glass coverslip and mount the stained sections.